Heat Transfer Performance Investigation of Nanofluids Flow in Pipe

UNIVERSITY
of
GLASGOW

GOUTAM SAHA

Heat Transfer Performance Investigation of Nanofluids Flow in Pipe

A Thesis Submitted for the degree
of Doctor of Philosophy

in the
School of Engineering
of the
University of Glasgow

By
Goutam Saha
B.Sc. & M.S.

Systems, Power & Energy Research Division
School of Engineering
University of Glasgow
Glasgow, UK

September, 2016

Supervised by
Dr. Manosh C. Paul

This work is dedicated to
my parents, my wife Mili Saha and my son
Asmit Ayaan Saha

Declaration

I hereby confirm that all the results presented in this thesis are of the original works of mine. Any ideas or techniques taken from the published works of others have been acknowledged properly in accordance with the standard referencing practices.

.....
Goutam Saha
September, 2016

Abstract

Different types of base fluids, such as water, engine oil, kerosene, ethanol, methanol, ethylene glycol etc. are usually used to increase the heat transfer performance in many engineering applications. But these conventional heat transfer fluids have often several limitations. One of those major limitations is that the thermal conductivity of each of these base fluids is very low and this results a lower heat transfer rate in thermal engineering systems. Such limitation also affects the performance of different equipments used in different heat transfer process industries. To overcome such an important drawback, researchers over the years have considered a new generation heat transfer fluid, simply known as nanofluid with higher thermal conductivity. This new generation heat transfer fluid is a mixture of nanometre-size particles and different base fluids. Different researchers suggest that adding spherical or cylindrical shape of uniform/non-uniform nanoparticles into a base fluid can remarkably increase the thermal conductivity of nanofluid. Such augmentation of thermal conductivity could play a more significant role in enhancing the heat transfer rate than that of the base fluid.

Nanoparticles diameters used in nanofluid are usually considered to be less than or equal to 100 *nm* and the nanoparticles concentration usually varies from 5% to 10%. Different researchers mentioned that the smaller nanoparticles concentration with size diameter of 100 *nm* could enhance the heat transfer rate more significantly compared to that of base fluids. But it is not obvious what effect it will have on the heat transfer performance when nanofluids contain small size nanoparticles of less than 100 *nm* with different concentrations. Besides, the effect of static and moving nanoparticles on the heat transfer of nanofluid is not known too. The idea of moving nanoparticles brings the effect of Brownian motion of nanoparticles on the heat transfer. The aim of this work is, therefore, to investigate the heat transfer performance of nanofluid using a combination of smaller size of nanoparticles with different concentrations considering the Brownian motion of nanoparticles. A horizontal pipe has been considered as a physical system within which the above mentioned nanofluid performances are investigated under transition to turbulent flow conditions.

Three different types of numerical models, such as single phase model, Eulerian-Eulerian multi-phase mixture model and Eulerian-Lagrangian discrete phase model have been used while investigating the performance of nanofluids. The most commonly used model is single phase model which is based on the assumption that nanofluids behave like a conventional fluid. The other two models are used when the interaction between solid and fluid particles is considered. However, two different phases, such as fluid and solid phases is also considered in the Eulerian-Eulerian multi-phase mixture model. Thus, these phases create a fluid-solid mixture. But, two phases in the Eulerian-Lagrangian discrete phase model are independent. One of them is a solid phase and the other one is a fluid phase.

In addition, RANS (Reynolds Average Navier Stokes) based Standard $\kappa - \omega$ and SST $\kappa - \omega$ transitional models have been used for the simulation of transitional flow. While the RANS based Standard $\kappa - \epsilon$, Realizable $\kappa - \epsilon$ and RNG $\kappa - \epsilon$ turbulent models are used for the simulation of turbulent flow. Hydrodynamic as well as temperature behaviour of transition to turbulent flows of nanofluids through the horizontal pipe is studied under a uniform heat flux boundary condition applied to the wall with temperature dependent thermo-physical properties for both water and nanofluids.

Numerical results characterising the performances of velocity and temperature fields are presented in terms of velocity and temperature contours, turbulent kinetic energy contours, surface temperature, local and average Nusselt numbers, Darcy friction factor, thermal performance factor and total entropy generation. New correlations are also proposed for the calculation of average Nusselt number for both the single and multi-phase models. Result reveals that the combination of small size of nanoparticles and higher nanoparticles concentrations with the Brownian motion of nanoparticles shows higher heat transfer enhancement and thermal performance factor than those of water.

Literature suggests that the use of nanofluids flow in an inclined pipe at transition to turbulent regimes has been ignored despite its significance in real-life applications. Therefore, a particular investigation has been carried out in this thesis with a view to understand the heat transfer behaviour and performance of an inclined pipe under transition flow condition. It is found that the heat transfer rate decreases with the increase of a pipe inclination angle. Also, a higher heat transfer rate is found for a

horizontal pipe under forced convection than that of an inclined pipe under mixed convection.

Acknowledgement

I would like to say thanks to my supervisor, Dr Manosh Paul, for his supervision and encouragement during this research. His inspiring comments and suggestions motivated me to continue my research work. From his remarkable support and advice during my PhD studies, I gained a lot of experience and knowledge which will help me in future. I would have never been able to reach the goal without his support. Also, Dr Manosh Paul gave me time to solve any of my problems and that discussion helped me to share my problems that would cause frustration during the transition periods of my PhD. I am also grateful to the Scottish Overseas Research Students Award Scheme (SORSAS) as well as the School of Engineering of the University of Glasgow for the financial support given to me for this study. I am extremely grateful to my parents, wife and son as well as all of my well-wishers for their support.

Contents

List of Figures

List of Tables

List of symbols

A_0, A_1, C_1, C_2, $C_{1\epsilon}$, $C_{2\epsilon}$	RANS model constants
$\vec{a}$	Nanoparticles acceleration
A	Al_2O_3-water nanofluid
A_r	Nanoparticles aspect ratio
Be	Bejan number
C_c	Cunningham correction
C_p	Specific heat capacity (J/kgK)
C_s	Roughness constant
C_μ	Turbulent viscosity (Pas)
D	Einstein diffusion coefficient
D_h	Diameter of a pipe (m)
d_f	Fluid molecular diameter (m)
d_p	Diameter of nanoparticles (nm)
D_w^+	Positive portion of the cross diffusion term
E_{gen}	Total Entropy generation
$E_{gen,t}$	Thermal entropy generation
$E_{gen,f}$	Frictional entropy generation
F_D	Drag coefficient
F_1, F_2	Blending functions
F	Darcy friction factor
f_r	Roughness function
f_μ	Dumping function
$\vec{g}$	Gravitational acceleration (m/s^2)
G_k	Generation of turbulent kinetic energy
G_ω	Production of ω
H	Heat transfer coefficient
H	Sensible enthalpy
I	Turbulent intensity
K_s	Roughness height
K_s^+	Non-dimensional roughness height
L	Length (m)
M	Molecular weight of the base fluid

M_{t0}	Model constant
$\dot{m}$	Mass flow rate (kg/s)
m_p	Mass of nanoparticles
N	Avogadro number
N	Number of phases
N_x, N_r	Number of grid distribution in axial and radial directions, respectively
Nu	Local Nusselt number
$\overline{Nu}$	Average Nusselt number
Nu_c	Critical Nusselt number
P	Pressure (N/m^2)
Pe	Peclet number
Pr	Prandtl number
$\dot{q}_s$	Heat flux of the pipe (W/m^2)
R	Radius of a pipe (m)
Re	Reynolds number
Re_p	Nanoparticles Reynolds number
$R_\kappa, R_\beta, R_\omega$	Model constants
R	Radial coordinate (m)
S	Modulus of the mean rate of strain tensor
S_m	Source terms for momentum equation
S_e	Source terms for energy equation
T	TiO_2-water nanofluid
T_{nf}, t	Time average and fluctuating temperature (K)
T_{fr}	Freezing point of the base fluid (K)
T_w	Temperature at the wall (K)
T_m	Mean temperature of a fluid (K)
u_B	Nanoparticles mean Brownian velocity (m/s)
u_τ	Friction velocity (m/s)
V_m	Mean fluid velocity (m/s)
v	Velocity (m/s)
$\vec{v}$	Time average velocity component (m/s)
$\vec{v}_{dr}$	Drift velocity
X	Axial coordinate (m)
$x_{c,V}$	Hydrodynamic critical distance (m)

$x_{c,T}$	Thermal critical distance (m)
Y_κ, Y_ω	Dissipation of κ and ω respectively
DPM	Discrete phase model
MPM	Multi-phase mixture model
SPM	Single phase model
RANS	Reynolds Average Navier Stokes

Greek symbols

P	Density (kg/m^3)
μ	Dynamic viscosity $(kg/\ ms)$
Λ	Thermal conductivity (W/mK)
λ_{mp}	Mean free path of fluid
λ_{mf}	Mean free path of nanoparticles
K	Turbulent kinetic energy (m^2/s^2)
ϵ	Dissipation rate of Turbulent kinetic energy (m^2/s^3)
κ	Kinematic viscosity (m^2/s)
σ_t	Constant of turbulent Prandtl number
μ_t	Turbulent molecular viscosity
σ_κ	Effective Prandtl number for turbulent kinetic
σ_ϵ	Effective Prandtl number for rate of dissipation
X	Nanoparticles concentration
Γ	Exchange coefficient for general transport
ξ	Thermal performance factor
ζ	Non-dimensional parameter
$\zeta^*, \beta^*_\infty, \beta_i, \beta_1, \beta_2$	Model constants
$\alpha^*_\infty, \alpha_\infty, \alpha_0, \alpha_1$	Model constants
τ_D	Time (s)
τ_w	Wall shear stress
$\overline{\tau_\tau}$	Ratio of average shear stress coefficient ratio
Ω	Rate of rotation tensor
ω_k	Angular velocity
Θ	Inclination angle

Subscripts

Av	Average
Eff	Effective

F	Base fluid
In	Inlet
Ls	Laminar sub-layer
M	Mixture
Mean	Mean
nf	Nanofluid
Out	Outlet
P	Nanoparticles
S	Solid phase
W	Wall

Chapter 1

1.1 Introduction

Fluids are frequently used as heat carriers in heat transfer equipment. Examples of important uses of heat transfer fluids include vehicular and avionics cooling systems in the transportation industry, hydraulic heating and cooling systems in buildings, industrial process heating as well as cooling systems in petrochemical, textile, pulp and paper, chemical, food and other processing plants. In all of these applications, the thermal conductivity of heat transfer fluids plays a vital role in the development of energy-efficient heat transfer equipment. No doubt, industries have a strong need to develop advanced heat transfer fluids with significantly higher thermal conductivities than are presently available during the period of an increasing global competition. [1]

It has to be admitted that despite considerable previous research and development efforts put on heat transfer enhancement, few important improvements in cooling capabilities have been constrained because of the low thermal conductivity of conventional heat transfer fluids. However, it is well known that metals in solid form have orders-of-magnitude larger thermal conductivities than fluids at room temperature. For example, the thermal conductivity of copper at room temperature is 700 times greater than that of water and is 3000 times greater than that of engine oil. And, the thermal conductivity of metallic liquids is much greater than that of non-metallic liquids. Therefore, the thermal conductivities of fluids that contain suspended solid metallic particles are expected to be significantly more enhanced when compared with conventional heat transfer fluids. [1]

A decade ago, a new kind of heat transfer fluid called nanofluid was introduced which was derived from stably suspending nanoparticles in conventional heat transfer fluids, usually liquids. Commonly used oxide nanoparticles are Aluminium (Al), Silicon (Si), Titanium (Ti), Copper (Cu), Zinc (Zn), Iron (Fe), Magnesium (Mg) and Silver (Ag); and base fluids are water, engine oil, kerosene, ethanol, methanol, ethylene glycol and mono ethylene glycol. Nanofluids consisting of such nanoparticles suspended in liquids have been shown to enhance the thermal conductivity as well as convective heat transfer performance of the base fluids. Hence, research is in

progress to introduce nanofluids in many thermal applications where the conventional fluids are not capable of improving the rate of heat transfer any further.

For the first time, Choi [1] at Argonne National Laboratory had used nanoparticles suspended in a conventional heat transfer fluid and proposed that the addition of nanometer size particles into the base fluid helped to increase the thermal conductivity and hence enhanced the heat transfer rate of nanofluid. Later on, various applications of nanofluids were found in electronic cooling components [2], transportation [3], industrial cooling [4], heating buildings and reducing pollution [5], nuclear systems cooling [6], space and defence [7, 8], energy storage [9], solar absorption [10], friction reduction [11], magnetic sealing [12], antibacterial activity [13], nanodrug delivery [14], intensify micro reactors [15], microbial fuel cells [16] and so on.

In conventional cases, the suspended particles into the base fluids are of micro meter dimension. The use of micro sized particle colloids generally causes particle settling, tube erosion and channel clogging or abrasion. These problems are highly undesirable in many practical applications. Nanofluids have pioneered in overcoming these problems by stably suspending in fluids nanometer sized particles instead of micrometer sized particles. Nanoparticles stay suspended much longer than microparticles and possess a much higher surface area than larger particles. If particles settle rapidly like microparticles, more particles need to be added to replace the settled particles resulting in extra cost and degradation in the heat transfer enhancement. To overcome this drawback, there is a strong motivation to develop advanced heat transfer fluids with substantially higher conductivities to enhance thermal characteristics. Also, nanoparticles have about 20% of their atoms near the surface allowing them to absorb and transfer heat efficiently. But, micro-particles have most of their atoms far beneath the surface where they cannot participate in heat transfer. In addition, the suspended particles increase the surface area and the heat capacity of fluid. That is, a significant improvement in the effective thermal conductivity is achieved as a result of decreasing the size of the suspended particles (nanometer sized particles) rather than using larger particles (micro-meter sized particles). Since heat transfer occurs on the surface of a solid, this feature greatly enhances the heat conduction contribution of the fluid. [1]

However, there are few differing results found by different researchers where they mentioned that degeneration of heat transfer could be possible using nanofluids. For example, Santra *et al.* [17, 18] studied heat transfer characteristics of copper-water nanofluid in a differentially heated square cavity by treating the nanofluid as both Newtonian and non-Newtonian fluids and they reported a decrease in heat transfer by increasing the nanoparticles concentration for a particular Rayleigh number (Ra). Also, Rashmi *et al.* [19] presented a study on numerical simulations of natural convection heat transfer in Al_2O_3-water nanofluids. Their numerical results showed decrease in the heat transfer with the increase in nanoparticles concentration. The reason of such degeneration of heat transfer was the combined effect of dynamic viscosity and thermal conductivity of nanofluid. Abu-Nada *et al.* [20, 21] also showed the degeneration of heat transfer in horizontal annuli using water-based nanofluids containing Cu, Ag, Al_2O_3 and TiO_2 nanoparticles. It was observed that for $Ra = 10^4$, the average Nusselt number had been reduced by increasing the nanoparticles concentration. It was due to the inertia forces which caused the adverse effect of the nanoparticles to become more severe. Therefore, there is still a controversy on the role of nanofluids in natural convection heat transfer. But to the best of our knowledge, no such controversy has been reported in forced and mixed convection heat transfer. Therefore, our focus of attention in the thesis is on the forced and mixed convection heat transfer of nanofluids flowing through a pipe under transition to turbulent flow regimes.

1.2 Outline of the Thesis

Chapter 1 presents an introduction to new generation heat transfer fluid known as nanofluid and how the use of nanofluid affects the heat transfer performance in engineering systems. Also, outline of the thesis is presented too. Besides, the list of publications and awards are also mentioned.

Chapter 2 presents a literature review on the nanofluids flow in pipe under the laminar, transition and turbulent flow regimes. The objective of the thesis is presented too.

Chapter 3 presents three different mathematical models namely single phase, multi-phase mixture and discrete phase models to govern the incompressible fluid flow and heat transfer in a pipe. Two different transitional $\kappa - \omega$ models namely SST $\kappa - \omega$

and Standard $\kappa-\omega$ models are introduced. And three different turbulent $\kappa-\epsilon$ models namely Standard $\kappa-\epsilon$, RNG $\kappa-\epsilon$ and Realizable $\kappa-\epsilon$ models are also presented. In addition, thermophysical properties of water, nanofluids and nanoparticles are presented.

In Chapter 4, hydrodynamic and heat transfer behaviours in a horizontal pipe with smooth pipe wall surface are investigated first by using the single phase model under transition flow regime. A particular investigation is then carried out for rough pipe wall with uniform roughness. Besides, new correlations are proposed for the calculation of hydrodynamic and thermal critical distances as well as the average Nusselt number using Al_2O_3-H_2O and TiO_2-H_2O nanofluids.

In Chapter 5, multi-phase mixture model is used to understand the effect of the interaction between nanoparticles and fluid particles on heat transfer under transition flow regime. Also, two new correlations are proposed for the average Nusselt number using Al_2O_3-H_2O and TiO_2-H_2O nanofluids. Moreover, a particular investigation is carried out for the rough pipe wall with uniform roughness. In addition, heat transfer enhancement analysis is presented to compare the performance of heat transfer rate using the single and multi-phase models.

In Chapter 6, heat transfer performance of Al_2O_3-H_2O and TiO_2-H_2O nanofluids using single phase model is investigated numerically under turbulent flow regime. Also, some new correlations are proposed for the calculation of average Nusselt number using the non-linear regression analysis.

In Chapter 7, heat transfer and entropy generation analysis are presented using the multi-phase mixture model under turbulent flow regime. Two new correlations are also proposed for the calculation of average Nusselt number using non-linear regression analysis.

In Chapter 8, performance of new solid-fluid mixture and the effect of interaction between water and nanoparticles on the heat transfer are investigated using discrete phase model under laminar, transition and turbulent flow regimes.

In Chapter 9, a numerical investigation is performed on heat transfer in mixed convection for transition flow in inclined pipe. Here, the effect of inclination angles and Buoyancy force on heat transfer is also presented.

Chapter 10 provides conclusion and recommendations for future work.

1.3 Publications and Recognitions

1. Saha, G., Paul, M.C. ,Heat transfer and entropy generation of turbulent forced convection flow of nanofluids in a heated pipe, International Communications in Heat and Mass Transfer, 61 (2015) 15-30. ISSN: 0735-1933.

2. Saha, G., Paul, M.C., Discrete Phase Approach for Nanofluids Flow in Pipe, International Journal of Material Science & Engineering– IJMSE, 2(1) (2015) 39-43. ISSN: 2374-149X.

3. Saha, G., Paul, M.C., Numerical analysis of the heat transfer behaviour of water based Al_2O_3 and TiO_2 nanofluids in a circular pipe under the turbulent flow condition, International Communications in Heat and Mass Transfer, 56 (2014) 96-108. ISSN: 0735-1933.

4. Saha, G., Paul, M.C., Analysis of Heat Transfer and Entropy Generation of TiO_2-Water Nanofluid Flow in a Pipe under Transition, 6th BSME International Conference on Thermal Engineering (ICTE 2014), 19 - 21 December, 2014, Dhaka, Bangladesh. Procedia Engineering, Volume 105, 2015, Pages 381–387. ISSN: 1877-7058.

5. Saha, G., Paul, M.C., Discrete Phase Approach for Nanofluids Flow in Pipe, Proceedings of the Second International Conference on Advances in Civil, Structural and Mechanical Engineering - CSM 2014, p. 99-103, November 16-17, 2014 at Birmingham, UK. ISBN: 978-1-63248-006-5.

6. Saha, G., Paul, M.C., Analysis of Heat Transfer Behaviour using Nanofluids, Poster Presentation, Book of Abstract is published in "Ideas Exchange: Exploring the Impact of PhD Research", 30th July, 2014, Organized by College of Science & Engineering, University of Glasgow, Scotland, UK.

7. Saha, G., Paul, M.C., Discrete Phase Approach for Nanofluids Flow in Pipe. Best paper Award in Second International Conference on Advances in Civil, Structural and Mechanical Engineering at Birmingham, UK, November 16-17, 2014.

8. Saha, G., Paul, M.C., Numerical analysis of the heat transfer behaviour of water based Al_2O_3 and TiO_2 nanofluids in a circular pipe under the turbulent flow condition. Awarded the certificate for ScienceDirect Top 25 List of Most Downloaded Articles Ranked 11th on the Top 25 for International Communications in Heat and Mass Transfer - July to September 2014.

9. Saha, G., Paul, M.C., Heat transfer and entropy generation of turbulent forced convection flow of nanofluids in a heated pipe. Awarded the certificate for ScienceDirect Top 25 List of Most Downloaded Articles Ranked 13th on the Top 25 for International Communications in Heat and Mass Transfer - January to March 2015.

Chapter 2

Literature Review

At present times, industrial technology related to heat transfer has considerably been concerned to design new tools and research to apply nanofluids is in progress in order to enhance the heat transfer rate. Therefore, the focus of concentration is on the experimental and numerical studies conducted in laminar to turbulent nanofluids flow with single phase, Eulerian-Eulerian mixture model and Eulerian-Lagrangian discrete phase approaches. In this chapter, several experimental and numerical research works related to nanofluids flow in pipe or tube have been presented and discussed. This chapter also illustrates the studies on laminar, transition and turbulent flows. Finally, the objective of the thesis is presented.

2.1 Laminar Flow

Heris *et al.* [22] and Hwang *et al.* [23] experimentally investigated the heat transfer behaviour of Al_2O_3–water nanofluid inside a circular tube under laminar flow regime. Their investigation showed, the heat transfer coefficient was increased for different nanoparticles concentrations and such enhancement was due to the presence of nanoparticles in the base fluid. It was also found that the increase of the thermal conductivity of nanofluid had not been the only reason for such enhancement. There were several factors including chaotic movement and Brownian motion of nanoparticles which might also assist to enhance the heat transfer rate. A similar experimental investigation was carried out by Anoop *et al.* [24] and Esmaeilzadeh *et al.* [25] and their work revealed how the nanoparticles diameters had made an impact on the enhancement of the heat transfer. Firstly Anoop *et al.* [24] demonstrated that Al_2O_3–water nanofluid with nanoparticles diameter of 45 nm had showed the higher heat transfer enhancement of 25% for $Re = 1550$ and $\chi = 4\%$ than that of the nanoparticles diameter of 150 nm. Esmaeilzadeh *et al.* [25] showed the heat transfer enhancement of about 6.8% for $\chi = 0.5\%$ and 19.1% for $\chi = 1.0\%$ with a nanoparticles diameter of 15 nm. In addition, Mojarrad *et al.* [26] carried out an experimental investigation using both Al_2O_3–water and Al_2O_3–water–ethylene glycol based nanofluids inside a circular tube under laminar flow regime. They observed,

the average heat transfer rate was higher for Al_2O_3–water–ethylene glycol nanofluid than Al_2O_3–water nanofluid. Also, a numerical investigation was carried out by Davarnejad *et al.* [27] in order to check the effect of different nanoparticles concentrations and diameters on heat transfer performance. Davarnejad *et al.* [27] numerically studied the heat transfer characteristics of Al_2O_3-water nanofluid flowing through a circular pipe. Five different concentrations and two different size diameters were used in this study. They observed that smaller diameter of nanoparticles with higher concentration had showed higher heat transfer coefficient.

From the above findings, it can be summarized that higher heat transfer rate was observed for Al_2O_3–water nanofluid than water. Also, higher enhancement was observed while using base fluid like water–ethylene glycol instead of water. Moreover, increase of the nanoparticles concentration showed the enhancement of heat transfer rate and such enhancement became more significant with the decrease of nanoparticles diameter. It suggested, the base fluids, nanoparticles, nanoparticles concentrations and diameters had effect on the heat transfer performance. That created a particular interest to see whether the different types of base fluids could play a role on the heat transfer performance which is discussed below.

Maiga *et al.* [28], Bajestan *et al.* [29] and Bayat and Nikseresht [30] numerically investigated the heat transfer characteristics of Al_2O_3 nanoparticles with different base fluids such as water, Ethylene Glycol (EG) or mixture of Ethylene Glycol (EG) and water inside a circular tube under laminar flow regime. After their investigation, it was reported that the water based nanofluids had showed inferior heat transfer enhancement than the other base fluids. Also, Moraveji *et al.* [31] numerically studied the effect of nanoparticles diameters for Al_2O_3–water nanofluid. They considered two different size of nanoparticles of 45 *nm* and 150 *nm* and four different nanoparticles concentrations of 1, 2, 4 and 6% respectively. And, the smaller sizes of nanoparticles were found to demonstrate higher heat transfer rate than the large sizes of nanoparticles with the increase of nanoparticles concentrations.

All these investigations were done using the spherical shape of nanoparticles. But, there are several other researches which have also been done using non-spherical nanoparticles. Some common non-spherical shapes of nanoparticles are disk, diamond, platelets, blades, cylinders, bricks and rectangular. Among those, cylindrical shape nanoparticles have been used extensively. Therefore, following researches

have been carried out to see the performance of cylindrical shape nanoparticles used in the base fluid like polyalphaolefins.

Lin *et al.* [32] numerically investigated the friction factor and heat transfer behaviour of non-aqueous polyalphaolefins-Al_2O_3 nanofluid containing cylindrical nanoparticles under laminar flow regime. In this research, non-aqueous polyalphaolefins-Al_2O_3 as nanofluid was used because it became infeasible in many practical applications due to their limits in the dielectric property and the operating temperature range [32]. Also, non-uniform distribution of nanoparticles along the pipe was considered during the research work because most of the research had been carried out using uniform distribution of nanoparticles. Moreover, many experimental research works have been found using cylindrical shape nanoparticles but very few numerical studies were done. According to Lin *et al.* [32], the goal of their research was to investigate the effect of non-uniform distribution of cylindrical nanoparticles inside the pipe on friction factor and heat transfer under laminar flow regime. It was observed that the heat transfer rate had been higher near the upstream than at the downstream because of non-uniform distribution of nanoparticles. They also proposed the following correlation to calculate the average Nusselt number for cylindrical nanoparticles with non-aqueous polyalphaolefins-Al_2O_3 nanofluids.

$$Nu = 4.47224 + 0.01114\,\zeta - 2.72459 \times 10^{-6}\zeta^2 + 2.31761 \times 10^{-10}\zeta^3 \tag{2.1}$$

where ζ was a non-dimensional parameter and was defined as

$$\zeta = \frac{Re\ Pr\ D_h \sqrt[4]{log(A_r \chi)}}{L} \tag{2.2}$$

Single phase models were used in the articles presented above and the performance of the model on heat transfer was shown. The interaction between fluid particles and nanoparticles were not taken into account in the single phase models. In order to consider the interaction between the fluid and solid particles, a new model was introduced known as multi-phase mixture model. Therefore, research articles related to the multi-phase model are presented hereafter.

Mirmasoumi and Behzadmehr [33] and Fard *et al*. [34] examined the effectiveness of multi-phase model compared to the single phase model for different nanofluids and nanoparticles diameter flowing through a horizontal circular tube in laminar flow regime. It was observed while comparing the results between the models and the

experimental data that the performance of multi-phase model had been more accurate than the single phase model to justify the enhancement of heat transfer rate. Also, Goktepe *et al.* [35] numerically investigated the performance of single phase model, single phase dispersion model, Eulerian-mixture two phase model and Eulerian-Eulerian two phase model. They found the performance of single phase dispersion model to be better than that of single phase model in order to check the results with the experimental data while both the multi-phase models over predicted the heat transfer coefficient. Although the single phase dispersion model showed good performance compared to the other models, there were no clear indication about the effect of the particles interactions. So, this has been remained an issue for the researchers and more research is required to justify such findings.

Very recently, He *et al.* [36] has investigated the heat transfer behaviour of laminar TiO_2-H_2O nanofluid flow in a horizontal circular pipe both experimentally and numerically using Eulerian-Lagrangian discrete phase model. In this research, discrete phase model has been used in order to see the effect of two different phases such as base fluid and nanoparticles on the heat transfer. This has provided a clear view of the performance of a simple mixture of solid-fluid particles than nanofluids. Also, particles interaction can be considered which is feasible for multi-phase model. They have also suggested that the heat transfer enhancement was more affected by thermal conductivity. Additionally they have concluded, different forces such as Brownian force, lift force and thermophoretic force may have insignificant effect to increase the heat transfer rate. A similar investigation was carried out by Bianco *et al.* [37] and Moraveji and Esmaeili [38] on laminar forced convection Al_2O_3-H_2O nanofluid flow using single phase and Eulerian-Lagrangian discrete phase models with constant and temperature dependent properties. A comparison was made between the results obtained by the two models and found that the maximum deviation of average heat transfer coefficient was only 10 to 11% for nanoparticles concentration of 4%. Ryzhkov and Minakov [39] numerically investigated the heat transfer behaviour of Al_2O_3-water nanofluid in a circular tube using both one and two component models. In his research, one component model referred to the homogeneous model based on RANS equations with thermophysical properties of nanofluids whereas two component models were considered the nanoparticles transport by diffusion and thermophoresis as discussed in [39]. It was observed that

local and average heat transfer coefficient had always been higher for two component model than that of one component model.

2.2 Transitional Flow

We know that internal flow behaves like a laminar flow when flow pattern of fluids forms a parallel layer inside the domain with no disturbance between the layers. But, imposing external disturbance can make the flow unstable sometimes. This can be seen from the flow fields where small fluctuation occurs in the parallel layer. Such behaviour is known as transitional behaviour and we simply say that transition flow is a state between the laminar and turbulent flow. It is important to note that the flow in a smooth pipe is said to be transitional when $2300 \leq Re \leq 10{,}000$. Very few researches have been done on pipe under transition flow region and most of them were experimental and details are discussed in the following section:

Tang *et al.* [40] experimentally investigated the hydrodynamic behaviour of Al_2O_3–water nanofluid flowing through a horizontal tube. Their results indicated that transition flow had been monitored at $Re{\sim}1500$ comparing with $Re{\sim}2300$ given in Cengel [41] for the transition regime. It suggested, the transition regime could start from $Re{\sim}1500$ although many researchers monitored it to be $2000 < Re < 4000$. However, few works have been done on horizontal tube with twisted tape or wire coil inserts in order to see the effect on the heat transfer performance under transition flow condition. Sharma *et al.* [42] and Chandrasekar *et al.* [43] observed the heat transfer behaviour experimentally using Al_2O_3–water nanofluid flowing through a circular tube with twisted tape or wire coil inserted under the transitional flow regime. The maximum heat transfer enhancement of 20% and 23.07% had been achieved for $\chi = 0.1\%$ at $Re = 5000$ and $Re = 9000$ respectively. A similar experimental investigation was done by Naik *et al.* [44] for water–propylene glycol based CuO nanofluid and the maximum enhancement of 76.06% had been attained at $Re = 10000$ and for $\chi = 0.5\%$. Analysing their findings, it is concluded that maximum enhancement of heat transfer can be observed for the high Reynolds number. Meyer *et al.* [45], first time in the recent years, has experimentally investigated the heat transfer behaviour influenced by multi-walled carbon nanotubes inside the smooth horizontal tube under transitional flow regime. In their investigation, transition flow

behaviour is observed in between $2900 \leq Re \leq 3600$. They have mentioned, the heat transfer rate decreases while using multi-walled carbon nanotubes.

2.3 Turbulent Flow

We know, a flow behaves like a turbulent flow because of the instabilities of laminar flow at some high disturbances applied to the flow. In general, almost all the flows are turbulent but it's still possible to understand the behaviour of laminar flow in experimental research laboratory. However, several experimental and numerical researches have been carried out on nanofluids turbulent flows in pipe and details are discussed below:

Qiang and Yimin [46] investigated experimentally the heat transfer characteristics of nanofluid in a circular tube under both the laminar and turbulent flow regimes. They measured the heat transfer coefficient and Darcy friction factor of Cu-water nanofluid and showed that the heat transfer rate had increased because of adding nanoparticles in the base fluid, while the Darcy friction factor remained unchanged for different nanoparticles concentrations. And. they proposed new correlations for the calculation of average Nusselt number. It can be used to compare the average Nusselt number with the other numerical or experimental data in order to check the maximum percentage deviation of the results.

For laminar flow:

$$\overline{Nu} = 0.4328\ (1 + 11.185\ \chi^{0.754} Pe^{0.218}) Re^{0.333} Pr^{0.4} \tag{2.3}$$

For turbulent flow:

$$\overline{Nu} = 0.0059\ (1 + 7.6286\ \chi^{0.6886} Pe^{0.001}) Re^{0.9238} Pr^{0.4} \tag{2.4}$$

Moreover, Xuan and Li [47] investigated the flow and heat transfer behaviour of Cu-water nanofluid experimentally under turbulent flow regime. Comparing with the above mentioned articles, it can be stated, the increase of thermal conductivity or the random movement of nanoparticles in nanofluid also causes the enhancement of heat transfer rate.

All the above articles put emphasis on thermal conductivity and Brownian motion of nanoparticles. But no attempt to see the effect of thermophysical properties of nanofluids on heat transfer has been found. However, an investigation was carried out by Mansour *et al.* [48] to see the performance of the different properties. Mansour *et al.* [48] investigated the effect of physical properties of nanofluid flowing through a

tube under uniform heat flux boundary condition experimentally. They demonstrated that the physical parameters had varied considerably with the thermophysical properties of the nanofluid.

In addition, effect of the different nanofluids on heat transfer is also an interest for different researchers. Details are discussed in the following:

Kim *et al.* [49] and Fotukian and Esfahany [50] experimentally studied the effect of nanofluid on heat transfer flowing through a circular horizontal tube under both laminar and turbulent flow regimes. In this research, alumina oxide nanoparticles were used because this was very environment friendly. It was observed that adding Al_2O_3 nanoparticles in the base fluids had helped to enhance the heat transfer rate. The maximum enhancement was observed to be 15% and 20% respectively at 3% under both the laminar and turbulent flow conditions. Moreover, Sajadi and Kazemi's [51] experimental results on TiO_2-water nanofluid in a circular pipe also showed the same behaviour. Torii [52], however, observed that the forced convective heat transfer rate had increased with the nanoparticles concentration flowing through a straight tube under the constant heat flux boundary condition. Kayhani *et al.* [53] also experimentally studied the convective heat transfer and pressure drop of TiO_2-water nanofluid flowing through a horizontal pipe. They observed, the maximum enhancement of average Nusselt number was approximately 8% at Re = 11780 compared to water. Besides, Sundar *et al.* [54] investigated the convective heat transfer and flow behaviours of Fe_3O_4 nanofluid experimentally inside a circular tube. There, adding magnetic nanoparticles in the base fluid enhanced the heat transfer rate more significantly in comparison with the other types of nanofluids. Esfe *et al.* [55] experimentally studied the heat transfer performance of MgO-water nanofluid under turbulent flow regime too. Results showed that the enhancement of heat transfer rate had been possible without the huge penalty in pumping power.

Experimental researches have also been carried out in order to make a comparison of the performance of two or more different types of nanofluids flow in tube. These research will provide us the insight of the choice of nanofluids that can be useful in practical applications.

Azmi *et al.* [56] experimentally investigated the friction factor and the heat transfer behaviours of TiO_2 and SiO_2 nanofluids flow in tube under the turbulent flow regime.

They observed that TiO_2 nanofluid had showed the higher heat transfer enhancement than SiO_2 nanofluid at the low concentrations. Though, the opposite behaviour had been observed for the high concentrations. On the other hand, Pouranfard *et al.* [57] experimentally studied the drag reduction by nanofluids through horizontal pipe of a Newtonian liquid under turbulent flow regime. There, the drag reduction in the rough pipes was more than that in the smooth pipes at the same flow conditions. And it increased when the relative roughness increased. Moreover, Pak and Cho [58] investigated the heat transfer behaviour of nanofluids experimentally in a circular pipe under the turbulent flow regime. This investigation was carried out for Al_2O_3-H_2O and TiO_2-H_2O nanofluids. The *Re* and *Pr* were varied in the ranges from 10^4 to 10^5 and 6.5 to 12.3 respectively. Finally, they established the following correlation depending only on *Re* and *Pr*. And this correlation depended neither on nanoparticles concentrations nor on the diameters.

$$\overline{Nu} = 0.021 Re^{0.8} Pr^{0.5} \tag{2.5}$$

All of the previous articles showed the experimental studied using different nanofluids under turbulent flow regimes. Some numerical studied are presented in details in the following section:

Maiga *et al.* [59] numerically studied the flow and heat transfer behaviours of Al_2O_3-water nanofluid at various nanoparticles concentrations in a tube under turbulent flow regime. $Re = 10^4$ to 5×10^5 and the fluid inlet temperature of 293.15 K were considered in this study. The effect of nanoparticles concentration and Reynolds number were also presented and a new correlation was proposed in the end. Their numerical outcomes revealed that the inclusion of nanoparticles into the base fluid had enhanced the heat transfer rate along with the increase in nanoparticles concentration. They proposed the following correlation for the calculation of average Nusselt number.

$$\overline{Nu} = 0.085\ Re^{0.71} Pr^{0.35} \tag{2.6}$$

Another similar investigation was carried out by Bianco *et al.* [60] using both single and multi-phase approaches. And, it was found that the accuracy of the multi-phase mixture model had been better than that of the single phase model. However, Namburu *et al.* [61] numerically analysed the forced convective flow and heat transfer behaviour of EG-water based CuO, Al_2O_3 and SiO_2 nanofluids flowing through

a circular tube. Results showed, the nanofluids had higher viscosity, thermal conductivity and heat transfer rate compared to the base fluid. Then again, Kumar [62] numerically studied the heat transfer behaviour of Al_2O_3-water nanofluid using the single phase approach covering both the laminar and turbulent flow regimes. It was observed that the heat transfer rate had been enhanced more significantly in the turbulent flow regime than in the laminar flow regime.

Besides, Behzadmehr *et al.* [63] numerically examined the turbulent forced convection heat transfer in a tube using Cu-water nanofluid with a two-phase mixture model. Their investigations showed that the multi-phase model had been more accurate than the single phase model. Again, Akbari *et al.* [64] carried out a numerical investigation on the turbulent forced convection flow in a horizontal tube. They concluded, the thermal predictions using two-phase model were very sensitive to the particles concentration. And, the single-phase and two-phase models predicted almost identical flow fields. Hejazian *et al.* [65] numerically studied the performance of Eulererian and mixture models for turbulent flow of Al_2O_3 nanofluid inside a horizontal tube. It was found that the mixture model had performed better than the Eulerian model while considering the experimental results of average Nusselt number. A similar investigation subjected to constant wall temperature using multi-phase mixture model was also carried out by Bianco *et al.* [66, 67]. It was observed, the heat transfer rate, friction factor and entropy generation increased along with the increase of nanoparticles concentrations.

2.4 Objective of the Thesis

Numerous experimental and numerical investigations have been carried out by the researchers on different geometries such as cavity, duct, tube, annulus, plate, and stretching sheet using nanofluids. They have conducted researches under laminar to turbulent flow regimes using both single and multi-phase approaches. However, to the best of our knowledge, a very limited number of research works have been found on the nanofluids flow in a horizontal pipe covering the transition to turbulent flow regimes. Further, no investigation has been carried out to the date to understand the effects of Brownian motion and size and concentration of different nanoparticles of Al_2O_3 and TiO_2-water nanofluids. Hence, the aim of our present investigation is to examine the effect of nanoparticles concentrations, diameters and Brownian motion

of the nanoparticles on the convective heat transfer for two particularly selected (Al_2O_3 and TiO_2-water) nanofluids.

Additionally, both the single and the Eulerian-Eulerian multi-phase mixture models will be under the study. A particular investigation is carried out to justify the effect of a uniform roughness along the pipe wall. Different roughness heights are chosen under transition flow regime. Furthermore, the interaction between the fluid and nanoparticles as well as its performance on the heat transfer is assessed by an Eulerian-Lagrangian discrete phase model. Here, two different phases such as water and nanoparticles instead of typical nanofluids are used. Finally, an in-depth investigation is carried out to understand the nanofluids flow in an inclined pipe under transition flow regime.

Chapter 3

Mathematical Modelling

Three different approaches have usually been used by the researchers to investigate the effect of inclusion of nanoparticles into base fluid [28-39, 59-66]. The first approach is single phase model in which both the fluid phase and the particles are in thermal equilibrium and flow with the same local velocity. The second approach is multi-phase model. And the third one is discrete phase model where a simple fluid-solid mixture principle is considered instead of nanofluid. Firstly, the details of the Reynolds-averaged Navier-Stokes (RANS) based governing equations for fluid continuity and momentum and energy equations of the three models are described in this chapter. Secondly, the volume concentration equation of the multi-phase model and a Lagrangian form of particle momentum and energy equations of the discrete phase model are presented. Moreover, different types of transitional and turbulent models, thermophysical properties of nanofluids, water and nanoparticles are presented. Finally, definition of pipe wall roughness and other useful definitions are presented.

3.1 Governing Equations

The RANS equations govern the transport of averaged flow quantities, with the whole range of scales of turbulence being modelled. The RANS-based modelling approach therefore greatly reduces the required computational effort and resources, and is widely adopted for practical engineering applications. In the following paragraph, the Reynolds-averaged Navier-Stokes equations for single phase, multi-phase and discrete phase models are presented and described [68].

3.1.1 Single Phase Model

The dimensional steady-state governing equations of fluid flow and heat transfer for the single phase model are presented and the following assumptions are made:

i. Fluid flow is incompressible and Newtonian,
ii. The Boussinesq approximation is negligible as the pipe is placed horizontally,
iii. Nanoparticles are spherical and uniform in size and shape,

iv. Radiation effects and viscous dissipation are negligible.

v. Fluid phase and nanoparticles phase are in thermal equilibrium and no-slip between them and they flow with the same local velocity,

Under the above assumptions, the dimensional steady state governing equations for the fluid flow and heat transfer in the single phase model can be expressed as (Fluent [68]):

For 2D Axisymmetric Model:

Continuity equation:

$$\frac{\partial v_x}{\partial x}+\frac{\partial v_r}{\partial r}+\frac{v_r}{r}=0 \tag{3.1}$$

x-momentum equation:

$$\frac{1}{r}\frac{\partial}{\partial x}(rv_xv_x)+\frac{1}{r}\frac{\partial}{\partial x}(rv_rv_x)=-\frac{1}{\rho}\frac{\partial p}{\partial x}+\frac{\mu}{\rho}\frac{\partial}{\partial x}\left[\left(2\frac{\partial v_x}{\partial x}-\frac{2}{3}(\nabla.\vec{v})\right)\right]+\frac{\mu}{\rho}\frac{\partial}{\partial r}\left[\left(\frac{\partial v_x}{\partial r}+\frac{\partial v_r}{\partial x}\right)\right] \tag{3.2}$$

r-momentum equation:

$$\frac{1}{r}\frac{\partial}{\partial x}(rv_xv_r)+\frac{1}{r}\frac{\partial}{\partial x}(rv_rv_r)=-\frac{1}{\rho}\frac{\partial p}{\partial r}+\frac{\mu}{\rho}\frac{\partial}{\partial x}\left[\left(\frac{\partial v_r}{\partial x}+\frac{\partial v_x}{\partial r}\right)\right]+\frac{\mu}{\rho}\frac{\partial}{\partial r}\left[\left(2\frac{\partial v_r}{\partial r}-\frac{2}{3}(\nabla.\vec{v})\right)\right]-2\frac{\mu}{\rho}\frac{v_r}{r^2}+\frac{2}{3}\frac{1}{r}\frac{\mu}{\rho}(\nabla.\vec{v}) \tag{3.3}$$

where

$$(\nabla.\vec{v})=\frac{\partial v_x}{\partial x}+\frac{\partial v_r}{\partial r}+\frac{v_r}{r} \tag{3.4}$$

Energy equation:

$$\frac{\partial\left(v_xT_{nf}\right)}{\partial x}+\frac{\partial\left(v_rT_{nf}\right)}{\partial r}=\frac{\lambda}{\rho}\left[\frac{\partial}{\partial x}\left(\frac{\partial T_{nf}}{\partial x}\right)+\frac{\partial}{\partial r}\left(\frac{\partial T_{nf}}{\partial r}\right)\right] \tag{3.5}$$

For 3D model:

Continuity equation:

$$\nabla.(\rho\vec{v})=0 \tag{3.6}$$

Momentum equation:

$$\nabla.(\rho\vec{v}\vec{v})=-\nabla p+\nabla.\left[\mu\left(\nabla\vec{v}+\nabla\vec{v}^{T}\right)-\frac{2}{3}\nabla.\vec{v}\,I\right]+\rho\vec{g} \tag{3.7}$$

Energy equation:

$$\nabla.\left(\rho\vec{v}C_pT_{nf}\right)=\nabla.\left(\lambda\,\nabla T_{nf}\right) \tag{3.8}$$

where x and r are the axial and radial coordinates respectively, v_x and v_r are the axial and radial velocity respectively, $\vec{v}$ is the velocity vector, T_{nf} is the temperature, $\vec{g}$ is the gravitational body force, I is the unit tensor, ρ is the density, p is the pressure, μ is the dynamic viscosity and λ is the thermal conductivity of nanofluid.

3.1.2 Multi-phase Mixture Model

The dimensional steady-state governing equations of continuity, momentum, energy and volume concentration for the multi-phase model are presented considering the assumptions (i) to (iv) given in the single phase model. Moreover, it is assumed that there is a strong coupling between the fluid and nanoparticles phases and these phases move at the same local velocity. Interaction between the fluid and nanoparticles is also taken into account.

It is also assumed that fluid and nanoparticles phases are in local thermal equilibrium in multi-phase mixture model. It means, mean temperature of the fluid phase and the nanoparticles phase are same.

Under the above assumptions, the governing equations for the multi-phase mixture model can be expressed as (Fluent [68]):

Continuity equation:

$$\nabla.\left(\rho\vec{v}\right)=0 \tag{3.9}$$

Momentum equation:

The multi-phase mixture model allows the phases to move at different or same velocities using the concept of drift velocity. When the phases can also be assumed to move at same velocities then the mixture model is called the homogeneous multi-phase model. Moreover, the momentum equation for the mixture can be obtained by summing the individual momentum equations for all the phases.

$$\nabla.\left(\rho\vec{v}\vec{v}\right)=-\nabla p+\nabla.\left[\mu\left(\nabla\vec{v}+\nabla\vec{v}^{\mathrm{T}}\right)\right]+\rho\vec{g}+\nabla.\left(\sum_{s=1}^{n}\chi_s\rho_s\vec{v}_{dr,s}\,\vec{v}_{dr,s}\right) \tag{3.10}$$

Energy equation:

$$\nabla.\left[\sum_{s=1}^{n}\chi_s\vec{v}_s(\rho_s H_s + p)\right] = \nabla.\left(\sum_{s=1}^{n}\chi_s(\lambda+\lambda_t)\,\nabla T_{nf}\right) \tag{3.11}$$

Volume concentration equation:

$$\nabla.\left(\chi_p\,\rho_p\vec{v}\right) = -\nabla.\left(\chi_p\,\rho_p\vec{v}_{dr,p}\right) \tag{3.12}$$

Also, $\vec{v}, \rho, \mu, \lambda, n, \lambda_t, \chi_s$ are the mass-average velocity, mixture density, viscosity of the mixture, mixture thermal conductivity coefficient, number of phases, turbulent thermal conductivity and nanoparticles concentration respectively.

These are defined as

$$\vec{v} = \sum_{s=1}^{n}\frac{\chi_s\rho_s\vec{v}_s}{\rho} \tag{3.13}$$

$$\rho = \sum_{s=1}^{n}\chi_s\,\rho_s \tag{3.14}$$

$$\mu = \sum_{s=1}^{n}\chi_s\,\mu_s \tag{3.15}$$

$$\lambda = \sum_{s=1}^{n}\chi_s\,\lambda_s \tag{3.16}$$

Here, H_s is the sensible enthalpy for phase *s*. The drift velocity ($\vec{v}_{dr,s}$) for the secondary phase *s* is defined as

$$\vec{v}_{dr,s} = \vec{v}_s - \vec{v} \tag{3.17}$$

The relative or slip velocity is defined as the velocity of the secondary phase (s) relative to the velocity of the primary phase (f):

$$\vec{v}_{sf} = \vec{v}_s - \vec{v}_f \tag{3.18}$$

Then the drift velocity related to the relative velocity becomes

$$\vec{v}_{dr,s} = \vec{v}_{sf} - \sum_{k=1}^{n}\vec{v}_{fk}\frac{\chi_k\rho_k}{\rho} \tag{3.19}$$

Manninen *et al.* [69] and Naumann and Schiller [70] proposed the following respective equations for the calculation of the relative velocity, $\vec{v}_{pf}$, and the drag function, f_{drag}.

$$\vec{v}_{pf} = \frac{\rho_p d_p^2}{18\mu_f\,f_{drag}}\frac{\rho_p-\rho}{\rho_p}\vec{a} \tag{3.20}$$

$$f_{drag} = \begin{cases} 1 + 0.15Re_p^{0.687} & Re_p \leq 1000 \\ 0.0183Re_p & Re_p > 1000 \end{cases} \quad (3.21)$$

Here, the acceleration $\vec{a}$ is determined by

$$\vec{a} = -(\vec{v}.\nabla)\vec{v} \quad (3.22)$$

And, d_p is the diameter of the nanoparticles of secondary phase s and $\vec{a}$ is the secondary phase particle's acceleration, T_{nf} is the temperature, p is the pressure.

Also, the buoyancy term in the momentum equations (3.7) and (3.10) is approximated (Fluent [68]) by

$$(\rho - \rho_0)\, g \approx -\rho_0 \beta (T - T_0) g \quad (3.23)$$

which is considered when Boussinesq approximation is taken into account for mixed convection case. Here β is the thermal expansion coefficient of the fluid, ρ_0 and T_0 are the reference density and temperature respectively.

3.1.3 Discrete Phase Model

In the discrete phase model, the fluid phase is considered as a continuous phase and is governed by the time averaged continuity, momentum and energy equations. Though, the solid phase is governed by momentum and energy equations. It is assumed that the solid phase occupies a low concentration of less than 10%, Moreover, each phase moves at different velocities with the assumption that the existence of local thermal equilibrium between the fluid and solid particles is not taken into account.

The governing equations for the discrete phase model can be expressed as (Fluent [68]):

$$\nabla.(\rho\vec{v}\,) = 0 \quad (3.24)$$

$$\nabla.(\rho\vec{v}\vec{v}) = -\nabla p + \nabla.(\mu\,\nabla\vec{v}) + S_m \quad (3.25)$$

$$\nabla.\left(\rho\vec{v}\,C_p T_f\right) = \nabla.\left(\lambda\,\nabla T_f\right) + S_e \quad (3.26)$$

$$\frac{d\vec{v}_p}{dt} = F_D\left(\vec{v} - \vec{v}_p\right) + \frac{\vec{g}\left(\rho_p - \rho\right)}{\rho_p} \quad (3.27)$$

$$\rho C_p \frac{dT_p}{dt} = \frac{6h}{D_h}\left(T - T_p\right) \quad (3.28)$$

Here, Eqs. (3.27) and (3.28) represent the Lagrangian form of particle momentum and energy equations respectively. And, $\vec{v}_p$ and T_p are the nanoparticles velocity and temperature respectively. Finally, ρ_p is the nanoparticles density.

The drag coefficient F_D is defined as [68]:

$$F_D = \frac{18\,\mu_f}{\rho_p d_p^2 C_c} \tag{3.29}$$

Here, the factor C_c is known as Cunningham correction which can be defined as [68]:

$$C_c = 1 + \frac{2\lambda_{mp}}{d_p}\left(1.257 + 0.4\,e^{-\left(1.1\,d_p/2\lambda_{mp}\right)}\right) \tag{3.30}$$

Here, λ_{mp} is the nanoparticles mean free path and μ_f is the dynamic viscosity of base fluid.

Also, the source terms S_m and S_e are defined as [68]:

$$S_m = \sum_{np} \frac{m_p}{\delta v} \frac{d\vec{v}_p}{dt} \tag{3.31}$$

$$S_e = \sum_{np} \frac{m_p C_p}{\delta v} \frac{dT_p}{dt} \tag{3.32}$$

For transition and turbulent flow regimes, both the terms λ and μ are replaced by their effective values and defined as (Nicholas and Markatos [71] and Bacharoudis *et al.* [72])

$$\mu_{eff} = \mu + \mu_t \tag{3.33}$$

$$\lambda_{eff} = \frac{\mu}{Pr} + \frac{\mu_t}{\sigma_t} \tag{3.34}$$

In that order, μ_t is the turbulent molecular viscosity, σ_t is the constant of turbulent Prandtl number and *Pr* is the Prandtl number of nanofluid.

3.2 Turbulence Modelling

In reality, no turbulence model which can be considered for all kinds of problems in the area of computational fluid dynamics exists. Hence, several factors can be considered in order to find a suitable turbulence model. Some of them are physics behind the flow field, the level of computational time and cost as well as accuracy. Therefore, it's very important to understand the nature of turbulence models to be used in real-life applications.

One of the objectives of this work is to assess the suitability of the various RANS based turbulence models in predicting the transient as well as turbulent features of the nanofluids flowing through the physical geometry considered as a pipe. Therefore, two different transitional models named as Standard $\kappa - \omega$ and SST $\kappa - \omega$ models as well as three different turbulent models called Realizable $\kappa - \epsilon$, Standard $\kappa - \epsilon$ and RNG $\kappa - \epsilon$ models are considered and their performances are compared in this thesis. In terms of the computational time taken by each method for flow modelling, literatures suggest that a Realizable $\kappa - \epsilon$ model usually takes a slightly higher CPU time than a Standard $\kappa - \epsilon$ model [68]. Simulating turbulent flow with a RNG $\kappa - \epsilon$ model is even more expensive and indicates a demand of approximately 10-15% higher CPU time than Standard $\kappa - \epsilon$ model [68]. But, in the context of nanofluids flow this information is unavailable thus it requires examination with their prediction accuracy. In the following sections, different transitional and turbulence RANS models used for the nanofluids flow are presented and briefly discussed.

3.2.1 Standard $\kappa - \omega$ Model

The Standard $\kappa - \omega$ model is an empirical model (Wilcox [73]) based on the transport equations for the turbulence kinetic energy (κ) and the specific dissipation rate (ω) as described in Fluent [68]. The equations for the turbulence kinetic energy (κ) and specific dissipation rate of turbulence kinetic energy (ω) used in the Standard $\kappa - \omega$ model are given with

$$div(\rho\kappa\vec{v}) = div\left\{\left(\mu + \frac{\mu_t}{\sigma_k}\right) grad\ \kappa\right\} + G_\kappa - Y_\kappa \tag{3.35}$$

$$div(\rho\omega\vec{v}) = div\left\{\left(\mu + \frac{\mu_t}{\sigma_\omega}\right) grad\ \omega\right\} + G_\omega - Y_\omega \tag{3.36}$$

In these equations, G_κ represents the production of turbulence kinetic energy due to the mean velocity gradients, G_ω represents the production of ω, σ_k and σ_ω are the effective Prandtl numbers for kinetic energy and specific rate of dissipation respectively. While, Y_κ and Y_ω respectively represent the dissipation of κ and ω due to turbulence. And the turbulent viscosity μ_t is modelled as

$$\mu_t = \alpha^* \frac{\rho\kappa}{\omega} \tag{3.37}$$

where

$$\alpha^* = \alpha_\infty^* \frac{\left(\alpha_0^* + \frac{Re_t}{R_\kappa}\right)}{\left(1 + \frac{Re_t}{R_\kappa}\right)} \tag{3.38}$$

$$\alpha_0^* = \frac{\beta_i}{3}, Re_t = \frac{\rho\kappa}{\mu\omega}$$

Here G_κ and G_ω are defined as

$$G_\kappa = \mu_t S^2 \tag{3.39}$$

$$G_\omega = \alpha \frac{\omega}{\kappa} G_\kappa \tag{3.40}$$

where S is the modulus of the mean rate-of-strain tensor, and the coefficient α is defined as

$$\alpha = \frac{\alpha_\infty}{\alpha^*} \frac{\left(\alpha_0 + \frac{Re_t}{R_\omega}\right)}{\left(1 + \frac{Re_t}{R_\omega}\right)} \tag{3.41}$$

Also for high Reynolds number flow, $\alpha^* = \alpha_\infty^* = 1$ and $\alpha = \alpha_\infty = 1$.

Here Y_κ and Y_ω are defined as

$$Y_\kappa = \rho\, \beta^*\, f_{\beta^*}\, \kappa\, \omega \tag{3.42}$$

$$Y_\omega = \rho\, \beta\, f_\beta \omega^2 \tag{3.43}$$

Here,

$$f_{\beta^*} = \begin{cases} 1 & , a \le 0 \\ \dfrac{1 + 680\, a^2}{1 + 400\, a^2} & , a > 0 \end{cases} \tag{3.44}$$

$$f_\beta = \frac{1 + 70\, b}{1 + 80\, b} \tag{3.45}$$

$$a \equiv \frac{1}{\omega^3}\, grad\, \kappa\, grad\, \omega \tag{3.46}$$

$$\beta^* = \beta_\infty^* \left(\frac{\frac{4}{15} + \left(\frac{Re_t}{R_\beta}\right)^4}{1 + \left(\frac{Re_t}{R_\beta}\right)^4} \right) [1 + \zeta^* F(M_t)] \tag{3.47}$$

$$F(M_t) = \begin{cases} 0 & , M_t \le M_{t0} \\ M_t^2 - M_{t0}^2 & , M_t > M_{t0} \end{cases} \tag{3.48}$$

$$M_t^2 \equiv \frac{2\kappa}{c^2}\, , c = \sqrt{\gamma RT} \tag{3.49}$$

And, model constants are

$$\zeta^* = 1.5, \beta_\infty^* = 0.09, \sigma_k = \sigma_\omega = 2, M_{t0} = 0.25, \beta_i = 0.072$$

$$R_\kappa = 6, R_\beta = 8, R_\omega = 2.95, \alpha_\infty^* = 1, \alpha_\infty = 0.52, \alpha_0 = \frac{1}{9}$$

Further information for transitional modelling is available in Fluent [68].

3.2.2 Shear-Stress Transport (SST) $\kappa - \omega$ Model

Menter [74] developed the SST $\kappa - \omega$ transitional model which is used here in the transitional modelling. The equations for the turbulence kinetic energy (κ) and specific dissipation rate of turbulence kinetic energy (ω) used in the SST $\kappa - \omega$ model are given with

$$div(\rho\kappa\vec{v}) = div\left\{\left(\mu + \frac{\mu_t}{\sigma_k}\right) grad\ \kappa\right\} + G_\kappa - \rho\ \kappa\ \omega\ \beta_1 \tag{3.50}$$

$$div(\rho\omega\vec{v}) = div\left\{\left(\mu + \frac{\mu_t}{\sigma_\omega}\right) grad\ \omega\right\} + G_\omega - \rho\ \omega^2\beta_2 + 2(1 - F_1)\rho\ \sigma_{\omega,2}\ \frac{grad\ \omega\ grad\ \kappa}{\omega} \tag{3.51}$$

In these equations, G_κ represents the generation of turbulence kinetic energy due to the mean velocity gradients, G_ω represents the production of ω, and σ_k and σ_ω are the effective Prandtl numbers for the kinetic energy and specific rate of dissipation respectively. And turbulent viscosity $\mu_{t,m}$ is modelled as

$$\mu_t = \frac{\rho\kappa}{\omega}\frac{1}{max\left(\frac{1}{\alpha^*}, \frac{SF_2}{\alpha_1\omega}\right)} \tag{3.52}$$

Here, $F_1$and F_2 are the blending functions, S is the strain rate magnitude and α^* is a model constant.

Here σ_k and σ_ω are defined as

$$\sigma_k = \frac{1}{\frac{F_1}{\sigma_{k,1}} + \frac{(1-F_1)}{\sigma_{k,2}}} \tag{3.53}$$

$$\sigma_\omega = \frac{1}{\frac{F_1}{\sigma_{\omega,1}} + \frac{(1-F_1)}{\sigma_{\omega,2}}} \tag{3.54}$$

The blending functions $F_1$and F_2 are defined as

$$F_1 = tanh(\Phi_1^4) \tag{3.55}$$

$$F_2 = tanh(\Phi_2^2) \tag{3.56}$$

Here,

$$\Phi_1 = min\left[max\left(\frac{\sqrt{\kappa}}{0.09\ \omega y}, \frac{500\mu}{\rho y^2\omega}\right), \frac{4\rho\kappa}{\sigma_{\omega,2}D_\omega^+ y^2}\right] \tag{3.57}$$

$$D_\omega^+ = max\left[2\rho\frac{grad\ \kappa\ grad\ \omega}{\sigma_{\omega,2}\ \omega}10^{-10}\right] \tag{3.58}$$

$$\Phi_2 = max\left[\left(\frac{2\sqrt{\kappa}}{0.09\,\omega y}\frac{500\mu}{\rho y^2\omega}\right)\right] \tag{3.59}$$

Besides, y is the near wall distance and D_ω^+ is the positive portion of the cross diffusion term. And, the model constants are $\beta_1 = 0.075$, $\beta_2 = 0.0828$, $\alpha_1 = 0.31$, $\sigma_k = 1.0$ and $\sigma_\omega = 1.168$. Further information of transitional modelling is available in Fluent [68].

3.2.3 Realizable $\kappa - \epsilon$ Model

Realizable $\kappa - \epsilon$ turbulent model was proposed by Shih *et al.* [75]. The equations for the turbulent kinetic energy (κ) and dissipation rate of turbulent kinetic energy (ϵ) used in the Realizable $\kappa - \epsilon$ turbulent model are given with

$$div(\rho\kappa\vec{v}) = div\left\{\left(\mu + \frac{\mu_t}{\sigma_k}\right) grad\ \kappa\right\} + G_\kappa - \rho\epsilon \tag{3.60}$$

$$div(\rho\epsilon\vec{v}) = div\left\{\left(\mu + \frac{\mu_t}{\sigma_\epsilon}\right) grad\ \epsilon\right\} + \rho C_1 S_\epsilon - \rho C_2 \frac{\epsilon^2}{\kappa + \sqrt{\nu\epsilon}} \tag{3.61}$$

Here,

$$C_1 = max\left[0.43, \frac{\eta}{\eta + 5}\right], G_\kappa = \mu_t S^2, \eta = S\frac{\kappa}{\epsilon} \text{and } S = \sqrt{2\,S_{ij}S_{ij}}$$

In these equations, G_κ represents the generation of turbulence kinetic energy due to the mean velocity gradients. Here, S is the modulus of the mean rate-of-strain tensor, σ_k and σ_ϵ are the effective Prandtl numbers for the turbulent kinetic energy and the rate of dissipation respectively.

Hence, μ_t is modelled as

$$\mu_t = \frac{\rho\kappa^2}{\epsilon}\left(A_0 + A_s\frac{\kappa U^*}{\epsilon}\right)^{-1} \tag{3.62}$$

Here, A_0 and A_s are the model constants given as $A_0 = 4.04$ and $A_s = \sqrt{6cos\phi}$ respectively with

$$\phi = \frac{1}{3}cos^{-1}\sqrt{6W}, U^* = \sqrt{S_{ij}S_{ij} + \tilde{\Omega}_{ij}\tilde{\Omega}_{ij}}\ ,\ \tilde{\Omega}_{ij} = \overline{\Omega_{ij}} - 3\epsilon_{ijk}\,\omega_k \text{and } W = \frac{S_{ij}S_{jk}S_{ki}}{\tilde{S}^3}.$$

Here, $\overline{\Omega_{ij}}$ is the mean rate-of-rotation tensor with the angular velocity ω_k. In Eqs. (3.60) and (3.61), the model constants are $C_1 = 1.44, C_2 = 1.9$, $\sigma_k = 1.0$ and $\sigma_\epsilon = 1.2$.

3.2.4 Standard $\kappa - \epsilon$ Model

Standard $\kappa - \epsilon$ turbulent model was proposed by Launder and Spalding [76]. The equations for the turbulent kinetic energy (κ) and dissipation rate of turbulent kinetic energy (ϵ) used in the Standard $\kappa - \epsilon$ turbulent model are given as

$$div(\rho\kappa\vec{v}) = div\left\{\left(\mu + \frac{\mu_t}{\sigma_\kappa}\right) grad\ \kappa\right\} + G_\kappa - \rho\epsilon \tag{3.63}$$

$$div(\rho\epsilon\vec{v}) = div\left\{\left(\mu + \frac{\mu_t}{\sigma_\epsilon}\right) grad\ \epsilon\right\} + \frac{\epsilon}{\kappa}C_{1\epsilon}G_\kappa - \rho C_{2\epsilon}\frac{\epsilon^2}{\kappa} \tag{3.64}$$

At this point,

$$C_{1\epsilon} = 1.44, C_{2\epsilon} = 1.92, G_\kappa = \mu_t S^2, \text{and } S = \sqrt{2\,S_{ij}S_{ij}}$$

In these equations, G_κ represents the generation of turbulence kinetic energy due to the mean velocity gradients. Now, S is the modulus of the mean rate-of-strain tensor, σ_k and σ_ϵ are the effective Prandtl numbers for turbulent kinetic energy and rate of dissipation respectively. And μ_t is modelled as

$$\mu_t = \frac{\rho}{\epsilon}C_\mu\kappa^2 \tag{3.65}$$

Here, $C_\mu = 0.09$, $\sigma_k = 1.0$ and $\sigma_\epsilon = 1.3$.

3.2.5 RNG $\kappa - \epsilon$ Model

RNG $\kappa - \epsilon$ turbulent model was proposed by Yakhot *et al.* [77] and the equations for the turbulent kinetic energy (κ) and dissipation rate of turbulent kinetic energy (ϵ) used in the RNG $\kappa - \epsilon$ turbulent model are given with

$$div(\rho\kappa\vec{v}) = div\left\{\alpha_\kappa\,\mu_{eff}\ grad\ \kappa\right\} + G_\kappa - \rho\epsilon \tag{3.66}$$

$$div(\rho\epsilon\vec{v}) = div\left\{\alpha_\epsilon\,\mu_{eff}\ grad\ \epsilon\right\} + \frac{\epsilon}{\kappa}C_{1\epsilon}G_\kappa - \rho C_{2\epsilon}\frac{\epsilon^2}{\kappa} - R_\epsilon \tag{3.67}$$

At this time,

$$C_{1\epsilon} = 1.42, C_{2\epsilon} = 1.68, G_\kappa = \mu_t S^2, \text{and } S = \sqrt{2\,S_{ij}S_{ij}}$$

In these equations, G_κ represents the generation of turbulence kinetic energy due to the mean velocity gradients. Here, S is the modulus of the mean rate-of-strain tensor, α_κ and α_ϵ are the inverse effective Prandtl numbers for turbulent kinetic energy and rate of dissipation respectively. And R_ϵ is the additional term related to the mean strain as well as the turbulent quantities.

So, μ_t is modelled as

$$\mu_t = \frac{\rho}{\epsilon} C_\mu \kappa^2 \tag{3.68}$$

At this point, $C_\mu = 0.0845$, $\alpha_\kappa = \alpha_\epsilon \approx 1.393$.

Also, the effective viscosity is determined by

$$\hat{\nu} = \frac{\mu_{eff}}{\mu} \tag{3.69}$$

where

$$d\left(\frac{\rho^2 \kappa}{\sqrt{\epsilon \mu}}\right) = 1.72 \, \frac{\hat{\nu} \, d\hat{\nu}}{\sqrt{\hat{\nu}^3 - 1 + C_\nu}} \tag{3.70}$$

and, $C_\nu \approx 100$.

The additional term R_ϵ in the ϵ equation is defined as

$$R_\epsilon = \frac{\epsilon^2}{\kappa} \frac{C_\mu \, \rho \, \eta^3 \left(1 - \frac{\eta}{\eta_0}\right)}{1 + \beta \, \eta^3} \tag{3.71}$$

where $\eta = S\frac{\kappa}{\epsilon}, \eta_0 = 4.38$ and $\beta = 0.012$. Further information for turbulent modelling is available in Fluent [68].

3.3 Thermophysical Properties for Nanofluids, Water and Nanoparticles

It is not easy to evaluate the thermophysical properties in nanofluids because we do not know which models might give us the most reliable results. We are often unaware of the ways the solutions are strongly affected by the thermophysical properties too. However, different types of models for nanofluids thermophysical properties are presented and published by many researchers. Nevertheless, categorisation of thermophysical properties of nanofluids still remains a matter of debate. Hence, no conclusion is drawn regarding the flow and heat transport applications because of its wide variety and intricacy. In this present analysis, thermophysical properties of density and heat capacitance of the nanofluids are calculated by using the following formulas which are considered as classical relationships between the base fluid and the nanoparticles (Buongiorno [78]).

3.3.1 Density

The density of the nanofluid is defined as

$$\rho_{nf} = (1 - \chi)\rho_f + \chi \rho_p \tag{3.72}$$

where, χ is the nanoparticles concentration, ρ_f and ρ_p are the density of the base fluid and nanoparticles respectively.

3.3.2 Specific Heat

The heat capacitance of the nanofluid is defined as

$$(\rho c_p)_{nf} = (1-\chi)(\rho c_p)_f + \chi(\rho c_p)_p \tag{3.73}$$

At this time, $(\rho c_p)_f$ and $(\rho c_p)_p$ are the heat capacitance of the base fluid and nanoparticles respectively.

3.3.3 Thermal Conductivity

There is a considerable shortage of the experimental results and correlations that depend on the nanoparticles diameter as well as temperature. Hence, the following correlations in relation to the thermophysical properties of nanofluid proposed by Corcione [79] are used in our analysis.

Corcione [79] introduced the following correlation to examine the thermal conductivity of nanofluid which depends on the temperature and concentration of nanofluid, diameter and thermal conductivity of nanoparticles as well as the base fluid. He used regression analysis and proposed the following correlation with 1.86% standard deviation of error:

$$\frac{\lambda_{nf}}{\lambda_f} = 1 + 4.4\, {Re_p}^{0.4} {Pr_f}^{0.66} \left(\frac{T_{nf}}{T_{fr}}\right)^{10} \left(\frac{\lambda_p}{\lambda_f}\right)^{0.03} \chi^{0.66} \tag{3.74}$$

Here, Re_p is the nanoparticles Reynolds number that is defined as

$$Re_p = \frac{\rho_f u_B\, d_p}{\mu_f} = \frac{2\rho_f \kappa_b T_{nf}}{\pi\, {\mu_f}^2 d_p} \tag{3.75}$$

At this time, T_{fr} is the freezing point of the base liquid ($273.16\, K$); κ_b is the Boltzmann constant ($\kappa_b \approx 1.38 \times 10^{-23}\, J/K$); d_f is the fluid molecular diameter; d_p is the diameter of nanoparticles ($10\, nm \le d_p \le 150\, nm$); T_{nf} is the nanofluid temperature ($294 \le T(K) \le 324$); χ is a nanoparticles concentration which is valid for $0.2\% \le \chi \le 9\%$, Pr_f is the Prandtl number of the base fluid; ρ_f and μ_f are the density and the dynamic viscosity of the base fluid respectively. In addition, u_B is the nanoparticle Brownian velocity which is calculated as the ratio between d_p and the

time $\tau_D = {d_p}^2/6D$ by assuming the absence of agglomeration. Here, D is the Einstein diffusion coefficient.

3.3.4 Dynamic Viscosity

Corcione [79] proposed another correlation to evaluate the dynamic viscosity of nanofluid. He used best-fit of the selected data specified in his research work and proposed the following correlation with 1.84% standard deviation of error:

$$\frac{\mu_f}{\mu_{nf}} = 1 - 34.87 \left(\frac{d_p}{d_f}\right)^{-0.3} \chi^{1.03} \tag{3.76}$$

Here, d_p is the diameter of nanoparticles ($25\ nm \leq d_p \leq 200\ nm$); χ is a nanoparticles concentration which is valid for $0.01\% \leq \chi \leq 7.1\%$; T_{nf} is the nanofluid temperature ($293 \leq T_{nf}(K) \leq 333$) and d_f is the base fluid molecular diameter defined as

$$d_f = 0.1 \left(\frac{6M}{N\pi\rho_f}\right)^{1/3} \tag{3.77}$$

In this equation, N is the Avogadro number and M is the molecular weight of the base fluid.

The above correlations are derived from an extensive selection of empirical data relative to nanofluids consisting of different mean diameter of nanoparticles suspended in water (H_2O) or Ethylene glycol (EG) for the development of thermal conductivity correlation and in water (H_2O), propylene glycol (PG), Ethylene glycol (EG) or ethanol (Eth) for the development of dynamic viscosity correlation. It is to note, the conventional Maxwell theory mostly fails when it is implemented to nanofluids. In fact, the conventional Maxwell equation tends either to underestimate or to overestimate the value of thermal conductivity of nanofluid according to the nanoparticles diameter is small or large and the temperature of the suspension is high or low as discussed in Corcione [79]. Similarly, the Brinkman equation mostly fails with a percentage of error that increases as the diameter of nanoparticles decreases when it is implemented to nanofluids. It should also be noted that this model is used in this study for the calculation of dynamic viscosity of nanofluid with nanoparticles diameter of 10 and 20 *nm* by assuming a possible standard deviation of error lower than 1.84%.

3.3.5 Properties for Water

The mass density, heat capacitance, kinematic viscosity and thermal conductivity of water are calculated using the following correlations proposed by Kays and Crawford [80]. All these correlations are valid over $278 \leq T_f(K) \leq 363$.

$$\rho_f = 330.12 + 5.92\,T_f - 1.63 \times 10^{-2}{T_f}^2 + 1.33 \times 10^{-5}{T_f}^3 \tag{3.78}$$

$$C_{p_f} = 10^{-3} \times \left(10.01 - 5.14 \times 10^{-2}T_f + 1.49 \times 10^{-4}{T_f}^2 - 1.43 \times 10^{-7}\,{T_f}^3\right) \tag{3.79}$$

$$\nu_f = 1.08 \times 10^{-4} - 9.33 \times 10^{-7}T_f + 2.70 \times 10^{-9}\,{T_f}^2 - 2.62 \times 10^{-12}{T_f}^3 \tag{3.80}$$

$$\lambda_f = -12.16 + 0.12\,T_f - 3.66 \times 10^{-4}{T_f}^2 + 3.81 \times 10^{-7}{T_f}^3 \tag{3.81}$$

3.3.6 Properties for Nanoparticles

The density, heat capacitance and thermal conductivity of Al_2O_3 at $T_{in} = 293\,K$ are considered as Masuda *et al.* [81]:

$$\rho_p = 3880\,\frac{kg}{m^3}, \qquad C_{p_p} = 773\,\frac{J}{kgK}, \qquad \lambda_p = 36\,\frac{W}{mK} \tag{3.82}$$

The thermal conductivity of TiO_2 is obtained from the following relation and designed by a curve fitting on the data of Powel *et al.* [82]:

$$\lambda_p = 100 \times (0.1813 - 4.768 \times 10^{-4}\,T + 5.089 \times 10^{-7}T^2), \tag{3.83}$$

where $273 \leq T(K) \leq 350$

The heat capacitance of TiO_2 is obtained from the following relation and designed by a curve fitting on the data of Smith *et al.* [83]:

$$C_{p_p} = 58.4528 + 3.02195\,T - 3.02923 \times 10^{-3}\,T^2, \tag{3.84}$$

where $269.35 \leq T(K) \leq 339.82$

The density of TiO_2 is considered as $4250\,\frac{kg}{m^3}$.

3.4 Wall Roughness

Analysing the experimental results in pipes and channels with rough wall surface, it is found that the semi-logarithmic mean velocity profile near the pipe wall has an identical gradient $(1/\kappa)$ but different intercept. Therefore, the modified law of the wall for rough surface is defined in the following way:

$$\frac{u^* u_p}{\frac{\tau_w}{\rho}} = \frac{1}{\kappa}\, ln\left(E\frac{\rho u^* y_p}{\mu}\right) - \Delta B \tag{3.85}$$

Here,

$$u^* = C_\mu^{1/4}\kappa^{\frac{1}{2}} \text{ and } \Delta B = \frac{1}{\kappa}\, ln(f_r) \tag{3.86}$$

In this equation, f_r is a roughness function that quantifies the shift of the intercept due to the effects of roughness. It is to be noted that ΔB generally depends on the type (uniform sand, rivets, threads, ribs, mesh-wire, *etc.*) and size of the roughness. There is no universal roughness function valid for all types of roughness [68].

For a sand-grain roughness, ΔB is found to be well-correlated with the non-dimensional roughness height,

$$K_s^+ = \frac{\rho K_s u^*}{\mu} \tag{3.87}$$

Here, K_s is the physical roughness height.

In Fluent, the whole roughness regime is subdivided into the three regimes and the formulas proposed by Cebeci and Bradshaw based on Nikuradse's data [84] are adopted [68].

For the hydro-dynamically smooth regime ($K_s^+ \leq 2.25$):

$$\Delta B = 0 \tag{3.88}$$

For the transitional regime ($2.25 < K_s^+ \leq 90$):

$$\Delta B = \frac{1}{\kappa} ln\left[\frac{K_s^+ - 2.25}{87.75} + C_s K_s^+\right] \times sin\{0.4258\ (\ln K_s^+ - 0.811)\} \tag{3.89}$$

Here, C_s is a roughness constant and $C_s = 0.5$ refers to uniform sand grain roughness.
For the fully rough regime $K_s^+ > 90$:

$$\Delta B = \frac{1}{\kappa} ln[1 + C_s K_s^+] \tag{3.90}$$

3.5 Some Useful Definitions

In this section, Reynolds number, mean fluid velocity, Darcy friction factor, local Nusselt number and heat transfer coefficient, mean temperature, average Nusselt number and turbulent intensity are defined and presented.

For the prediction of flow in a circular pipe, the Reynolds number is defined as

$$Re = \frac{v_m D_h}{\nu} \tag{3.91}$$

Here, v_m is the mean fluid velocity defined as

$$v_m = \frac{2}{R^2}\int_0^R v(r,x)\, r\, dr \tag{3.92}$$

At this point, ν is the kinematic viscosity of the nanofluid, $v(r,x)$ is the axial velocity profile and R is the radius of pipe.

The Darcy friction factor and local Nusselt number are evaluated according to the following relations:

Darcy friction factor for turbulent flows in a circular pipe is defined as

$$f = \frac{2D_h \Delta p}{\rho L v_m^2} \tag{3.93}$$

Local Nusselt number and heat transfer coefficient are defined as

$$Nu(x) = \frac{h(x)D_h}{\lambda_f} \text{ where } h(x) = \frac{\dot{q}_s}{T_w - T_m(x)} \text{and } \dot{q}_s = -\lambda_f \frac{\partial T}{\partial r}\Big|_{r=R} \tag{3.94}$$

For constant and uniform heat flux boundary condition, the mean temperature of a fluid flowing through a circular pipe is expressed as

$$T_m(x) = T_{m,i} + \frac{\dot{q}_s \pi D_h}{\dot{m} C_p} x \tag{3.95}$$

Here, $\dot{q}_s$ and $\dot{m}$ are the heat flux of the pipe and mass flow rate of the fluid respectively.

According to the above equations, the average Nusselt number is defined as

$$\overline{Nu} = \frac{1}{L}\int_0^L Nu(x)\, dx \tag{3.96}$$

This numerical integration has been performed by using the Simpson's 1/3 rule.
The turbulent intensity can be defined as

$$I = 0.16\, Re^{-\frac{1}{3}} \tag{3.97}$$

3.5.1 Entropy Generation

The entropy generation analysis is considered as an effective tool to investigate and optimise thermal design [85] by Bianco *et al.* [67]. Better working conditions can be achieved by minimising it. Usually, entropy generation represents the irreversibility of a system. Therefore, a more efficient system has been obtained by reducing it.

Minimisation of entropy generation is a well-established approach to pursue the optimisation of a thermal system, as reported in Ref. [85, 86]. It is also of great importance to determine the optimal concentration to use and the most convenient particles dimension to consider while working with nanofluids. Therefore, entropy generation analysis offers a rigorous physical framework to solve the above mentioned problems (Bianco *et al.* [67]).

The total entropy generation is defined as

$$E_{gen} = E_{gen,t} + E_{gen,f} \tag{3.98}$$

Here, $E_{gen,t}$ and $E_{gen,f}$ are thermal and frictional entropy generation respectively. The equations for the thermal and frictional entropy generations for a circular pipe of length L are proposed by Ratts and Raut [86]. These are defined as

$$E_{gen,t} = \frac{\pi D_h^2 \, L \, \dot{q}_s^2}{\lambda_{nf} \, \overline{Nu} \, T_{av}} \tag{3.99}$$

$$E_{gen,f} = \frac{32\dot{m}^3 f L}{\rho_{nf}^2 \pi^2 D_h^5 \, T_{av}} \tag{3.100}$$

Here, T_{av} is the average temperature which is defined as follows:

$$T_{av} = \frac{(T_{in} - T_{out})}{ln\left(\frac{T_{in}}{T_{out}}\right)} \tag{3.101}$$

Now, T_{out} can be defined as

$$T_{out} = T_{in} + \frac{q'' A_s}{\dot{m} C_p} \tag{3.102}$$

Moreover, Bejan number (*Be*) is defined as

$$Be = \frac{E_{gen,t}}{E_{gen}}, 0 \leq Be \leq 1 \tag{3.103}$$

3.5.2 Thermal Performance Factor and Performance Evaluation Criterion

Thermal performance factor is denoted with ξ and defined as follows (Xu *et al.* [87]):

$$\xi = \left(\frac{\overline{Nu}_{nf}}{\overline{Nu}_f}\right)\left(\frac{f_{nf}}{f_f}\right)^{\frac{1}{3}} \tag{3.104}$$

Performance evaluation criterion (PEC) is defined as follows (Roy *et al*. [88]):

$$PEC = \frac{\rho_{nf} \, Cp_{nf} \, \Delta T_{nf}}{\Delta p} \tag{3.105}$$

Here, ΔT_{nf} and Δp are the temperature and pressure differences between the outlet and inlet of the pipe respectively.

3.6 Summary of the Numerical Methods

The computational domain is formed by using the commercial pre-processor software GAMBIT 2.4.6 which is also used for meshing and setting the boundary conditions. Then the governing non-linear partial differential equations for the continuity, momentum, energy and other scalars, such as, turbulence together with the suitable boundary conditions are discretised. And hence, they are solved by using the Finite volume solver Fluent 6.3.26. The finite volume technique converts the non-linear partial differential equations with the second order upwind scheme to a system of nonlinear algebraic equations that are solved numerically. Second order upwind scheme is employed to achieve higher-order accuracy at the cell faces through a Taylor series expansion of the cell-centred solution about the cell centroid. The pressure-based solver is employed to solve the pressure based equation which is derived from the momentum and continuity equations. All these equations are solved sequentially and iteratively so as to obtain a converged numerical solution. For all the simulations carried out in the present analysis, convergence criteria for the solutions are considered when the residuals become less than 10^{-6}.

Different types of models like single phase, multi-phase and discrete phase models have been used throughout the thesis. Also, different types of transitional models called Standard $\kappa - \omega$ and SST $\kappa - \omega$ models and turbulent models named Standard $\kappa - \epsilon$, RNG $\kappa - \epsilon$ and Realizable $\kappa - \epsilon$ models have been used.

In chapter 4, single phase model is used which is described in §3.1.1 of Chapter 3. Also, two different transitional models named Standard $\kappa - \omega$ and SST $\kappa - \omega$ models are also used that are described in §3.2.1 and §3.2.2 of Chapter 3 respectively.

In chapter 5, multi-phase model is used which is described in §3.1.2 of Chapter 3. Also, SST $\kappa - \omega$ transitional model is used and described in §3.2.2 of Chapter 3.

In chapter 6, single phase model is used which is described in §3.1.1 of Chapter 3. Also, three different turbulent models named Realizable $\kappa - \epsilon$, Standard $\kappa - \epsilon$ and RNG $\kappa - \epsilon$ models are also used that are shown in §3.2.3, §3.2.4 and §3.2.5 of Chapter 3 respectively.

In chapter 7, multi-phase model is used which is described in §3.1.2 of Chapter 3. Also, Realizable $\kappa - \epsilon$ turbulent model is used and is described in §3.2.3 of Chapter 3.

In chapter 8, discrete phase model is used which is described in §3.1.3 of Chapter 3. Also, SST $\kappa - \omega$ transitional and Realizable $\kappa - \epsilon$ turbulent models are used that are explained in §3.2.2 and §3.2.3 of Chapter 3 respectively.

In chapter 9, single and multi-phase models are used which are described in §3.1.1 and §3.1.2 of Chapter 3 respectively. Also, SST $\kappa - \omega$ transitional model is used and is described in §3.2.2 of Chapter 3.

Chapter 4

Transition of Nanofluids Flow, Part 1: Performance of a Single Phase Model

4.1 Introduction

Reynolds [89] found the transition flow behaviour to change unpredictably between the laminar and turbulent flow. It is observed in this research that the laminar flow can be sustained at high Reynolds numbers if different types of disturbances in the flow are eluded (Cengel [41]). Later on, Ekman [90] and Pfenniger [91] performed experimental investigations and stated that the laminar flow could have been maintained up to a Reynolds number of 40,000 and 100,000 respectively by reducing the flow disturbances. Cengel [41] also suggested, that it was better to have some specific values of Reynolds number for laminar, transitional and turbulent flows in a smooth pipe. But this was tricky since flow disturbances were generated by various mechanisms such as surface roughness, noise, and vibrations. In most cases, the flow in a smooth pipe is said to be laminar when $Re < 2300$, fully turbulent when $Re > 10{,}000$ and transitional when $2300 \leq Re \leq 10{,}000$. Cengel [41] however stated that even though transitional flow exists for $2300 \leq Re \leq 10{,}000$, a fully turbulent condition in many practical applications can be achieved when $Re > 4000$.

In this chapter, numerical investigations are carried out using single phase model (SPM) under transition flow condition. Here, two-dimensional axi-symmetric model of a horizontal pipe with the length L of 1.0 m and internal diameter, D_h of 0.019 m is considered to analyse the transition flow and heat transfer performance of Al_2O_3 and TiO_2–water nanofluids through it. The geometry is shown in Fig. 4.1. In this investigation, two different transition models, such as, Standard $k-\omega$ and SST $k-\omega$ models are used. And, the details about these models are given in §3.2.1 and §3.2.2 of Chapter 3. The main objective of this research is to analyse the effects of different nanoparticles size and concentrations with and without the Brownian motion of nanoparticles on heat transfer under transition flow condition. Besides, the effect of

roughness on heat transfer is investigated for the above parameters. Finally, results are presented in terms of mean velocity, mean temperature, turbulent kinetic energy, Darcy friction factor, local and average Nusselt number, average wall shear stress coefficient ratio, thermal performance factor and entropy generation. Such results facilitate the understanding about the mean velocity, turbulent kinetic energy and mean temperature behaviours as well as the pressure drop and the behaviour of heat transfer performance.

4.2 Boundary Conditions

The following boundary conditions are used to solve the system of nonlinear partial differential equations which are given in §3.1.1 of Chapter 3.

At the pipe inlet, a uniform velocity ($v_{x,in}$) as well as a uniform temperature ($T_{in} = 293\ K$) with a turbulent intensity ($I = 2$ to 4%) and hydraulic diameter ($D_h = 0.019\ m$) are stated. And, all the thermal properties used in this work are calculated at the inlet temperature (T_{in}) that also is considered to be the reference temperature.

At the pipe outlet, a static gauge pressure, $p_{gauge} = 0$, is specified. And, the finite volume solver extrapolates the other flow and the scalar quantities such as the temperature and the turbulent quantities from the interior domain.

On the pipe wall, a no-slip boundary condition is introduced with uniform heat flux, q" = 5000 W/m^2.

Furthermore, the roughness of the pipe wall which is considered here is similar to a sand grain roughness. For this, a modified law of wall equation is implemented. Then, different roughness height, $K_s = 0.375, 0.5,$ and $0.625\ mm$ with a uniform roughness constant, $C_s = 0.5$ (Xiao-wei *et al.* [92]) are considered throughout the investigation. Particulars of the roughness of wall are given in §3.4 of Chapter 3.

Besides, all the calculations of thermophysical properties of water, nanoparticles as well as nanofluids are taken at T_{in}. The specific details of these thermophysical properties are given in §3.3 of Chapter 3.

4.3 Grid Sensitivity Test

Extensive computational simulations are performed in order to assess the accuracy of the numerical findings. Initially, the grid sensitivity analysis is performed using both the Standard $k-\omega$ and SST $k-\omega$ transition models to find out an appropriate combination of the mesh distributions. This is applicable to resolve both the velocity and the temperature fields inside the horizontal pipe. The grid sensitivity test is done by varying the total number of grid distributions in both the axial *(Nx)* and the radial *(Nr)* directions. Here, five different grid combinations such as 500×25, 500×50, 500×100, 500×150, and 1000×100 are used. Then, the uniform grid in the axial direction and non-uniform structured grid in the radial direction are considered in order to control any large deviations of flow and temperature fields near the upstream as well as near the wall regions. Besides, a mesh successive ratio of 1.1 is considered to generate such non-uniform grids in the near wall region.

Two different test cases are considered for water of Prandtl number, $Pr = 7.04$, $Pr_t = 0.85$ and Reynolds number, Re = 3900 and 10,000 respectively while performing the grid sensitivity test. Then various combinations of grid are analysed to justify that the numerical results are grid independent. Figure 4.2 shows the variation of radial velocity, temperature (T) and turbulent kinetic energy (κ) profiles at the horizontal location, $x = 0.99$ m, for $K_s = 0$ (smooth pipe wall). These results are generated by using the SST $k-\omega$ transition model and the selection of this particular transition model for the grid sensitivity test is clarified in §4.4. It is observed that the grids 500×100, 500×150 and 1000×100 generate the most reasonable results because the differences found among the results are quite insignificant. In order to save the computing time and to avoid any inconsistencies in the numerical results, particular grid for the present calculations is selected to be consisted of 500 and 100 nodes along the axial and the radial directions respectively.

4.4 Validation

Validation of the present numerical findings is done for water against the existing experimental data as well as correlations for different $Re = 2300$ to 10^4 and $Pr = 7.04$. Besides, the accuracy of the two different transition models such as the Standard $\kappa-\omega$ and SST $\kappa-\omega$ transitional models are investigated.

In the following, numerical results of Darcy friction factor and Nusselt number are presented and compared with different correlations as well as experimental results. Details are given below:

Firstly, numerical results of the Darcy friction factor is compared with the correlation suggested by Blasius [93] and the experimental results of Chandrasekar *et al.* [43] and Naik *et al.* [44]. Then, it is followed by the comparison of the average Nusselt number with the experimental results of Sharma *et al.* [42], Chandrasekar *et al.* [43] and Naik *et al.* [44] and correlation suggested by Gnielinski [94].

A suitable use of the turbulent intensity at the upstream of the pipe domain is always important for the transient simulation. So, three different values of the turbulent intensity are tested and findings are compared with the relevant data for a smooth pipe wall, as shown in Fig. 4.3.

The only available correlation for average Nusselt number is the Gnielinski equation [94] which provides a prediction of average Nusselt number for a fully developed turbulent flow in a pipe or channel. This correlation can be useful for a transitional flow because, as suggested, it is valid for $Re > 3000$. However, since it is developed from the data values of a fully developed turbulent flow, its accuracy in transitional flow needs to be tested carefully. The results presented in Figure 4.3(b) suggest that this correlation cannot predict the average Nusselt number for the transition flow correctly for all the Reynolds numbers under consideration.

It is observed that Darcy friction factor results of Chandrasekar *et al.* [43] are in good agreement with the results of Blasius [93]. But the Darcy friction factor results of Naik *et al.* [44] found to be slightly lower for low Reynolds numbers and when compared with the results of Blasius [93] and Chandrasekar *et al.* [43]. It is also observed that Nusselt number results of Chandrasekar *et al.* [43] for low Reynolds number seems to be close to the results of Gnielinski [94]. And, Nusselt number results of Sharma *et al.* [42] for high Reynolds number found to be close to the results of Naik *et al.* [44]. Considering these observations, following comparisons are considered:

While varying the turbulent intensity from 2% to 4%, the maximum deviation on the average Nusselt number is found to be 19.45%, 2.94% and 1.85% respectively comparing with the results of Naik *et al.* [44]. On the other hand, the maximum deviation on the Darcy friction factor for I = 2% is 20.49% and 12.68% respectively

in comparison with the results of Blasius [93] and Naik *et al.* [44]. And, for the turbulent intensity of 3%, the maximum deviation is 30.93% and 22.39% respectively and is increased further to 35.70% and 26.85% for I = 4%.

Although the turbulent intensity of 2% seems to be a reliable option because of the results of Darcy friction factor showing slightly better agreement with the correlation and experimental results, a significantly higher percentage of deviation in the average Nusselt number is disappointing. A higher Darcy friction factor is observed for the turbulent intensity of 4% compared to that of 3%. And, the maximum percentage deviation between the results of the average Nusselt number for 3% is not significant. That is why, the turbulent intensity of 3% is considered throughout the investigations.

It is also observed that there is no significant variation between the results of average Nusselt number using the Standard $\kappa - \omega$ and the SST $\kappa - \omega$ transitional models. But the Darcy friction factor result of the SST $\kappa - \omega$ transitional model is slightly better than that of the Standard $\kappa - \omega$ transitional model in comparison with the experimental results and correlation. Hence, the SST $\kappa - \omega$ transitional model is considered to carry out all the numerical simulations in this research.

Blasius [93] equation:

$$f = \frac{0.316}{Re^{0.25}}, \qquad 3000 \leq Re \leq 10^5 \tag{4.1}$$

Gnielinski [94] equation:

$$\overline{Nu} = \frac{\frac{f}{8}(Re - 1000)Pr}{1.0 + 12.7\left(\frac{f}{8}\right)^{0.5}\left(Pr^{\frac{2}{3}} - 1\right)}, \qquad \begin{pmatrix} 0.5 \leq Pr \leq 2000 \\ 3000 < Re \leq 5 \times 10^6 \end{pmatrix} \tag{4.2}$$

$$f = (1.82 \ln Re - 1.64)^{-2}, \qquad 3000 < Re \leq 5 \times 10^6$$

4.5 Results and Discussion

4.5.1 Smooth Pipe Wall

Extensive numerical simulations are performed using the single phase model for Al_2O_3-water and TiO_2-water nanofluids with $Re = 2300$ to 10×10^3, $Pr =$ 7.04 to 20.29, $\chi = 2$ to 6%, and $d_p = 10$ to 40 nm. The effects of nanoparticles

concentrations and diameters on the heat transfer as well as the entropy generation are discussed in the following sections and some new correlations are also proposed.

4.5.1.1 Mean Velocity and Temperature Behaviours

The details of hydrodynamic and thermal physics and the strength of turbulence along the pipe are presented in Figs. 4.4 to 4.9 for a selected $Re = 3500$. Hereafter, overall results for different Reynolds numbers are summarised.

Figures 4.4 and 4.5 show the variations of different nanoparticles concentrations and diameters on the flow field of Al_2O_3-water and TiO_2-water nanofluids along the axial direction. Here, the effect of without and with Brownian motion of nanoparticles is taken into account too. It is observed that the flow field initially behaves like a laminar flow and after a certain distance, it suddenly changes the flow pattern causing transition followed by the laminar flow breakdown.

Moreover, it is observed that the development of momentum boundary layer near the upstream moves the fluid in the direction of the centreline regime. After the laminar breakdown point, the thickness of the momentum boundary layer becomes larger and it helps to drive the fluids closer to the centreline region. And then, the mean velocity is found to be the highest in that region and the centreline velocity starts to decrease in an attempt to satisfy the equation of continuity. Besides, the thickness of the momentum boundary layer starts to reduce and becomes constant beyond this regime and the velocity profile starts to be fully developed. On the whole, as it is shown in Figs. 4.4 and 4.5, the mean velocity increases with the increase of χ and d_p. But, the higher velocity magnitude is observed when the effect of Brownian motion of nanoparticles is considered. This is due to the variation of nanoparticles' velocity with the nanoparticles diameters which is also added to the fluid particles velocity. And then, nanofluids velocity becomes higher for smaller size of nanoparticles than the large size of nanoparticles because small nanoparticles move faster than the large nanoparticles.

The variation of different χ and d_p in the temperature field of Al_2O_3 and TiO_2-water nanofluids are shown in Figs. 4.6 and 4.7 in order to understand the transition behaviour in the temperature field. The effect of without and with Brownian motion of nanoparticles with different nanoparticles concentrations and diameters are also

presented as it was done with the flow field. In the present investigation, nanofluids behave like a coolant fluid. When uniform temperature is applied at the upstream with a higher value of heat flux to the wall, the wall temperature is found to be higher near the pipe wall regime along the axial direction indicating the lower temperature of the nanofluids flowing through the pipe. It is observed that the temperature field also behave like a laminar flow initially and then, the laminar flow begins to breakdown at some points near the upstream.

In the following figures, it is seen that most of the inner region is covered with deep blue colour. Also, the near wall temperature is found always higher than the inner region. It indicates, there is a temperature difference between the pipe wall temperature and the coolant fluids. Also, the maximum temperature difference is found to be approximately 7K without considering the Brownian motion. But this difference reduces up to 6K approximately when the Brownian motion of nanoparticles is considered. Furthermore, this coolant regime starts to increase in size with the increase of χ and decrease of d_p due to the decay of thermal boundary layer.

In addition, decreases in the wall temperature and the thickness of thermal boundary layer are observed with the decrease of d_p from 40 to 10 nm. The reason behind the fact is, the higher mean velocity of lower size of nanoparticles forces the fluid to move quickly to the downstream region, and the development of wall temperature becomes less prominent for higher size of nanoparticles. These behaviours are important because such reduction has impacts on the enhancement of heat transfer. It is important to note that very small variation is seen for the temperature field of both the Al_2O_3 and TiO_2-water nanofluids. But the variation between the flow field and the higher thermal conductivity of Al_2O_3-water nanofluid compared to the lower thermal conductivity of TiO_2-water nanofluid may be a vital reason to see the increase in the heat transfer rate. Further details are provided in section 4.5.1.2.

Variations of the turbulent kinetic energy of Al_2O_3 and TiO_2-water nanofluids are presented in Figs. 4.8 and 4.9 in order to comprehend the strength of the turbulent kinetic energy in the flow. Initially the turbulent kinetic energy remains negligibly small because of the laminar flow behaviour near the upstream and then it starts to increase gradually. Later, a rapid growth of turbulent kinetic energy is observed at the near wall region and the laminar breakdown point. Such growth becomes

maximum after the laminar breakdown point and then starts to decrease slightly again. Beyond this position, turbulent kinetic energy profile tends to become fully developed. Besides, generation of turbulence is found in the development of boundary layer and diffusion is noticed in the direction of centreline regime. In the context of a fully developed turbulent flow in a pipe [95, 96], it is understood that the viscous dissipation takes place in the near wall region but the maximum turbulence generation occurs at the edge of the viscous sub-layer. This edge appears to be the boundary from where the diffusion takes place towards the centre of the pipe. It, therefore, suggests that the turbulence generation is always observed between the wall and the hydrodynamic boundary layer. Moreover, the rate of turbulence generation becomes zero at the wall because of the no-slip velocity boundary condition applied on the pipe wall which causes the velocity fluctuations to diminish at the wall. Further validation with a comparison between the numerical and experimental results of the turbulent kinetic energy is given in Chapter 6.

It also is detected that the turbulence kinetic energy increases with the increase of nanoparticles concentrations. Also, such enhancement becomes more pronounced when the Brownian motion and diameter of nanoparticles are considered. It concludes that the higher χ and lower d_p result in the higher value for turbulent kinetic energy at the laminar breakdown point. It can be caused by that the velocity of the smaller nanoparticles absorbs energy in a low rate. Additionally, Al_2O_3-water nanofluid is found to show slightly higher values of turbulent kinetic energy than TiO_2-water nanofluid. It is feasible in a sense that Al_2O_3-water nanofluid shows higher values of mean velocity than TiO_2-water nanofluid. It is essential to note that when $d_p = 40\ nm$, maximum value of turbulent kinetic energy for both the Al_2O_3 and TiO_2-water nanofluids is identical. It might be concluded after the analysis of the findings that both the nanofluids produce similar results for $d_p \geq 40\ nm$ when the effect of Brownian motion of nanoparticles is under consideration.

The above mentioned results are found on a particular Reynolds number. Overall findings for different Reynolds number are presented and discussed in the following paragraph.

It is generally been observed that if the Reynolds number increases, the mean velocity also increases and the laminar breakdown of flow field occurs earlier and moves very close to the upstream. This effect is reasonable because the momentum boundary

layer thickness decreases as the Reynolds number increases for high Prandtl number fluids. It indicates the increase of mean velocity at the centreline regime too. Moreover, rapid movement of small sized nanoparticles helps to increase the mean velocity of nanofluids. On the contrary, the mean velocity of nanofluids remains low for the low Reynolds number flow. In such cases, diffusion plays a significant role in transferring heat from one place to another. Then again, the higher mean velocity brings forced convection for high Reynolds number flow. It helps to transfer heat quickly when the temperature difference between the pipe wall and the coolant nanofluids is very low. It is also found that as the Reynolds number and nanoparticles concentrations increase, the wall temperature and the thickness of thermal boundary layer decrease. And, the turbulent kinetic energy profile shifts towards the upstream with the increase of Reynolds number. Moreover, turbulent kinetic energy increases with the increase of Reynolds number. It is also because of the increase of mean velocity with the increase of Reynolds number.

Variations of Darcy friction factor of Al_2O_3-water nanofluid with different Reynolds numbers are presented in Fig. 4.10 in order to understand the pressure drop behaviour with different Reynolds numbers. A strong agreement between the results of Darcy friction factor of Al_2O_3-water nanofluid and water is observed. It means, the nanoparticles concentrations and diameters have an insignificant effect on the enhancement of the pressure drop and the Darcy friction factor. Hence, it is possible to draw a conclusion that nanofluids can be used as a new generation heat transfer fluid without the penalty for pumping power. Similar behaviours are also observed for TiO_2-water nanofluid.

4.5.1.2 Heat Transfer Behaviour

The local and average Nusselt number results are presented and discussed in this section with the purpose of understanding both the local and average heat transfer behaviour. To better quantify the transition regimes presented in Figs. 4.4 to 4.7, axial variation of the local Nusselt number with different Re ($1130 < Re < 17 \times 10^3$) for the Al_2O_3-water nanofluid ($d_p = 10\ nm, \chi = 2\%$) is shown in Fig. 4.11. It is observed that the local Nusselt number is always found maximum near the entrance region. Then it starts to decrease rapidly with the axial distance until a minimum value can be predicted from the breakdown of laminar flow. When this minimum value is achieved, Nusselt number starts to increase again and form a plateau-like profile. And

finally, it reaches a constant value when the flow tends to be fully developed. Abraham *et al.* [97] also reported the similar behaviour for air flow in pipe under transition flow condition. In addition, the local Nusselt number behaviour is observed to indicate the existence of laminar and turbulent flow regimes for $Re \leq 1130$ and $Re \geq 17 \times 10^3$ respectively.

Moreover, from Fig. 4.11, it is seen that the distance of laminar breakdown point from the inlet varies from approximately $0.85\,m$ to $0.06\ m$ as the Reynolds number varies from2300 to 10×10^3. Furthermore, such distance moves to a distance close to the upstream of the pipe when the Reynolds number increases from 2300 to 10×10^3. And then, it tends to decrease rapidly for the Reynolds number that is greater than10×10^3. In particular, the value of such distance is approximately $0.06\ m$ for $Re = 10 \times 10^3$. However for $Re = 15 \times 10^3$ and 17×10^3, the values of such distance are approximately $0.037\ m$ and $0.0\ m$ respectively. It also means that there is a laminar state between the upstream and the breakdown point. These outcomes strongly support the observations made by Abraham *et al.* [97] too. It is also observed that the transition behaviour actually begins for $Re > 1130$ and flow becomes fully turbulent for $Re = 17 \times 10^3$. It thus suggests, the transition regime can be extended up to $Re = 17 \times 10^3$because the distance of break down point from the origin tends to vanish when the Reynolds number is very close to $Re = 17 \times 10^3$. Considering the above observations, we can determine that the transitional regime can be considered as $1130 < Re < 17 \times 10^3$ for the smooth pipe wall case.

Consequently, the following definitions are introduced and the related results are presented in Figs. 4.12 and 4.13.

- The distance from the upstream to the laminar breakdown point is called the 'critical distance'.
- Critical distances for flow and thermal fields are known as 'hydrodynamic critical distance' and 'thermal critical distance' respectively.
- Local Nusselt number calculated at the laminar breakdown point is known as critical Nusselt number.

Fig. 4.12 shows that the hydrodynamic and thermal critical distances decrease along with the increase of Reynolds numbers. It is realistic in a sense that as the Reynolds number increase, flow and thermal transition behaviour tends to diminish and also tends to become fully turbulent. Such behaviour is also physically valid because, in

nature, all the flows are turbulent and transition from laminar to turbulent flows will not sustain for a long time. Arithmetically, hydrodynamic critical distance at $x_{c,V}$ can be calculated from the drops of the velocity gradient on the left and the rises of the velocity gradient on the right. However, thermal critical distance at $x_{c,T}$ can be calculated from the rises of the temperature gradient on the left and the drops of the temperature gradient on the right. It means, the velocity and temperature gradients change sign from the left to the right of the laminar breakdown point. Besides, the hydrodynamic critical distance is also found to be smaller than the thermal critical distance. And, it suggests that transition begins earlier in the flow field than in the temperature field.

As it is also shown in the Fig. 4.12, the hydrodynamic and thermal critical distances are strongly dependent on the Reynolds number. But, both of them are absolutely independent of different types of fluids, nanoparticles diameters and concentrations. Such findings are realistic and physically valid (Cengel [41]). We find that both the hydrodynamic and thermal entrance lengths are independent of the nanofluids and also of their d_p and χ. While, the hydrodynamic entrance length depends on the Reynolds number and pipe diameter, the thermal entrance length only depends on the pipe diameter. It thus further suggests that when the transition to turbulent flow tends to be fully hydro-dynamically and thermally developed, it remains unaffected by the types of fluids as well as d_p and χ.

In general, significant variations in the flow and temperature fields are observed inside the pipe with the increase of turbulent intensity. Moreover, velocity and temperature critical distances changed significantly with different turbulent intensity. It suggests that both the velocity and temperature critical distances are fully dependent on turbulent intensity.

Finally, two new correlations are proposed to describe the behaviour of hydrodynamic and thermal critical distances with a maximum deviation of 1% under the transition regime. To do this, a total of 80 simulations are carried out for the Reynolds number ranging from 1130 to 17×10^3. These correlations are not valid when $Re < 1130$ and $Re > 17 \times 10^3$ because the transition behaviour disappears in this stage. And, fully developed laminar flow ($Re \leq 1130$) and turbulent flow ($Re \geq 17 \times 10^3$) behaviours are observed too.

$$x_{c,V} = Exp\ (Alog(Re) + B)$$
$$\text{where } A = -1.26306, B = 8.70204, 1130 < Re < 17 \times 10^3 \tag{4.3}$$

$$x_{c,T} = Exp\ (Alog(Re) + B)$$
$$\text{where } A = -1.20263, B = 8.27248, 1130 < Re < 17 \times 10^3 \tag{4.4}$$

Investigations are also carried out for different nanoparticles diameters and concentrations to study their effects on heat transfer and results are presented in the following paragraphs.

Initially, variations of the critical Nusselt number with different Re for $d_p =$ 10 to 40 nm and $\chi = 2$ to 6% has are shown in Fig. 4.13. This figure illustrates that the critical Nusselt number using Al_2O_3-water nanofluid increases with an increase in both the Reynolds number and nanoparticles concentration. Such increase is more significant for the higher value of χ, suggesting that the enhancement of heat transfer rate is strongly dependent on Re and χ. It is also seen that the critical Nusselt number is fully dependent on the type of nanofluids as well as on d_p. This finding is reasonable because the critical Nusselt number has been calculated from the local Nusselt number which also varies with d_p and χ. Similar behaviour also is observed for different d_p of TiO_2-water nanofluid.

The variations of average Nusselt number with the Reynolds number are presented in Figs. 4.14 and 4.15 considering without / with the effects of Brownian motion. The purpose is to examine the behaviour of average Nusselt number calculated from the local Nusselt number.

As shown in Fig. 4.14, the average Nusselt number increases with the increase of nanoparticles concentration. Besides, the maximum percentage of the heat transfer enhancement for Al_2O_3–water nanofluid with $\chi = 2\%, 4\%$ and 6% is found to be approximately 1.72, 4.54 and 7.83 respectively. However, it is approximately 0.61, 2.84 and 6.02 respectively for TiO_2–water nanofluid. This is because the thermal conductivity of Al_2O_3-water nanofluid is higher than that of TiO_2-water nanofluid. Additionally, the development of hydrodynamic and thermal boundary layers of Al_2O_3-water nanofluid compared to TiO_2-water nanofluid plays a more important role in enhancing the heat transfer rate as already described in Section 4.5.1.1.

The results presented in Fig. 4.15 confirm that the average Nusselt number monotonically increases with the increase of nanoparticles concentration.

Particularly for Al_2O_3–water nanofluid with $d_p = 10\ nm$, the minimum and maximum percentages of the heat transfer enhancement are approximately 3.25 and 3.40, 11.07 and 11.55, 28.66 and 29.48 respectively. When $d_p = 20\ nm$, such percentages of the heat transfer enhancement are reduced and found approximately 2.27 and 2.36, 7.47 and 7.79, 16.59 and 17.17 respectively. This degeneration of minimum and maximum percentage of heat transfer continues when d_p increases further. For example, when $d_p = 40\ nm$, they are predicted to be approximately 1.53 and 1.63, 4.71 and 5.11, 10.71 and 11.00 respectively. The trend in which the average *Nu has* changed remains to be the same for the TiO_2–water nanofluid. But, a slight difference in magnitude is obtained for the percentages of the heat transfer enhancement compared to those of the Al_2O_3–water nanofluid.

Overall, the Al_2O_3–water nanofluid always shown the higher heat transfer rate than the TiO_2–water nanofluid irrespective to the change in Reynolds numbers, nanoparticles concentration and diameter when the Brownian motion of nanoparticles is considered. Also, the reason for improving the average Nusselt number is related to different aspects. Increase in the thermal conductivity; Brownian motion of nanoparticles and its size and shape; decrease in the boundary layer thickness and delay in the boundary layer growth are the most prominent ones among them.

4.5.1.3 Average Shear Stress Coefficient Ratio

Average shear stress ratio is defined as the ratio of the average shear stresses of nanofluid and water.

In order to understand the behaviour of average shear stress ratio, Figs. 4.16 and 4.17 show the variation of the nanoparticles concentration and diameter on the average shear stress ratio, $\overline{\tau_\tau}$, with Reynolds number considering the effects of Brownian force of nanoparticles.

When the Brownian motion of nanoparticles is ignored, the average shear stress ratio for the Al_2O_3–water nanofluid with $\chi = 2\%, 4\%$ and 6%, is approximately $1.35, 1.99$ and 3.02 respectively. However, for the TiO_2–water nanofluid the ratio is approximately $1.25, 1.71$ and 2.47 respectively. It suggests, although nanofluids have significant effects on the enhancement of heat transfer, some disadvantages on the

wall shear stress is unavoidable. Brownian motion of nanoparticles even causes further drawback, as shown in Fig. 4.17, resulting in higher values of the average shear stress ratio though depending on d_p. In particular, the average shear stress ratio for Al_2O_3–water nanofluid, is approximately 1.66, 3.58 and 14.60 respectively for χ = 2%, 4% and 6% with $d_p = 10\ nm$. This is reduced to approximately 1.47, 2.54 and 5.79 respectively with $d_p = 20\ nm$ and is further reduced with the higher values of d_p. Additionally, a rapid reduction in the average shear stress ratio is also predicted when χ is increased and this remains to the case for all the cases investigated. To compare these two nanofluids, the prediction of $\overline{\tau_\tau}$ is almost same apart from the higher value of χ for which some variations in $\overline{\tau_\tau}$ are also reported. Further, the wall shear stress ratio of nanofluids is always found to be higher than that of water and such enhancement is independent to the Reynolds numbers.

Therefore, a significant setback with respect to various practical applications of the nanofluids can be encountered as the effect of the wall shear stress.

4.5.1.4 Entropy Generation Analysis

It is crucial to determine the appropriate nanoparticles concentration as well as the diameter while using nanofluids. For, these are required to calculate the optimal Reynolds numbers. Here, entropy generation analysis suggests a way to work on the issue. The necessary equations used in the entropy generation analysis are given in §3.5.1 of Chapter 3. Besides, when Brownian motion of nanoparticles is considered, the results of the entropy generation analysis are presented in the following paragraphs:

Figure 4.18 and 4.19 show the variations of the frictional, thermal and total entropy generations with Reynolds numbers for the two nanofluids. It is seen that the total entropy generation decreases as the Reynolds number increases with the decrease of the nanoparticles diameter from 40 to 10 *nm*. This is caused by the decrease of the thermal entropy generation with the significant enhancement of heat transfer rate already shown in Fig. 4.15. However, when χ is increased from 2% to 6%, the total entropy generation rapidly decreases as the Reynolds number increases due to the enhancement of average Nusselt number as well as the increase of thermal conductivity of nanofluids. Additionally, the rapid reduction of total entropy generation indicates that the effect of friction entropy generation is negligible, as

shown in Fig. 4.18. Whereas, the effect of thermal entropy generation is more significant and that is why, the behaviour of both the thermal and total entropy generation is similar.

The total entropy generation also becomes maximum for low Reynolds numbers but with higher χ. While, this finding indicates that an increase in χ has an impact on the total entropy generation being reduced. However, no optimal Reynolds number is observed which could minimise the total entropy generation. It further suggests that suitable χ and d_p which could potentially help to find an optimal thermal system are not found.

4.5.1.5 Correlations

Developing a correlation is necessary to determine an average Nusselt number for a particular selection of Reynolds number, nanoparticles concentration as well as diameter. The main advantage here is that one can generate the value of average Nusselt number at any given parameters without running a full set of numerical simulations. Thus it reduces the time, cost and effort required to engineering practice too.

The following correlations are developed for the numerical computation of the average Nusselt number by using a non-linear regression analysis. These correlations are fully dependent on the Reynolds numbers, the Prandtl numbers as well as the d_p. At the same time, these are also valid when the Brownian motion of nanoparticles is taken into account.

The value of maximum standard deviation of error for the Al_2O_3-water nanofluid is found to be 0.21%. Though, it is 0.19% for the TiO_2-water nanofluid. Besides, a validation between the present numerical results of the average Nusselt number and the suggested correlations are presented in Fig. 4.20. This figure confirms having a good agreement between the numerical results and the proposed correlations.

Al_2O_3-H_2O Nanofluid : $$\overline{Nu} = 0.03945\, Re^{0.76746} Pr^{0.24025} \left(\frac{d_f}{d_p}\right)^{-0.0004483} \quad (4.5)$$

TiO_2-H_2O Nanofluid : $$\overline{Nu} = 0.03930\, Re^{0.76745} Pr^{0.24165} \left(\frac{d_f}{d_p}\right)^{-0.0007074} \quad (4.6)$$

where

$2300 \leq Re \leq 10 \times 10^3, 8.45 \leq Pr \leq 20.29, 10 \leq d_p(nm) \leq 40, 0 < \chi(\%) \leq 6.$

4.5.2 Effect of Wall Roughness

Fluid flows over rough surfaces are encountered in diverse situations. Prominent examples are flows over the surfaces of aeroplanes, ships, turbo machineries, heat exchangers, piping systems, and atmospheric boundary layers over terrain of varying roughness. Wall roughness usually affects drag (resistance) and processes by which heat and mass transfer take place on / near the walls of a system. Thus modelling transition or turbulent wall-bounded flow affected by the wall roughness is considered to be noteworthy. A modified law-of-the-wall for roughness is considered in the numerical simulations with details already given in §3.4 of Chapter 3 [68].

In §4.5.1.2., the maximum percentage of the enhancement of heat transfer rate has been found for the smaller nanoparticles with a higher concentration for both the Al_2O_3- and TiO_2-water nanofluids with the Brownian motion. Therefore, we fix the concentration (χ) and the diameters (d_p) to 6% and 10 nm respectively in this section. Since the particular focus is to examine the various effects of the pipe wall roughness, different roughness heights (0.375 mm, 0.5 mm and 0.625 mm) are chosen throughout this investigation (Xiao-wei *et al.* [92]) with Re varying from 2300 to 10×10^3.

4.5.2.1 Roughness Effect on Flow Field and Turbulent Kinetic Energy

The contour plots of the mean velocity and the turbulent kinetic energy along the pipe with rough surface are presented in Figs. 4.21 and 4.22 respectively for a selected $Re = 3500$ to investigate how the wall roughness affects the flow field as well as the flow separation process.

Figure 4.21 shows the variations of flow field of Al_2O_3-water and TiO_2-water nanofluids with different roughness heights. It is seen that with an increase of roughness height, thickness of the momentum boundary layer remains unchanged near the downstream location. But the region where the higher fluid velocity is predicted starts to reduce, which is clearly visible near the laminar breakdown point and forces the fluid moving towards the centreline regime. Thereafter, the growth of the momentum boundary layer starts to increase and the mean velocity is found to be maximum at the centreline region. Also, a steady state pattern of momentum

boundary layer is observed beyond this regime. Moreover, the laminar breakdown point moves closer to the upstream with an increase of the roughness heights of the pipe wall.

Also, Fig. 4.22 shows the variations of turbulent kinetic energy of Al_2O_3-water and TiO_2-water nanofluids with different roughness heights. It is observed that like the flow field, the development of turbulent kinetic energy profile moves closer to the upstream with the increase of roughness heights of the pipe wall. Also, the laminar breakdown point of both the velocity and turbulent kinetic energy profiles are found identical. Initially the blue regions covers the area near the upstream indicates a laminar state of the flow field. thus further clarifies that the transition begins where the breakdown of the laminar flow occurs. After that region and also very close to the wall, growth of the turbulent kinetic energy becomes maximum and tends to be steady state beyond the laminar breakdown regime. It is also observed that the maximum value of turbulence kinetic energy remains constant for both the nanofluids with the increase of roughness heights of the pipe wall. It shows that wall roughness heights have insignificant effect on the enhancement of turbulent kinetic energy regardless of the fluids.

In general, the laminar breakdown of flow field starts to move more towards the upstream and transition flow behaviour starts to diminish with the increase of Reynolds numbers. And, the flow goes to be fully turbulent with the increase of roughness heights. Also, the distance between the upstream and the laminar breakdown point is found to be fully independent of fluids though it depends on both Reynolds number and roughness height of the pipe wall. This is also realistic because the development of flow field only depends on Reynolds number and is also affected by the roughness height of pipe wall.

4.5.2.2 Roughness Effect on Wall Temperature

Figure 4.23 shows the variations of wall temperature with different roughness heights along the pipe. It is to be noted that a rapid increase of pipe wall temperature near the upstream is observed for all the cases considered in this study. And then, suddenly it starts to decrease at some points and such behaviour is realistic for transition regime. It is also observed that the increase of roughness height has a positive impact on the pipe wall temperature which is attributed to the decrease of

wall temperature with the increase of roughness height of the wall. In Particular, the maximum temperature difference at $x = 0.99\ m$ between the smooth wall and rough wall cases with $K_s = 0.625\ mm$ is about $2K$. This indicates, the effect of roughness height is not negligible. It is also observed that the TiO_2-water nanofluid always shows little bit higher wall temperature than Al_2O_3-water nanofluid for rough wall cases. It means, the thermal effect on heat transfer can be improved due to roughness height and such effect is helpful to enhance the heat transfer rate while using both Al_2O_3-water and TiO_2-water nanofluids.

4.5.2.3 Roughness Effect on Darcy Friction Factor

In Fig. 4.24(a), variations of Darcy friction factor, *f*, with different Reynolds number and roughness heights are presented using both the Al_2O_3-water and TiO_2-water nanofluids. The Darcy friction factor is observed to increase with the increase of the roughness height but decreases monotonically with the increase of Reynolds number. For a higher roughness height, increase of Darcy friction factor is found to be the maximum. Particularly, for the Al_2O_3-water nanofluid and $K_s = 0.375, 0.5$ and $0.625\ mm$, the maximum respective variations of 9.65%, 23.57% and 39.7% are observed compared with the smooth pipe wall results of water. Similar results are found for the TiO_2-water nanofluid.

Figure 4.24(b) presents the Darcy friction factor ratios of the fluids with different roughness heights at *Re* = 2300, 3100, 5500, 8000 and 10000 respectively. Here, the Darcy friction factor ratios are found to increase monotonically when $K_s \leq 0.4\ mm$ for all the Reynolds numbers. And then, these start to rise rapidly with the increase of roughness heights. However, the enhancement of Darcy friction factor ratios is found significantly higher compared to other cases particularly for a superior Reynolds number with higher roughness heights. Thus, it indicates, an increase of roughness heights enhances the pressure drop resulting in higher penalty for pumping power in practical applications.

4.5.2.4 Heat Transfer Performance

In Fig. 4.25, axial variations of local Nusselt number with different roughness heights, $K_s(mm)$ for $Re = 2300$ are shown. It is seen that the local Nusselt number behaviours for different roughness heights remain similar as described in Fig. 4.11. But it is

observed that when the roughness height increases, critical distance decreases and moves towards the upstream. It happens due to the increase of roughness height of pipe wall which creates more disturbances on flow and thermal fields and force to start transition behaviour earlier. Effect of roughness heights on critical distances is shown in Fig. 4.26.

In Fig. 4.26, variations of non-dimensional hydrodynamic and thermal critical distances with different Reynolds number for different roughness heights, $K_s(mm)$, have been are shown using both Al_2O_3-water and TiO_2-water nanofluids. It is found that non-dimensional hydrodynamic and thermal critical distances decrease with the increase of the Reynolds number and roughness heights. Also, such critical distance is fully independent of fluids as well as nanoparticles diameter and concentration. It is also found that the decrease of critical distance with the increase of roughness height is very small when $Re \leq 3840$. When $3840 < Re < 5800$,. Such deviation of critical distance with the increase of roughness heights starts to rise and then a significant variation is observed when $Re > 5800$. It is to be noted that when $K_s = 0.375, 0.5$ and $0.625\ mm$, the transition behaviour seems to be vanished for $Re > 10000,\ 9900$, and 8700 respectively. And the flow and temperature fields tends to become fully turbulent as it is expected.

In Fig. 4.27, variations of average Nusselt number with different Reynolds numbers for Al_2O_3-water and TiO_2-water nanofluids and roughness heights (K_s) are shown. It is observed that when $Re < 8000$ with $K_s = 0.375\ mm$, the heat transfer rate enhance monotonically with the Reynolds numbers and the maximum enhancement is approximately 52.01% and 50.02% which is higher than that of smooth pipe wall case of water. However, when $Re \geq 8000$, the heat transfer rate starts to increase rapidly and the maximum enhancement is observed approximately 62.44% and 61.09% for both Al_2O_3-water and TiO_2-water nanofluids respectively. For $K_s = 0.5\ mm$, the enhancement of heat transfer rate is found higher than that of $K_s = 0.375\ mm$. It is observed that the rapid increase of heat transfer rate begins earlier when $Re > 7500$ and such enhancement is approximately 115.4% and 114.65% for smooth pipe wall case of water for both Al_2O_3-water and TiO_2-water nanofluids respectively. For $K_s = 0.625\ mm$, it is observed that the enhancement is more pronounced than that of smooth pipe wall as well as $K_s = 0.375$ and $0.5\ mm$. Also when $Re = 10000$, the maximum heat transfer rate is found to be

approximately 160.75% and 160.18% compared with smooth pipe wall case of water for both Al_2O_3-water and TiO_2-water nanofluids respectively. From Fig. 4.27, it is observed that for all the roughness heights and $Re < 4000$, the enhancement of heat transfer is not so high. But when the Reynolds number starts to increase and so does the roughness height, such enhancement becomes more significant. The reason behind such phenomena may be the degeneration of the thickness of viscous sublayer with the increase of Reynolds number.

4.5.2.5 Average Shear Stress Coefficient Ratio

Average Shear Stress Coefficient Ratio for smooth pipe wall is discussed in details in the Fig. §4.5.1.3 of Chapter 4. Fig. 4.28 shows the variation of the roughness heights with Reynolds number for Al_2O_3 and TiO_2-water nanofluids in order to understand the behaviour of average shear stress ratio for rough pipe wall.

It is found that the maximum average shear stress ratio of Al_2O_3–water nanofluid for different roughness heights, K_s = 0.375, 0.5 and 0.625 *mm* is approximately 14.94, 16.71 and 18.81 respectively. However, the maximum average shear stress ratio of TiO_2–water nanofluid for different roughness heights is approximately 14.70, 16.40 and 18.46 respectively. It is also found that when $Re > 7500$, the average shear stress ratio is increased with a raise in the roughness height of the pipe wall as well as the Reynolds number. But for $Re \leq 7500$, the average shear stress ratio values remains constant with the increase of roughness heights and such results are identical in comparison with the results of smooth pipe wall case for both Al_2O_3-water and TiO_2-water nanofluids.

From the above findings, following conclusion can be drawn:

For high Reynolds number flow, nanofluids can be useful to enhance the heat transfer rate when both the smooth and rough surfaces of pipe wall are considered. But, the higher enhancement of average wall shear stress ratio with the increase of roughness heights creates a main obstacle to use this in practical applications of the nanofluids.

4.5.2.6 Thermal Performance Factor Analysis

From the above investigations, it is observed that nanoparticles diameter and concentration; Brownian motion of nanoparticles; smoothness and roughness of pipe

wall; and different nanofluids rather than conventional fluids play a significant role to enhance the heat transfer rate. Also, such enhancement of heat transfer rate depends on the other findings like pressure drop as well as wall average shear stress ratio. So, it is necessary to find optimum performance of these findings in order to make a conclusion about the increase of pressure drop and heat transfer rate when the roughness height of pipe wall is under consideration. Therefore, the thermal performance factor analysis is considered to understand the overall performance of above parameters.

Figure 4.29 shows the variation of thermal performance factor with different Reynolds number for Al_2O_3-water and TiO_2-water nanofluids when the effect of roughness heights is considered. It is observed that the thermal performance factor is always greater than 1 for all the possible cases. It means that the enhancement of heat transfer rate is feasible when wall roughness is considered with penalty in pumping power. Particularly, the maximum thermal performance factors of 1.82, 2.22 and 2.80 are observed for Al_2O_3-water nanofluid and K_s = 0.375, 0.5 and 0.625 mm. And for TiO_2-water nanofluid, its variations remain almost the same apart from the case of K_s = 0.375 for which the maximum thermal performance factor is slightly down.

It is also clearly seen that the thermal performance factor increases with the increase of roughness heights. That means, no optimal Reynolds number exists to find the optimum thermal performance factor. This further indicates, the enhancement of thermal performance factor depends on the increase of roughness heights and the roughness heights have a huge impact on the heat transfer enhancement with penalty for pumping power.

4.5.2.7 Entropy Generation Analysis

Entropy generation for smooth pipe wall has been discussed in details in §4.5.1.4. In this section, the results of the entropy generation analysis for rough surface are presented.

Figure 4.30 shows the variation of thermal, frictional and total entropy generation as well as Bejan number with different Reynolds number for different roughness heights, K_s. The frictional entropy generation is observed to have an opposite behaviour of the thermal entropy generation which decreases with the increase of

Reynolds number as well as the roughness heights. However the opposite trend is seen for the frictional entropy generation. Reduction of thermal entropy generation due to the increase of roughness heights helps to enhance the heat transfer rate. But, a significant rise of frictional entropy generation which occurs due to the higher penalty of pumping power contributed by the roughness. It is also interesting to see that the thermal entropy generation of TiO_2-water nanofluid is higher than that of Al_2O_3-water nanofluid, whereas an opposite trend is observed for the frictional entropy generation. It further demonstrates that the higher thermal conductivity of Al_2O_3-water nanofluid than that of TiO_2-water nanofluid plays an important role for the augmentation of heat transfer rate.

Additionally, the total entropy generation decreases slowly with the increase of Reynolds number and roughness heights when $Re < 8000$. This is due to the rapid increase of frictional entropy generation and decrease of thermal entropy generation, and such rapid growth of frictional entropy generation has a significant impact on total entropy generation. This behaviour can also be examined from the results of Bejan number. For example, when $Re \leq 4000$, Bejan number decreases monotonically but when $Re > 4000$, Bejan number decreases rapidly with the increase of Reynolds number and roughness heights. The reason behind this fact is the dominant behaviour of frictional entropy generation compared to the thermal entropy generation. When $Re \sim 8000$, sudden rise of total entropy generation indicates that the optimal Reynolds number exists when the wall roughness effect is taken into account. It shows that minimization of total entropy generation is possible when $Re \sim 8000$. This is due to the balance of the effects of frictional and thermal entropy generation at $Re \sim 8000$ which provides the optimal condition of total entropy generation. Finally, it is noticed that TiO_2-water nanofluid shows little bit higher Bejan number and total entropy generation than Al_2O_3-water nanofluid although optimal Reynolds number is almost independent of wall roughness heights for both these nanofluids.

4.6 Conclusion

In this chapter, heat transfer analysis, thermal performance factor and entropy generation analysis have been presented to investigate the effect of smooth and roughness of the pipe wall surface of transition nanofluids flow inside a circular pipe

using single phase model. Investigation is carried out for the parameters such as Reynolds number, nanoparticles concentration, without and with Brownian motion and diameter of nanoparticles and different roughness heights. According to our investigations, summary of the overall findings are presented in the following way:

For smooth pipe wall case:

1. It is seen that Al_2O_3-water nanofluid shows slightly higher values of mean velocity and turbulent kinetic energy than TiO_2-water nanofluid.

2. It is also seen that nanoparticles diameter of $d_p \geq 40\ nm$ produces similar results of flow and thermal fields for both the nanofluids.

3. It is found that without and with Brownian motion of nanoparticles and diameters and concentrations of nanoparticles have insignificant effect on Darcy friction factor and that result no penalty in the pumping power.

4. It his also found that Al_2O_3-water nanofluid shows higher heat transfer rate than TiO_2-water nanofluid when without and with Brownian motion of nanoparticles and diameters and concentrations of nanoparticles are considered.

5. It is observed that average wall shear stress ratio of Al_2O_3-water nanofluid is slightly higher than of TiO_2-water nanofluid.

6. No optimal Reynolds number is been observed which can minimize the total entropy generation.

For rough pipe wall case:

7. It is seen that wall temperature decreases with the increase of roughness height of the pipe wall. It was also seen that TiO_2-water nanofluid shows higher wall temperature than Al_2O_3-water nanofluid.

8. Reasonable penalty of pumping power and higher enhancement of heat transfer rate are found with the increase of roughness height of the pipe wall. This encourages us to further use of uniform roughness on pipe when heat transfer augmentation is the main objective in practical application.

9. It is observed that the average shear stress ratio and thermal performance factor increases with the increase of roughness height of the pipe wall.

10. Optimal Reynolds number $Re \sim 8000$ is observed for different roughness heights which minimize the total entropy generate

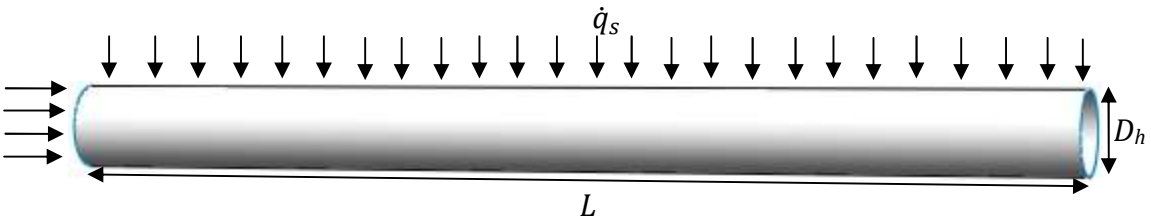

Figure 4.1: Schematic diagram of the geometry under consideration

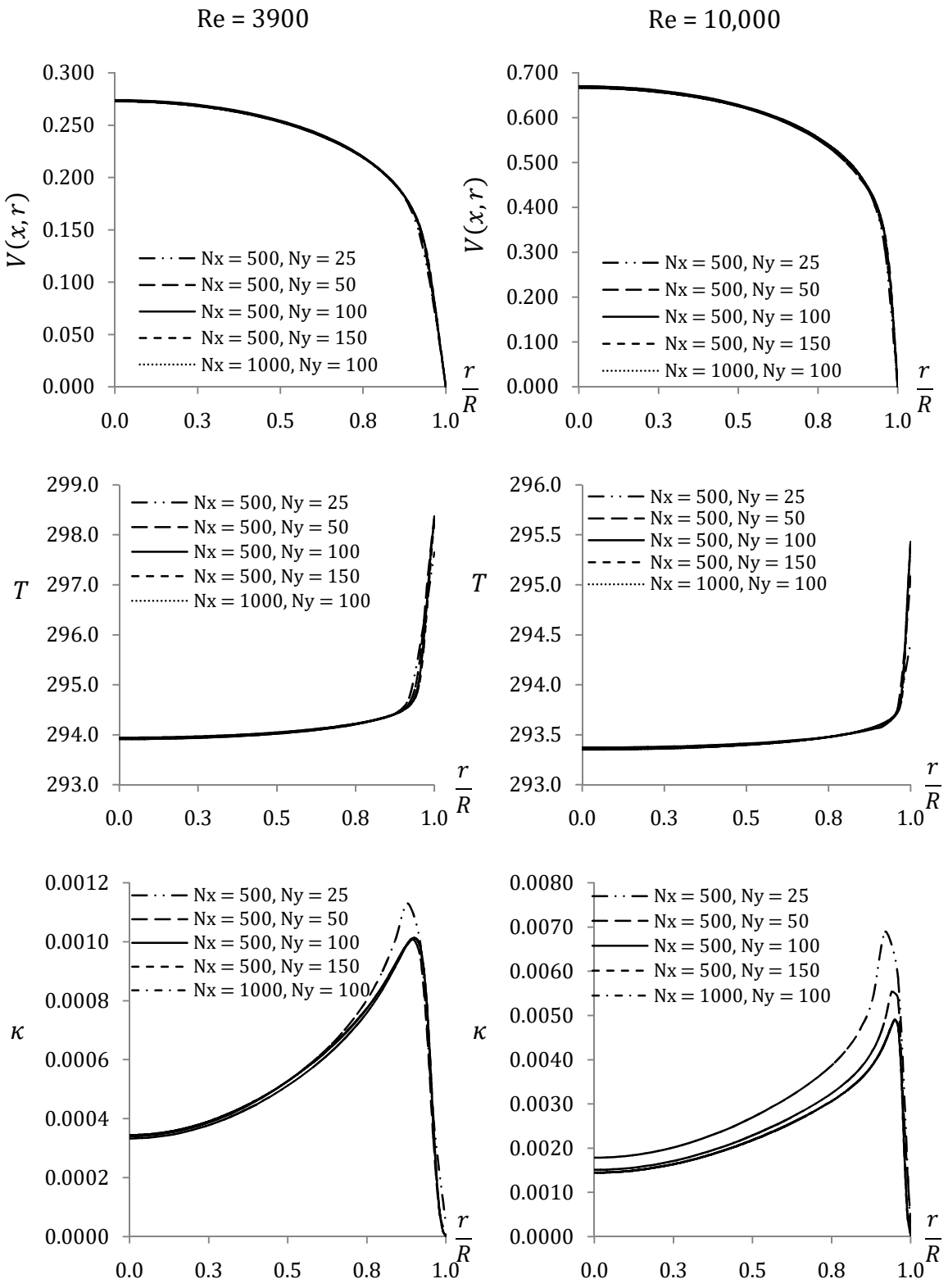

Figure 4.2: Variations of radial velocity, temperature and turbulent kinetic energy at $x = 0.99\ m$

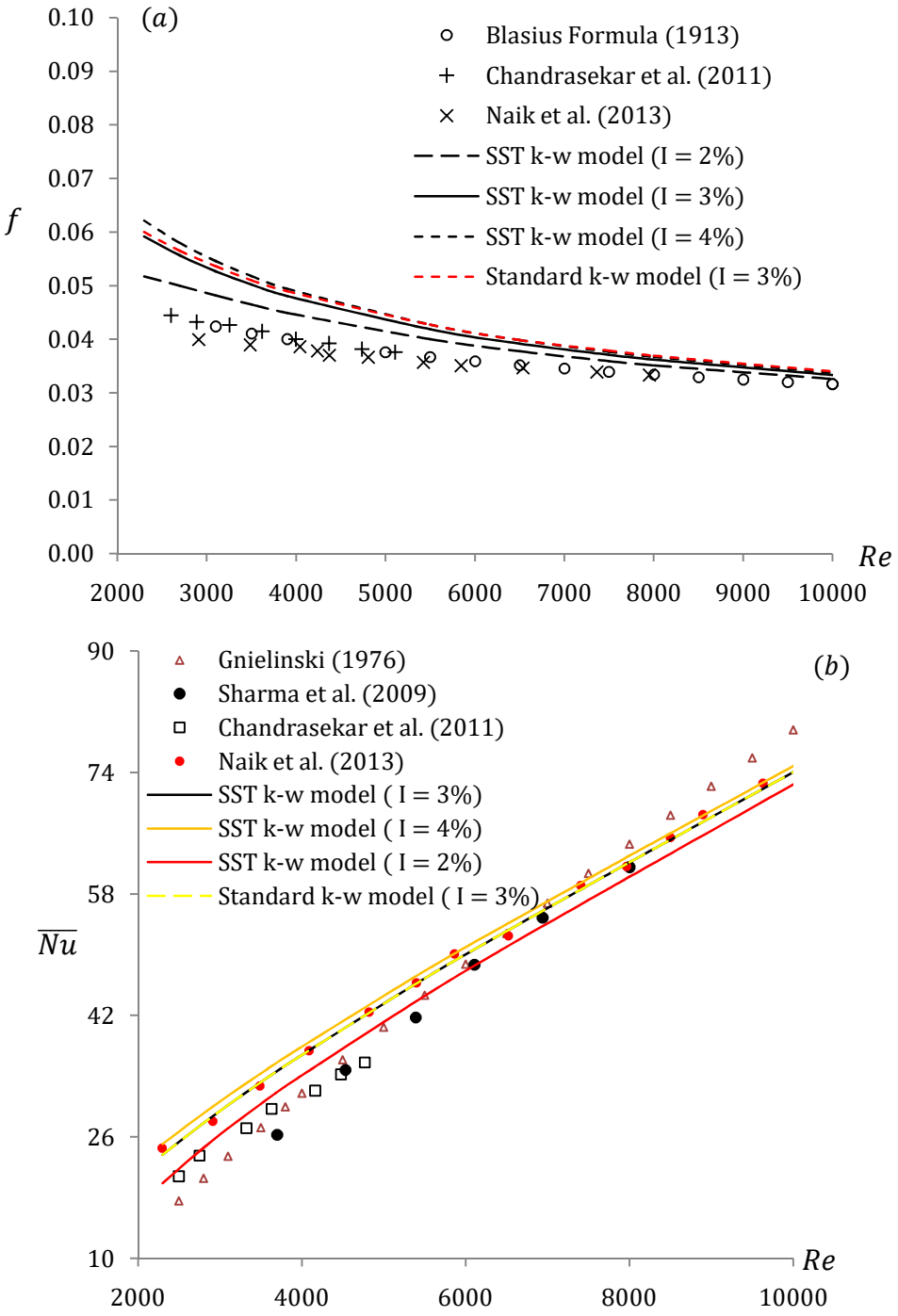

Figure 4.3: Comparisons of the (a) Darcy friction factor, f and (b) average Nusselt number of water with different correlations and experimental results for different Re

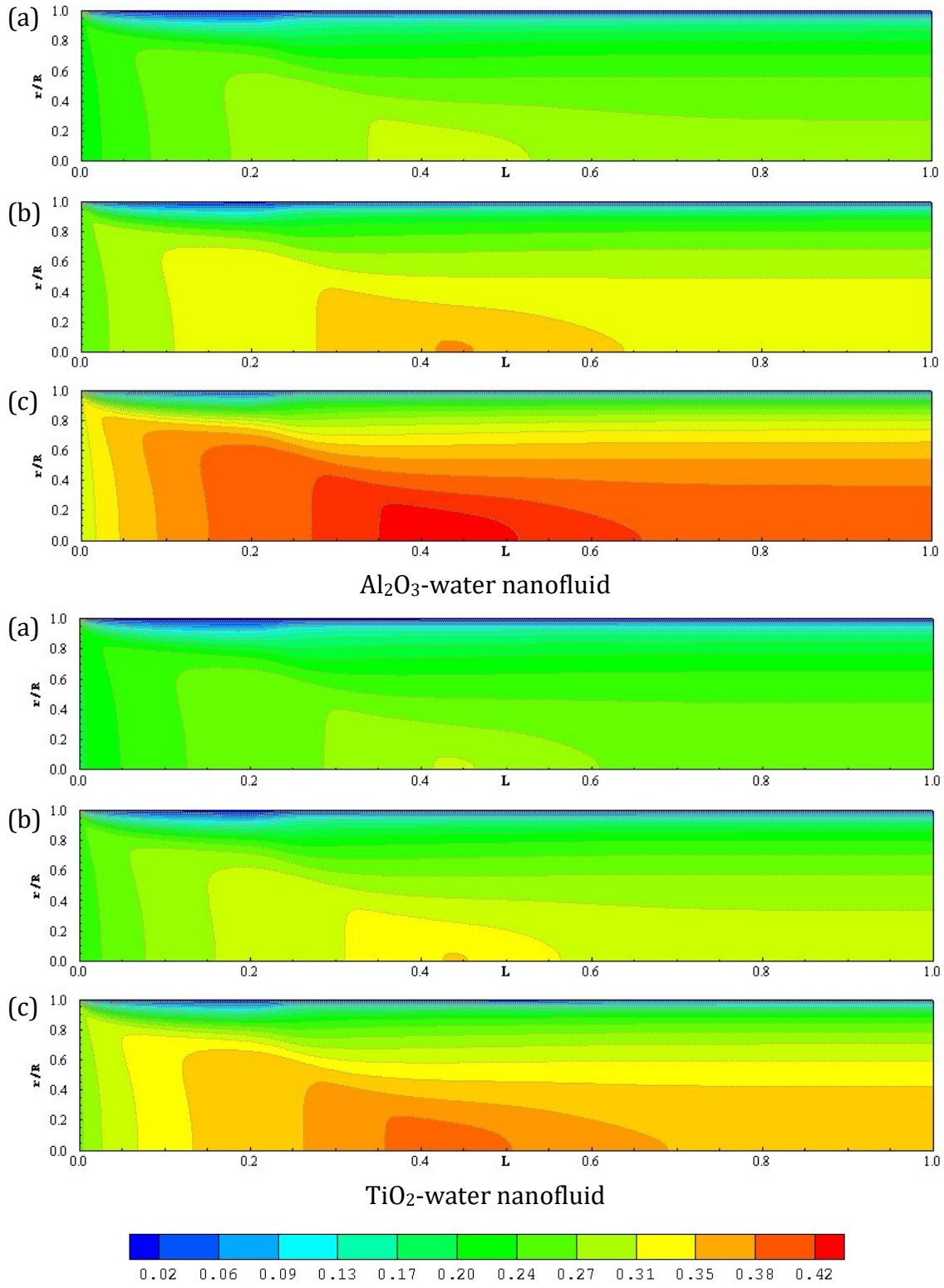

Figure 4.4: Variations of mean velocity profile of Al_2O_3-water and TiO_2-water nanofluids along the axial direction for (a) χ = 2% (b) χ = 4% and (c) χ = 6% respectively and *Re* = 3500, when Brownian motion of nanoparticles is not considered

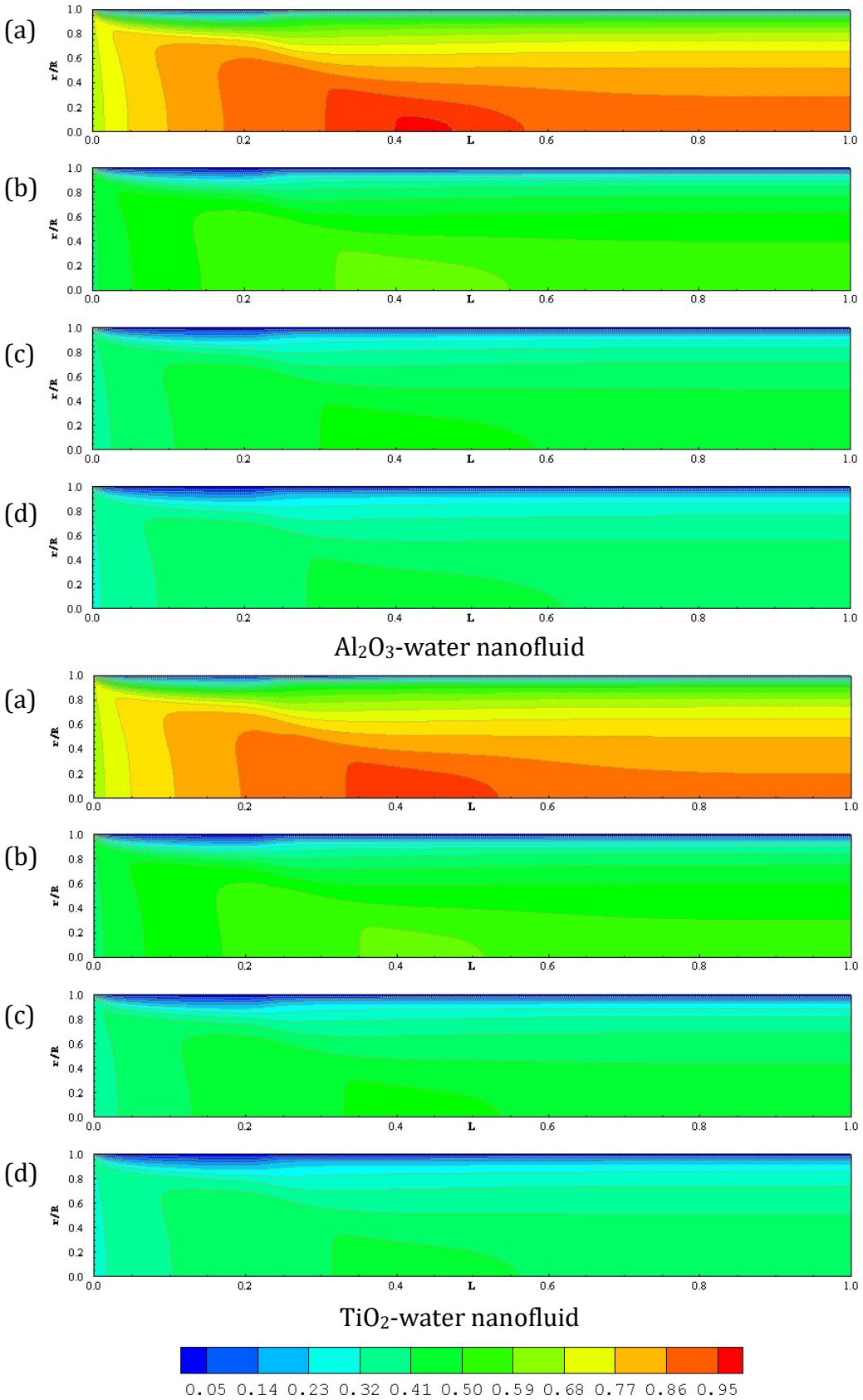

Figure 4.5: Variations of mean velocity profile of Al_2O_3-water and TiO_2-water nanofluids along the axial direction for (a) d_p = 10 *nm* (b) d_p = 20 *nm* (c) d_p = 30 *nm* (d) d_p = 40 *nm* respectively and *Re* = 3500, χ = 6% when Brownian motion of nanoparticles is considered

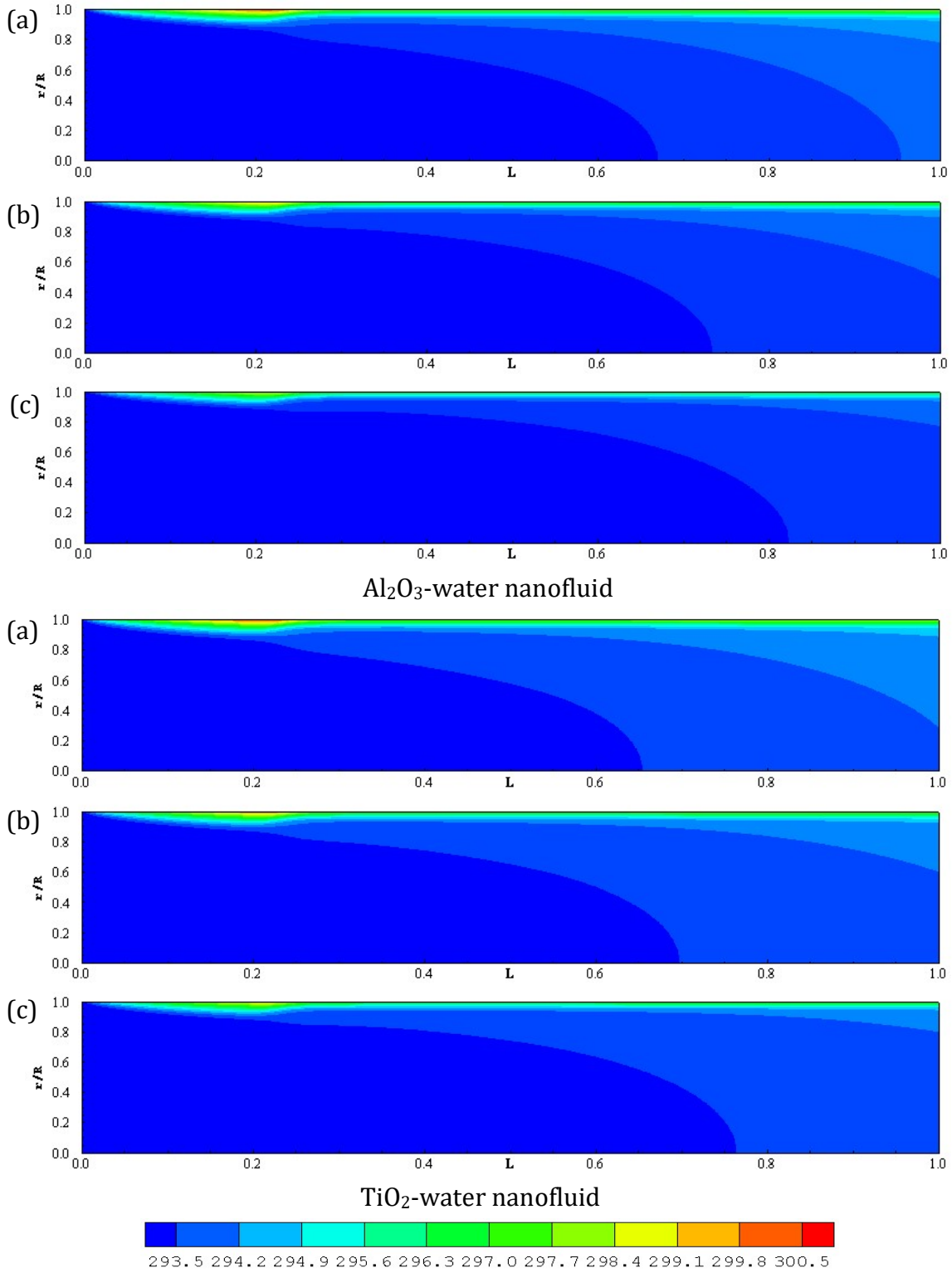

Figure 4.6: Variations of mean temperature profile of Al_2O_3-water and TiO_2-water nanofluids along the axial direction for (a) χ = 2% (b) χ = 4% and (c) χ = 6% respectively and *Re* = 3500 when Brownian motion of nanoparticles is not considered

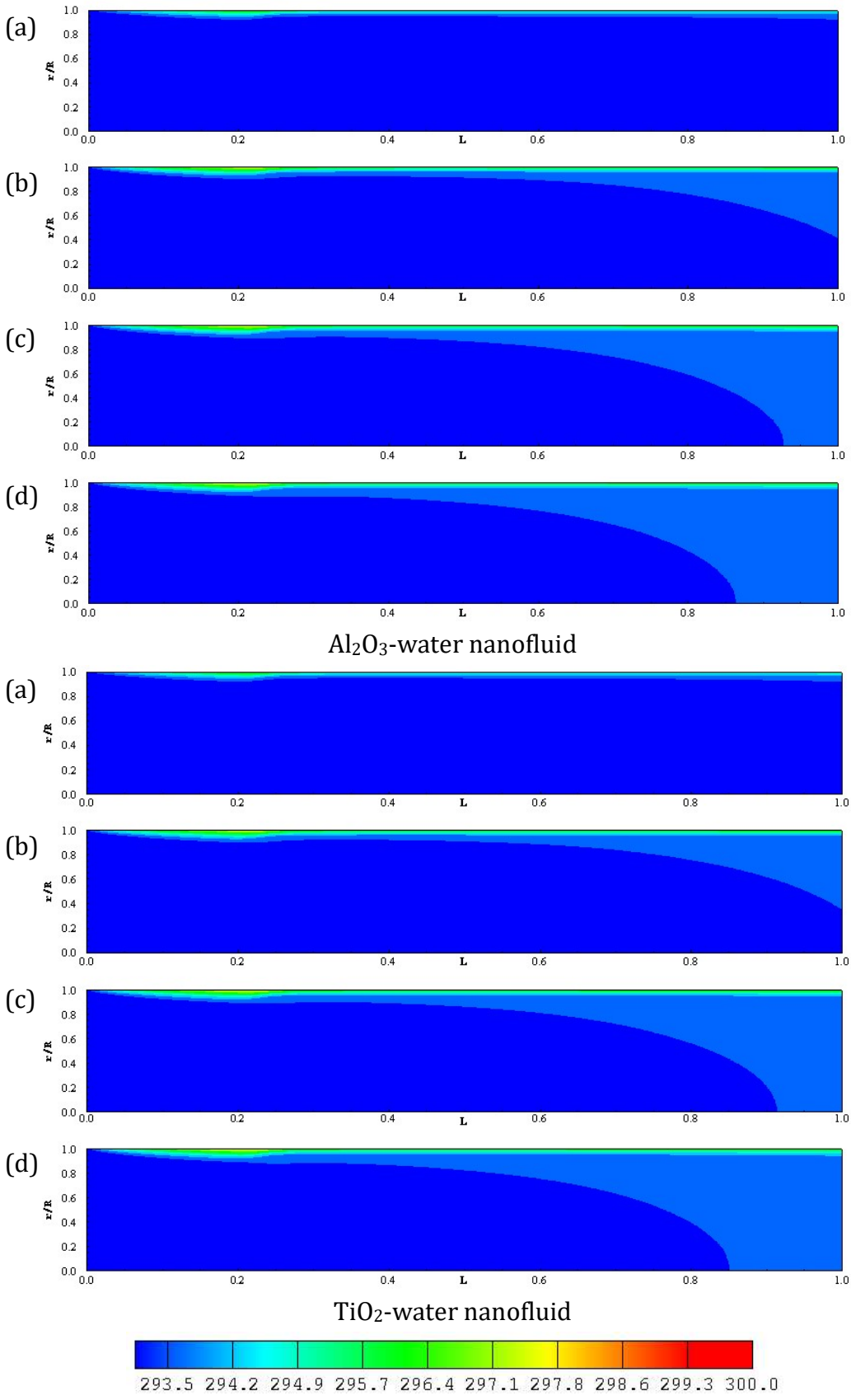

Figure 4.7: Variations of mean temperature profile of Al_2O_3-water and TiO_2-water nanofluids along the axial direction for (a) d_p = 10 *nm* (b) d_p = 20 *nm* (c) d_p = 30 *nm* (d) d_p = 40 *nm* respectively and *Re* = 3500, χ = 6% when Brownian motion of nanoparticles is considered

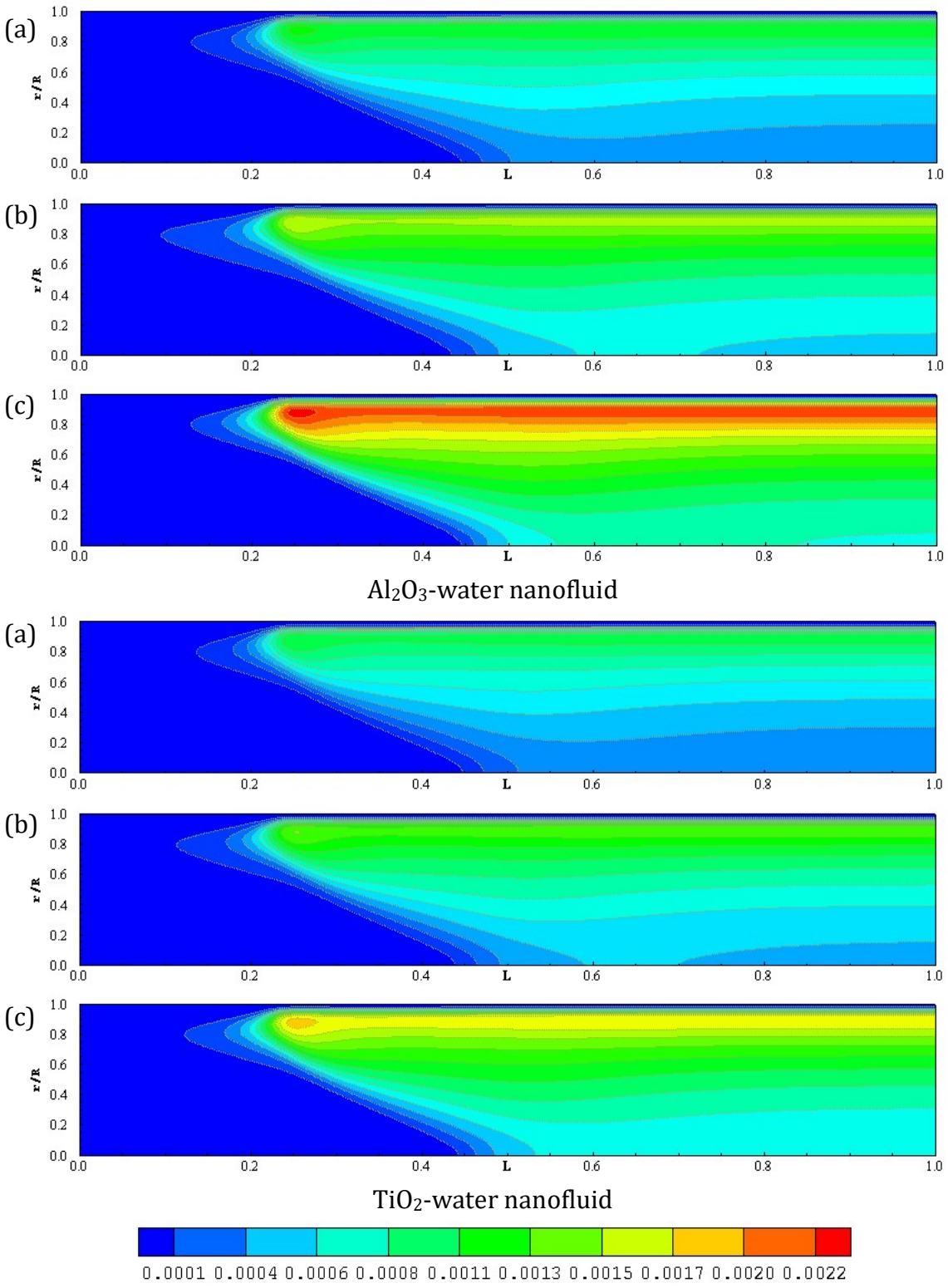

Figure 4.8: Variations of turbulent kinetic energy of Al_2O_3-water and TiO_2-water nanofluids along the axial direction for (a) χ = 2% (b) χ = 4% and (c) χ = 6% respectively and *Re* = 3500 when Brownian motion of nanoparticles is not considered

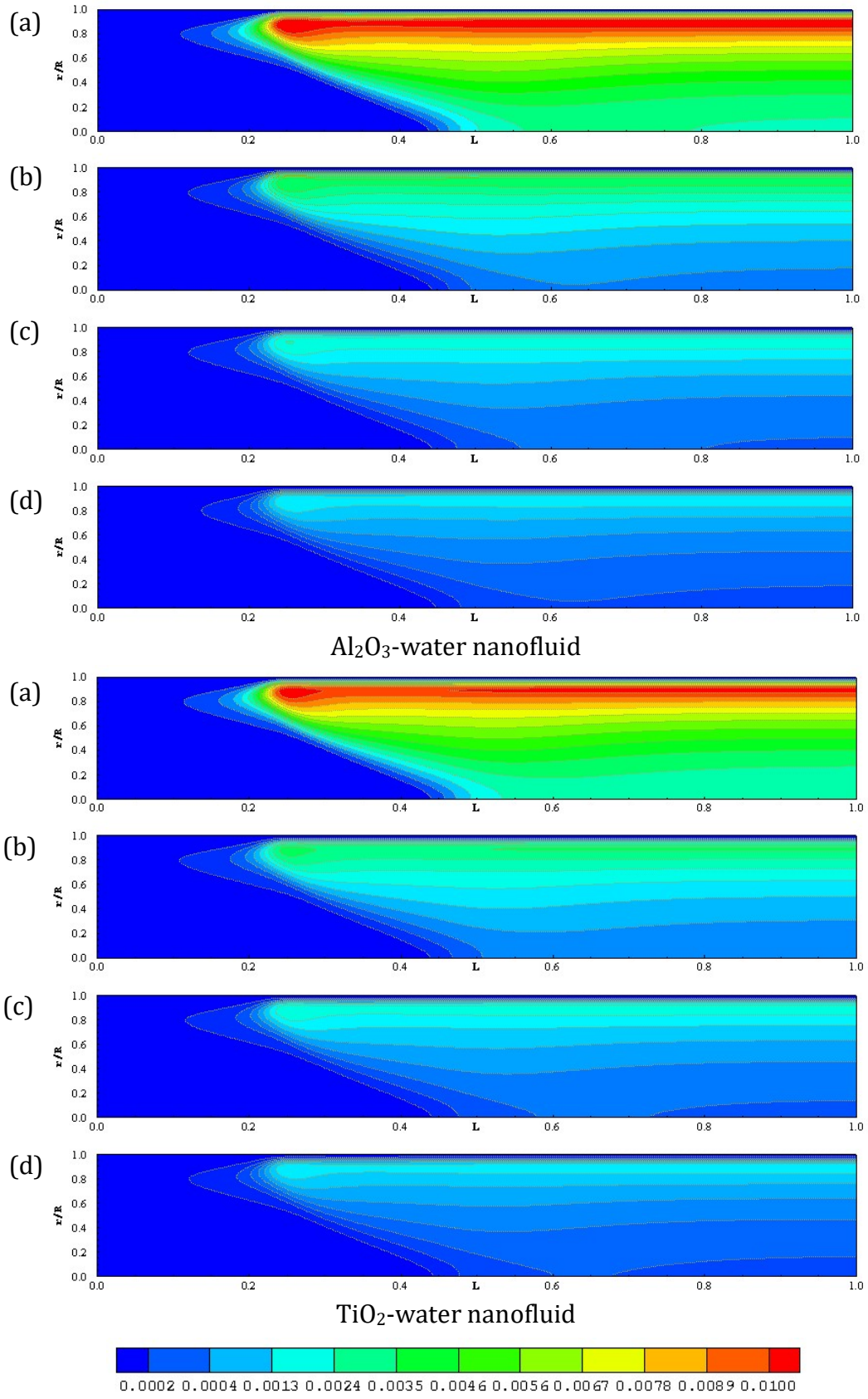

Figure 4.9: Variations of turbulent kinetic energy of Al_2O_3-water and TiO_2-water nanofluids along the axial direction for (a) d_p = 10 nm (b) d_p = 20 nm (c) d_p = 30 nm (d) d_p = 40 nm respectively and Re = 3500, χ = 6% when Brownian motion of nanoparticles is considered

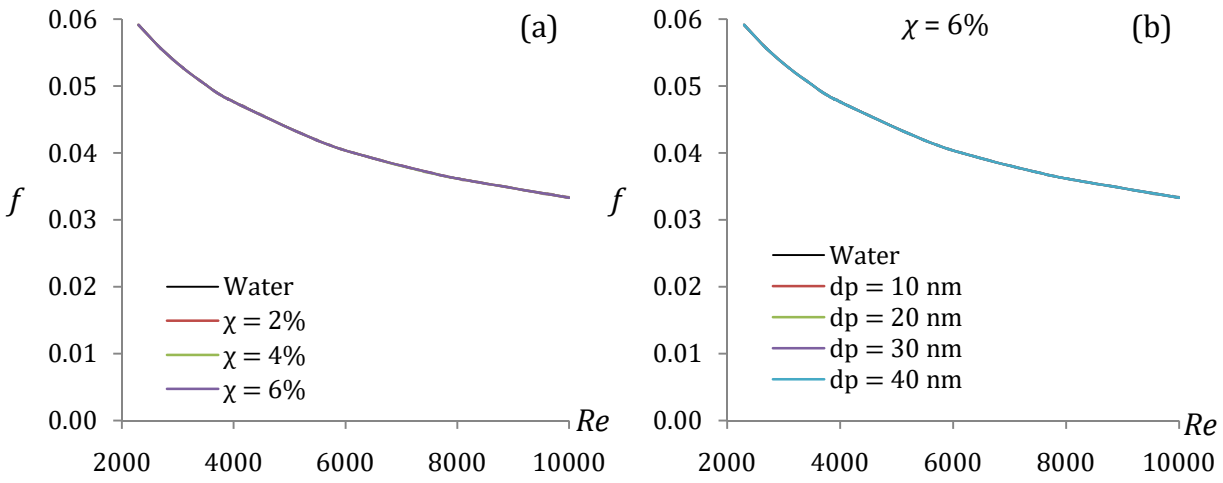

Figure 4.10: Variations of Darcy friction factor of Al_2O_3-water nanofluid with Reynolds number for (a) different nanoparticles concentrations and (b) nanoparticles diameters respectively when without and with Brownian motion of nanoparticles are considered

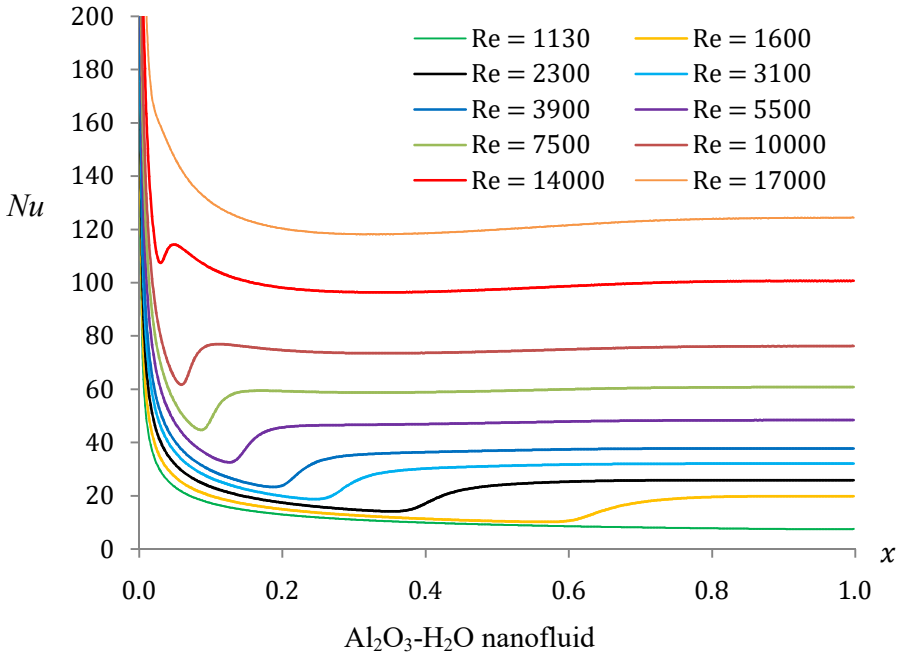

Figure 4.11: Axial variations of the local Nusselt number with different *Re* for Al_2O_3-H_2O nanofluid, d_p = 10 *nm* and χ = 2% when Brownian motion of nanoparticles is considered

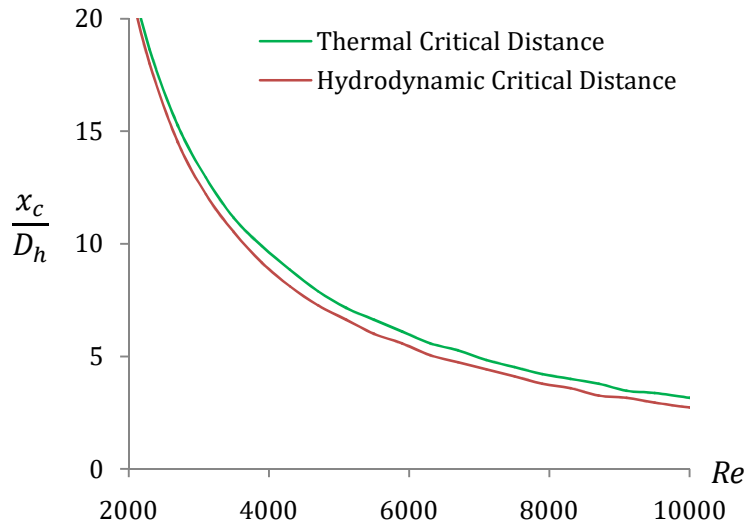

Figure 4.12: Variations of the hydrodynamic and thermal critical distances with different Reynolds numbers

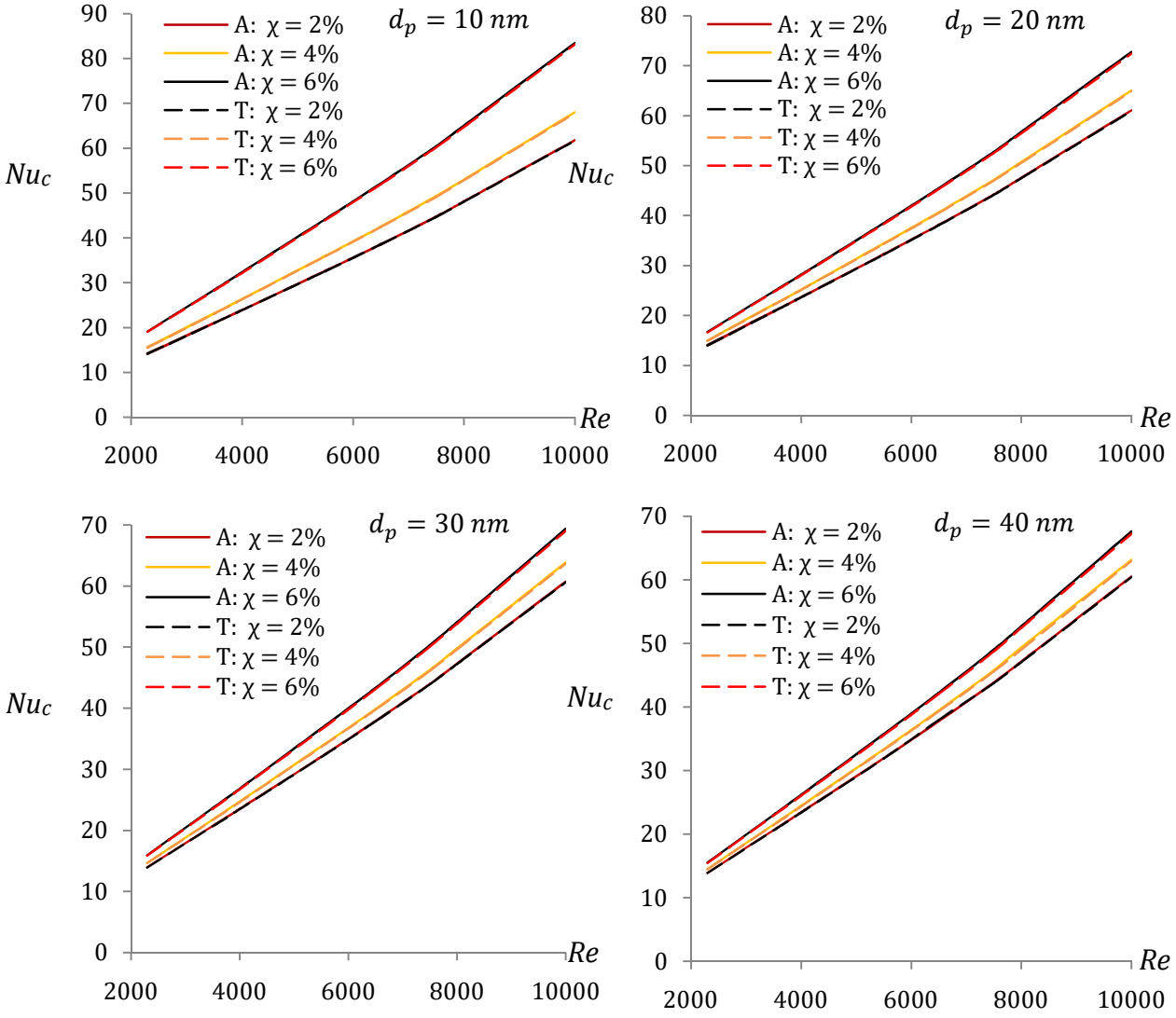

Figure 4.13: Variations of critical Nusselt number with different Reynolds numbers. (Al_2O_3-water (A) and TiO_2-water (T) nanofluids)

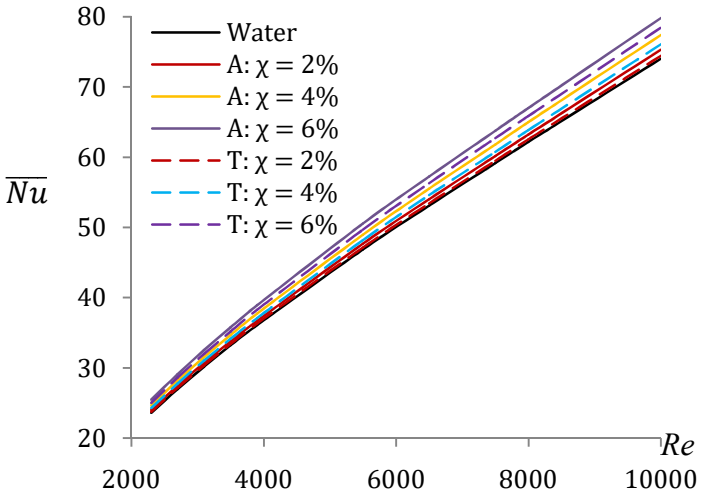

Figure 4.14: Variations of average Nusselt number with different *Re* and χ when Brownian motion of nanoparticles is not considered

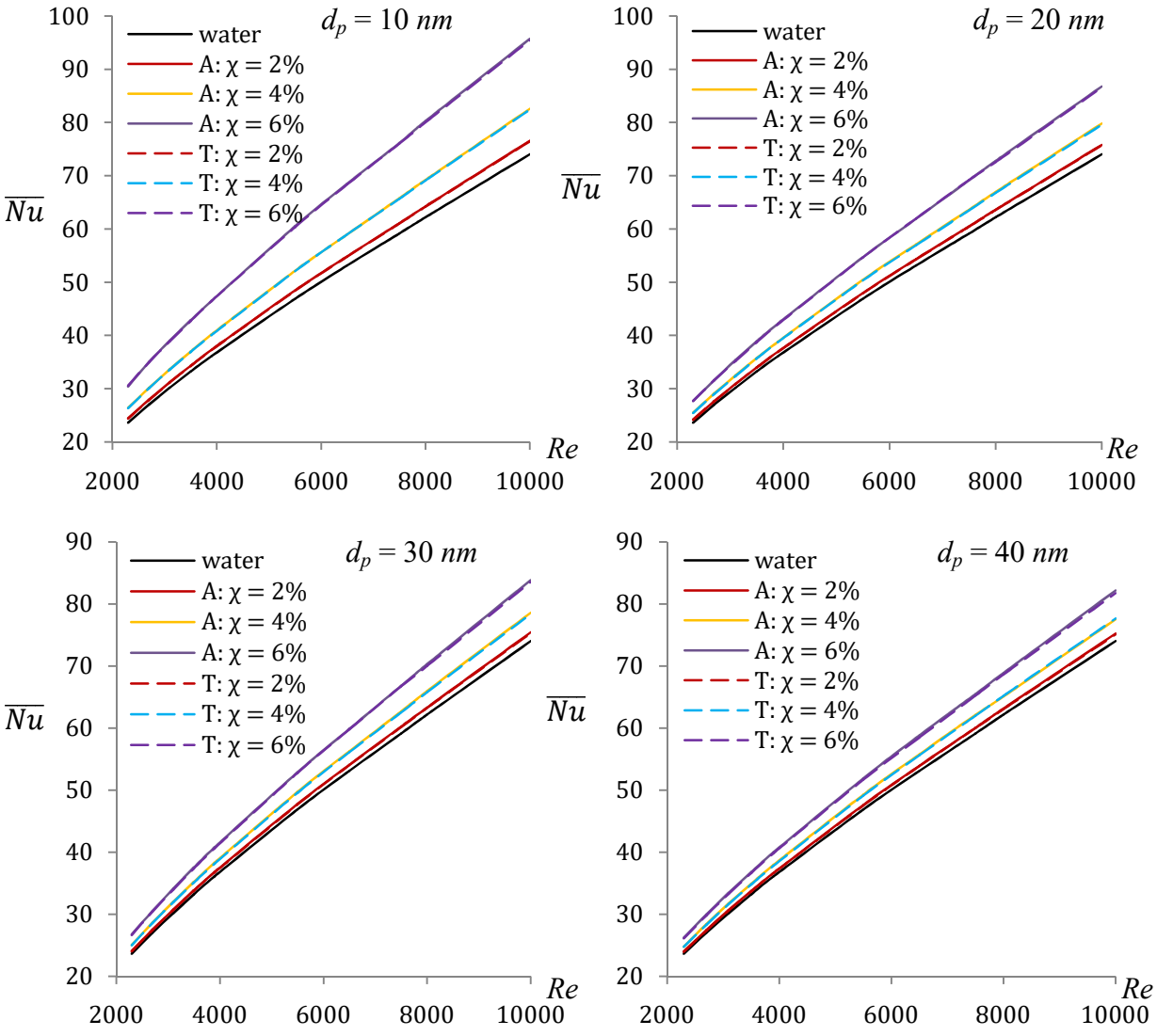

Figure 4.15: Variations of average Nusselt number with different *Re* and χ for smooth pipe wall case when Brownian motion of nanoparticles is considered

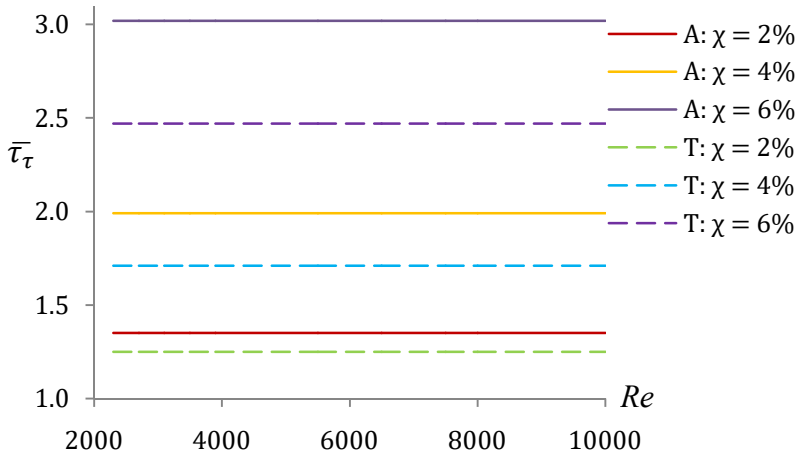

Figure 4.16: Variations of average shear stress ratio with different *Re* and χ when Brownian motion of nanoparticles is not considered

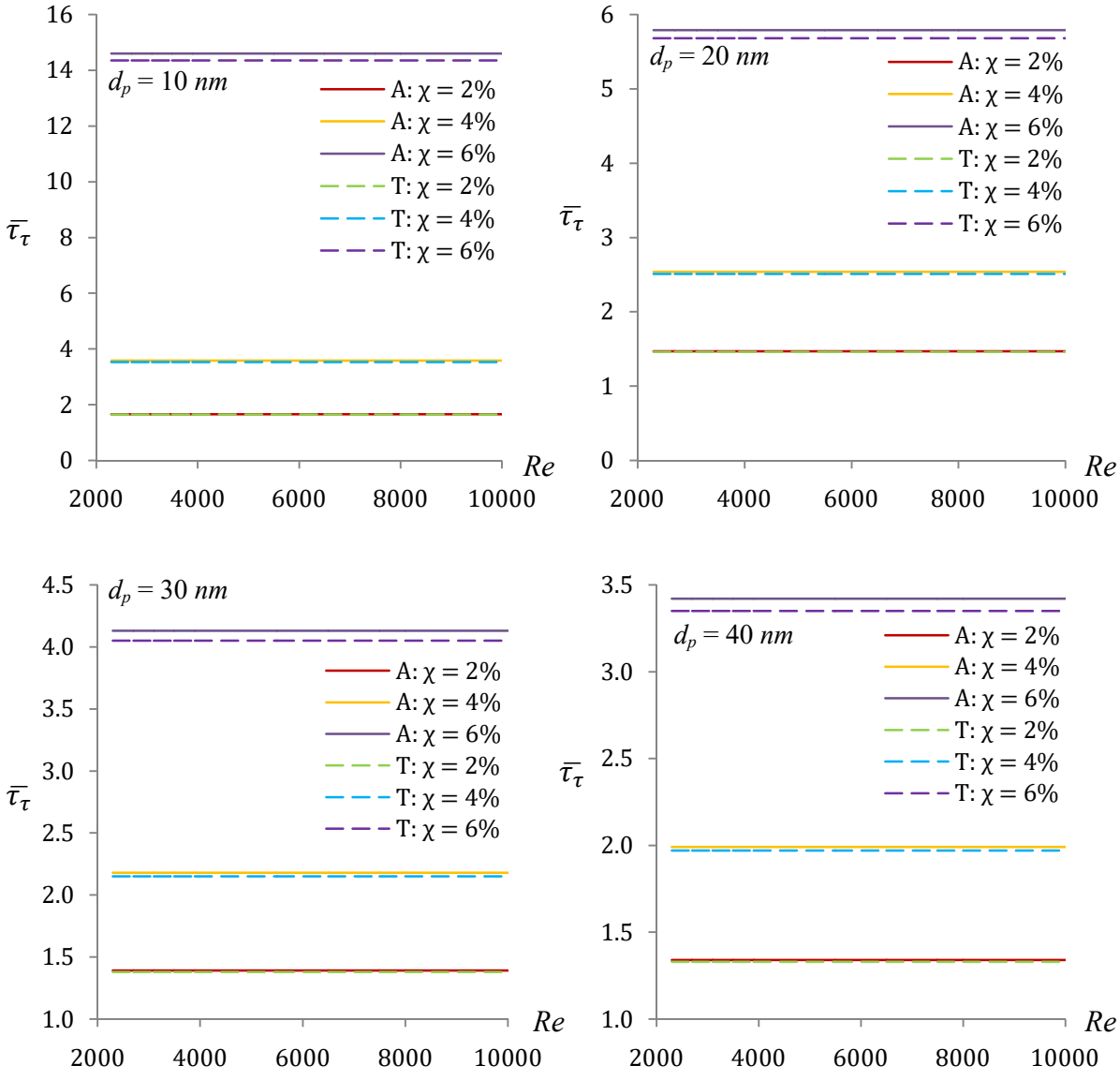

Figure 4.17: Variations of average shear stress ratio with different *Re* and χ when Brownian motion of nanoparticles is considered

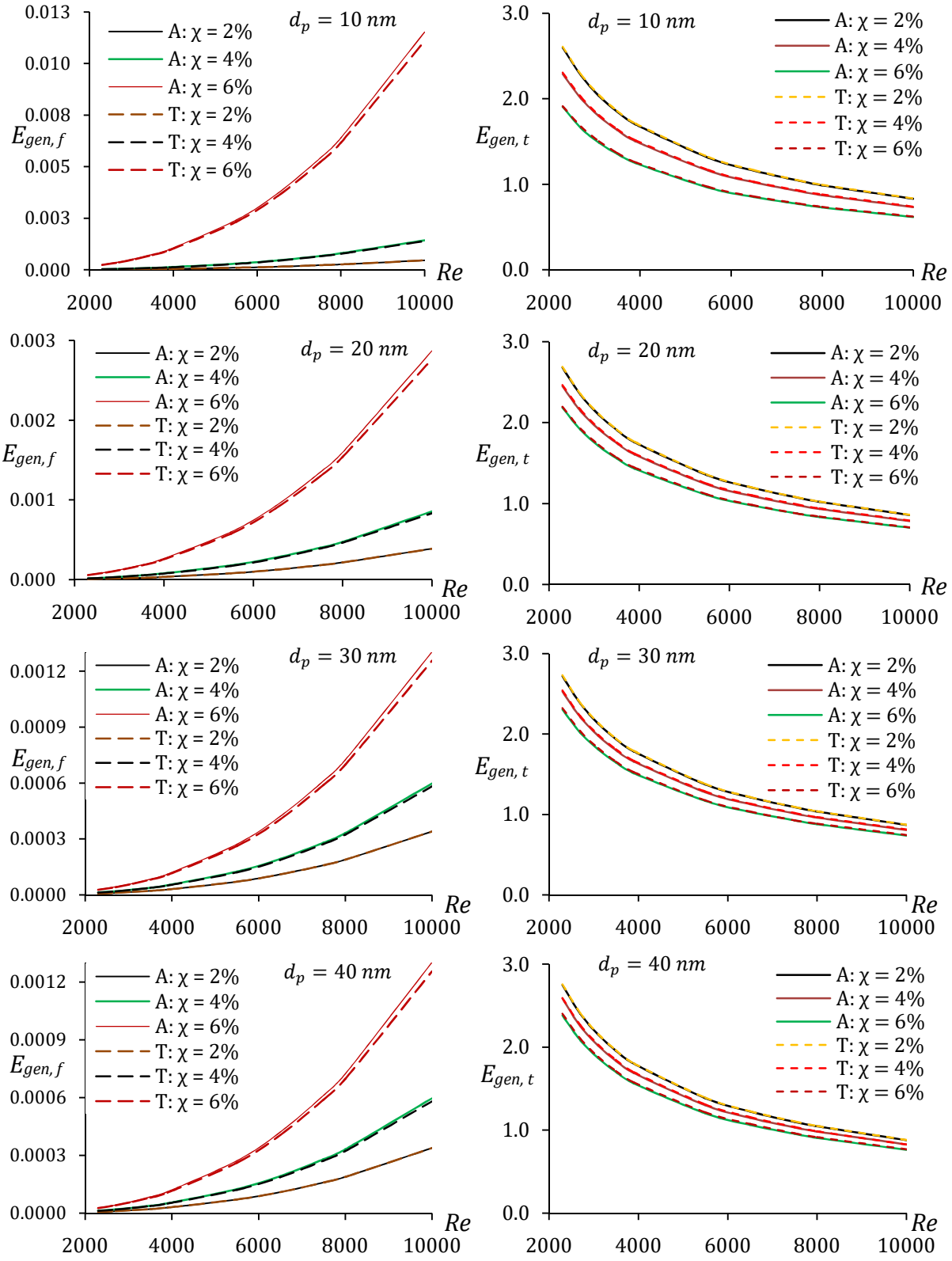

Figure 4.18: Variations of frictional (left) and thermal entropy generations with different *Re*

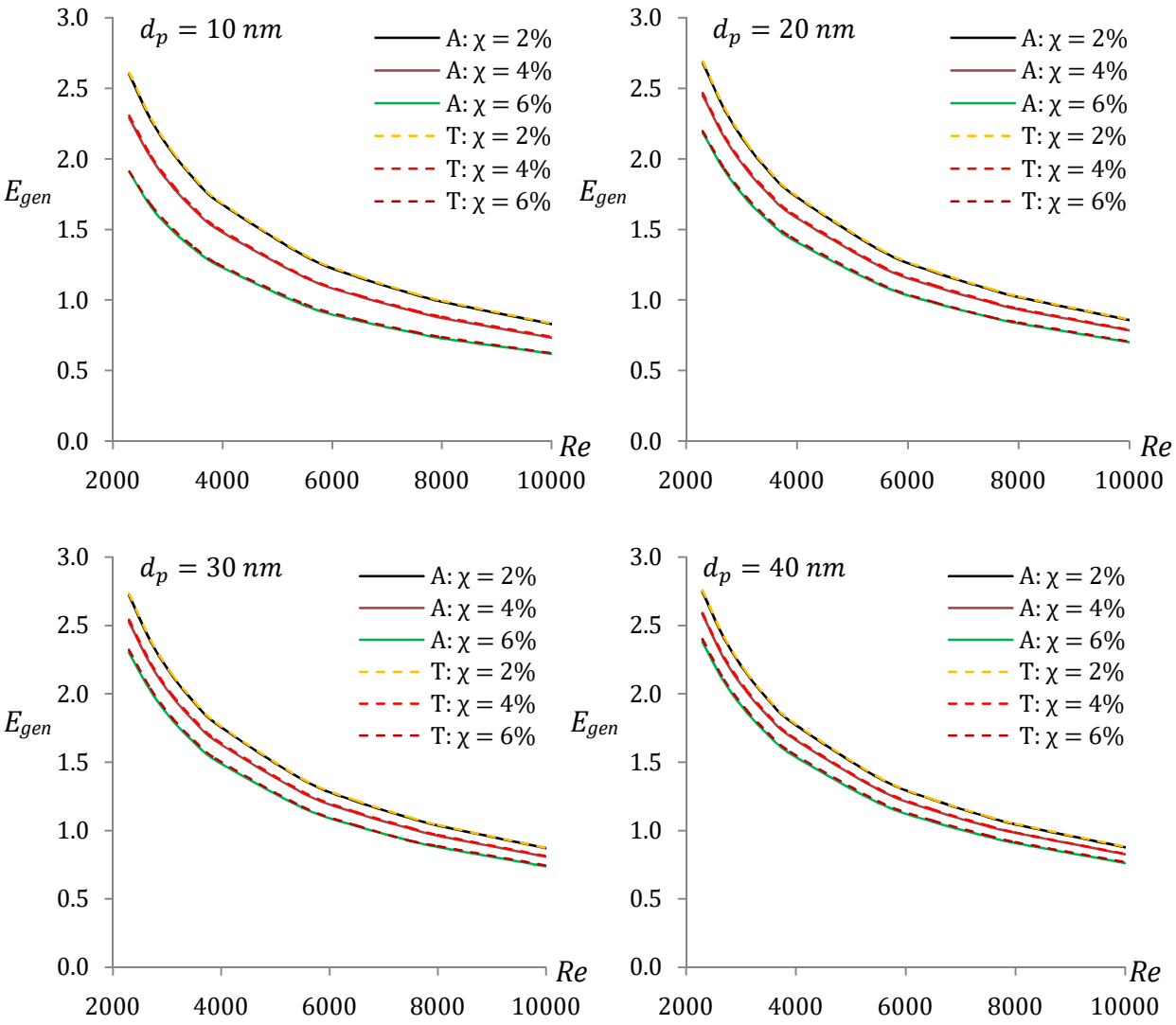

Figure 4.19: Variations of total entropy generation with different *Re* when Brownian motion of nanoparticles is considered

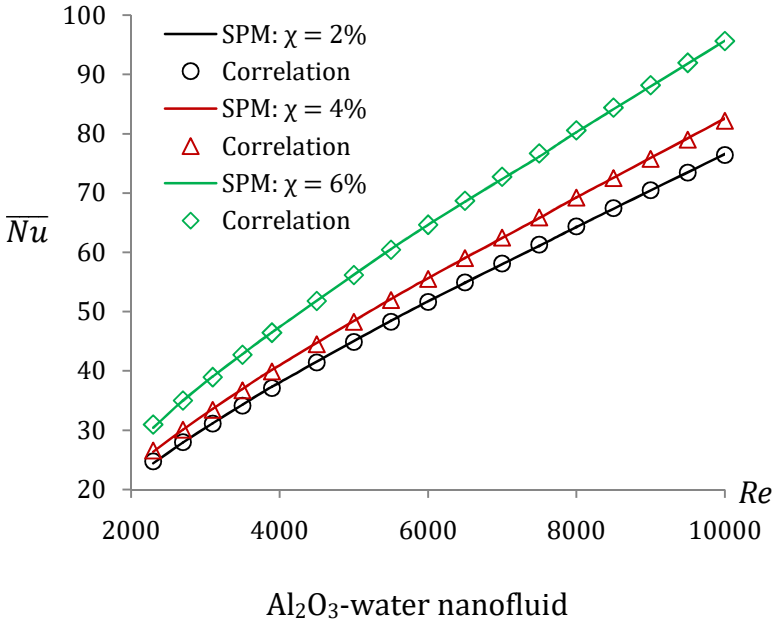

Al_2O_3-water nanofluid

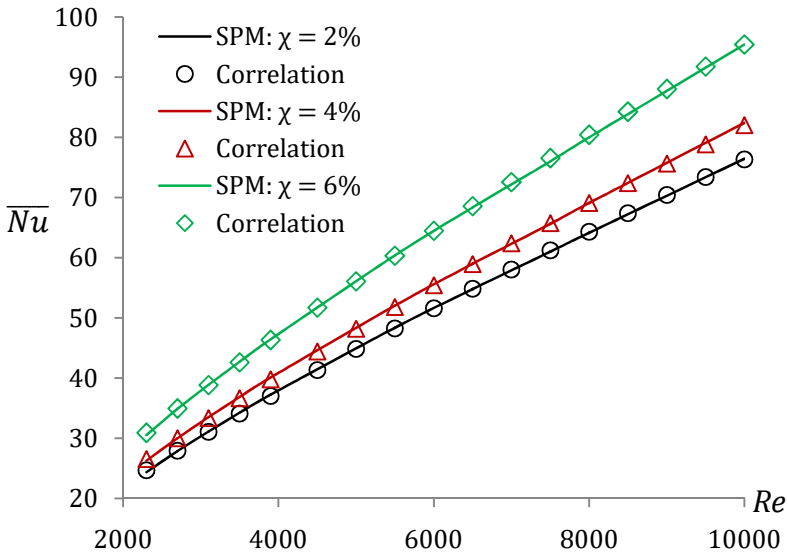

TiO_2-water nanofluid

Figure 4.20: Validations of the proposed correlations with the numerical results of Al_2O_3-water and TiO_2-water nanofluids for d_p = 10 nm when Brownian motion of nanoparticles is considered

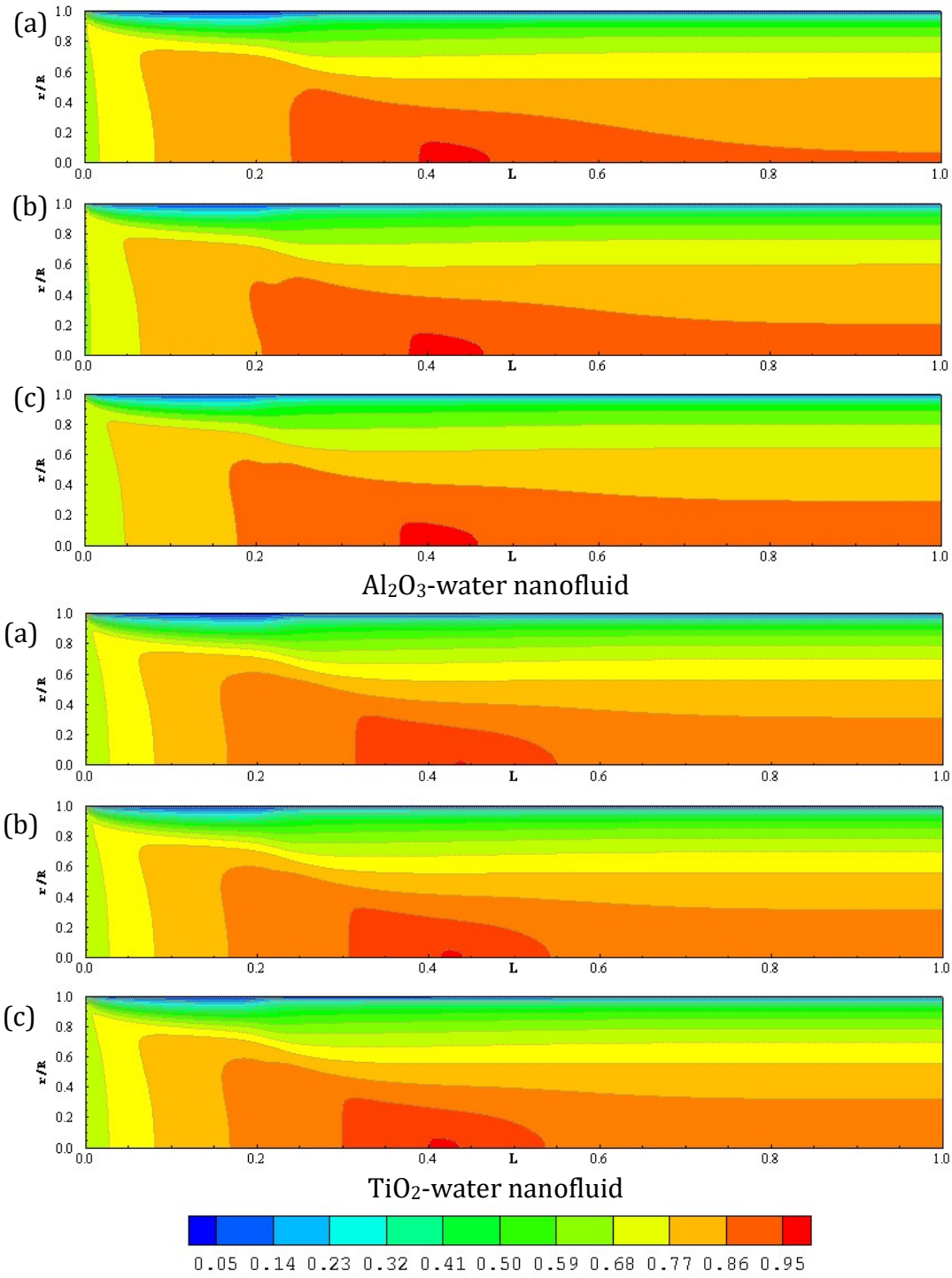

Figure 4.21: Variations of mean velocity profile of Al_2O_3-water and TiO_2-water nanofluids along the axial direction for (a) K_s = 0.375 *mm* (b) K_s = 0.5 *mm* (c) K_s = 0.625 *mm* respectively and *Re* = 3500

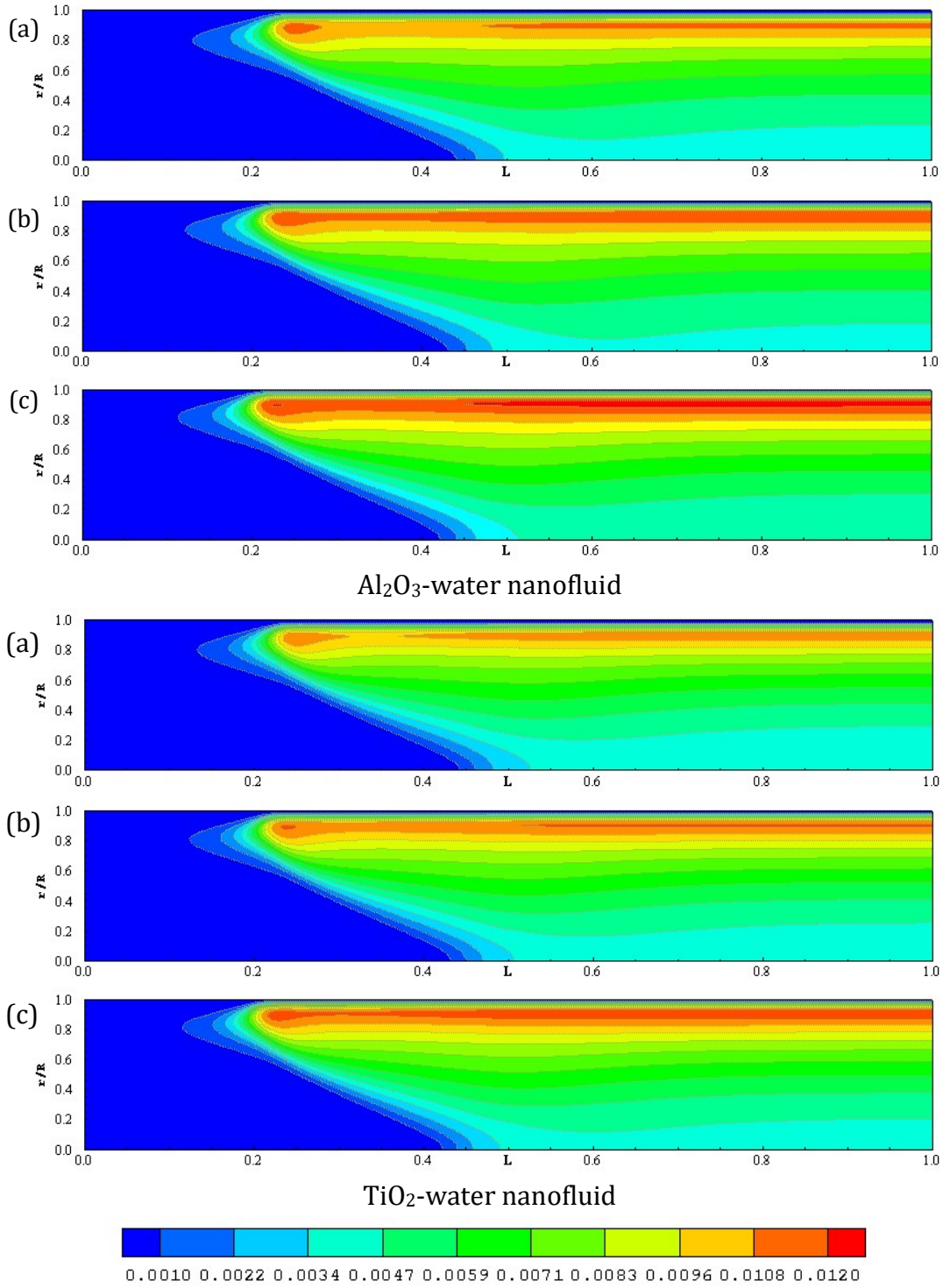

Figure 4.22: Variations of turbulent kinetic energy of Al_2O_3-water and TiO_2-water nanofluids along the axial direction for (a) K_s = 0.375 *mm* (b) K_s = 0.5 *mm* (c) K_s = 0.625 *mm* respectively and *Re* = 3500

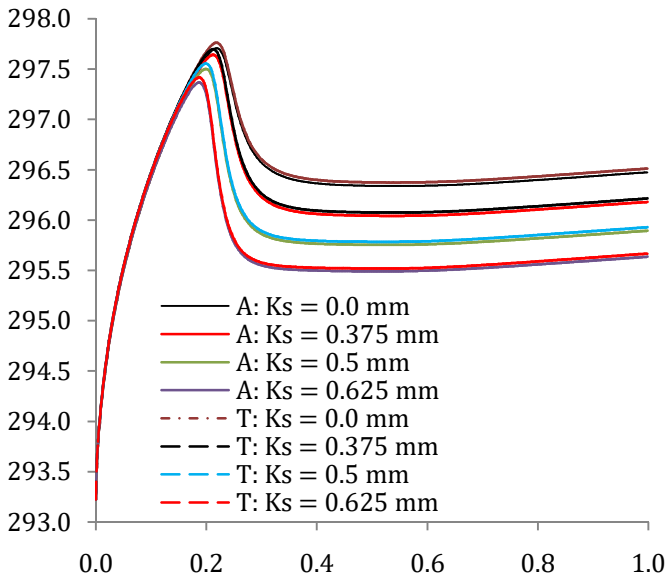

Figure 4.23: Variations of wall temperature with different roughness heights along the pipe for *Re* = 3500

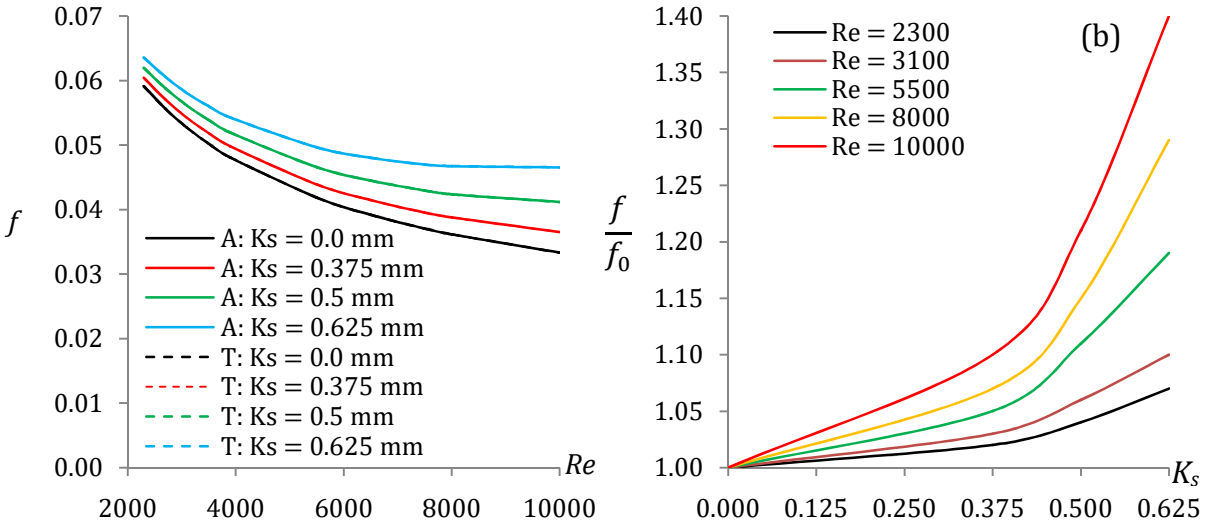

Figure 4.24: Variations of Darcy friction factor and friction factor ratios with different Reynolds numbers and different roughness heights, K_s (mm)

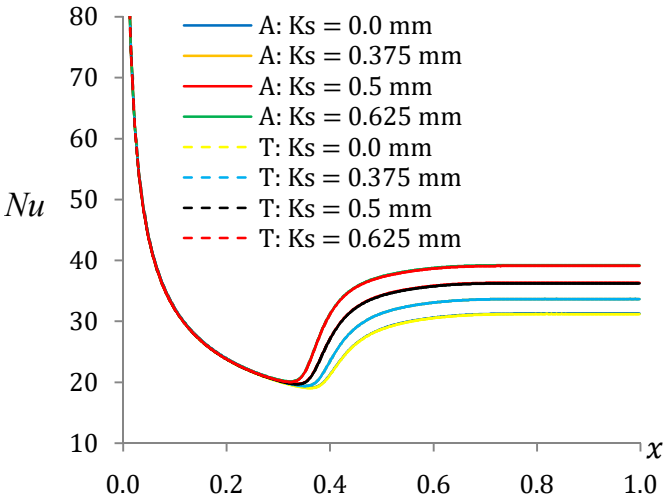

Figure 4.25: Axial variations of the local Nusselt number with different roughness heights, K_s for Re = 3500

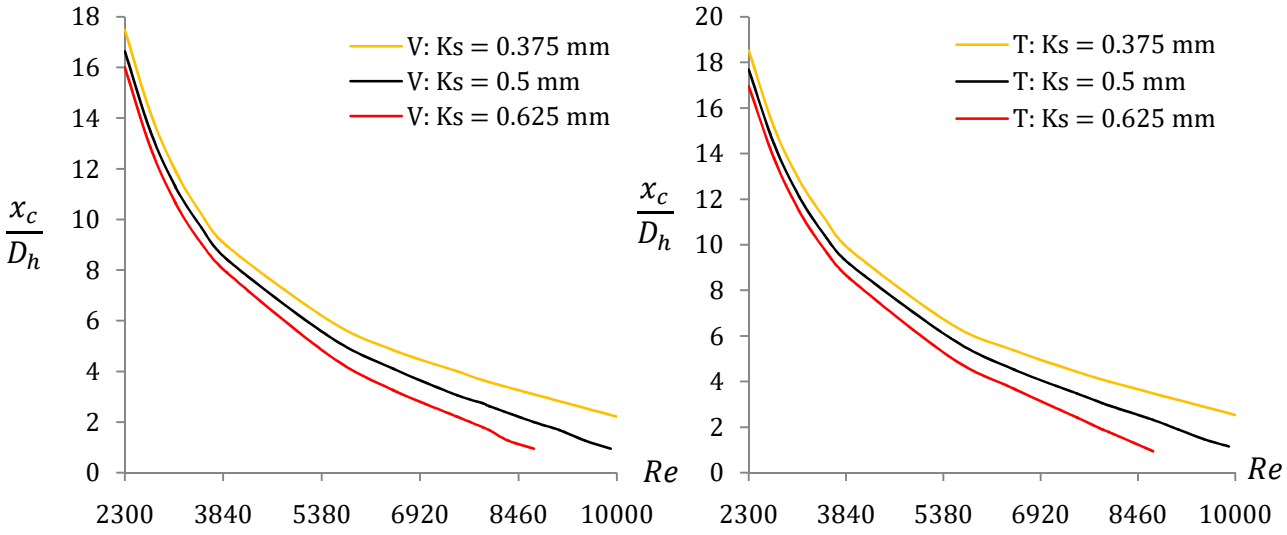

Figure 4.26: Variations of non-dimensional V: hydrodynamic and T: thermal critical distances with Reynolds numbers for different roughness heights, K_s

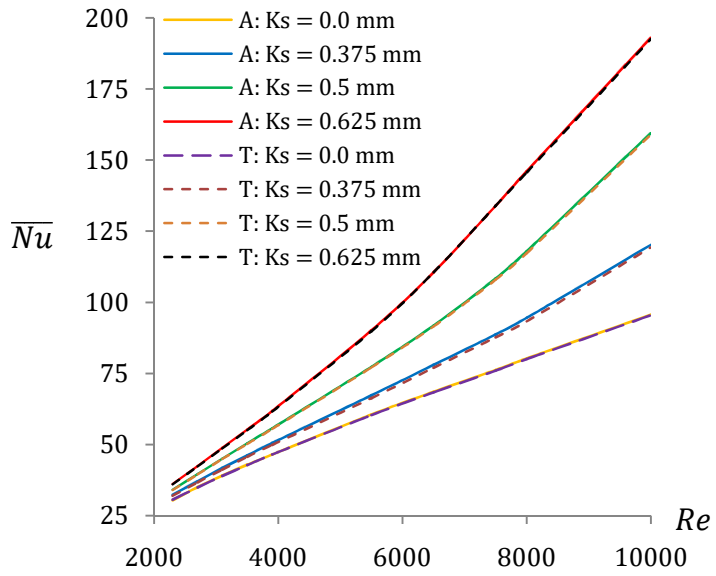

Figure 4.27: Variations of the average Nusselt number with different Reynolds numbers for different roughness heights, K_s

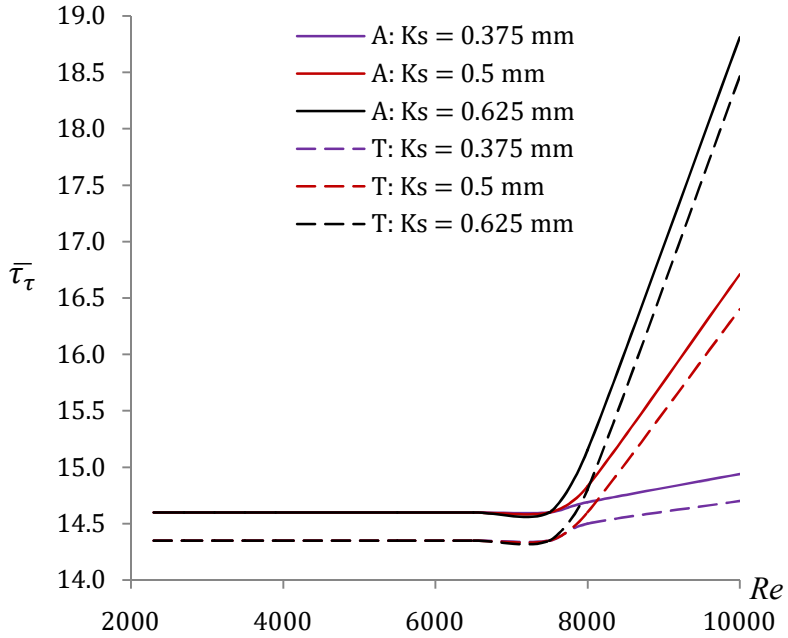

Figure 4.28: Variations of the average shear stress coefficient ratio with different Reynolds numbers for different roughness heights, K_s

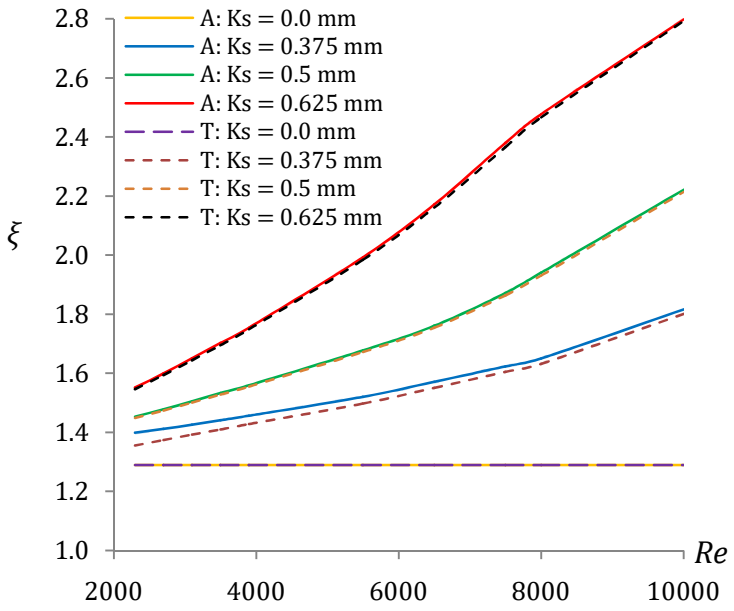

Figure 4.29: Variations of the thermal performance factor with different Reynolds numbers for different roughness heights, K_s

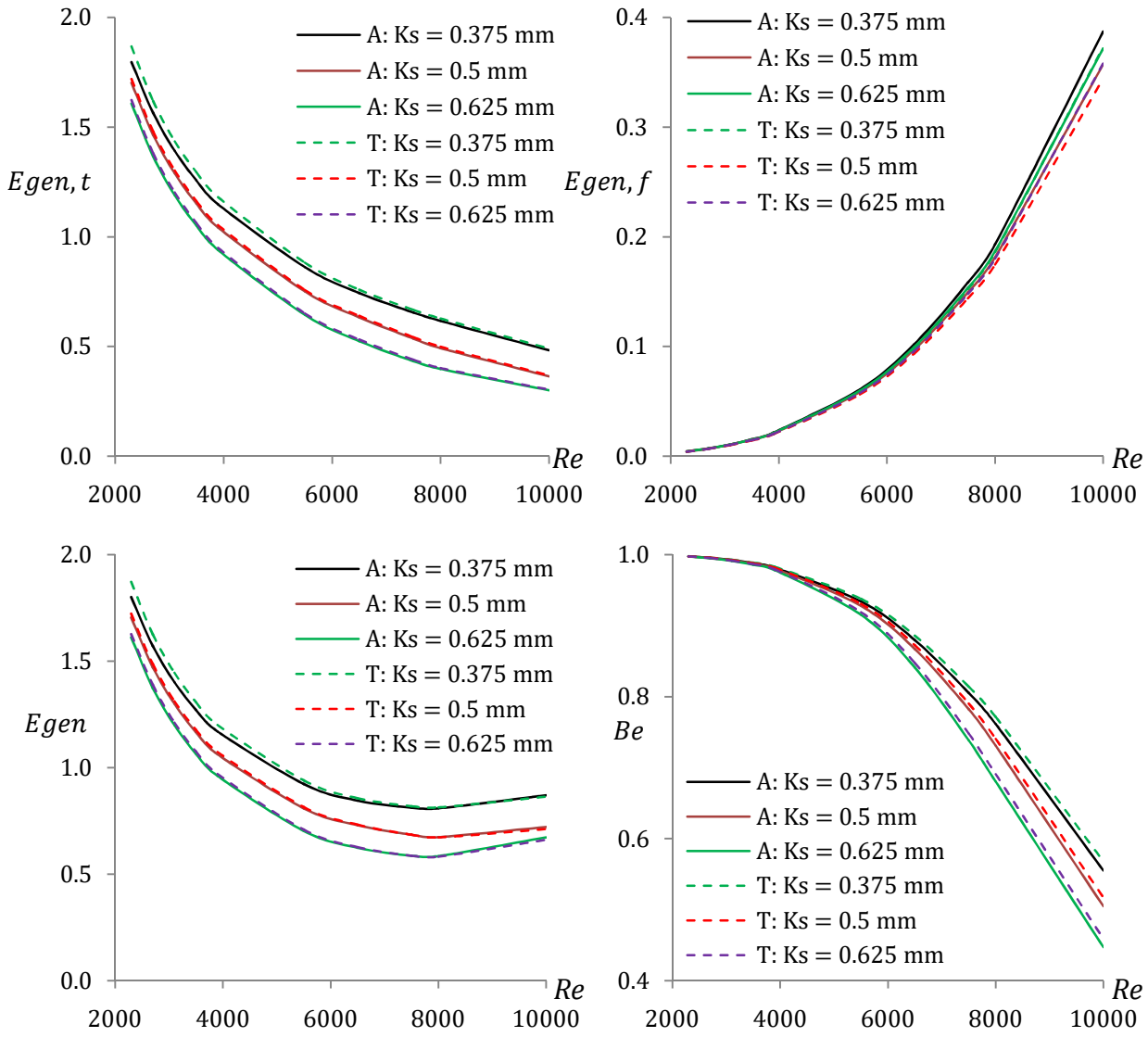

Figure 4.30: Variations of thermal, frictional and total entropy generation as well as Bejan number with different Reynolds numbers for different roughness heights, K_s

Chapter 5

Transition of Nanofluids Flow, Part 2: Performance of a Multi-phase Model

5.1 Introduction

Different types of flows that are experienced in nature and industrial technologies are considered as a mixture of different phases such as fluids and solids. In practical problems, the idea of multi-phase flow is developed from the concept of such mixture. In order to get a clear view of multi-phase system, different phases can be defined in different ways. Such phases can be identified as a group of different solids or group of different fluids or group of different solids and fluids. But, the combination of different phases will work only if there is a strong inertial bonding between the phases and also an interaction with the flow field.

Throughout the study, one of the simplest multi-phase mixture models is used to understand the behaviour of multi-phase flows where both the fluid and nanoparticles phases move at the same local velocities. This type of model can also be used for homogeneous multi-phase flows with the assumption that there is a very strong coupling between the primary and secondary phases and both the phases can be moved at the same or different velocities. In addition, multi-phase mixture model can be extended to *n* different phases through solving equation of continuity, equation of motion and conservation of energy equation for the mixture and concentration equations for the secondary phases.

In this chapter, a multi-phase mixture model (MPM) is used to investigate the transition of nanofluids flow in pipe. Then, an overall comparison between the single and multi-phase models is done in order to assess the performance of average heat transfer rate with Brownian motion. The reason for this particular choice is that the heat transfer rate with Brownian motion is always higher, discussed in §4.5.1.2 of Chapter 4.

As already shown in Figure 4.1 of Chapter 4, the physical model considered here is a horizontal circular pipe with the length L of $1.0\,m$ and a circular section with diameter, D_h of $0.019\,m$. Two-dimensional axi-symmetric model also is used to explain the heat transfer behaviour of Al_2O_3 and TiO_2–water nanofluids flowing through the pipe. The main objective of this study is to analyse the effects of different nanoparticles diameters, d_p and concentrations, χ on the heat transfer with pipe roughness. Results characterising the effects are presented in terms of mean velocity, temperature, turbulent kinetic energy, average Nusselt number, average shear stress ratio, and entropy generation. At the end, a comparison between the results of single and multi-phase models is presented to justify the overall performance of these models.

5.2 Boundary Conditions, Grid Sensitivity Test and Validation

Appropriate boundary conditions necessary to solve the set of non-linear partial differential equations are shown in §3.1.2 of Chapter 3. Boundary conditions considered in the numerical simulations have already been described in §4.2 of Chapter 4. However, the boundary conditions used in the single-phase model have been specified in the multi-phase mixture model for both the fluid and solid phases as well as for the mixture. Details of these boundary conditions are given below:

The velocity is specified for the fluid and nanoparticles phases at the pipe inlet where it is assumed that fluid and nanoparticles are flowing with the same local velocity. The nanoparticles concentration ($\chi = 6\%$) for the nanoparticles phase in set too. And, turbulent intensity ($I = 3\%$) and hydraulic diameter, $D_h = 0.019\,m$, as well as the inlet temperature ($T = 293\ K$) are specified for the mixture. In addition, details discussion on the choice of turbulent intensity is given in §4.4 of Chapter 4.

However, no conditions are applied for the fluid and nanoparticles phases at the pipe outlet. Also, turbulent intensity ($I = 3\%$) and hydraulic diameter, $D_h = 0.019\,m$ are specified for the mixture.

No conditions are applied for the fluid and nanoparticles phases at the pipe wall too. And, a no-slip boundary condition as well as uniform heat flux ($q'' = 5000\ W/m^2$) on the pipe wall are specified for the mixture.

Moreover, extensive computations are done to identify the number of grid points that produce a suitable arrangement of result in order to ensure the accuracy as well as the consistency of the numerical results. Besides, different combinations of grid are considered in the axial and radial directions and such combinations are 500 × 25, 500 × 50, 500 × 100, 500 × 150, and 1000 × 100 respectively. Hence, it is found that the grids 500 × 100, 500 × 150 and 1000 × 100 produce the similar results with insignificant differences. Therefore, the combination of 500 × 100 is considered for the present simulations in order to avoid any inconsistency throughout the investigation. Further, accuracy of the numerical results for water against existing correlations and experimental data for different Reynolds number, Re = 2300 to 10^4, are tested. The details of grid sensitivity test and validation are presented in §4.3 and §4.4 of Chapter 4.

5.3 Results and Discussion

Various numerical simulations are performed using different parameters, such as Re= 2300 to 10×10^3, $\chi = 6\%$, $d_p = 10$ to 40 nm and roughness heights (0.375 mm, 0.5 mm and 0.625 mm) in this research unit. Multi-phase mixture model is used to investigate the heat transfer behaviour of Al_2O_3-water and TiO_2-water nanofluids flow in pipe under transition flow condition. The effects of Brownian motion of nanoparticles, nanoparticles concentrations and diameters on heat transfer and entropy generation are discussed in the following sections. Besides, two new correlations are proposed for a smooth pipe wall case. A similar investigation is carried out to justify the effect of a uniform roughness along the pipe wall for different roughness heights using the multi-phase mixture model as it is done in the single phase model.

5.3.1 Behaviours of Mean Velocity, Temperature and Turbulent Kinetic Energy

Figures 5.1 and 5.2 illustrate the flow field behaviour of the Al_2O_3-water and TiO_2-water nanofluids along the axial direction for the smooth and rough pipe wall respectively. At first, the mean velocity profile is found to behave like a laminar flow though a sudden change of hydrodynamic pattern is observed at some points. Such behaviour indicates the transition behaviour of flow field. The initial growth of momentum boundary layer thickness near the upstream is found to push the fluid

into the centreline area. And, the growth of momentum boundary layer thickness is maximum near the breakdown point. Also, such development of hydrodynamic boundary layer forces the fluid to move closer to the centreline area. The maximum mean velocity is observed at this region too. After that, the hydrodynamic boundary layer has reduced. Then as the flow tends to be fully developed, the growth of this boundary layer is found to be constant. Here, the lower is the size of nanoparticles; the higher is the nanofluids mean velocity. That means, the smaller nanoparticles move faster than the larger ones. Such findings are also observed while using the single phase model as discussed in §4.5.1.1 of Chapter 4. It suggests that the hydrodynamic behaviour inside the pipe and the thickness of boundary layer for the smooth pipe wall remain unchanged in both the single and multi-phase models. Thus it means, the impact of different fluids and nanoparticles phases have a very little effect on the flow field.

As the roughness height is increased, the hydrodynamic critical distance decreases due to the disturbances created by the pipe wall roughness inside the flow field. As a result, transition starts earlier and transition points shift towards the upstream. Such behaviour is clearly visible in Fig. 5.2. However, the growth of the velocity boundary layer with the increase of roughness height remains almost constant. But as the transition begins earlier because of the increase of roughness height, higher velocity region moves towards the centreline area and seems to be reduced near the transition point. After that transition point, growth of the velocity boundary layer becomes higher and the mean velocity is found to be maximum.

Figure 5.3 demonstrates the mean temperature behaviour of Al_2O_3-water and TiO_2-water nanofluids along the pipe. There is an initial development of laminar behaviour of temperature field followed by the breakdown of laminar flow at some points that indicates the transition behaviour of temperature field. The coolant nanofluids are found to cover almost the whole region in Fig. 5.3. Though, the higher temperature of nanofluids with a temperature difference between the hot and cold nanofluids which is approximately $6K$ is visible near the wall region. Moreover, Figure 5.4 explains the behaviour of wall temperature with different roughness heights for both the nanofluids. It is observed that the wall temperature increases initially though it starts to decrease suddenly. And, a monotonic increase of wall temperature is observed after some distance. It is detected that the wall temperature decreases with the

increase of roughness heights too. Such behaviour is significant in a sense that the lower wall temperature plays an important role to enhance the heat transfer rate (already discussed in the previous Chapter 4). However, TiO_2-water nanofluid always shows a bit higher wall temperature than Al_2O_3-water nanofluid does in all the roughness heights. It indicates that, Al_2O_3-water nanofluid might show a bit higher heat transfer rate in different roughness heights than TiO_2-water nanofluid does. Comparing these findings with those presented in Chapter 4, a higher magnitude of temperature is found in the single phase model than that in the multi-phase model. But, the growth of the thickness of thermal boundary layer seems to be a bit higher in the multi-phase model than that in the single phase model.

Figures 5.5 and 5.6 illustrate the turbulent kinetic energy behaviour of Al_2O_3-water and TiO_2-water nanofluids along the axial direction for the smooth and rough pipe wall respectively. The distance between the upstream and laminar breakdown point of turbulent kinetic energy is the same as the hydrodynamic critical distance. That is, the transition begins at the same point for both the flow field and the turbulent kinetic energy. Initially, the turbulent kinetic energy is found to be constant near the centreline region and close to the laminar breakdown point though it starts to rise monotonically later. Subsequently, it starts to enhance rapidly at the laminar breakdown point and such enhancement becomes maximum at the near wall regime. After the breakdown point, a slight decrease in turbulent kinetic energy is observed and then it becomes constant as the flow tends to be fully developed. Again, turbulence kinetic energy increases with the decrease of nanoparticles diameters from 40 to 10 *nm* as well as the increase of nanoparticles concentrations. Besides, the maximum value of mean turbulent kinetic energy with the increase of roughness heights for a fixed Reynolds number is found almost similar for both the nanofluids. This suggests, the roughness heights have little effect on the development of turbulent kinetic energy profile though it forces the transition to start early. So, the above findings reveal that the behaviour of turbulent kinetic energy along the pipe while using multi-phase model for smooth pipe wall is identical with that in the single phase model. It is also found that the higher magnitude of turbulent kinetic energy region seems to be more evident for rough pipe wall in the single phase model than in the multi-phase model.

In general, the thickness of thermal boundary layer is found to decrease with the increase of Reynolds number and the decrease of nanoparticles diameter from 40 to 10 nm. It implies that the enhancement of heat transfer depends on the size of nanoparticles. Additionally, turbulent kinetic energy is found to increase with the increase of Reynolds number and Al_2O_3-water nanofluid shows higher values of turbulent kinetic energy than TiO_2-water nanofluid. The cause of these facts is, the smaller nanoparticles absorb lower energy than the higher size of nanoparticles and the mean velocity of Al_2O_3-water nanofluid is found higher than TiO_2-water nanofluid with the increase of Reynolds number. Similar behaviour is noticed for different Reynolds numbers, nanoparticles concentrations and diameters.

5.3.2 Darcy Friction Factor

There is an insignificant difference between the results of Darcy friction factor of nanofluids and water for the smooth pipe wall case as discussed in §4.5.1.1 of Chapter 4. Similar results are also found while using the multi-phase model. Therefore, our focus of attention is the variations of Darcy friction factor, *f*, with different Reynolds numbers for different roughness heights using Al_2O_3-H_2O nanofluid that is presented in Fig. 5.7(a).

The friction factor for a rough pipe wall is always found to be higher than that of the smooth pipe wall. Again, the Darcy friction factor increases when the roughness heights increase and higher Darcy friction factor indicates higher penalty in pumping power. In particular, maximum variations of 6.64%, 19.47% and 33.78% for Al_2O_3-water nanofluid and $K_s = 0.375, 0.5$ and $0.625\ mm$, in comparison with the smooth pipe wall results for water is observed. In addition to that, Darcy friction factor results for $K_s = 0.375, 0.5$ and $0.625\ mm$ in multi-phase model are approximately 3%, 4% and 6% lower than that of single phase model respectively. Similar results are found for TiO_2-water nanofluid.

Figure 5.7(b) presents the Darcy friction factor ratio of the nanofluid to water with different roughness heights at *Re* = 2300, 3100, 5500, 8000 and 10000 respectively. Darcy friction factor ratio is seen to increase gradually for roughness height, $K_s \leq 0.4\ mm$ and such increase becomes significant when the roughness height starts to increase. This means, the higher roughness heights force the pressure drop

to rise rapidly and because of that higher penalty in pumping power is expected in any practical applications.

5.3.3 Average Heat Transfer Behaviour

Figures 5.8 and 5.9 clarify the behaviour of average Nusselt number with the Reynolds number for Al_2O_3 and TiO_2-water nanofluids for both the smooth and rough pipe wall respectively. Here, the average Nusselt number is found to increase with the decrease of nanoparticles diameter from 40 to 10 nm. Particularly for Al_2O_3–water nanofluid and $\chi = 2\%, 4\%$ and 6% with $d_p = 10\,nm$, the minimum and maximum percentages of the growth of average Nusselt number are approximately 3.55 and 3.68, 11.56 and 12.41, 30.51 and 31.41 respectively. Nevertheless, when $d_p = 20\,nm$, such percentages reduce and are found approximately 2.51 and 2.74, 8.61 and 9.31, 18.52 and 19.39 respectively. This deterioration of the minimum and maximum percentages of the growth of average Nusselt number are also observed when d_p increases from 10 to 40 nm. To conclude the findings, such percentages of the growth of average Nusselt number decreases in case of gradually increasing the nanoparticles diameter.

Again for TiO_2–water nanofluid and $\chi = 2\%, 4\%$ and 6% with $d_p = 10\,nm$, the minimum and maximum percentages of the growth of average Nusselt number are found to be approximately 2.54 and 3.50, 11.56 and 12.37 and 30.51 and 31.24 respectively. On the other hand, the percentages decrease more and are found approximately 2.51 and 2.71, 8.55 and 9.21, 18.51 and 19.06 respectively when $d_p = 20\,nm$. Such deterioration is always observed with the increase of nanoparticles diameter as it is in case of Al_2O_3–water nanofluid. For example, when $\chi = 2\%, 4\%$ and 6% and $d_p = 40\,nm$, the minimum and maximum percentages of the growth of average Nusselt number are approximately 1.50 and 2.03, 5.64 and 6.25, 11.51 and 12.23 respectively.

Then, the average Nusselt number increases with the increase of Reynolds number for $K_s = 0.375\,mm$. And, the maximum percentage of enhancement is found to be 64.61% and 63.21% comparing with the smooth pipe wall results for Al_2O_3-water and TiO_2-water nanofluids respectively. It is also found that for $K_s = 0.5\,mm$ and $K_s = 0.625\,mm$ enhancement of average Nusselt number is always higher than that of $K_s = 0.375\,mm$. Therefore, the maximum percentages of enhancements are found

to be 117.8% and 116.07%, 162.91%, and 162.10% for Al_2O_3-water and TiO_2-water nanofluids respectively. Details of such findings for single phase model are also described in §4.5.1.2 and §4.5.2.4 of Chapter 4.

To sum up the above investigations, slightly higher percentages of the growth of average Nusselt number is observed for both Al_2O_3–water and TiO_2–water nanofluids when the interaction between fluid particles and nanoparticles is considered. Later on, heat transfer enhancement analysis is discussed in §5.3.6 of Chapter 5.

5.3.4 Performance of Average Shear Stress Ratio

Figures 5.10 and 5.11 illustrate the variations in the behaviour of average shear stress ratio, $\overline{\tau_\tau}$ with Reynolds numbers for Al_2O_3-water and TiO_2-water nanofluids for smooth and rough pipe wall respectively. It is observed that this ratio increases with the decrease of nanoparticles diameter from 40 to 10 nm and such increase is completely independent of Reynolds number. Particularly for Al_2O_3–water nanofluid and $\chi = 2\%, 4\%$ and 6% with $d_p = 10\ nm$, $\overline{\tau_\tau}$ is approximately 1.77, 3.80 and 15.55 respectively. But when $d_p = 20\ nm$, $\overline{\tau_\tau}$ decreases and is found approximately 1.57, 2.70 and 6.15 respectively. Again, when nanoparticles diameter increases from 10 to 40 nm, $\overline{\tau_\tau}$ decreases more and such reduction is significant for higher nanoparticles concentration. For example, $\overline{\tau_\tau}$ is found to be approximately 1.43, 2.13 and 3.63 respectively when $d_p = 40\ nm$,.

However, the average shear stress ratio is approximately 1.75, 3.75 and 15.25 respectively for TiO_2–water nanofluid and $\chi = 2\%, 4\%$ and 6% with $d_p = 10\ nm$. But when $d_p = 20\ nm$, this ratio starts to decrease more and is found to be approximately 1.56, 2.66 and 6.05 respectively. A similar behaviour is also observed for TiO_2–water nanofluid when nanoparticles diameter is increases from $d_p = 10$ to 40 nm. Such as, $\overline{\tau_\tau}$ is found approximately 1.42, 2.09 and 3.56 respectively when $\chi = 2\%, 4\%$ and 6% and $d_p = 40\ nm$.

Analysing the above findings for both the single and multi-phase models as shown in Figs. 4.16, 4.17 and 4.28 of Chapter 4 and Figs. 5.10 and 5.11, the variation between the average shear stress coefficient ratio results are found to be insignificant when $\chi = 2\%$. But, multi-phase model shows higher values of $\overline{\tau_\tau}$ for higher nanoparticles concentration than the single phase model does. Besides, average shear

stress coefficient ratio of Al_2O_3-water nanofluid is always found higher than TiO_2-water nanofluid for both the single and multi-phase models.

In Fig. 5.11, the average shear stress coefficient ratio is found to remain constant for $Re \leq 7500$. Though, the ratio has increased rapidly with the increase of roughness height for $Re > 7500$. Such behaviour is found to be identical for both Al_2O_3-water and TiO_2-water nanofluids. On the other hand, Al_2O_3-water nanofluid shows higher ratios than TiO_2-water nanofluid. In particular, the maximum average shear stress coefficient ratio of Al_2O_3–water nanofluid for different roughness heights, K_s = 0.375, 0.5 and 0.625 *mm* is found to be approximately 15.92, 17.70 and 18.68 respectively. However, the maximum ratios of TiO_2–water nanofluid for different roughness heights are approximately 15.62, 17.37 and 18.33 respectively. Also, lower average shear stress ratio is observed while using single phase model for both the nanofluids except for the case K_s = 0.5 *mm*. Details are discussed in §4.5.2.5 of Chapter 4. Hence, the results indicate that the wall roughness plays an important role to enhance heat transfer rate and average shear stress coefficient ratio. Though, such ratio is supposed to be the main disadvantages in the practical applications.

5.3.5 Entropy Generation Analysis

Initially, Fig. 5.12 illustrates the changing behaviour of the total entropy generation with Reynolds number for Al_2O_3-water and TiO_2-water nanofluids. It is observed that thermal entropy generation decreases with the increase of nanoparticles diameter from 10 to 40 *nm*. And, the values of frictional entropy generation are found to be negligible. It means that only thermal entropy generation has impact on the total entropy generation and the behaviour of total entropy generation is similar to the thermal entropy generation. Therefore, the total entropy generation decreases with the decrease of Reynolds number and the increase of nanoparticles diameter. Besides, the total entropy generation of TiO_2-water nanofluid has always found to be slightly higher than that of Al_2O_3-water nanofluid for both the single and multi-phase models.

Later, the thermal entropy generation is found to be the maximum for the low Reynolds numbers as well as the higher nanoparticles concentration. It means that nanoparticles concentration has impact on the enhancement of heat transfer. And, such enhancement has an important role to decrease the thermal entropy generation which decreases with the decrease of nanoparticles diameter from 40 to 10 *nm*. Like

frictional entropy generation, a similar behaviour of having an insignificant effect on total entropy generation is observed for the thermal entropy generation too. Moreover, no optimal Reynolds number is found for both single and multi-phase models as shown in Figs. 4.18 and 4.19 of Chapter 4 and also in Fig. 5.12. It indicates that minimization of the total entropy generation is not possible for the smooth pipe wall case under transition flow regime when the Brownian motion of nanoparticles is considered.

Figure 5.13 shows the behaviour of thermal, frictional and total entropy generation with different Reynolds number for different roughness heights, K_s *(mm)*. It is found that the thermal entropy generation decreases and the frictional entropy generation increases along with the increase of Reynolds number as well as the roughness heights. Increase of thermal entropy generation has occurred due to the increase of roughness heights which contributes to increase the heat transfer rate. Again, increase of the frictional entropy generation is noticed because of the increase of pressure drops which helps to increase the Darcy friction factor. It is also seen that the thermal entropy generation decreases monotonically and the frictional entropy generation increases significantly for the higher Reynolds number and roughness heights. Moreover, it is noticed that the opposite trends of the thermal and frictional entropy generation have considerable impacts on the total entropy generation. Besides, total entropy generation is observed to decrease monotonically when $Re < 8000$ though this has started to increase when $Re \sim 8000$. It suggests that an optimal Reynolds number exits at $Re \sim 8000$. Such behaviour is observed for different roughness heights when $Re \sim 8000$. And, the frictional entropy generation of Al_2O_3-water nanofluid is always higher than that of TiO_2-water nanofluid. But, there is very slight variation between the results of thermal and total entropy generation while using Al_2O_3-water and TiO_2-water nanofluids. It indicates that the impact of frictional entropy generation on the total entropy generation is significant to achieve optimal Reynolds number which can minimize the total entropy generation.

5.3.6 Heat Transfer Enhancement Analysis

Figures 5.14 and 5.15 compare the variations of the maximum percentages of heat transfer enhancement along with the nanoparticles diameters obtained by using the

single- (SPM) and multi-phase (MPM) models for the smooth and rough pipe wall respectively. The maximum percentages of heat transfer rate using the multi-phase model is always slightly higher than that of the single phase model. This is feasible because collusion between the fluid particles and nanoparticles as well as the Brownian motion of nanoparticles are taken into account in the multi-phase model and thus both of these help to increase the heat transfer rate. Moreover, the maximum percentages of the heat transfer enhancement are found to be higher for the higher roughness heights and results are found significant when $Re > 7500$. This occurs due to the significant increase of average Nusselt number for the different roughness heights when $Re > 7500$. Again, the variations between the maximum percentages of heat transfer augmentations are significantly enhanced for higher nanoparticles volume concentrations in both of the single and multi-phase models. This is due to the increase of thermal conductivity of Al_2O_3-water and TiO_2-water nanofluids along with the increase of nanoparticles concentration.

5.3.7 Correlations

Two new correlations developed by using non-linear regression analysis are proposed to calculate the average Nusselt number. These correlations are depending on Reynolds number, Prandtl number and ratio of nanoparticles and fluid particles diameters. And, the maximum standard deviation of error is found less than 0.4% for both the nanofluids. In addition, Fig. 5.16 illustrates a comparison between the present results and the proposed correlations and that shows a good agreement between the results.

Al_2O_3-H_2O Nanofluid : $\overline{Nu} = 0.03833\, Re^{0.76601} Pr^{0.25565} \left(\frac{d_f}{d_p}\right)^{-0.0040367}$ (5.1)

TiO_2-H_2O Nanofluid : $\overline{Nu} = 0.037768\, Re^{0.76536} Pr^{0.26123} \left(\frac{d_f}{d_p}\right)^{-0.0062903}$ (5.2)

where

$2300 \leq Re \leq 10 \times 10^3, 8.45 \leq Pr \leq 20.29, 10 \leq d_p(nm) \leq 40, 0 < \chi(\%) \leq 6.$

5.4 Conclusion

In this chapter, the behaviours of the Darcy friction factor and the average Nusselt number as well as the thermal, frictional and total entropy generation analysis have been presented for both the smooth and rough pipe wall under transition flow

regimes. Two different nanofluids such as Al_2O_3-water and TiO_2-water have been considered throughout this investigation and Eulerian-Eulerian multi-phase mixture model is used. Comparison of the results of maximum percentages of heat transfer enhancement using single and multi-phase models has also been presented. In the end, the following findings are summarised below:

1. The enhancement of heat transfer rate is predicted slightly higher when the interaction between the fluid and nanoparticles is taken into account. It, therefore, suggests that using a homogeneous single phase model in practical application could potentially lead to an over-prediction/increased rate of heat transfer.

2. Darcy friction factor results for the pipe with a smooth wall are unaffected by the choice of the models whether it is a single or multi-phase model. They also show having an insignificant effect on the predicted averaged wall shear stress ratio when the pipe wall is smooth. But, a slightly higher penalty of pumping power is found in MPM than in SPM for the rough pipe wall case due to a slightly higher prediction of the shear stress ratio.

3. Moreover, higher enhancement of the heat transfer rate is found with the increase of roughness height of the pipe wall. Although a slightly higher penalty in pumping power is reported, the results overall indicate that the pipe roughness may be considered to achieve a significant enhancement of heat transfer rate.

4. On the whole, the wall roughness has had a significant effect on the enhancement of heat transfer compared to the smooth pipe wall. Also, the Al_2O_3 and TiO_2-water nanofluids always show a higher heat transfer rate than water when the nanoparticles diameter and concentrations with/without its Brownian motion are taken into account.

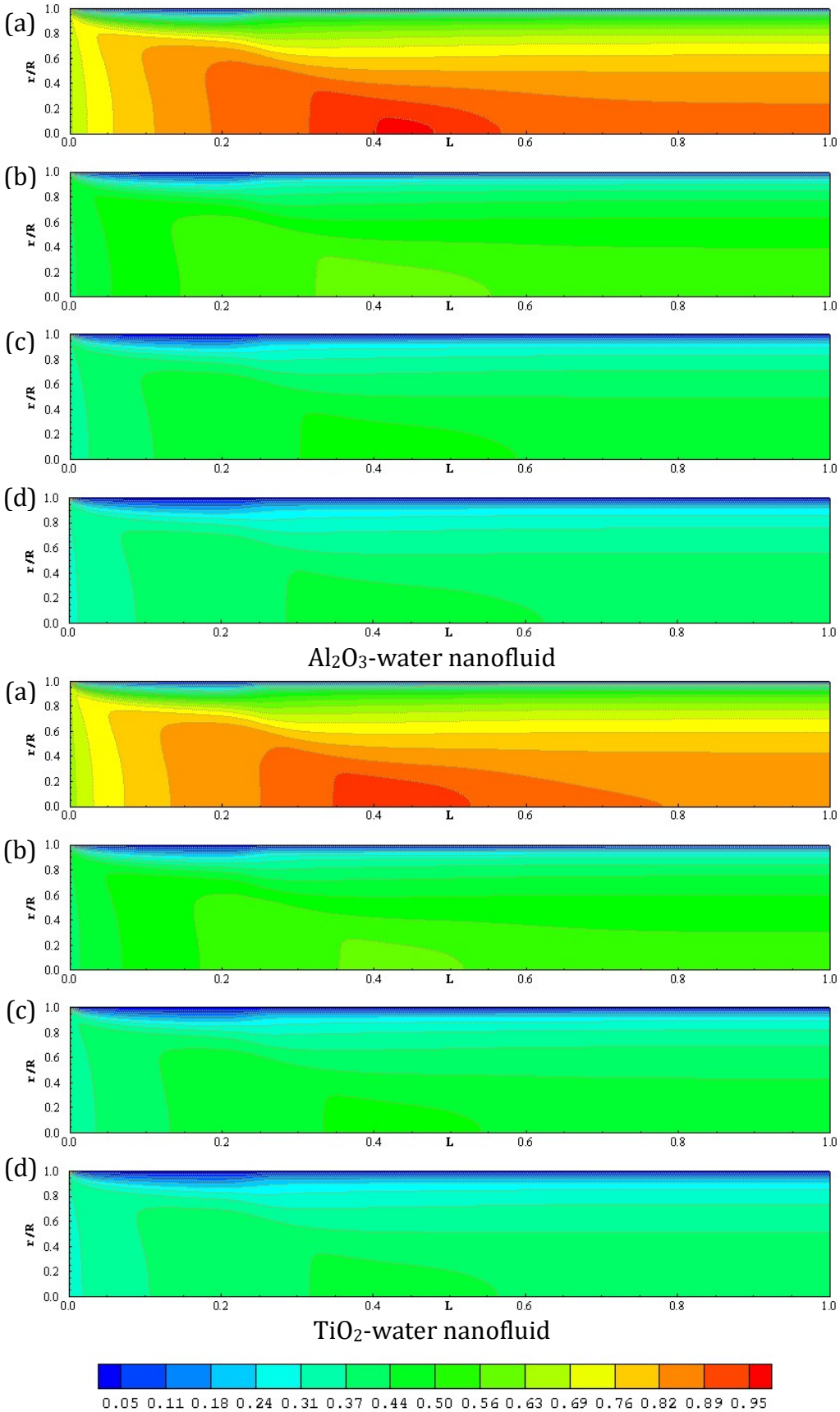

Figure 5.1: Variations of mean velocity of Al_2O_3-water and TiO_2-water nanofluids along the axial direction for (a) $d_p = 10\,nm$ (b) $d_p = 20\,nm$ (c) $d_p = 30\,nm$ (d) $d_p = 40\,nm$ respectively and $Re = 3500$, $\chi = 6\%$

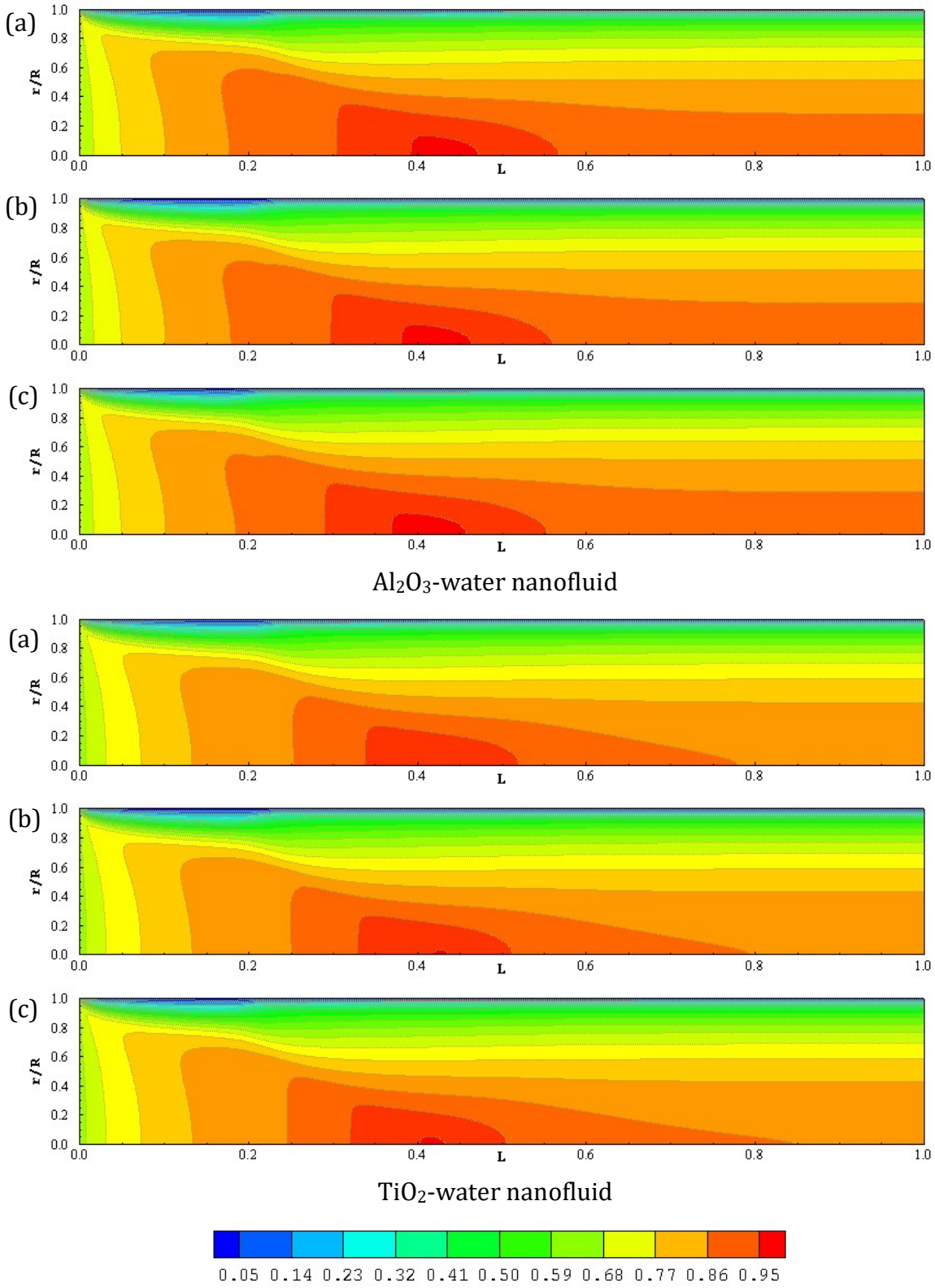

Figure 5.2: Variations of mean velocity of Al_2O_3-water and TiO_2-water nanofluids along the axial direction for (a) $K_s = 0.375\,mm$ (b) $K_s = 0.5\,mm$ (c) $K_s = 0.625\,mm$ respectively and $Re = 3500$

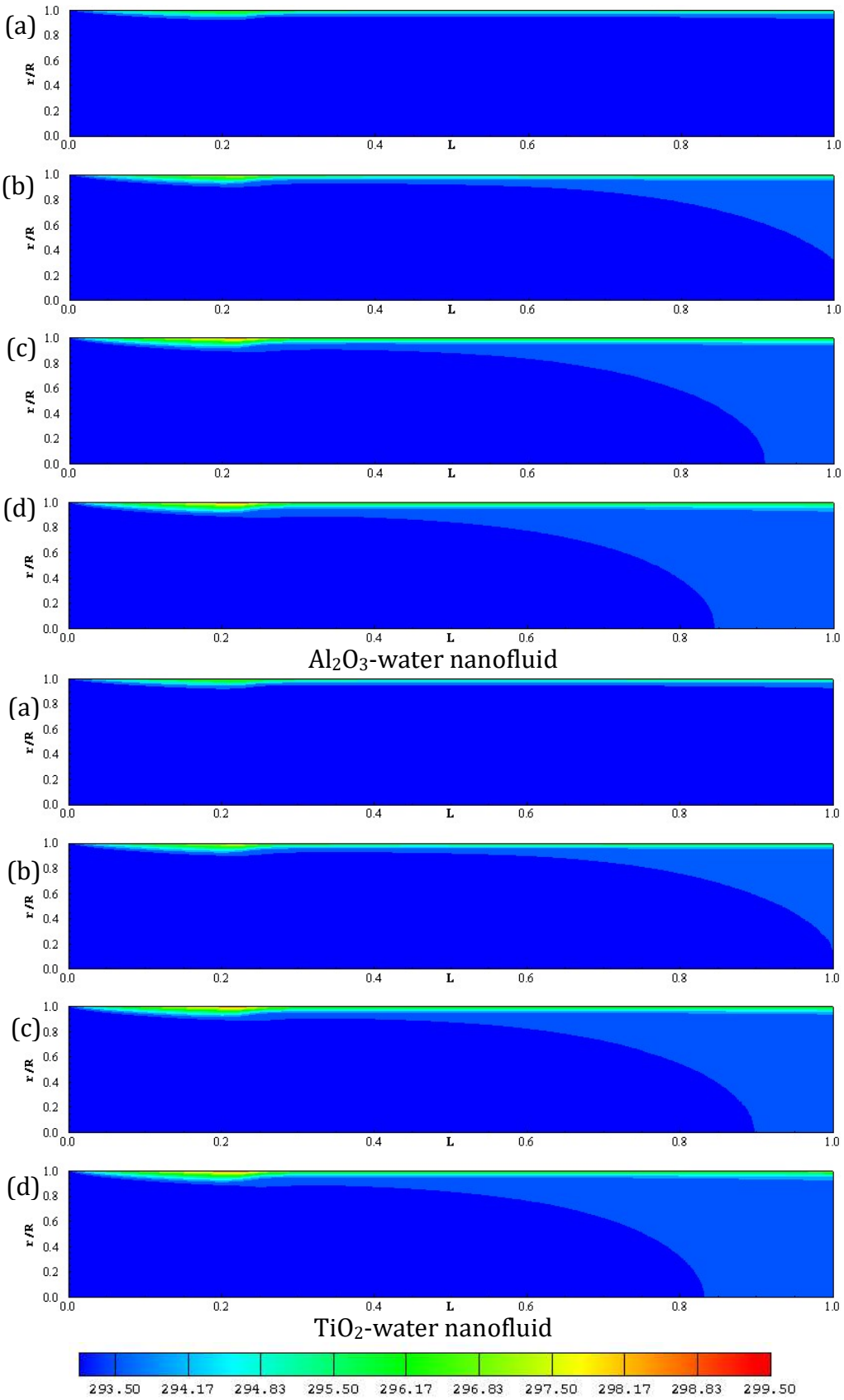

Figure 5.3: Variations of mean temperature of Al_2O_3-water and TiO_2-water nanofluids along the axial direction for (a) $d_p = 10\,nm$ (b) $d_p = 20\,nm$ (c) $d_p = 30\,nm$ (d) $d_p = 40\,nm$ respectively and $Re = 3500$, $\chi = 6\%$

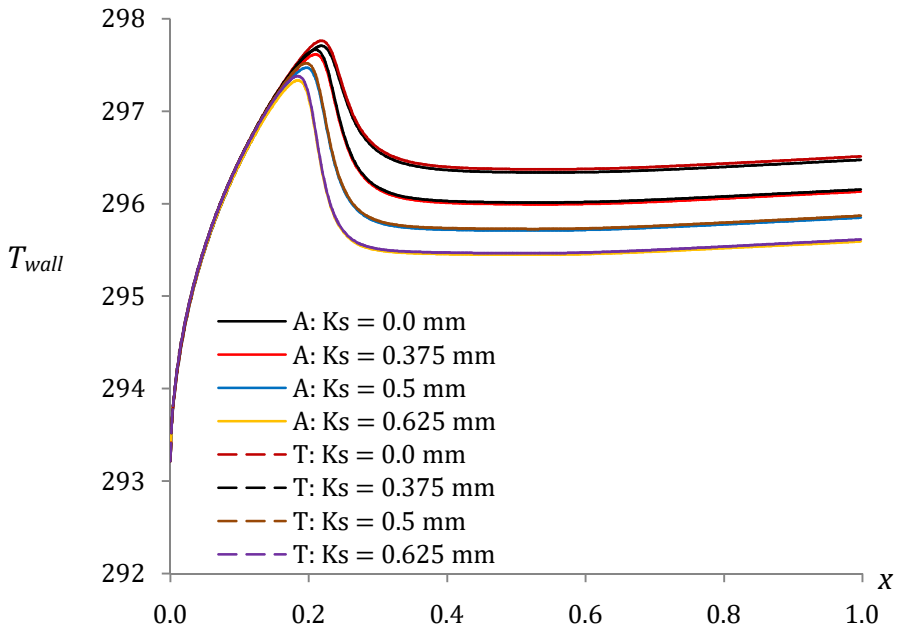

Figure 5.4: Variations of wall temperature of Al_2O_3-water and TiO_2-water nanofluids along the axial direction for (a) $K_s = 0.375\,mm$ (b) $K_s = 0.5\,mm$ (c) $K_s = 0.625\,mm$ respectively and $Re = 3500$

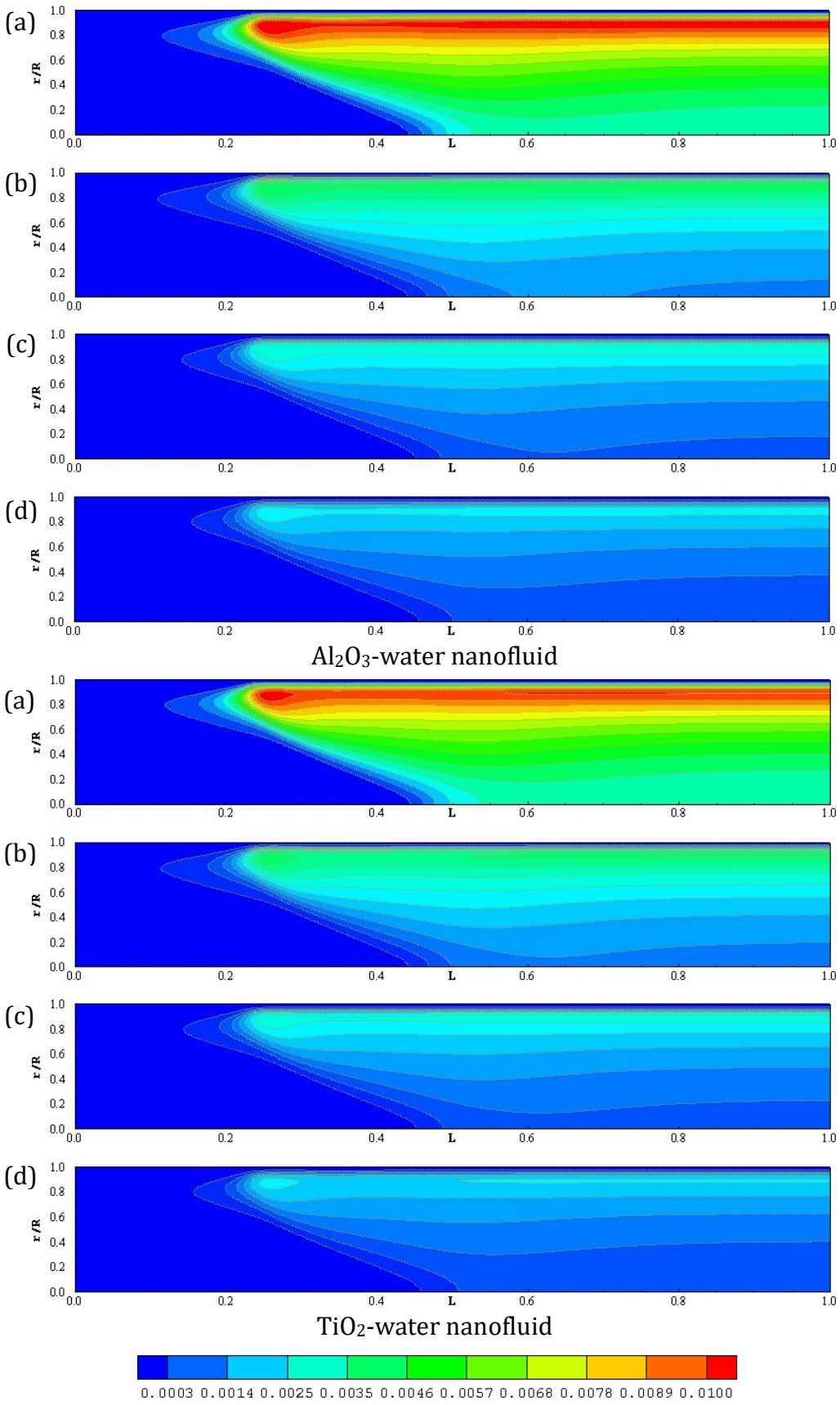

Figure 5.5: Variations of turbulent kinetic energy of Al_2O_3-water and TiO_2-water nanofluids along the axial direction for (a) $d_p = 10\,nm$ (b) $d_p = 20\,nm$ (c) $d_p = 30\,nm$ (d) $d_p = 40\,nm$ respectively and $Re = 3500$, $\chi = 6\%$

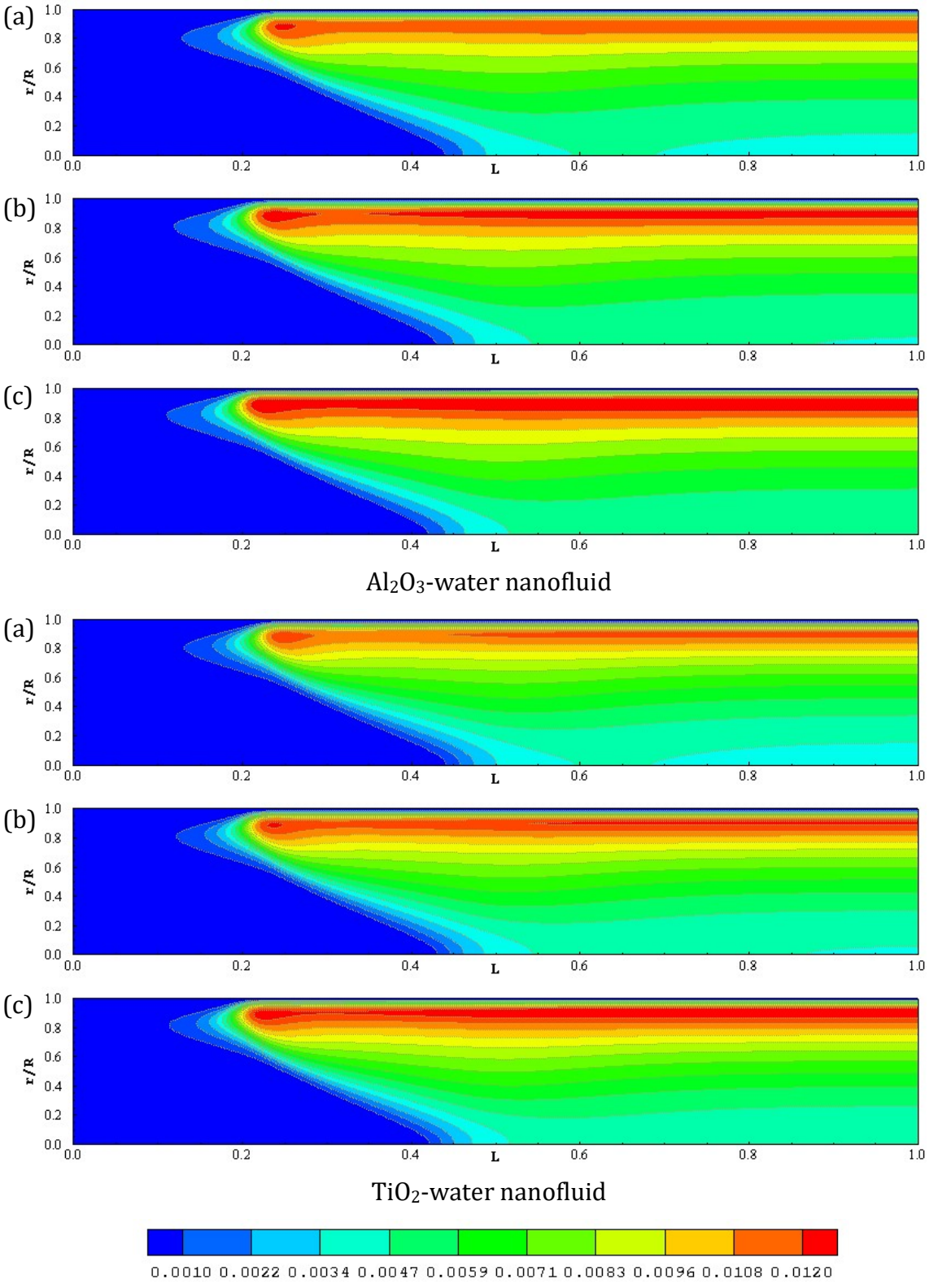

Figure 5.6: Variations of turbulent kinetic energy of Al_2O_3-water and TiO_2-water nanofluids along the axial direction for (a) $K_s = 0.375\,mm$ (b) $K_s = 0.5\,mm$ (c) $K_s = 0.625\,mm$ respectively and $Re = 3500$

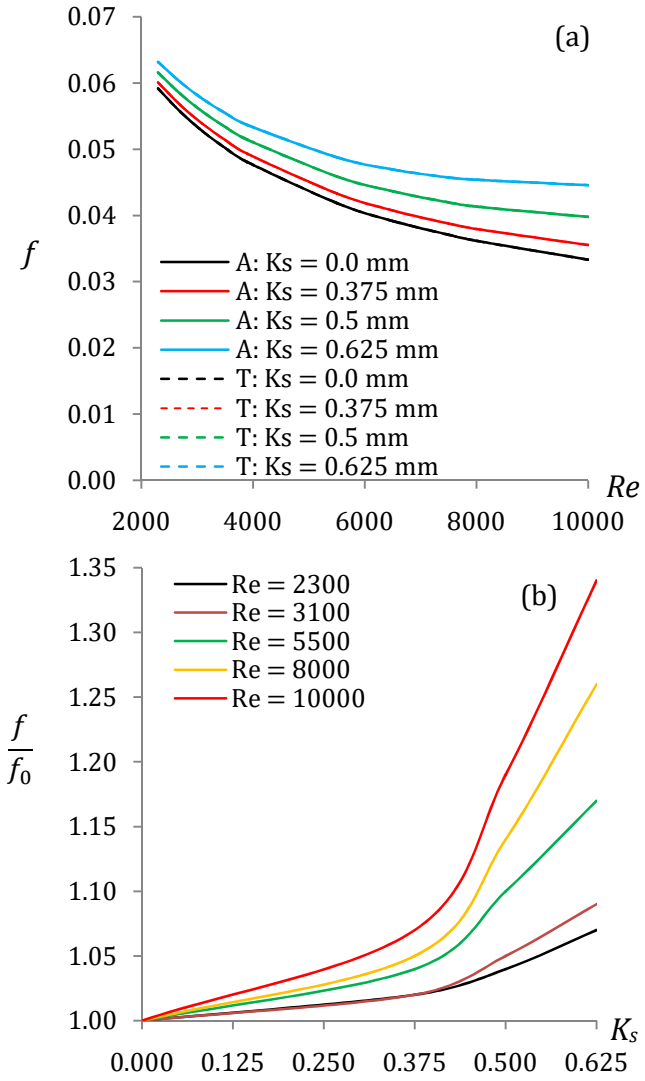

Figure 5.7: Variations of Darcy friction factor and friction factor ratios with different Reynolds numbers and different roughness heights, K_s (mm)

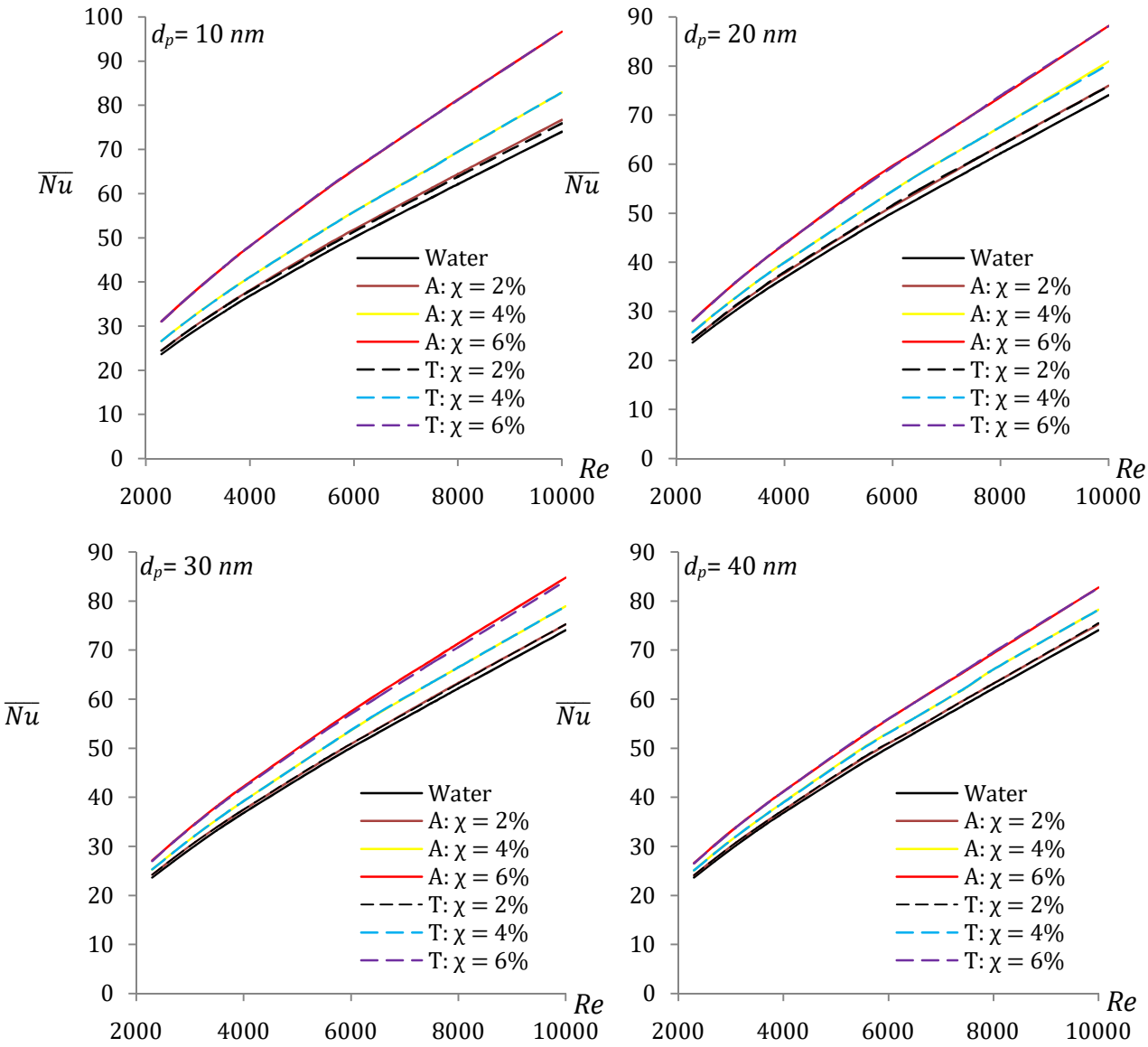

Figure 5.8: Variations of average Nusselt number with different Reynolds numbers

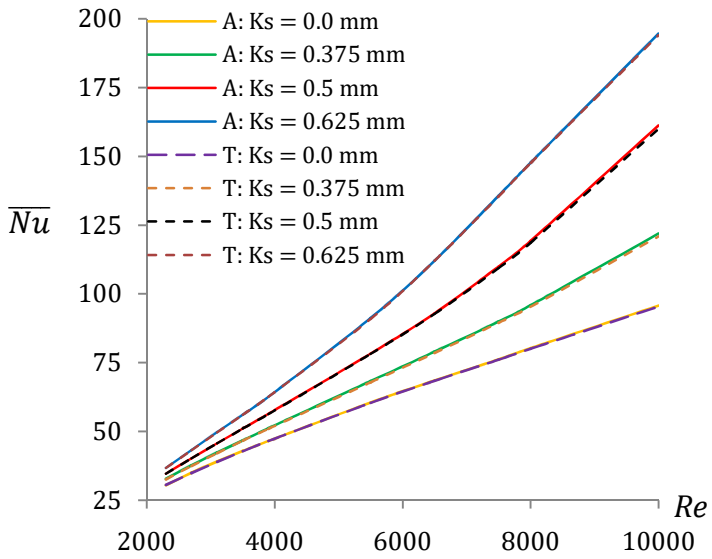

Figure 5.9: Variations of the average Nusselt number with different Reynolds numbers for different roughness height, K_s

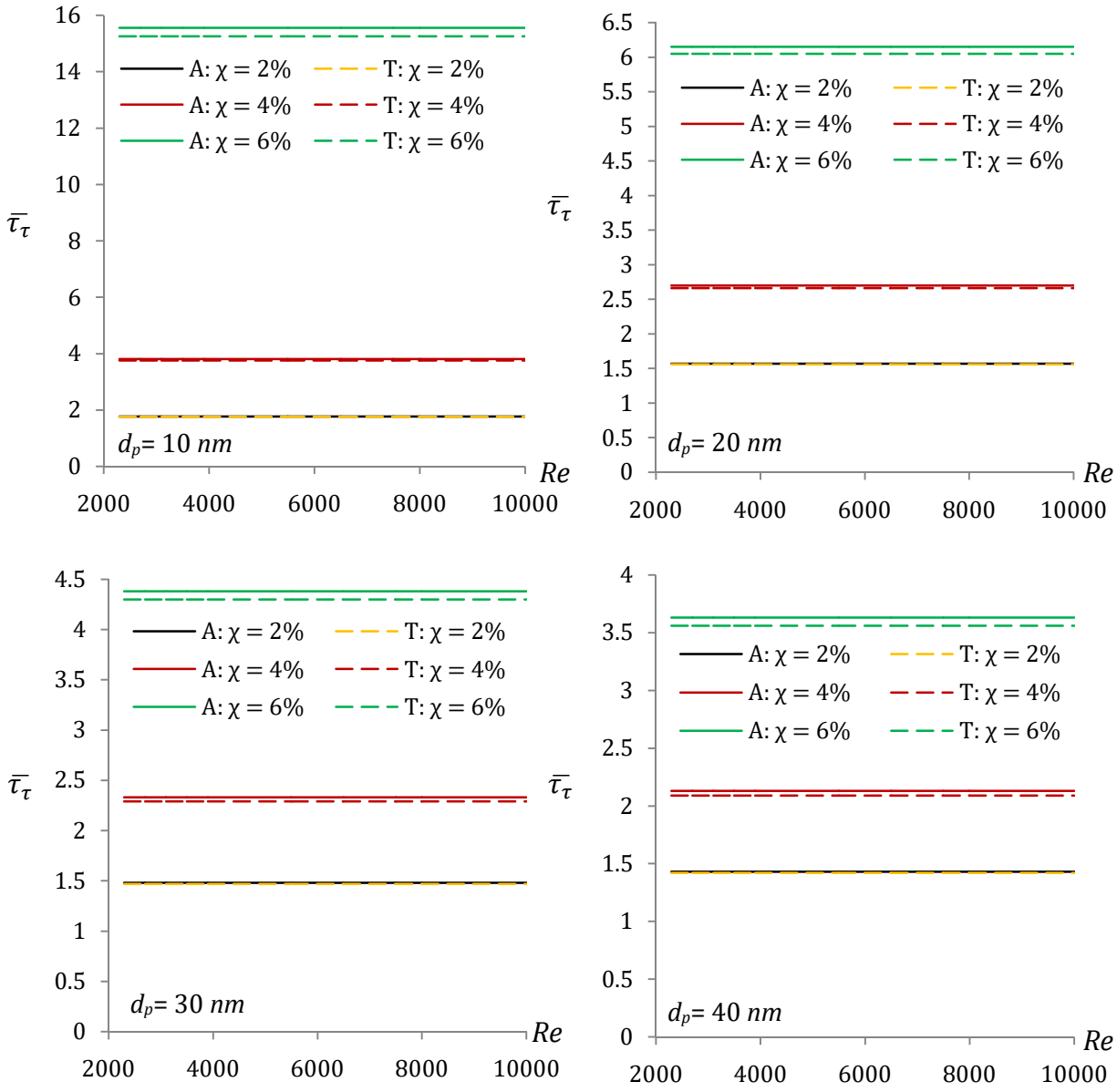

Figure 5.10: Variations of average shear stress coefficient ratio with different Reynolds numbers

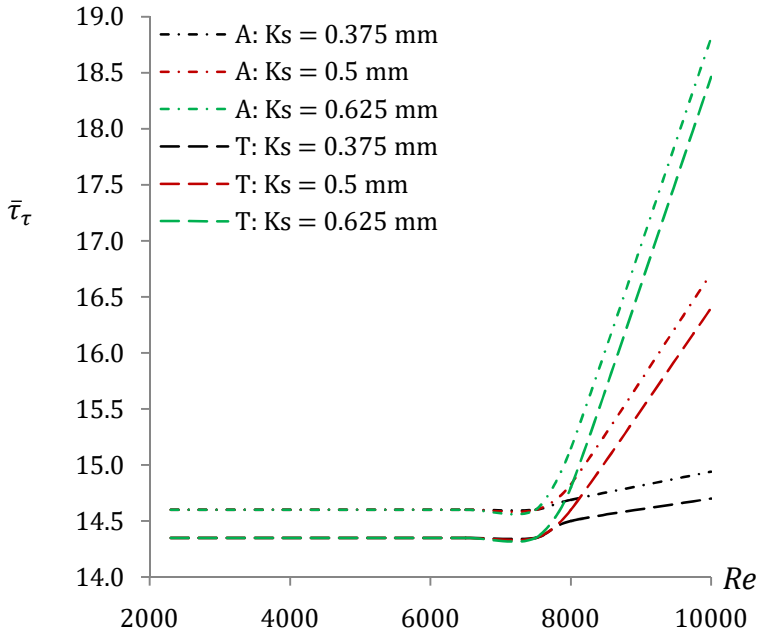

Figure 5.11: Variations of the average shear stress coefficient ratio with different Reynolds numbers for different roughness heights, K_s

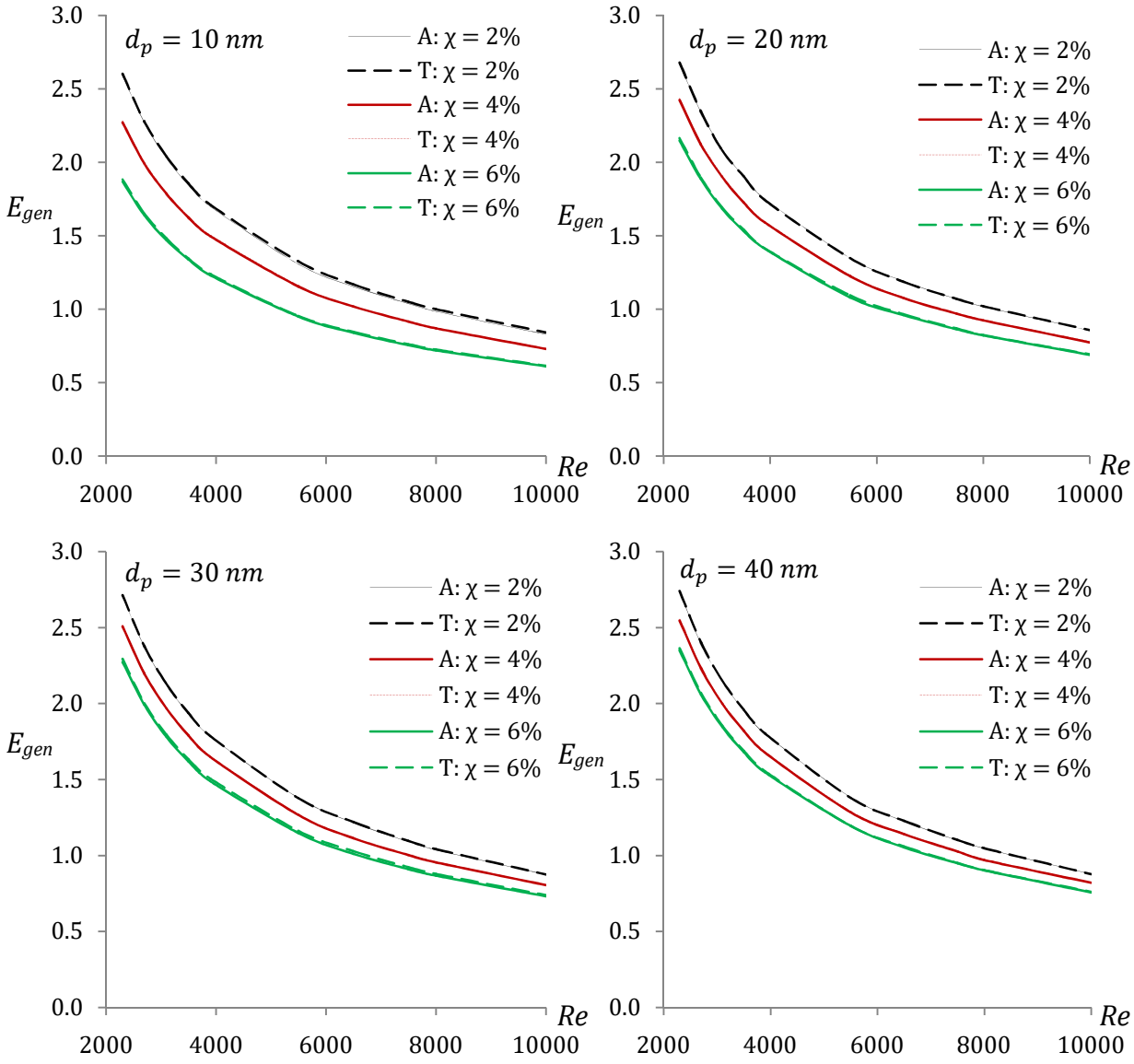

Figure 5.12: Variations of total entropy generation with different *Re*

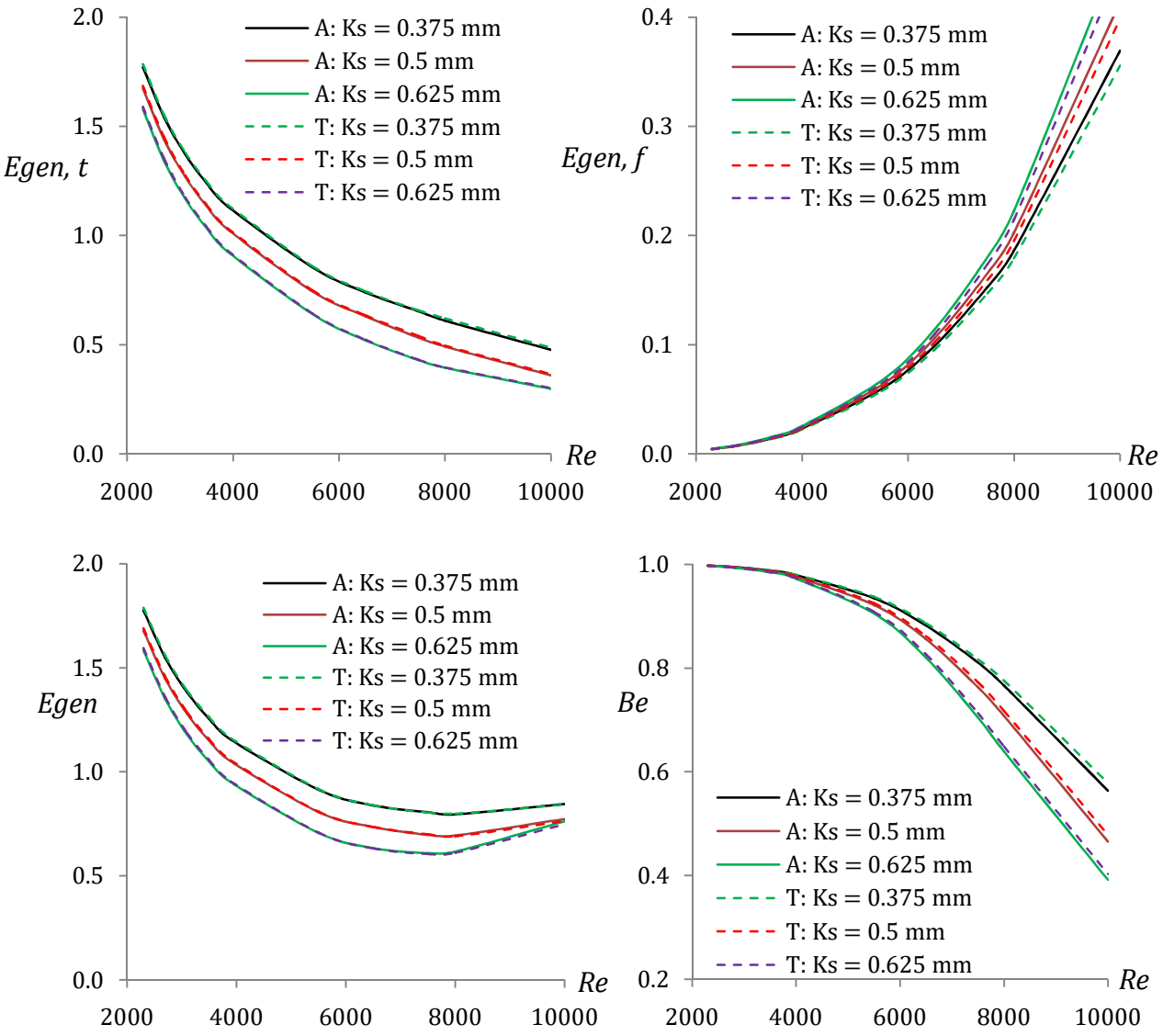

Figure 5.13: Variations of thermal, frictional and total entropy generations as well as Bejan number with different Reynolds numbers for different roughness heights, K_s

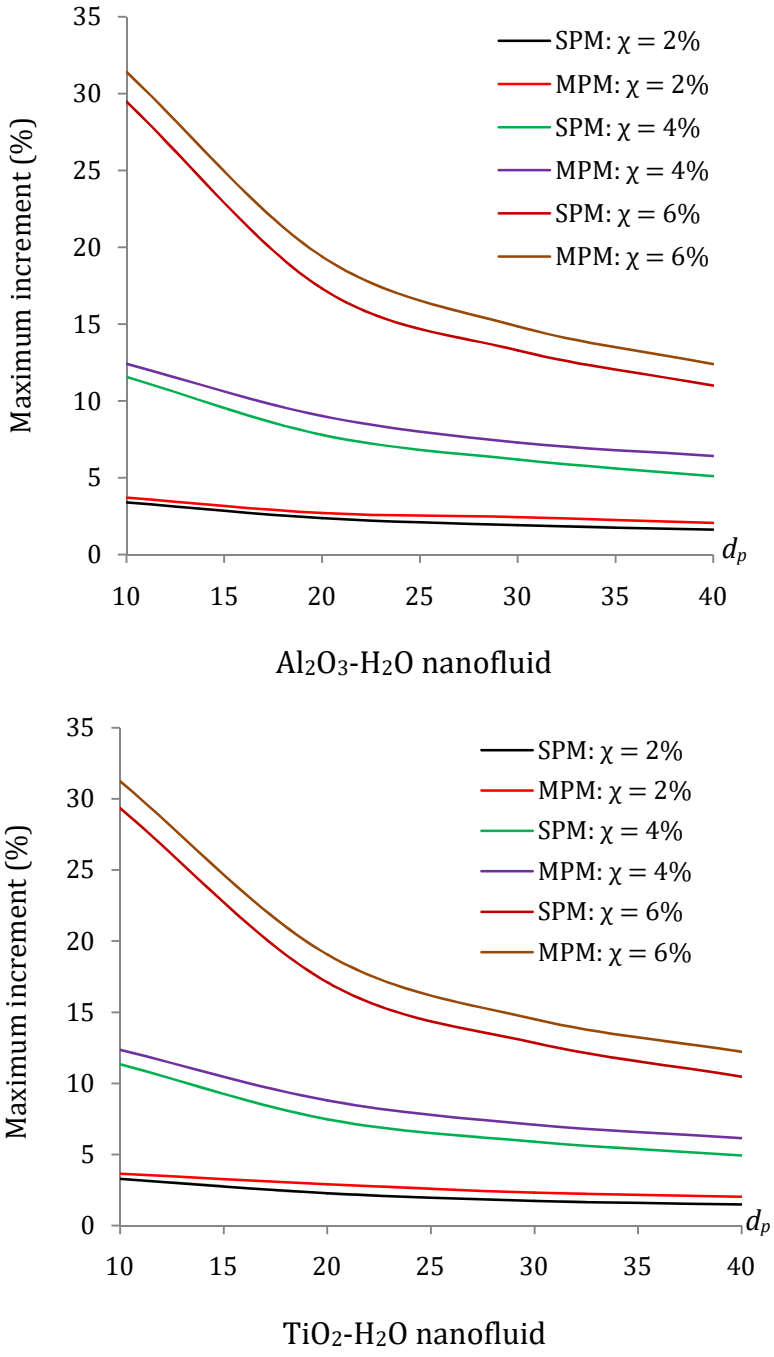

Figure 5.14: Variations of maximum heat transfer enhancement (%) with different nanoparticles diameters for Al_2O_3-water and TiO_2-water nanofluids

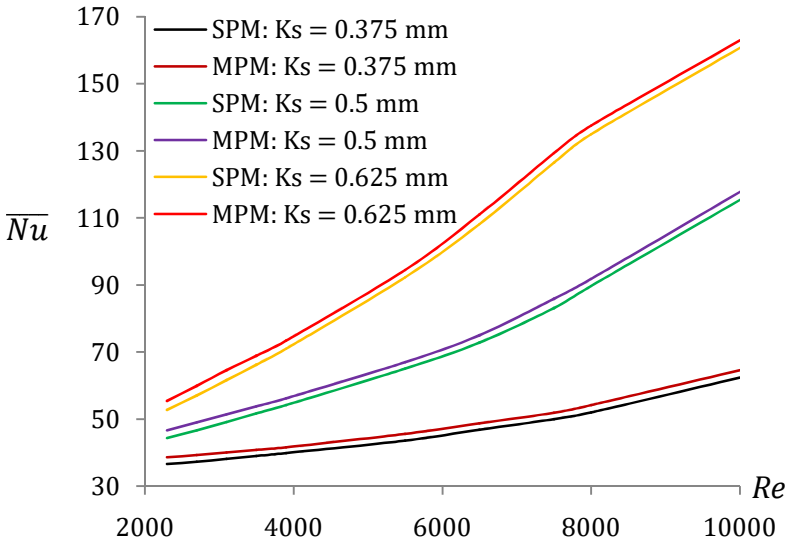

Al_2O_3-H_2O nanofluid

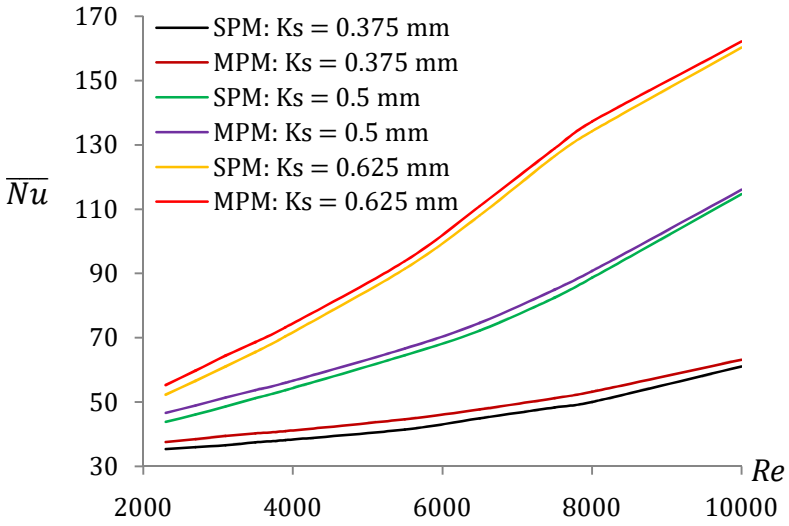

TiO_2-H_2O nanofluid

Figure 5.15: Variations of maximum heat transfer enhancement (%) with different roughness heights using SPM and MPM

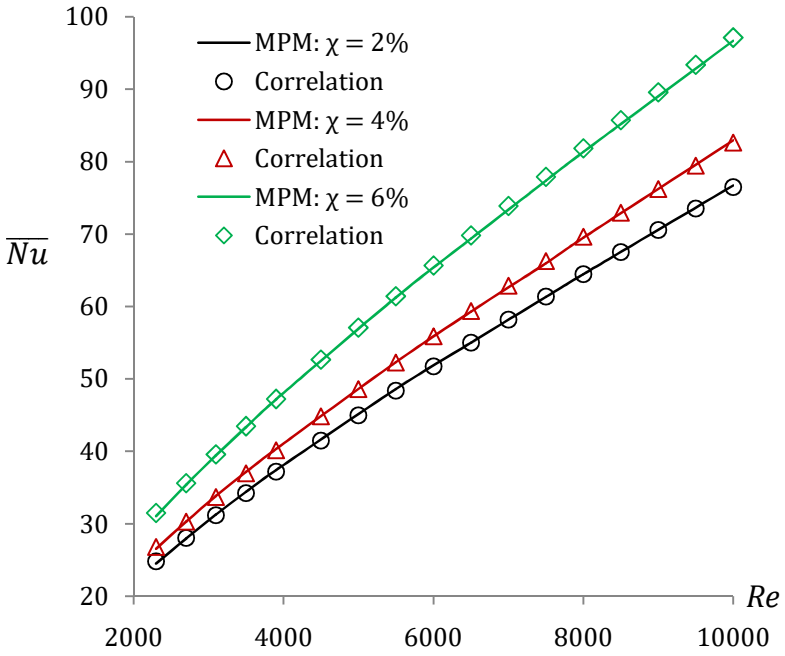

Al_2O_3-water nanofluid

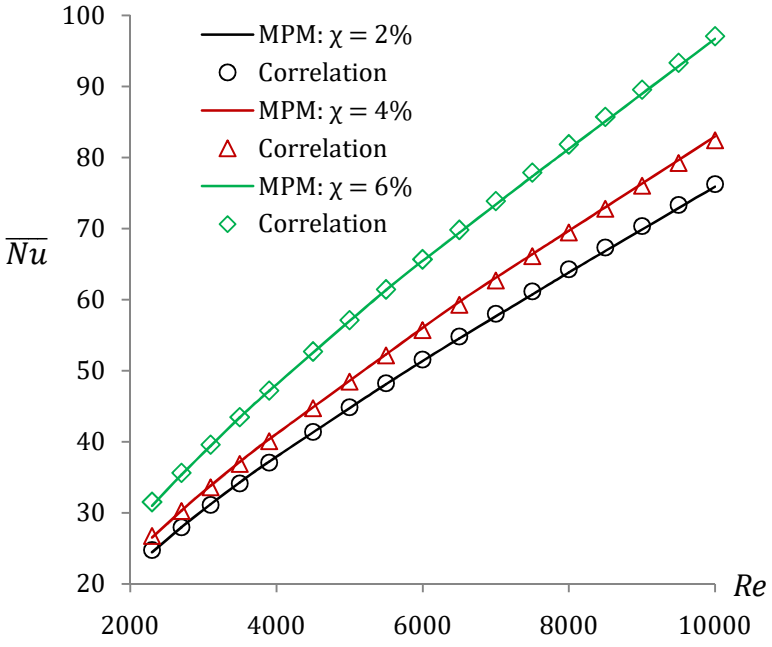

TiO_2-water nanofluid

Figure 5.16: Comparisons between the proposed new correlations and present results of Al_2O_3-water and TiO_2-water nanofluids for $d_p = 10\ nm$

Chapter 6

Turbulent Nanofluids Flow, Part 1: Performance of a Single Phase Model

6.1 Introduction

Almost all of the flows are turbulent in practical situation, and many of these experience extremely high Reynolds numbers *e.g.* flows in aircraft wings, cars, ships, submarines, turbine blades and large pipe. It is important to understand the phenomena of high Reynolds number turbulence in order to develop models for energy efficient applications. Therefore, the present investigation that has a particular focus on the thermal energy application has been carried out to explore the effects of Brownian motion and various sizes of nanoparticles of TiO_2-water and Al_2O_3-water nanofluids under the turbulent flow condition for $Re = 10 \times 10^3$ to 100×10^3. Prandtl number, Pr, ranges from 7.04 to 20.29, the nanoparticles concentration of 4% and 6% and diameter of the nanoparticles of $10, 20, 30$ and $40\ nm$ are considered in this investigation. To the best of our knowledge, no investigation has been carried out to understand the effect of Brownian motion and size of different nanoparticles of Al_2O_3 and TiO_2-water nanofluids considering the above parameters. Hence, the aim of our study is to examine how they affect the convective heat transfer of Al_2O_3 and TiO_2-water nanofluids using a single phase model.

In the present work, single phase approach and two-dimensional axi-symmetric model are considered to describe the turbulent flow and heat transfer behaviour of nanofluids in a horizontal circular pipe under uniform heat flux boundary condition. Computational geometry consists of a pipe with length L of $1.0\ m$ and a circular section with diameter, D_h, of $0.019\ m$ as shown in Fig. 4.1 of Chapter 4. The flow and thermal fields are supposed to be axisymmetric with respect to the horizontal plane parallel to the x-axis.

6.2 Boundary Conditions

The set of governing partial differential equations which are given in §3.1.1 of Chapter 3 are non-linear and coupled. Hence, the solution of the system of nonlinear partial differential equations depends on suitable boundary conditions and so, the following boundary conditions are used.

At the pipe inlet, uniform velocity $v_{x,in}$ as well as uniform temperature $T_{in} = 293\ K$, turbulent intensity $I = 0.16\ Re^{-1/8}$ and hydraulic diameter, $D_h = 0.019\ m$ have been stated. All the thermal properties calculation is taken at T_{in} which is also considered as a reference temperature.

At the pipe outlet, a static gauge pressure, $p_{gauge} = 0$ is specified and the solver has extrapolated the other flow and scalar quantities such as temperature and turbulent quantities from the interior domain. Note that the length of the pipe considered is sufficiently large for the flow and temperature fields in order to develop fully by the outlet section. On the pipe wall, a no-slip boundary condition is introduced and uniform heat flux ($q'' = 50 \times 10^3\ W/m^2$) boundary condition is implemented.

Enhanced wall treatment is a near-wall modelling method that combines a two-layer model with enhanced wall functions. If the near-wall mesh is fine enough to be able to resolve the laminar sublayer, then the enhanced wall treatment will be identical to the traditional two-layer model. However, the restriction that the near-wall meshes must be sufficiently fine everywhere which might impose to large computational requirement. So, ideally one would like to have a near-wall formulation that can be used with coarse meshes as well as fine meshes. In addition, excessive error should neither be incurred for intermediate meshes that are too fine for the near-wall cell centroid to lie in the fully turbulent region, nor too coarse to properly resolve the sublayer (Fluent [68]). That is why; enhanced wall treatment is used in the present analysis.

6.3 Grid Sensitivity Analysis

In order to justify the correctness as well as the stability of the numerical findings, extensive computations are performed to determine the total number of grid points that generate a suitable arrangement result which will be appropriate to determine the turbulent flow and thermal field in the pipe. The grid sensitivity study is carried

out by varying the total number of grid distributions in both the radial (Nr) and axial (Nx) directions too. For a particular test case of the base fluid water of Prandtl number, $Pr = 7.04$ and Reynolds number, $Re = 100 \times 10^3$, various combinations of grid have been analysed to justify that the numerical results are grid independent.

Figure 6.1 shows the variations of radial velocity, temperature and turbulent kinetic energy profiles at the fully developed location ($x = 0.9\,m$) near the outlet. It can be seen that the grids 500×100, 500×150 and 1000×100 generate most reasonable results as the differences found among the results are insignificant. Therefore, the selected grid for the present calculations consisted of 500 and 100 nodes respectively along the axial and radial directions to save the computational time and to avoid any inconsistencies in the numerical results. In addition, to capture the large variations of flow field behaviour near the inlet and pipe wall, uniform grid in the axial direction and non-uniform grid in the radial direction are considered.

6.4 Choice of Turbulent Models

In the present numerical investigation, Realizable $\kappa - \epsilon$ turbulent model is used because it differs from the Standard $\kappa - \epsilon$ model in two important ways. Firstly, the Realizable $\kappa - \epsilon$ model has included a new formulation for the turbulent viscosity and secondly, a new transport equation for the dissipation rate is drawn from an exact equation for the transport of the mean-square vorticity fluctuation (Fluent [68]). To justify the use of Realizable $\kappa - \epsilon$ turbulent model in the present analysis, following investigation is initially carried out.

Three different turbulent models such as Realizable $\kappa - \epsilon$ turbulent model, Standard $\kappa - \epsilon$ turbulent model and RNG $\kappa - \epsilon$ turbulent model have used to see the variation of fully developed turbulent kinetic energy profile for $Re = 21800$ and $Pr = 7.04$ as shown in Fig. 6.2. The details of these turbulent models are given in §3.2.3, §3.2.4 and §3.2.5 of Chapter 3. The profiles of turbulent kinetic energy (Fig. 6.3) are compared with the experimental results of Schildknecht *et al.* [98] as well as of different $\kappa - \epsilon$ models suggested by Launder and Sharma [99], Chien [100] and Fan *et al.* [101]. And, the Realizable $\kappa - \epsilon$ turbulent model is obviously found to perform better than the other two $\kappa - \epsilon$ turbulent models.

6.5 Validation

6.5.1 Water

At first, the radial velocity and turbulent kinetic energy profile for $Re = 21800$ and $Pr = 7.04$ taken at the fully developed section near the outlet are validated in order to validate the accurateness of the present numerical findings against the experimental result of Schildknecht *et al.* [98] as well as with different $\kappa - \epsilon$ models suggested by Launder and Sharma [99], Chien [100], Fan *et al.* [101], Jones and Launder [102, 103], Lai and So [104] and Myong and Kasagi [105]. These researchers have used the following model to determine the turbulent kinematic viscosity with the model constants summarised in Table 6.1.

$$\nu_T = C_\mu f_\mu \frac{\kappa^2}{\epsilon} \tag{6.1}$$

where f_μ is a damping function.

Table 6.1: Model constants

Researchers	C_μ	C_1	C_2	σ_κ	σ_ϵ
Launder and Sharma [99]	0.09	1.44	1.92	1.0	1.3
Chien [100]	0.09	1.35	1.8	1.0	1.3
Fan *et al.* [101]	0.09	1.40	1.8	1.0	1.3
Jones and Launder [102, 103]	0.09	1.45	2.0	1.0	1.3
Lai and So [104]	0.09	1.35	1.8	1.0	1.3
Myong and Kasagi [105]	0.09	1.40	1.8	1.4	1.3

In Fig. 6.3, radial velocity and turbulent kinetic energy are non-dimensionalised by the fiction velocity, u_τ and then are presented. From Fig. 6.3(a), it can be perceive that the non-dimensional velocity profile shows good agreement with the models proposed by Launder and Sharma [99], Chien [100] and Fan *et al.* [101]. It is also found that the present result differs from the models proposed by Jones and Launder [102, 103] and Lai and So [104] as well as the experimental result of Schildknecht *et al.* [98]. In fact, a significant variation is observed between all the models as well as the present result with the experimental result. The reason behind this fact may be the over estimation of the maximum mean velocity obtained from the experimental results., Jones and Launder [102, 103] show the poorest prediction of the non-dimensional velocity profile among all the results.

Further, the highest value of turbulent kinetic energy are found at some radial location near the wall and, this radial location does not differ extensively among the experimental and numerical results shown in Fig. 6.3(b). It is seen that most of the models proposed by the different researchers have predicted relatively good value of the magnitude of highest turbulent kinetic energy compared with the experimental result. But the findings of Jones and Launder [102, 103], Launder and Sharma [99] and also the present result show an under prediction of the maximum peak intensity. It can be due to the different models for the turbulent viscosity as well as different model constants and damping functions used by the researchers.

Additional validation is done against the existing correlations for different $Re = 10 \times 10^3$ to 100×10^3 and $Pr = 7.04$. The numerical results of Darcy friction factor have been compared with the correlations suggested by Blasius [93] and Petukhov [106] in order to perform the validation. And also, average Nusselt number have been compared with the correlations proposed by Petukhov [106], Notter and Rouse [107] and Gnielinski [94] which are given as follows:

Petukhov [106] equation:

$$\overline{Nu} = \frac{\frac{f}{8} Re\, Pr}{1.07 + 12.7 \left(\frac{f}{8}\right)^{0.5} \left(Pr^{\frac{2}{3}} - 1\right)}, \qquad \begin{pmatrix} 0.5 \le Pr \le 2000 \\ 10^4 \le Re \le 5 \times 10^6 \end{pmatrix} \tag{6.2}$$

$$f = (0.79 \ln Re - 1.64)^{-2}, \qquad 10^4 \le Re \le 5 \times 10^6$$

Notter-Rouse [107] equation:

Notter and Rouse [107] introduced the following correlation for the calculation of average Nusselt number for pure fluid:

$$\overline{Nu} = 5.0 + 0.015\, Re^{0.856} Pr^{0.347} \tag{6.3}$$

Also, Gnielinski [94] equation is given in §4.4 of Chapter 4.

Figure 6.4(a) shows compatible results of the Darcy friction factor between the present numerical result on the base fluid and other correlations of Blasius [93] and Petukhov [106]. The maximum deviation of 8.91% for $Re = 20 \times 10^3$ and the minimum deviation of 3.47% for $Re = 100 \times 10^3$ are observed. It can be due to the higher pressure drop obtained for different Re in the present simulation.

Also, the result of average Nusselt number is presented in Fig. 6.4(b). The maximum deviation between our numerical result and the correlations of Petukhov [106], Notter and Rouse [107] and Gnielinski [94] are 3.84%, 1.63% and 5.40% respectively which shows very good agreement with these correlations. It is important to note that all these available correlations are not highly accurate. The accuracy of each correlation is fully dependent on different types of application. So, more or less variation will occur depending on the problems. Hence, it is to say that the percentage error of 3.84%, 1.63% and 5.40% are very close to the acceptable region. Other factors like near wall mesh distribution and temperature gradient at the wall are also responsible for such variations.

6.5.2 Al_2O_3-water Nanofluid

From the comparisons presented in the section above, we can conclude that our computational model is producing the correct outcomes. Hence, Al_2O_3-H_2O nanofluid flow in a circular pipe with different $\chi = 0.01, 0.04$ and 0.06 is now investigated for different $Re = 10 \times 10^3$ to 100×10^3 with $7.04 < Pr < 10.0$. Also, The heat flux $\dot{q}_s = 50 \times 10^3 \mathrm{W/m^2}$ applied on the pipe wall has been considered [60, 61] in the present analysis.

Initially, a comparison has been made between the computed Nusselt number and the Pak and Cho [58] correlation. Also, the following correlations are used to model the dynamic viscosity as well as thermal conductivity of Al_2O_3-H_2O nanofluid for the purpose of validation.

$$\mu_{nf} = \mu_f(123\,\chi^2 + 7.3\,\chi + 1) \tag{6.4}$$

$$\lambda_{nf} = \lambda_f(4.97\,\chi^2 + 2.72\,\chi + 1) \tag{6.5}$$

Eq. (6.4) has been derived from the experimental data of Masuda *et al.* [81], Lee *et al.* [108] and Wang *et al.* [109] by using least square curve fitting. Other classical models like Einstein [110] or Brinkman [111] can be used but it is found that these models underestimate the dynamic viscosity of nanofluid as shown by Maiga *et al.* [112]. Besides, Eq. (6.5) has been developed using the model suggested by Hamilton and Crosser [113] with the assumption that nanoparticles are spherical in size and shape, and then it has been implemented in this work because of its simplicity.

In Fig. 6.5, a comparison between the present result and that of Pak and Cho [58] is shown graphically for the Al_2O_3-H_2O nanofluid and $\chi = 0.01, 0.04$ and 0.06. It is found

that the present numerical findings are in very good agreement with the results of Pak and Cho [58]. which is completely empirical referred by Buongiorno [78]. Although Eqs. (6.4 and 6.5) have been developed using Al_2O_3-H_2O and TiO_2-H_2O nanofluids, this correlation should be applicable in general (Das *et al.* [114]). It is also crucial that Eqs. (6.4 and 6.5) have been valid for relatively low nanoparticles concentration *e.g.* when $\chi \leq 3.2\%$ though we have considered the trend and applied this for higher χ by assuming a higher standard deviation of error.

6.6 Results and Discussion

The numerical investigations are performed using Al_2O_3-H_2O and TiO_2-H_2O nanofluids with the subsequent choices of parameters: the Reynolds number from $Re = 10 \times 10^3$ to 100×10^3, Prandtl number from 7.04 to 20.29, the nanoparticles concentration of 4% and 6% and diameter of the nanoparticles of $10, 20, 30$ and $40\ nm$. The outcomes are presented hereafter focusing on the impacts of nanoparticles concentration: Brownian motion and size diameter of Al_2O_3 and TiO_2 nanoparticles; and different Reynolds number on the hydrodynamic and thermal performance of the nanofluids under the turbulent flow condition.

6.6.1 Behaviour of Mean Velocity

Figure 6.6 displays variations of the flow field with various nanoparticles concentrations and diameters of Al_2O_3-water nanofluid for Re =100×10^3. In general, the kinematic viscosity of nanofluid is always higher than the base fluid and hence, the velocity of nanofluid always possesses higher value than the base fluid. Also, It is observed that the maximum peak value of the velocity is the highest for $dp = 10\ nm$ and $\chi = 6\%$. Similar behaviour is also observed for all the other Reynolds numbers as well as for the TiO_2-water nanofluid. It is to note that the maximum velocity varies significantly at the centreline position for different nanoparticles diameter and concentration.

6.6.2 Behaviour of Turbulent Kinetic Energy

Figure 6.7 shows the variation of turbulent kinetic energy profile with different nanoparticles concentrations and diameters of Al_2O_3-water nanofluid for $Re = 100 \times 10^3$. When the nanoparticles concentration is changed from 4% to 6% of the Al_2O_3-water nanofluid, the radial location where the highest value of the turbulent

kinetic energy comes out does not differ considerably for the different nanoparticles diameter. Here, the maximum peak value of κ is observed for $d_p = 10\,nm$. Similar behaviour is observed for all the other Reynolds numbers as well as for the TiO_2-water nanofluid. It should be noted that as the nanoparticles diameter increases from 10 to 40 nm, the maximum peak value of κ which shows the lower turbulent intensity near the surface rapidly decreases. Therefore, the turbulent strength in the flow tends to reduce. This result further indicates that the smaller diameter of nanoparticles plays more important role in turbulence generation than that of the large diameter of nanoparticles. The reason behind this fact can be the Brownian motion as well as the shape and size of the nanoparticles.

6.6.3 Behaviour of Mean Temperature

Figure 6.8(a) shows the variations of fully developed temperature profile with different nanoparticles diameters at x = 0.99 m for the Reynolds number of 10^5, $\chi = 6\%$ and Al_2O_3-water nanofluid. The mean temperature is observed to raise along with the increase of nanoparticles diameters.

Also, Fig. 6.8(b) shows the variations of wall temperature with different nanoparticles diameters for Reynolds number of 10^5, $\chi = 6\%$ and Al_2O_3-water nanofluid. It is found that the wall temperature increases with the increase of nanoparticles diameters. Thus the inclusion of small nanoparticles has a positive effect on the wall temperature. Similar behaviour is observed with the increase of nanoparticles concentrations too. But the maximum temperature difference is achieved at the outlet for higher nanoparticles concentrations and small size of nanoparticles. Such effect plays a major role to increase the thermal performance of any thermal system used in the practical application.

6.6.4 Average Shear Stress Coefficient Ratio Analysis

Figure 6.9 shows the effect of various nanoparticles concentrations, different nanoparticles diameters of water based Al_2O_3 and TiO_2 nanofluids on the average shear stress coefficient ratio. From this investigation, it is found that the average shear stress coefficient ratio increases with the increase of nanoparticles concentration and decrease of nanoparticles diameter of 40 to 10 nm and such enhancement is independent to the Reynolds number. In particular, for $Re = 20 \times$

10^3 and Al_2O_3-water nanofluid, $\overline{\tau_\tau}$ has a value of 2.0, 2.19, 2.54 and 3.58 for $\chi = 4\%$ and $dp = 40, 30, 20$ and $10\ nm$ respectively. Also, $\overline{\tau_\tau}$ has a value of 3.42, 4.13, 5.79 and 14.63 for $dp = 40, 30, 20$ and $10\ nm$ respectively for higher nanoparticles concentration *e.g.* $\chi = 6\%$. Similar performances are also noticed for the TiO_2-water nanofluid. It is possible to conclude from the above findings that the increase of the average shear stress coefficient ratio concerning the nanoparticles concentration as well as the nanoparticles diameter emerge to be noticeably more significant for both the water based Al_2O_3 and the TiO_2 nanofluids. Such enhancement of the average shear stress coefficient ratio is to be due to the adverse effects of increase frictional force or pressure.

6.6.5 Average Heat Transfer Analysis

Figure 6.10 shows the effect of various concentrations, different nanoparticles diameter of water based Al_2O_3 and TiO_2 nanofluids along with the results of the base fluid on the average Nusselt number. The average heat transfer rate is found to increase with the increase of Reynolds number and nanoparticles concentration when the nanoparticles diameter changes from 40 to $10\ nm$. Also, the average heat transfer rate of the water based Al_2O_3 and TiO_2 nanofluids is found to be higher than that of the base fluid at any Reynolds number. The explanation for such augmentation in the average heat transfer rate is to be associated to different aspects such as enhancement of thermal conductivity, nanoparticles size and shapes, Brownian motion of particles, decrease in boundary layer thickness and delay in boundary layer growth.

The average Nusselt number is very responsive to the types and diameter of the nanoparticles, as it is observed. From our investigation, it is examined that the effect of average heat transfer rate increases with the decrease of nanoparticles diameter. For example, the maximum enhancement is approximately 21.75% and 59.83% respectively for the Al_2O_3–water nanofluid and $\chi = 4\%$ and 6% with $d_p = 10\ nm$. While for $d_p = 20\ nm$, the maximum enhancement is approximately 14.34% and 33.60% respectively. However for the TiO_2–water nanofluid and $\chi = 4\%$ and 6% with $d_p = 10\ nm$, the maximum enhancement is approximately 21.28% and 58.79% respectively. Whereas for $d_p = 20\ nm$, the maximum enhancement is approximately 13.80% and 32.79% respectively. Similar trend is observed as

nanoparticles diameter increases from 20 to 30 nm or 30 to 40 nm. In order to achieve a higher heat transfer rate, 10 nm diameter particles is found to be the best for both water based Al_2O_3 and TiO_2 nanofluids. It is also observed that Al_2O_3–H_2O nanofluid gives us slightly better heat transfer rate than the TiO_2–H_2O nanofluid for all the Reynolds numbers, nanoparticles concentration as well as nanoparticles diameter. Values of the maximum increment in the average heat transfer rate of water based Al_2O_3 and TiO_2 nanofluids are shown in Table 6.2 for different nanoparticles diameter and concentration.

Table 6.2: Maximum increment (%) of average Nusselt number for different nanofluids

	Al_2O_3-water		TiO_2-water	
$d_p(nm)$	$\chi = 4\%$	$\chi = 6\%$	$\chi = 4\%$	$\chi = 6\%$
10	21.75	59.83	21.28	58.79
20	14.34	33.60	13.83	32.79
30	11.27	25.14	10.75	24.30
40	09.45	20.63	08.90	19.78

It is observed in Fig. 6.10 that smaller diameter and Brownian motion of nanoparticles assist to increase the viscosity for same nanoparticles concentration and hence, these have an impact on the Nusselt number enhancement. This is quite reasonable because smaller nanoparticles with higher velocity move faster than the large particles, and thus reduce the possibility of collision with each other. Also, smaller diameter of nanoparticles will be more in number in comparison with large diameter of nanoparticles and will make a contact with the neighbouring fluid over a greater surface area. It will help in increasing the viscosity and thermal conductivity which result in the enhancement of heat transfer of water based Al_2O_3 and TiO_2 nanofluids.

Also, as the nanoparticles diameters increase from 10 to 40 *nm*, thermal conductivity of nanofluid decreases. And, nanoparticles concentration increase with the decrease of density and thermal conductivity. Therefore, the increase in thermal conductivity with the decrease of nanoparticles diameter from 40 to 10 *nm* and the decrease in density with the increase of nanoparticles concentration indicates the higher mean velocity along the pipe and it may help to increase the heat transfer rate. Moreover,

the mean velocity of large nanoparticles is lower than the small nanoparticles. This indicates, diffusion plays an important role to transfer heat from one place to another. But for small nanoparticles, fluid mean velocity increases and thus forced convection comes into effect and helps to transfer more heat. This means that the lower is the wall temperature, the higher is the heat transfer rate.

6.6.6 Thermal Performance Factor Analysis

Figure 6.11 shows the thermal performance factor which is investigated with the use of various concentrations of 4% and 6%, different nanoparticles diameter of 10 to 40 nm and water based Al_2O_3 and TiO_2 nanofluids. The value of the thermal performance factor is observed to remain greater than 1 (one) for all the possible cases considered and it is very close to the ratio of the average heat transfer rate of nanofluid and water. Also, the ratio of Darcy friction factor of nanofluid and water is observed to be approximately close to 1. Hence, it is possible to draw a conclusion that the heat transfer enhancement is possible with little or without penalty in the pumping power. This can lead to less energy cost and more effectiveness in practical applications.

It is also evident in the above investigation that the thermal performance factor increases as the nanoparticles concentration increases and the higher values of ξ is achieved for smaller nanoparticles diameter for water based Al_2O_3 and TiO_2 nanofluids. Another reason is, when the nanoparticles diameter decreases from 40 to 10 nm, the dynamic viscosity and thermal conductivity of nanofluid increases with the increase of nanoparticles concentration. Hence, the higher viscosity directs to a diminution of boundary layer thickness resulting in the enhancement of heat transfer whereas the higher thermal conductivity directs to an intensification of thermal performance factor.

6.6.7 Correlations

In the present analysis, the following correlations is proposed for the calculation of average Nusselt number using the non-linear regression analysis and the average Nusselt number is the function of Reynolds number, Prandtl number and nanoparticles diameter. It is to note, these correlations are valid when the Brownian motion of nanoparticles is taken into account. Also, the values of maximum standard

deviation of error are 7.35% and 7.25% for Al_2O_3 and TiO_2 nanofluids respectively. Further, comparisons between the numerical results of average Nusselt number computed by the proposed correlations are presented in Fig. 6.12. This Figure shows a good agreement between the numerical results and the proposed correlations.

Al_2O_3-H_2O nanofluid : $\overline{Nu} = 0.01272\, Re^{0.85861} Pr^{0.42986} \left(\frac{d_f}{d_p}\right)^{-0.00017} - 0.5$ (6.6)

TiO_2-H_2O nanofluid : $\overline{Nu} = 0.01259\, Re^{0.85926} Pr^{0.43020} \left(\frac{d_f}{d_p}\right)^{-0.00068}$ (6.7)

where

$10 \times 10^3 \leq Re \leq 100 \times 10^3, 8.45 \leq Pr \leq 20.29, 10 \leq d_p(nm) \leq 40, 2 \leq \chi(\%) \leq 6.$

6.7 Conclusion

In this research work, numerical investigations have been carried out to understand the flow and heat transfer behaviour of different nanofluids in a horizontal circular pipe under turbulent flow condition. The effects of Reynolds number and Prandtl number, two different nanofluids, nanoparticles concentration, size and Brownian motion of nanoparticles on flow and heat transfer are investigated. According to our findings, following conclusion can be made and summarised as follows:

(a) It is found that for $\chi = 4\%$ and 6%, water based Al_2O_3 and TiO_2 nanofluids with 10 to 40 nm nanoparticles diameter with Brownian motion of nanoparticles, average Nusselt number and shear stress ratio are significantly higher compared to water.

(b) The water based Al_2O_3 and TiO_2 nanofluids with 10 nm and $\chi = 6\%$ show higher thermal performance factor for any Reynolds number and nanoparticles diameter.
(c) The friction factor of nanofluids is observed to have no significant effect compared to water and hence induces no extra penalty in pump power.

Furthermore, we have found that the Al_2O_3-H_2O nanofluid shows slightly better heat transfer performance than that of the TiO_2-H_2O nanofluid. And, it is seen that the heat transfer performance is more influenced by the Brownian motion and diameter of nanoparticles than the thermal conductivity of nanofluid.

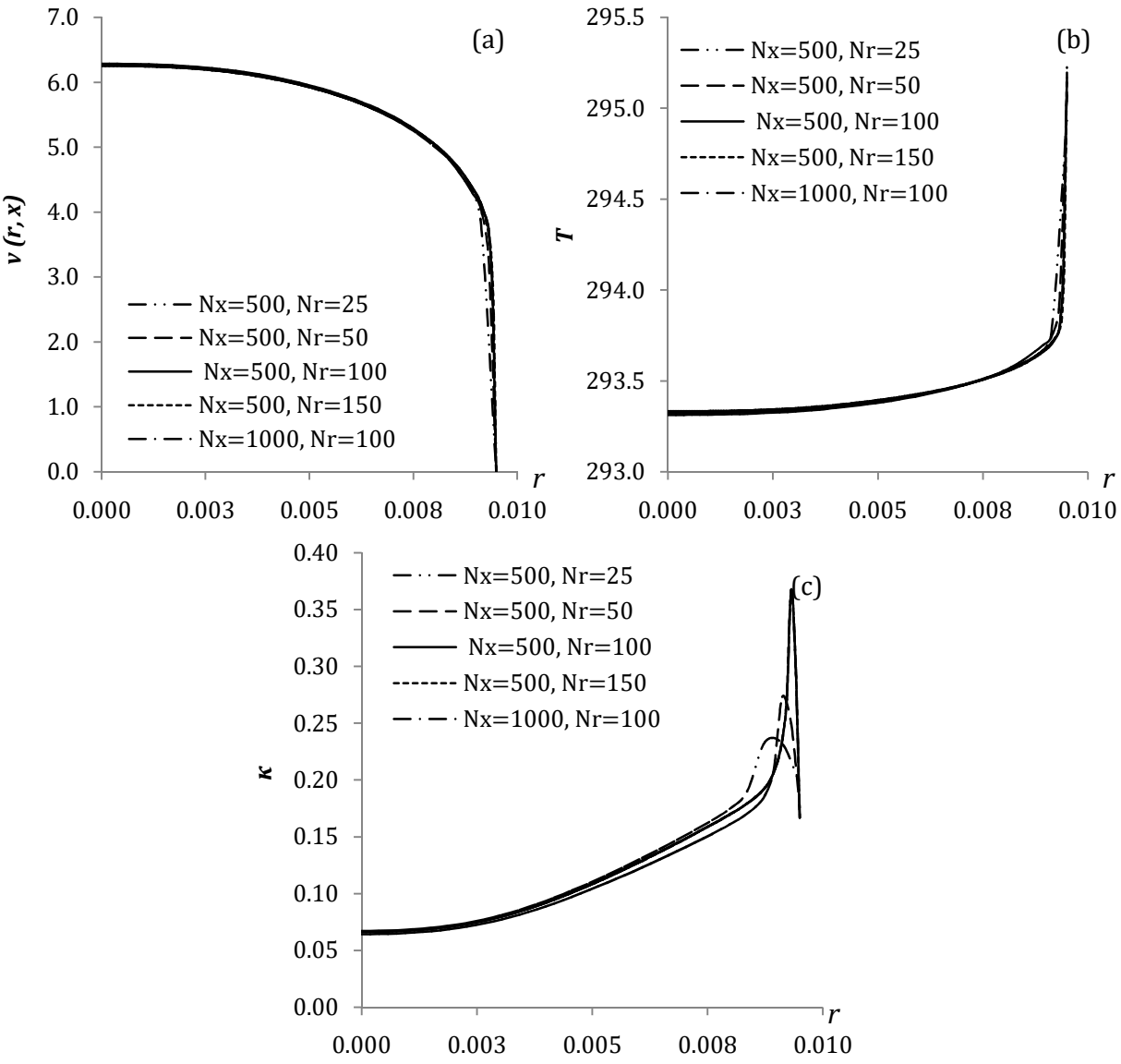

Figure 6.1: Variations of radial (a) velocity, (b) temperature and (c) turbulent kinetic energy at the fully developed location near the outlet

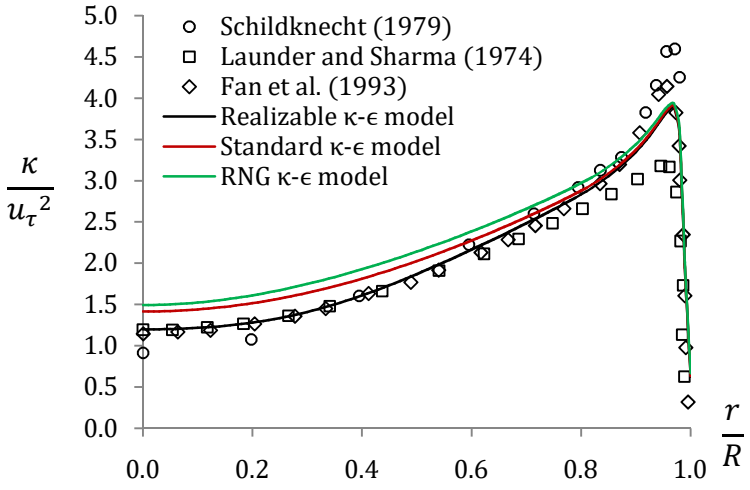

Figure 6.2: Variations of radial turbulent kinetic energy at the fully developed location near the outlet using different $\kappa - \epsilon$ models for $Re = 21800$

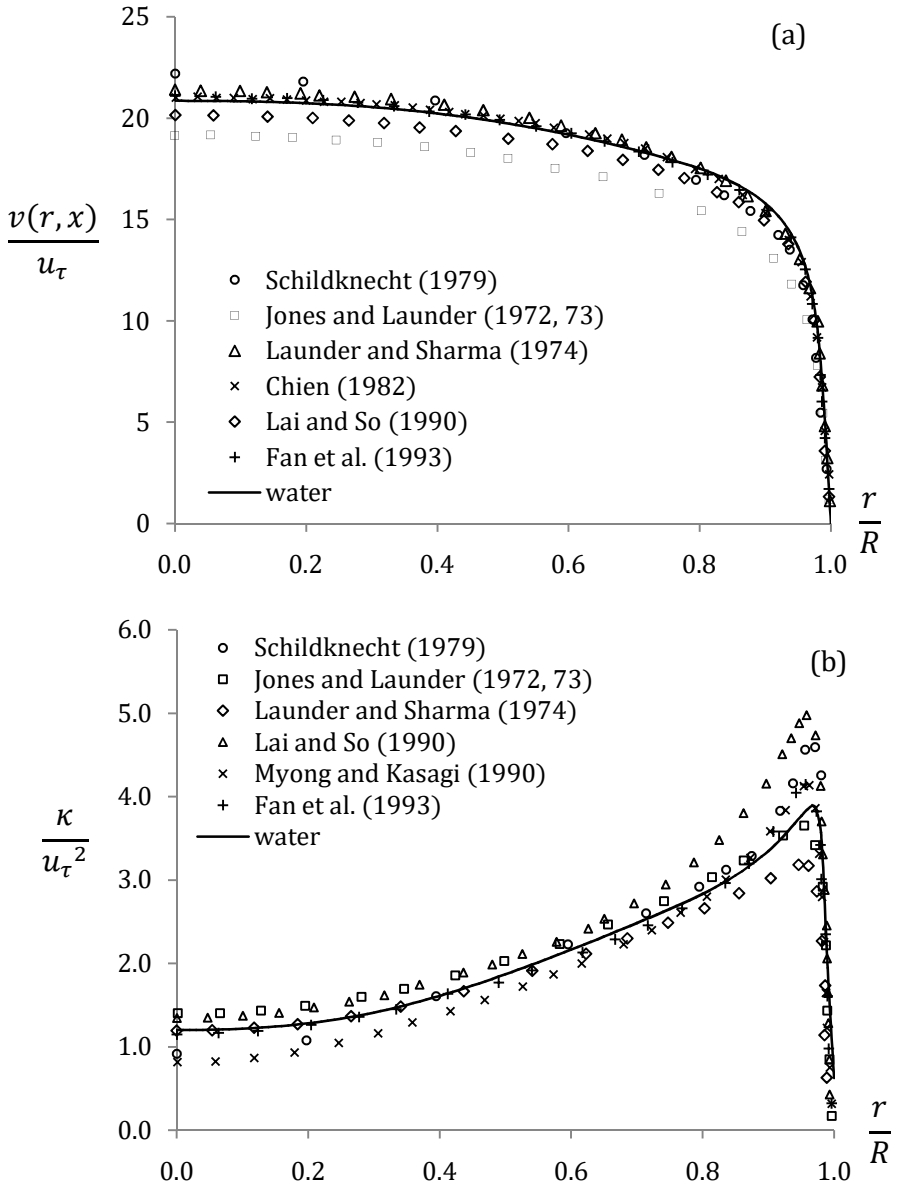

Figure 6.3: Variations of radial (a) velocity and (b) turbulent kinetic energy at the fully developed location near the outlet for $Re = 21800$ and $Pr = 7.04$

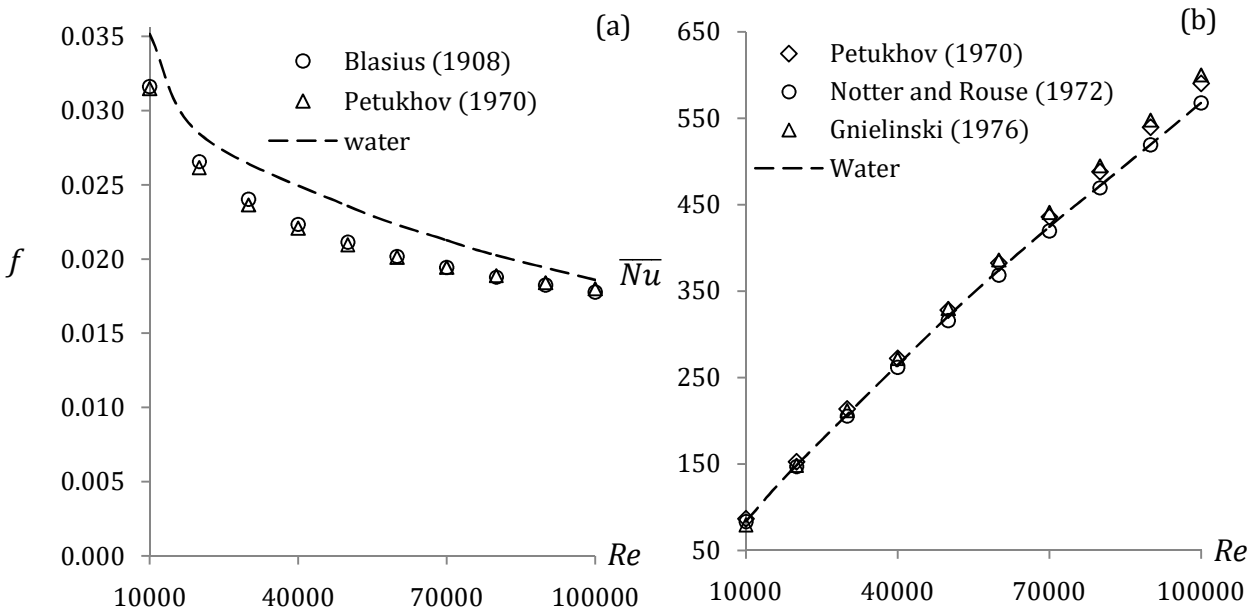

Figure 6.4: Comparisons of the (a) Darcy friction factor, f and (b) average Nusselt number, $\overline{Nu}$ with the different correlations for different Re

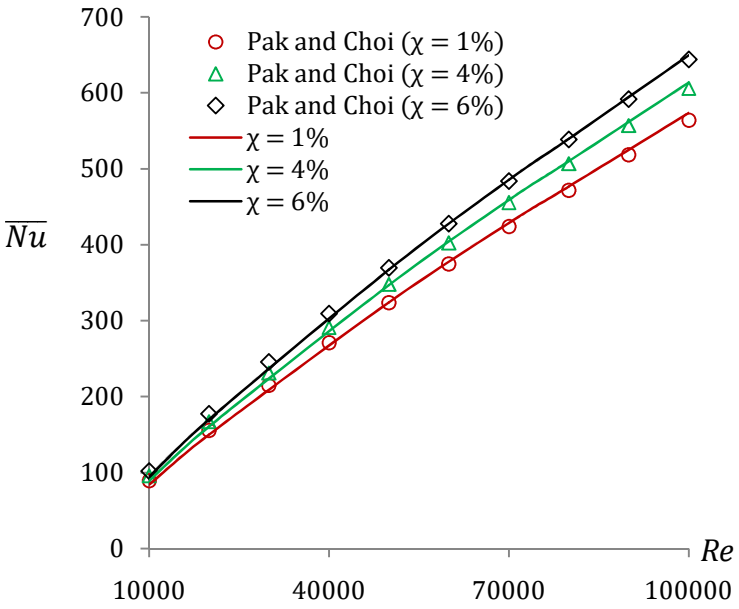

Figure 6.5: Comparisons of the average Nusselt number for Al_2O_3-H_2O nanofluid with the Pak and Cho [58] correlation for different Re

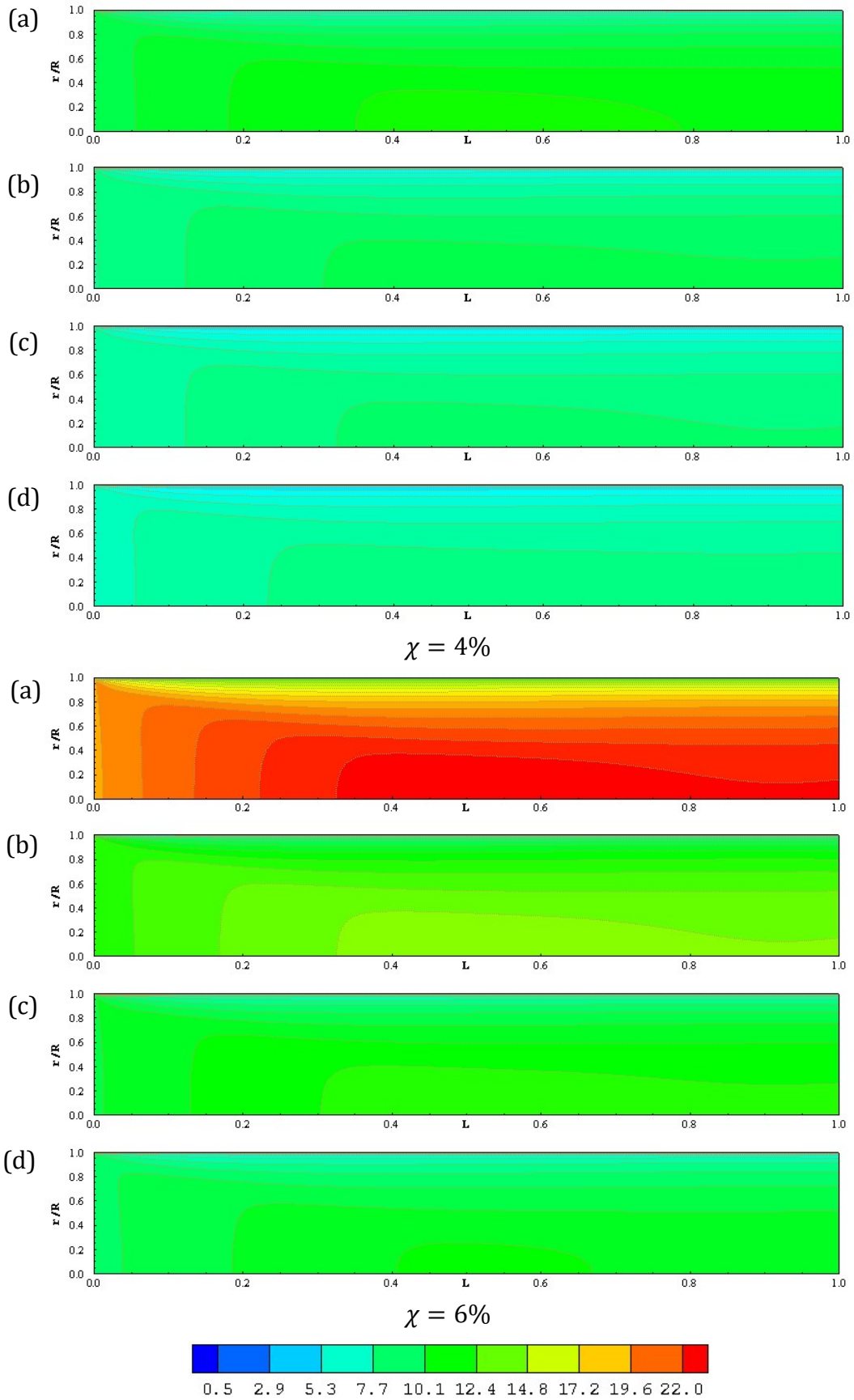

Figure 6.6: Variations of mean velocity along the pipe for Al_2O_3-water nanofluids, nanoparticles concentration of 4% and 6%, $Re = 100 \times 10^3$ and nanoparticles diameter of (a) 10 nm, (b) 20 nm, (c) 30 nm and (d) 40 nm

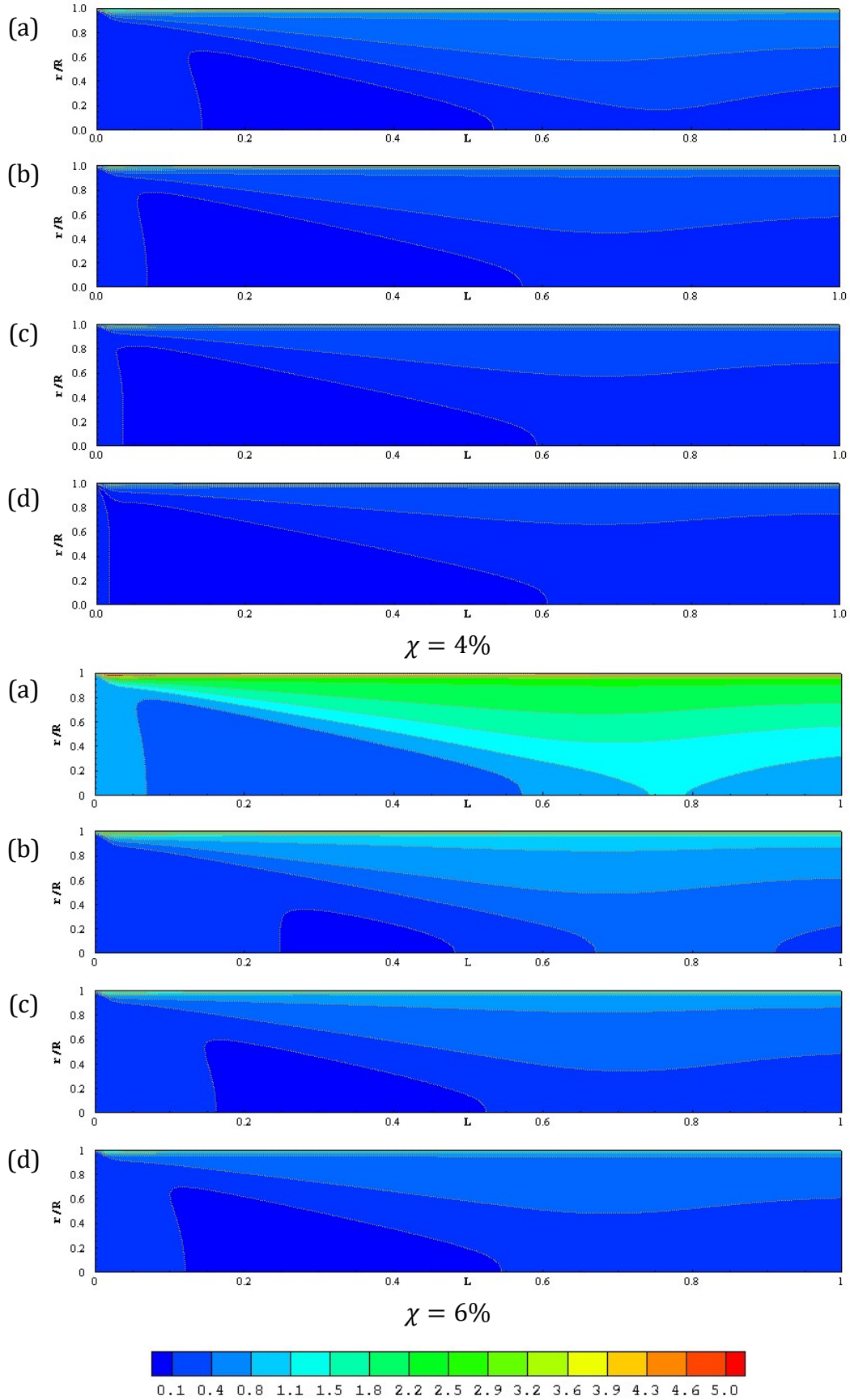

Figure 6.7: Variations of turbulent kinetic energy along the pipe for Al_2O_3-water nanofluids, nanoparticles concentration of 4% and 6%, $Re = 100 \times 10^3$ and nanoparticles diameter of (a) 10 nm, (b) 20 nm, (c) 30 nm and (d) 40 nm

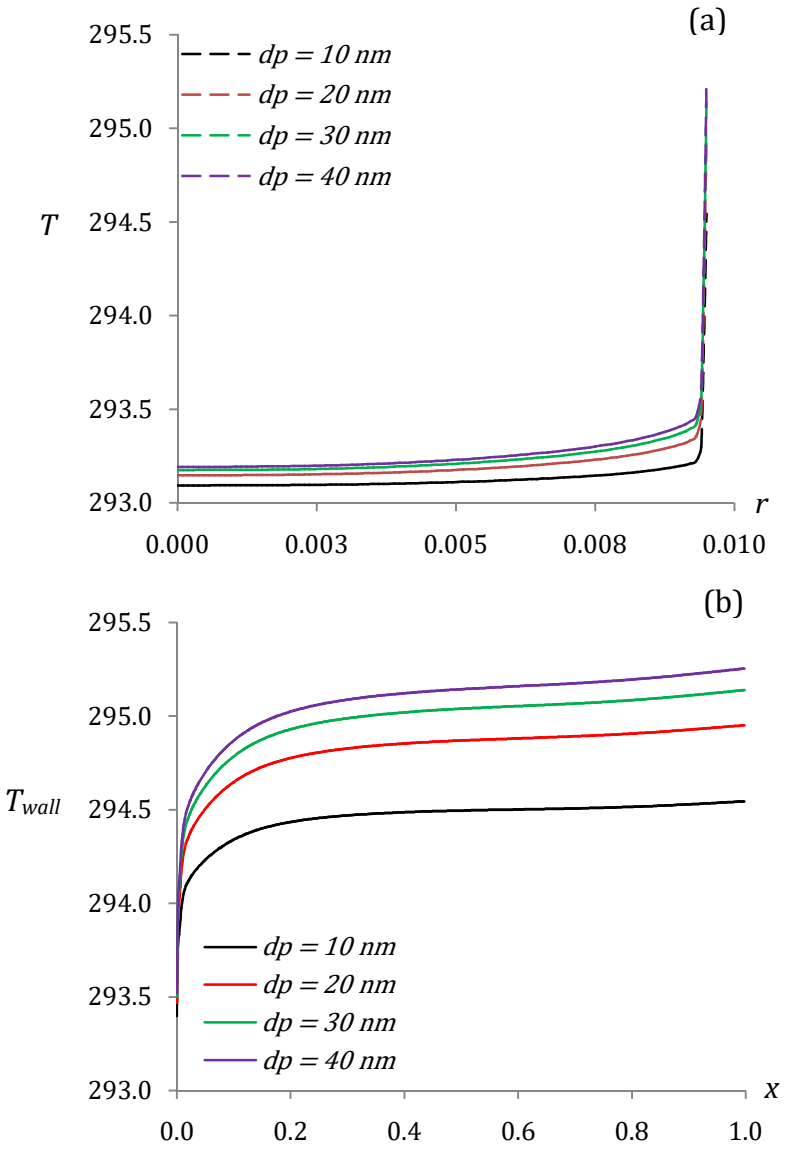

Figure 6.8: Variations of (a) radial velocity profile at $x = 0.99\,m$ and (b) wall temperature along the pipe for Al_2O_3-water nanofluids, nanoparticles concentrations of 6%, $Re = 100 \times 10^3$

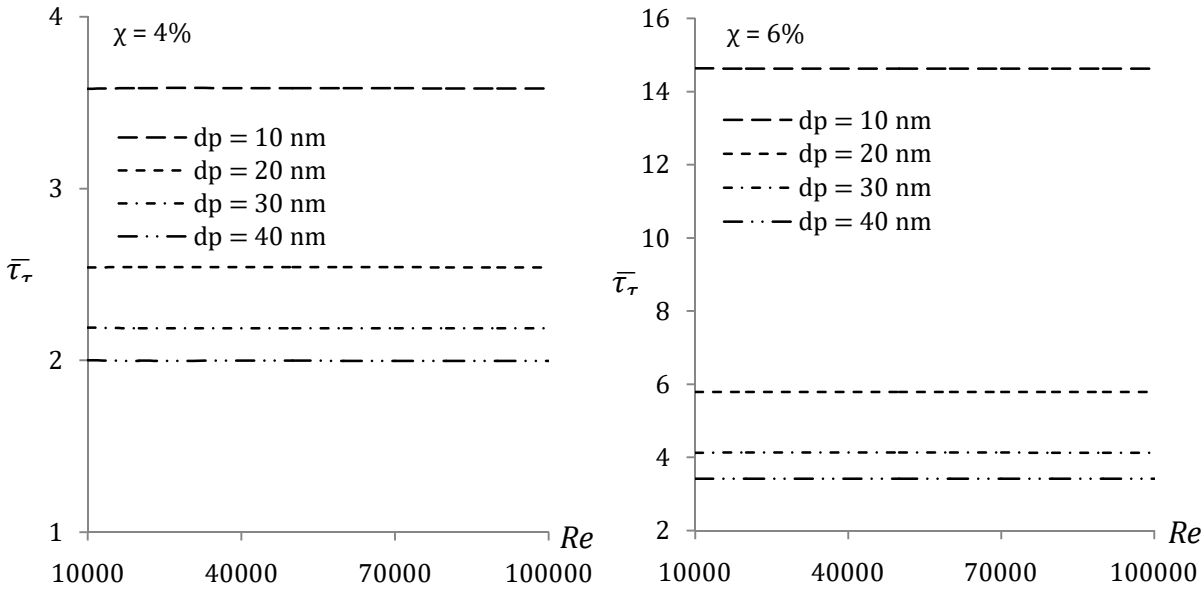

(a) Al_2O_3-H_2O nanofluid

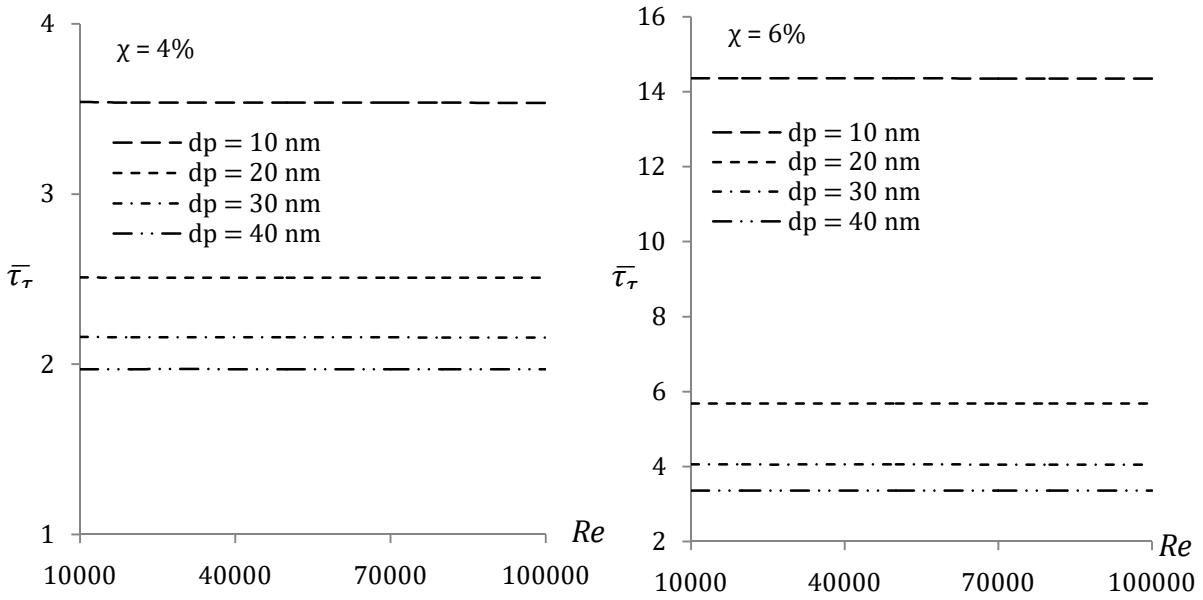

(b) TiO_2-H_2O nanofluid

Figure 6.9: Variations of average shear stress ratio with Reynolds numbers for Al_2O_3-water and TiO_2-water nanofluids, nanoparticles concentration of 4% and 6% and nanoparticles diameter of 10, 20, 30 and 40 nm

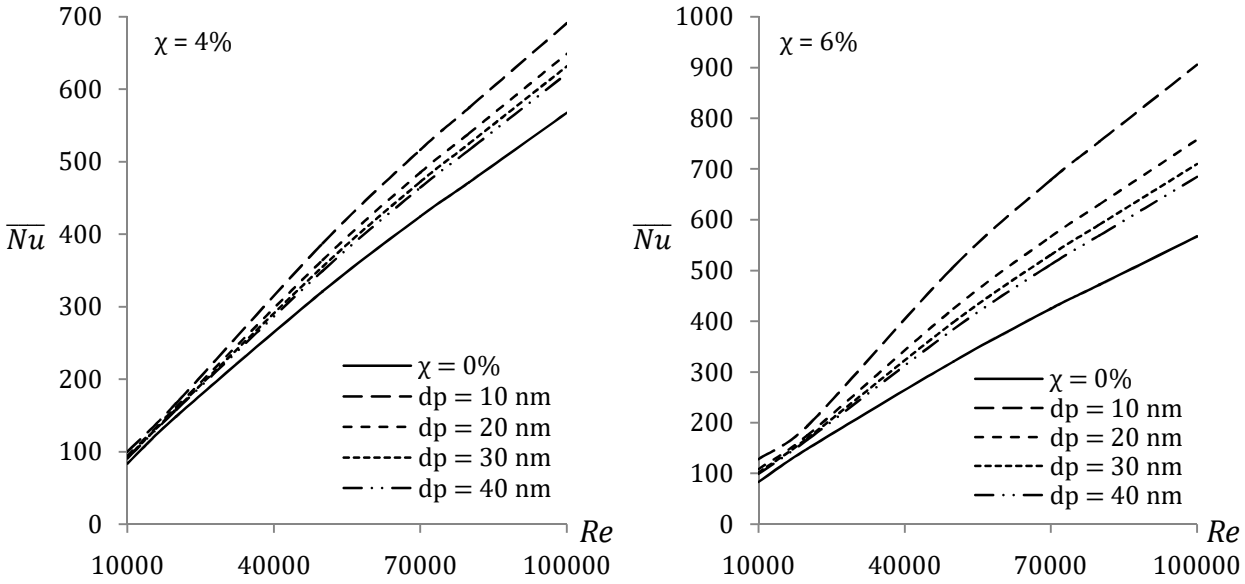

(a) Al_2O_3-H_2O nanofluid

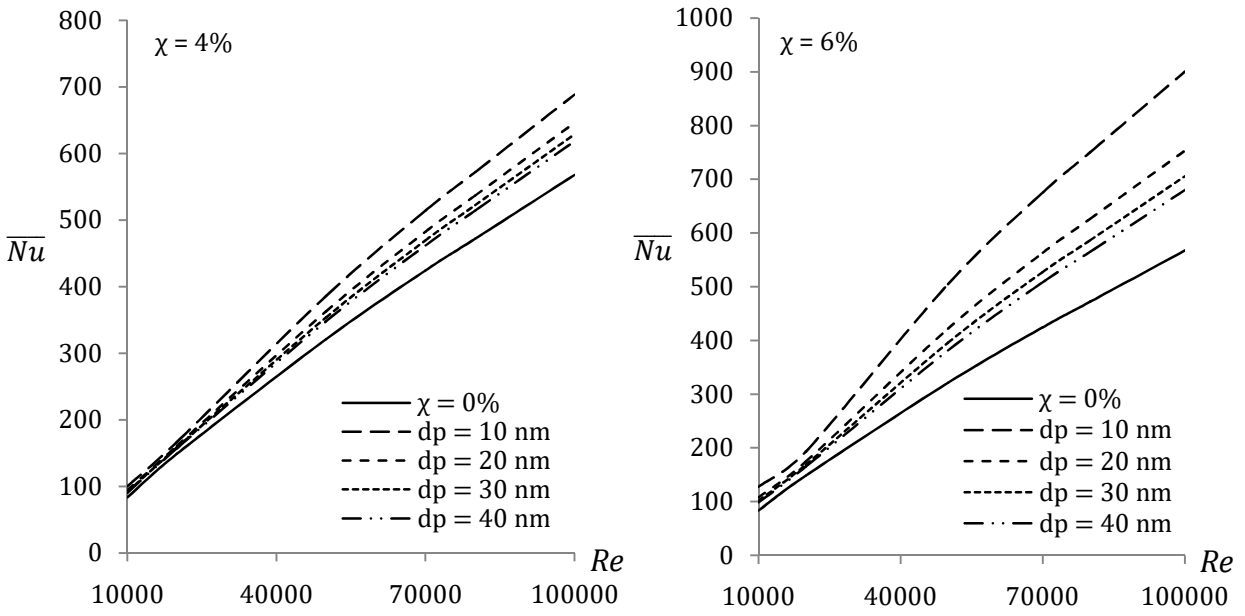

(b) TiO_2-H_2O nanofluid

Figure 6.10: Variations of average Nusselt number with Reynolds numbers for Al_2O_3-water and TiO_2-water nanofluids, nanoparticles concentration of 4% and 6% and nanoparticles diameter of 10, 20, 30 and 40 nm

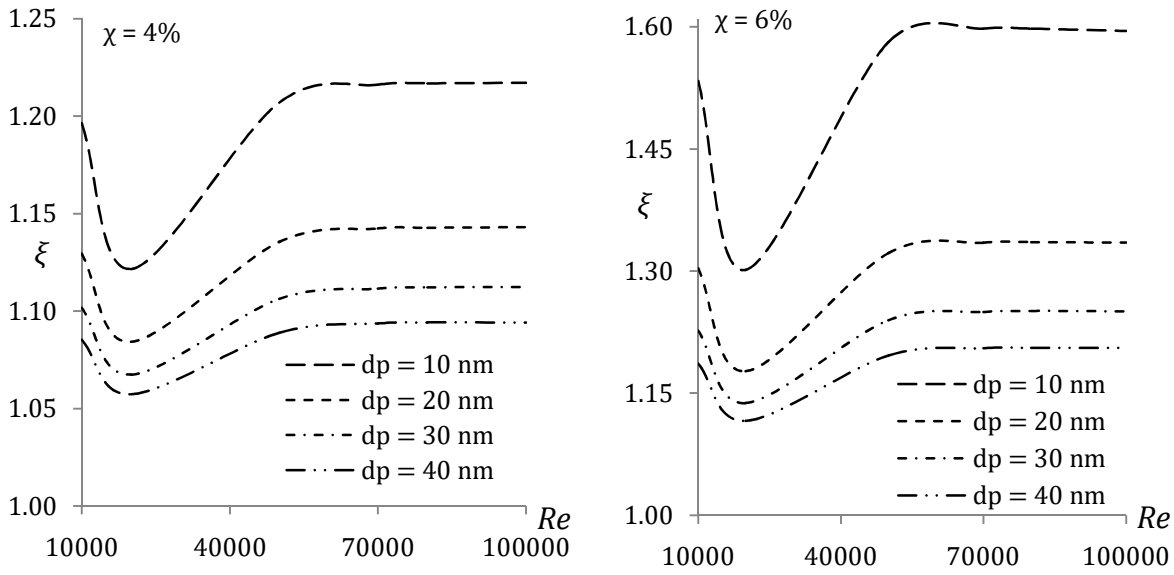

(a) Al_2O_3-H_2O nanofluid

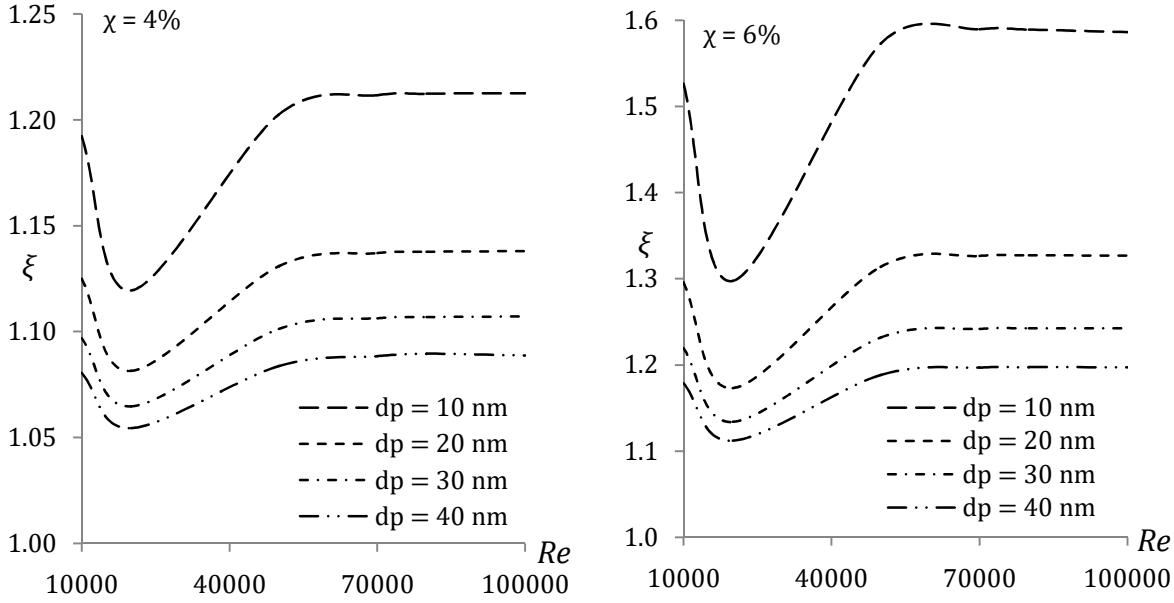

(b) TiO_2-H_2O nanofluid

Figure 6.11: Variations of thermal performance factor with Reynolds numbers for Al_2O_3-water and TiO_2-water nanofluids, nanoparticles concentration of 4% and 6% and nanoparticles diameter of 10, 20, 30 and 40 nm

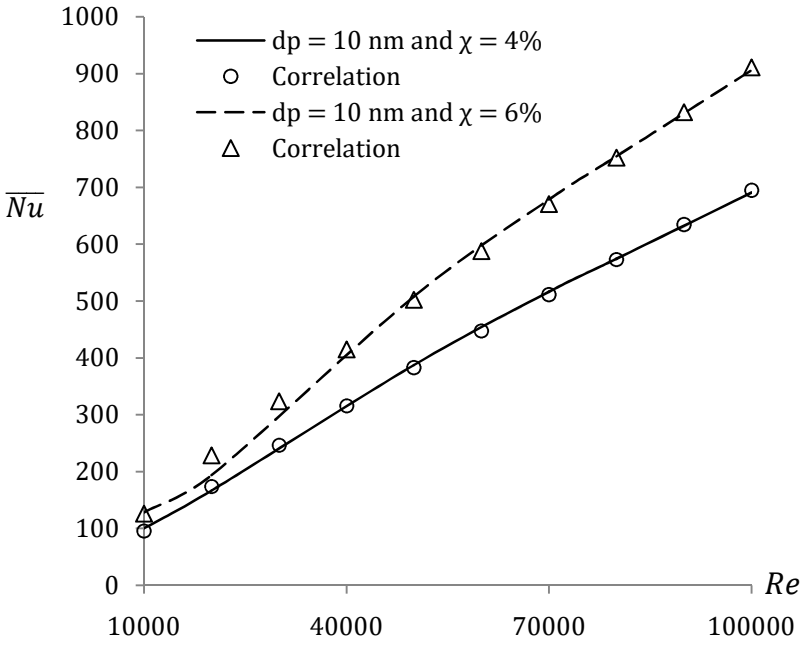

Al_2O_3-H_2O nanofluid

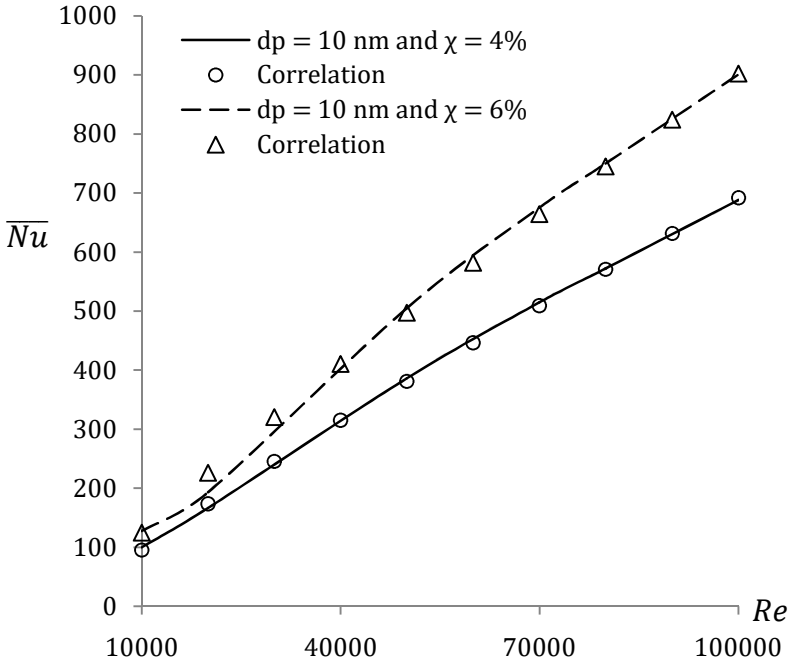

TiO_2-H_2O nanofluid

Figure 6.12: Comparisons of the proposed correlations with the numerical results for Al_2O_3-water and TiO_2-water nanofluids

Chapter 7

Turbulent Nanofluids Flow, Part 2: Performance of a Multi-phase Model

7.1 Introduction

Turbulence is a complex nature and much more difficulty is observed to understand the turbulence behaviour of single phase model. In case of multi-phase flow, the nature of turbulence is more complex and it's still an issue in many engineering applications in order to understand the behaviour of turbulence for all kinds of flows in general. In this chapter, a particular investigation is carried out to understand the behaviour of turbulent nanofluids flow in pipe for multi-phase model which is presented and discussed.

In Chapter 6, we have examined the effect of nanoparticles concentration, diameter and Brownian motion of nanoparticles on the convective heat transfer of turbulent flow of Al_2O_3 and TiO_2-water nanofluids using a single-phase model. The aim of this piece of work is to extend the numerical model to investigate the effects of multi-phase turbulent flow of Al_2O_3 and TiO_2-water nanofluids. Particular attention is paid to the entropy generation of these two nanofluids and importantly, how the performance factor of nanofluids is varied if the numerical simulation is switched from the single to multi-phase model.

Eulerian-Eulerian mixture model is used to model the multi-phase flows with the assumption that the phases between fluid and solid particles move at a same velocity with a very strong coupling between them. Also, the phases are supposed to be interpenetrating. That means each phase has its own velocity vector field and within any control volume there is a volume concentration of each phase. It should also be noted that the mixture model solves the continuity, momentum and energy equation for the mixture and the volume fraction equation for the secondary phases. An axi-

symmetric model is considered which is shown in Fig. 4.1 of Chapter 4 to describe the characteristics of nanofluids flowing through a straight pipe under a constant heat flux boundary condition and within a turbulent flow regime.

7.2 Boundary Conditions

To solve the set of non-linear governing equations presented in §3.1.2 of Chapter 3, appropriate boundary conditions are necessary. And these are considered in the numerical simulations which are already described in §6.2 of Chapter 6. However, the boundary conditions used in the single-phase model are specified for both the fluid and solid phases as well as for the mixture in the multi-phase mixture model. Also, the nanoparticles concentration is used for the solid phase.

Details of the boundary conditions are given below:

At the pipe inlet, we have specified the velocity for the fluid and nanoparticles phases where we assume that fluid particles and nanoparticles are flowing with the same local velocity. We have set the nanoparticles concentration ($\chi = 1$ to 6%) for the nanoparticles phase too. And for the mixture, turbulent intensity $I = 0.16\, Re^{-1/8}$ and hydraulic diameter, $D_h = 0.019\, m$ as well as the inlet temperature ($T = 293\ K$) are specified.

At the pipe outlet, there are no conditions applied for the fluid and nanoparticles phases. Also, turbulent intensity $I = 0.16\, Re^{-1/8}$ and hydraulic diameter, $D_h = 0.019\, m$ are specified for the mixture.

At the pipe wall, no conditions are applied for the fluid and nanoparticles phases too. Again, a no-slip boundary condition as well as a uniform heat flux ($q^{''} = 50000\ W/m^2$) on the pipe wall are specified for the mixture.

7.3 Grid Sensitivity Analysis

In order to ensure the accuracy as well as the consistency of the numerical results, extensive computations have been performed to identify the number of grid points that produce a suitable arrangement result which will be applicable to determine the turbulent flow and thermal field inside the pipe with the multi-phase model. The grid

sensitivity study similar to the one presented in §6.4 of Chapter 6 has been performed and the grid combination 500×100 was acceptable.

7.4 Validation

Accuracy of the numerical results for water against existing correlations for the different Reynolds number, $Re = 10 \times 10^3$ to 100×10^3, has been tested in §6.6.1 of Chapter 6. a comparison between the present result and that of Pak and Cho [58] is shown graphically for the Al_2O_3-H_2O nanofluid and $\chi = 0.01, 0.04$ and 0.06 In Fig. 7.1. It is shown that the present numerical results are in very good agreement with the correlation of Pak and Cho [58]. The details of the Pak and Cho [58] correlation, the dynamic viscosity and the thermal conductivity model used in this analysis are also given in §6.6.2 of Chapter 6.

From the comparing point of view, validation result of single phase model as shown in Fig. 6.5 of Chapter 6 is in good agreement with the result of Pak and Cho [58]. However, the present result shown in Fig. 7.1 very marginally deviates with the experimental data of Pak and Cho [58]. It does not mean that the result of single phase model is better than that of multi-phase model. This suggests, the interaction between the fluid and nanoparticles has some impact on the average Nusselt number which makes sense.

7.5 Results and Discussion

Numerical simulations are carried out using Al_2O_3-H_2O and TiO_2-H_2O nanofluids, with the following range of governing parameters: Reynolds number from $Re = 10 \times 10^3$ to 100×10^3, Prandtl number from 7.04 to 20.29, nanoparticles concentration of 4% and 6%, and diameter of nanoparticles of $10, 20, 30$ and $40\ nm$. The results and discussion presented hereafter focus on the effects of nanoparticles concentration, mean diameter and Brownian motion of different nanoparticles and different Reynolds number on the flow and heat transfer performance as well as on the entropy generation of the nanofluids in the turbulent flow regime. Also, comparison between the results of heat transfer enhancement of both single phase and multi-phase models are presented.

7.5.1 Nanoparticles Concentrations

Figure 7.2 shows the radial variation of the nanoparticles concentration at the outlet for the Al_2O_3-water nanofluid with $Re = 100 \times 10^3$ and $dp = 10\,nm$. The nanoparticles concentration is observed to be absolutely uniform and constant. This further indicates, the nanoparticles distribution in the fluid is also uniform. This is valid in a sense that the suspended nanoparticles remain uniform in the fluid – an assumption that is implicitly integrated in the single-phase model. The similar behaviour is also observed for all the Reynolds numbers with different size of nanoparticles using both the Al_2O_3-water and TiO_2-water nanofluids. It is also to be noted that the similar behaviour was found by other researchers (Behzadmehr *et al.* [63], Bianco *et al.* [60]).

7.5.2 Average Shear Stress Coefficient Ratio Analysis

Figure 7.3 shows the effect of various concentrations, different nanoparticles diameters of Al_2O_3-water and TiO_2-water nanofluids on the average shear stress ratio. It is found in the investigation that the average shear stress ratio has increased with an increase in the nanoparticles concentration and decrease in the nanoparticles diameter from 40 to 10 nm and such enhancement is independent to the Reynolds number. For example, when the Reynolds number and nanoparticles concentration for the Al_2O_3-water nanofluid are fixed to be $Re = 20 \times 10^3$ and $\chi = 4\%$, the average shear stresses $(\overline{\tau_\tau})$ has a value of $1.99, 2.19, 2.54$ and 3.58 for $d_p = 40, 30, 20$ and $10\,nm$ respectively. For a higher nanoparticles concentration, e.g. $\chi = 6\%$, $\overline{\tau_\tau}$ increases again and has a value of $3.36, 4.06, 5.69$ and 14.35 for $d_p = 40, 30, 20\ and\ 10\,nm$ respectively. Similar behaviours is also observed for the TiO_2-water nanofluid and therefore, it can generally be concluded that the increase of the average shear stress ratio with respect to the nanoparticles concentration as well as the nanoparticles diameter emerges to be noticeably more significant for both the Al_2O_3-water and TiO_2-water nanofluids. Such enhancement of the average shear stress ratio is to be due to the adverse effects of increase frictional force or pressure in the nanofluids.

Overall, the average shear stress ratios for both the single and multi-phase models are found to be almost identical. Therefore, it suggests that the interaction between the fluid particles and nanoparticles has an insignificant impact on the average shear

stress ratio. Moreover, the Darcy friction factor results of water as well as nanofluids for both the single and multi-phase models are also found to be identical. This thus further confirms that nanofluids could potentially be used in practical applications with no penalty in pumping power.

7.5.3 Average Heat Transfer Performance Analysis

Figure 7.4 shows the results of the effect of various concentrations, nanoparticles diameter of Al_2O_3-water and TiO_2-water nanofluids on the average Nusselt number. A comparison of the findings with those of water is also made. The average Nusselt number is found to increase with the increase of Reynolds number and nanoparticles concentration when the nanoparticles diameter changes from 40 to 10 nm. Also, The average Nusselt number of the nanofluids is seen to be higher than that of water at any given Reynolds number. The explanation for such enhancement in the average Nusselt number is associated with different aspects, such as, enhancement of thermal conductivity, nanoparticles size and shapes, Brownian motion of particles, decrease in boundary layer thickness and delay in boundary layer growth.

However, the average Nusselt number is very sensitive to the nanoparticles diameter. And generally, the heat transfer rate increases as the nanoparticles diameter decreases as already shown in §4.5.1.2 of Chapter 4, §5.3.3 of Chapter 5 and §6.6.5 of Chapter 6. It is due to the fact that as the nanoparticles diameter decreases from 40 to 10 nm, the thickness of thermal boundary layer decreases thus having an impact on the heat transfer enhancement. For example, the maximum enhancement is approximately 23.26% and 62.34% respectively for the Al_2O_3–water nanofluid and $\chi = 4\%$ and 6% with $d_p = 10\,nm$. While for $d_p = 20\,nm$, it is approximately 15.87% and 35.76% respectively. However for the TiO_2–water nanofluid and $\chi = 4\%$ and 6% with $d_p = 10\,nm$, the maximum enhancement is approximately 23.60% and 62.53% respectively. While for $d_p = 20\,nm$, it is approximately 16.31% and 36.12% respectively. Similar trend is observed as the nanoparticles diameter increases from 20 to 30 nm or 30 to 40 nm. The 10 nm nanoparticles diameter is found to be best in order to get a higher heat transfer rate for both the Al_2O_3–water and TiO_2–water nanofluids. This result has a close link to the corresponding flow velocity in the sense that the heat transfer enhancement becomes more significant when the Reynolds number is increased. Further to note, the TiO_2–water nanofluid gives the higher heat transfer enhancement

than Al_2O_3–water irrespective to the change in Reynolds number, nanoparticles concentration and diameter, although its thermal conductivity is lower than that of Al_2O_3–water nanofluid. For a quantitative assessment, values of the minimum and maximum increments in the Nusselt number of different nanofluids are shown in Table 7.1 for different nanoparticles concentration and diameter. Smaller diameter and Brownian motion of nanoparticles assist to increase the viscosity for the same nanoparticles concentration making an impact on the Nusselt number enhancement. This is reasonable because smaller nanoparticles with higher velocity move faster than the large particles and thus, reduce the possibility of collision with each other. Also, smaller diameter of nanoparticles will be more in number compared to large nanoparticles and will therefore make a strong contact with the neighbouring fluid over a greater surface area. Consequently, the process will help to increase the viscosity and thermal conductivity of nanofluids with a result in the heat transfer enhancement.

Table 7.1: Minimum and maximum increments (%) of average Nusselt number for different nanofluids

	Al_2O_3-water				TiO_2-water			
$d_p\ (nm)$	$\chi = 4\%$		$\chi = 6\%$		$\chi = 4\%$		$\chi = 6\%$	
	Min	Max	Min	Max	Min	Max	Min	Max
10	18.58	23.26	58.60	62.34	21.07	23.60	60.25	62.53
20	11.44	15.87	30.83	35.76	14.61	16.31	33.53	36.12
30	07.81	12.53	21.25	27.30	11.09	12.95	25.42	27.72
40	06.43	10.84	16.47	22.65	09.92	11.28	21.31	23.09

7.5.4 Thermal Performance Factor Analysis

Thermal performance factor is reported in Fig. 7.5 for the different values of concentrations and nanoparticles diameters. It is observed that the thermal performance factor remains greater than one for all the possible cases considered and it is very close to the ratio of the average Nusselt number of nanofluid to water. Also, the ratio of the friction factor of nanofluids to the base fluid is approximately close to 1. After comparing the results of the thermal performance factor using both the single and multi-phase models, it is possible to conclude that the thermal performance factor is found slightly higher for the multi-phase model than the single

phase model. This is due to the slightly higher heat transfer rate that is observed for the multi-phase model compared to the single phase model and such details are shown in §7.5.6. However, such enhancement is found to be insignificant. It suggests, one can use either single or multi-phase model under turbulent flow condition in practical applications.

7.5.5 Entropy Generation Analysis

Figure 7.6 shows the variation of the total entropy generation on the Al_2O_3-water and TiO_2-water nanofluids with the Reynolds number, nanoparticles concentrations and diameters. For $\chi = 4\%$ and Al_2O_3-water nanofluid, it is observed that the total entropy generation decreases as the Reynolds number increases with the decrease of the nanoparticles diameter. The reason behind this is the decrease of thermal entropy generation with the decrease of the nanoparticles diameter. It happens because when the nanoparticles diameter decreases from 40 to 10 nm, the heat transfer enhances significantly. The frictional entropy generation is also observed to have insignificant effect on the reduction of the total entropy generation because the maximum value of the frictional entropy generation for all the Reynolds numbers and nanoparticles size diameter is always remained less than 1. Further, the frictional entropy generation monotonically increases with the Reynolds number but decreases with the nanoparticles size diameter. It is due to the increase of the flow velocity. For $\chi = 6\%$ and Al_2O_3-water nanofluid, similar behaviour is observed for the entire nanoparticles size diameter except for $d_p = 10\,nm$. For $\chi = 6\%$, $d_p = 10\,nm$ and $Re > 50 \times 10^3$, the velocity is found to increase significantly and so, the frictional entropy generation becomes stronger. The optimal Reynolds number is found to be $Re = 60 \times 10^3$ for $\chi = 6\%$ and $d_p = 10\,nm$, which minimises the total entropy generation. Again for$Re > 60 \times 10^3$, the frictional entropy generation becomes more and more strong and hence, the total entropy generation starts to rise. It is to be note that the similar performance is also observed for the TiO_2-water nanofluid with the variation of the Reynolds number, nanoparticles concentration and diameter. And, the Al_2O_3-water nanofluid is found to show higher total entropy generation than the TiO_2-water nanofluid. Moreover, from the above findings, it is found that the average Nusselt number is slightly higher predicted for the multi-phase model than the single phase model. But, the variation of the Darcy friction factor results with the nanoparticles diameters as well as concentrations for both the single and multi-phase models are

found to be identical. Since the total entropy generation is simply a function of the average Nusselt number and Darcy friction factor, no significant difference between the results of entropy generation of using the single and multi-phase models is reported. It further suggests that the fluid particles and nanoparticles interaction in the two-phase flow has an insignificant effect on the entropy generation.

Values of the minimum and maximum thermal entropy generation of different nanofluids are shown in Table 7.2 for the different nanoparticles concentration and diameter.

Table 7.2: Minimum and maximum values of the thermal entropy generation

	Al_2O_3-water				TiO_2-water			
$d_p\ (nm)$	$\chi = 4\%$		$\chi = 6\%$		$\chi = 4\%$		$\chi = 6\%$	
	Min	Max	Min	Max	Min	Max	Min	Max
10	8.65	59.01	6.32	42.70	8.67	59.31	6.37	43.13
20	9.51	64.50	7.86	53.42	9.52	64.53	7.90	53.54
30	9.94	67.12	8.55	57.73	9.95	67.22	8.58	58.09
40	10.20	68.78	8.99	60.96	10.21	68.89	9.01	60.98

7.5.6 Heat Transfer Enhancement Analysis

Figure 7.7 shows the variations of the maximum heat transfer enhancement with the nanoparticles diameters obtained by the single- (SPM) and multi-phase (MPM) models for the Al_2O_3-water and TiO_2-water nanofluids. It is found that slightly lower heat transfer rate is achieved using the single-phase model compared to that of the multi-phase model due to the fact that the assumption of fluid phase and nanoparticles phase are in thermal equilibrium and no-slip between them when using the single-phase model.

7.5.7 Performance Evaluation Criterion Analysis

Figure 7.8 shows the variation of the performance evaluation criterion (PEC) values and They are observed to decrease as the Reynolds number increases along with the increase of the nanoparticles diameter. For $\chi = 6\%$ and the Al_2O_3-water nanofluid, similar behaviour is observed for the entire nanoparticles diameter and this is also true for the TiO_2-water nanofluid. However, the TiO_2-water nanofluid shows a slightly

higher performance evaluation criterion than the Al_2O_3-water nanofluid and therefore, it is concluded that the TiO_2-water nanofluid is the most energy efficient coolant for this particular system.

7.5.8 Correlations

From the numerical results and using the non-linear regression analysis, the following correlations are proposed for the calculation of the average Nusselt number with the Reynolds number, Prandtl number and nanoparticles diameter. These correlations are valid when the Brownian motion of nanoparticles is taken into account. Also, the values of maximum standard deviation of error are reported to be 4.81% and 3.77% for the Al_2O_3 and TiO_2 nanofluids respectively. Further, comparisons between the numerical results of the average Nusselt number and computed by the proposed correlations are presented in Fig. 7.9. This figure shows a good agreement between the numerical results and the proposed correlations.

Al_2O_3-H_2O nanofluid : $\overline{Nu} = 0.01260\, Re^{0.85589} Pr^{0.44709} \left(\frac{d_f}{d_p}\right)^{-0.00176}$ (7.1)

TiO_2-H_2O nanofluid : $\overline{Nu} = 0.01518\, Re^{0.84071} Pr^{0.44083} \left(\frac{d_f}{d_p}\right)^{-0.00534}$ (7.2)

where

$10 \times 10^3 \leq Re \leq 100 \times 10^3, 8.45 \leq Pr \leq 20.29, 10 \leq d_p(nm) \leq 40, 4 \leq \chi(\%) \leq 6.$

7.6 Conclusion

Numerical simulations have been carried out on the turbulent mixed convection heat transfer of the Al_2O_3-water and TiO_2-water nanofluids flowing through a horizontal circular pipe using the two-phase mixture model. The effects of Reynolds and Prandtl numbers, two different nanofluids, nanoparticles concentration, Brownian motion and diameter of nanoparticles on the flow and heat transfer have been investigated. According to our findings, the following conclusion are made and summarised as follows:

(a) It is found that for $\chi = 4\%$ and 6%, the Al_2O_3-water and TiO_2-water nanofluids, with the 10 to 40 nm nanoparticles diameters and Brownian motion of nanoparticles, the average Nusselt number is significantly higher than water. It is also seen that the average shear stress ratio becomes superior for small diameter of nanoparticles

compared to the large diameter of nanoparticles with the increase of the nanoparticles concentration.

(b) The Darcy friction factor of nanofluids has no significant effect compared to water and hence induces no extra penalty in the pump power.

(c) The nanofluid with $10\,nm$ and $\chi = 6\%$ shows the higher thermal performance factor for any Reynolds numbers and nanoparticles diameter.

(d) The TiO_2–water nanofluid gives the higher heat transfer enhancement than the Al_2O_3–water nanofluid for all the Reynolds numbers, nanoparticles concentration as well as nanoparticles diameter.

(e) The Al_2O_3-water nanofluid shows the higher total entropy generation than the TiO_2-water nanofluid. But, the TiO_2-water nanofluid shows slightly higher performance evaluation criterion values than the Al_2O_3-water nanofluid.

Furthermore, the TiO_2-H_2O nanofluid shows slightly higher heat transfer performance than that of the Al_2O_3-H_2O nanofluid using the multi-phase model compared with the results of the single-phase model. Since TiO_2 nanoparticles are more environment-friendly and eco-friendly [115] than the Al_2O_3 nanoparticles, hence it is better to use TiO_2-water nanofluid in real life application. Also, it is seen that the heat transfer performance and the total entropy generation are more affected by the nanoparticles diameter and Brownian motion of nanoparticles than the thermal conductivity.

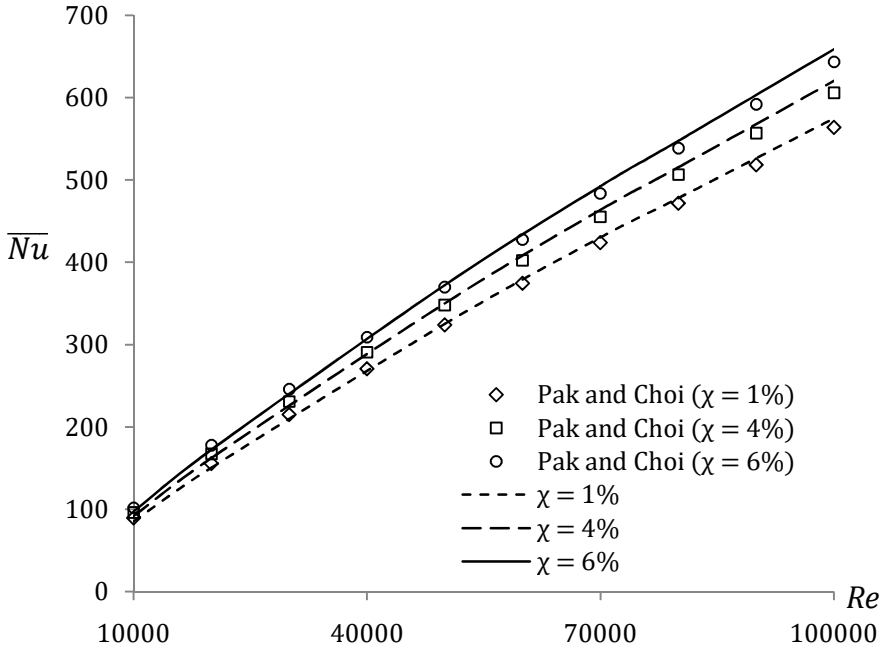

Figure 7.1: Comparisons of the average Nusselt numbers for Al_2O_3-H_2O nanofluid with the Pak and Cho [58] correlation for different Re

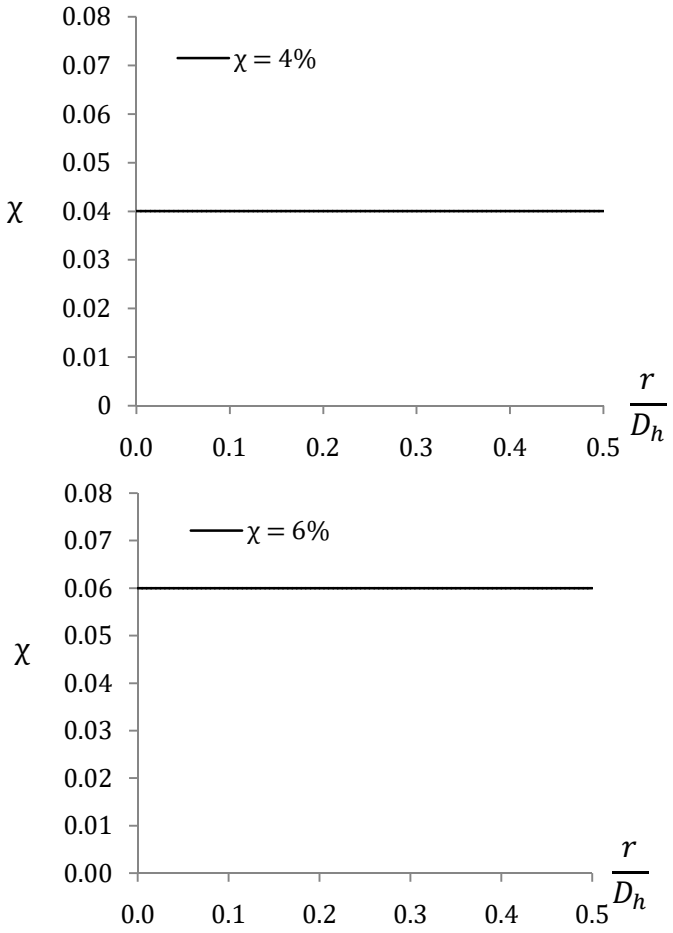

Figure 7.2: Variations of radial nanoparticles concentration at the outlet for Al_2O_3-water nanofluid with $Re = 100 \times 10^3$ and $d_p = 10\ nm$

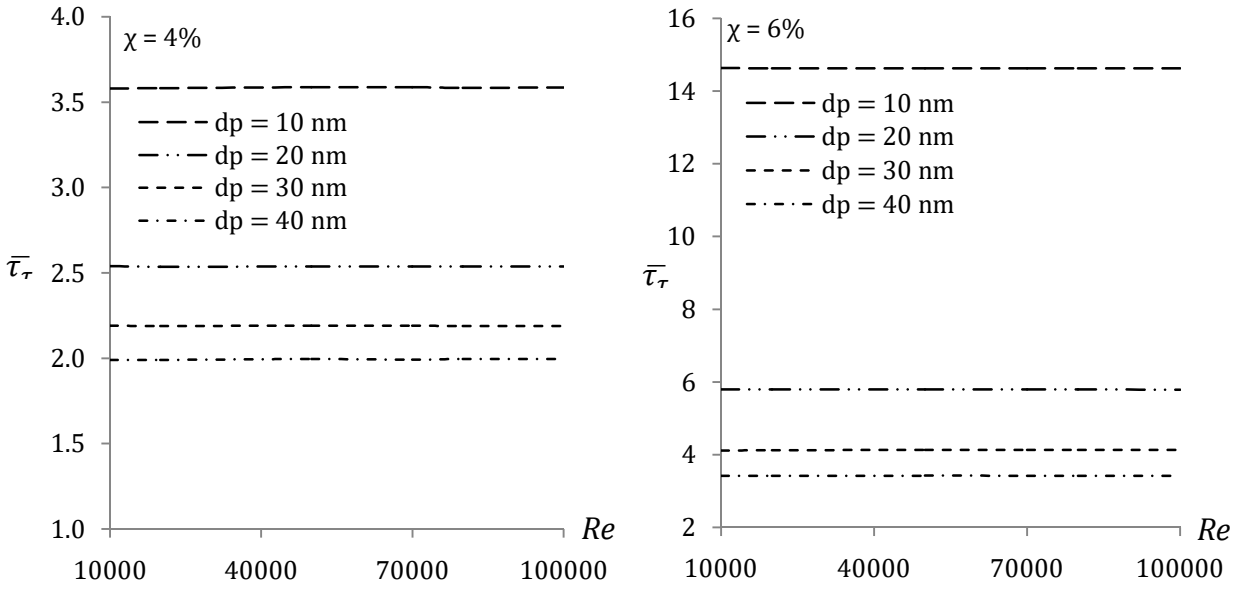

(a) Al_2O_3-H_2O nanofluid

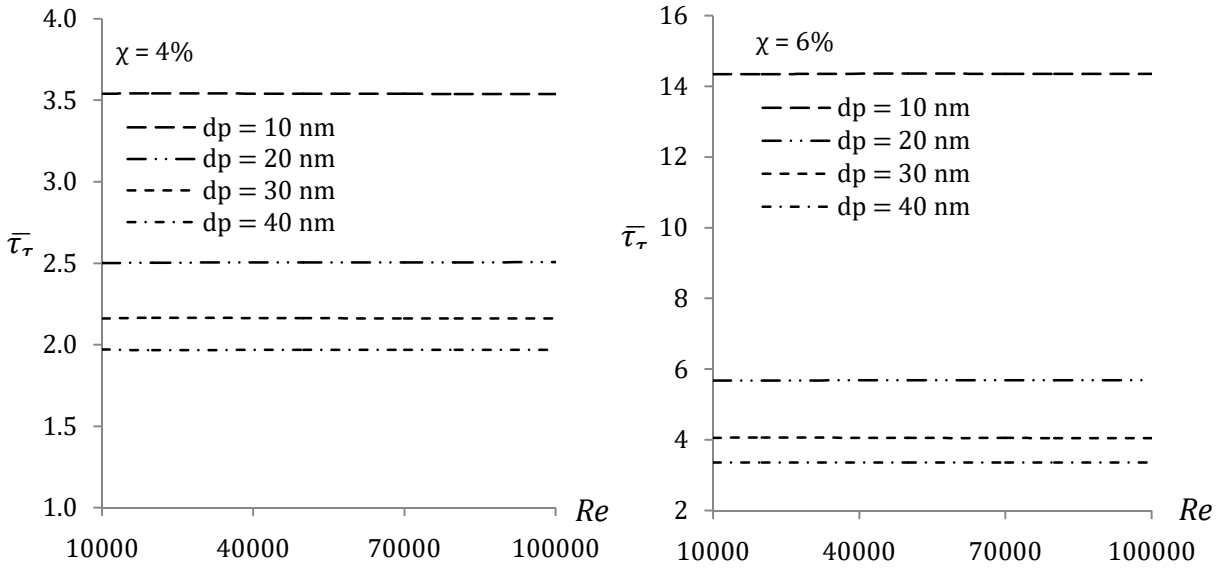

(b) TiO_2-H_2O nanofluid

Figure 7.3: Variations of average shear stress ratio with different Reynolds numbers for Al_2O_3-water and TiO_2-water nanofluids, nanoparticles concentration of 4% and 6% and nanoparticles diameter of 10, 20, 30 and 40 nm

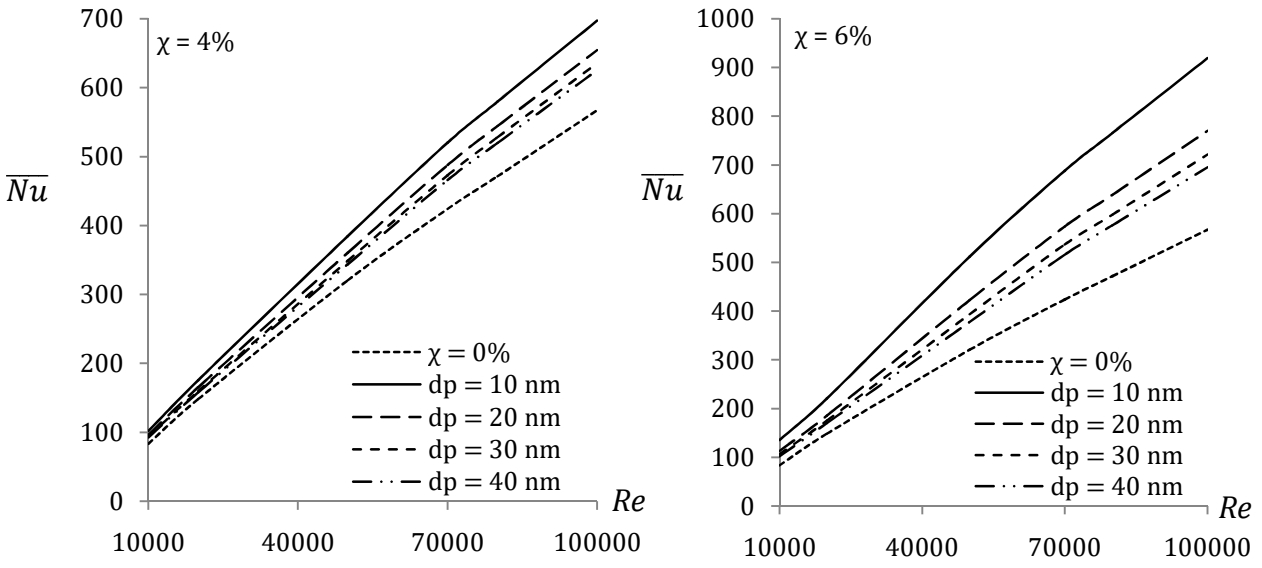

(a) Al_2O_3-H_2O nanofluid

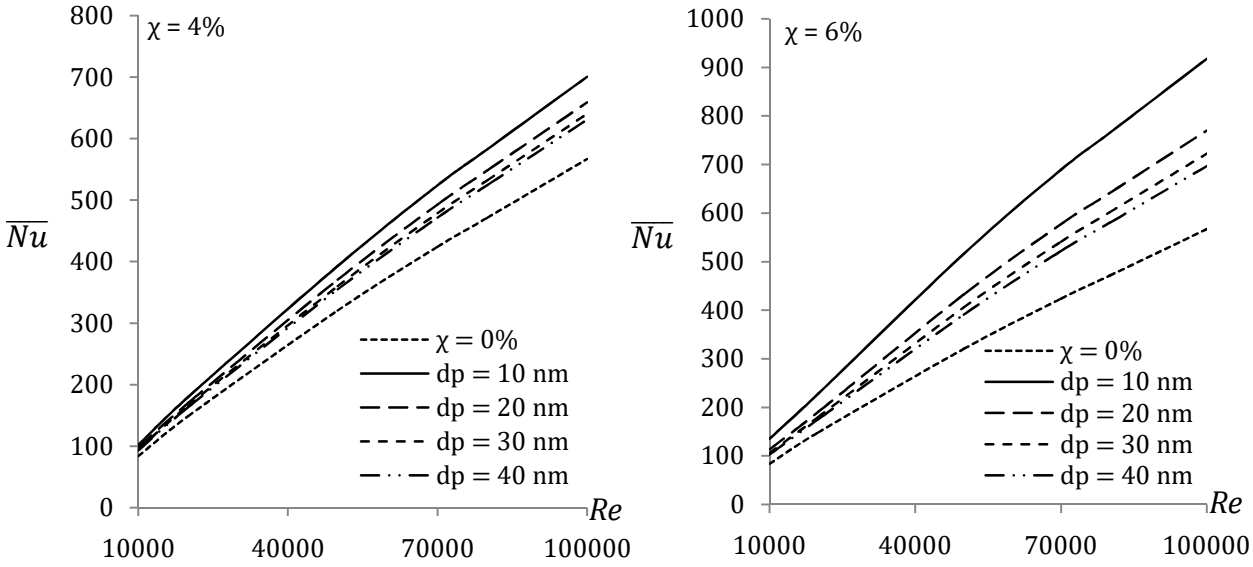

(b) TiO_2-H_2O nanofluid

Figure 7.4: Variations of average Nusselt number with different Reynolds numbers for Al_2O_3-water and TiO_2-water nanofluids, nanoparticles concentration of 4% and 6% and nanoparticles diameter of 10, 20, 30 and 40 nm

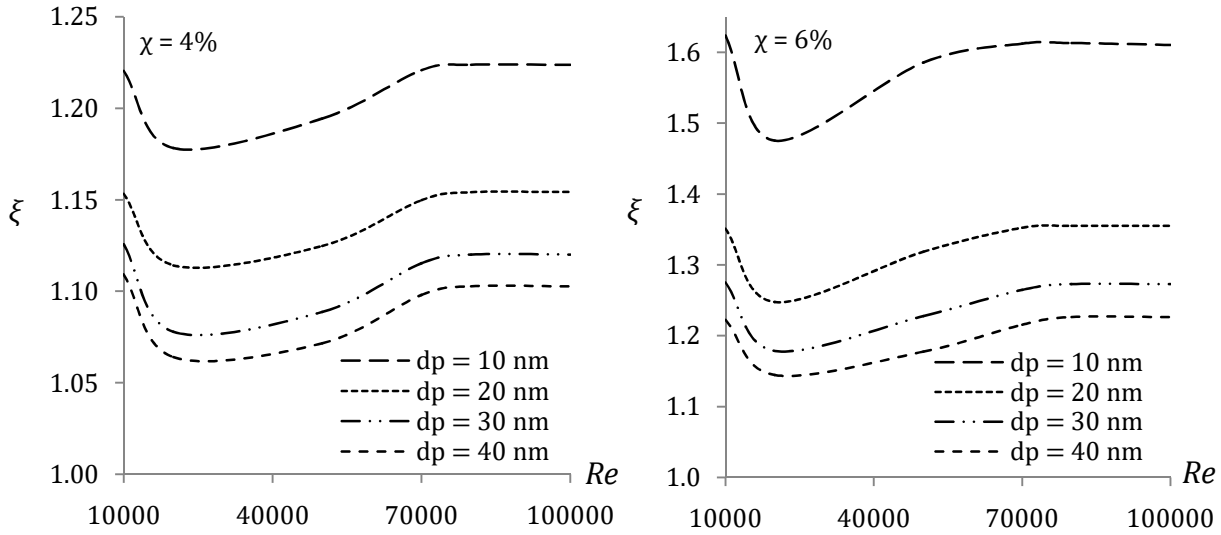

(a) Al_2O_3-H_2O nanofluid

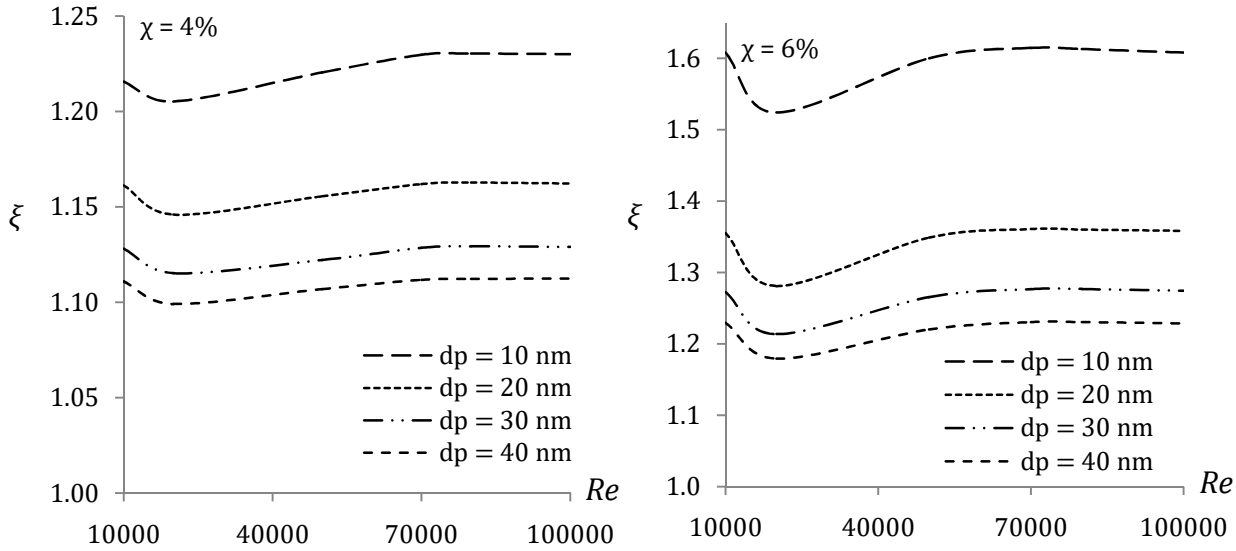

(b) TiO_2-H_2O nanofluid

Figure 7.5: Variations of thermal performance factor with different Reynolds numbers for Al_2O_3-water and TiO_2-water nanofluids, nanoparticles concentration of 4% and 6% and nanoparticles diameter of 10, 20, 30 and 40 nm

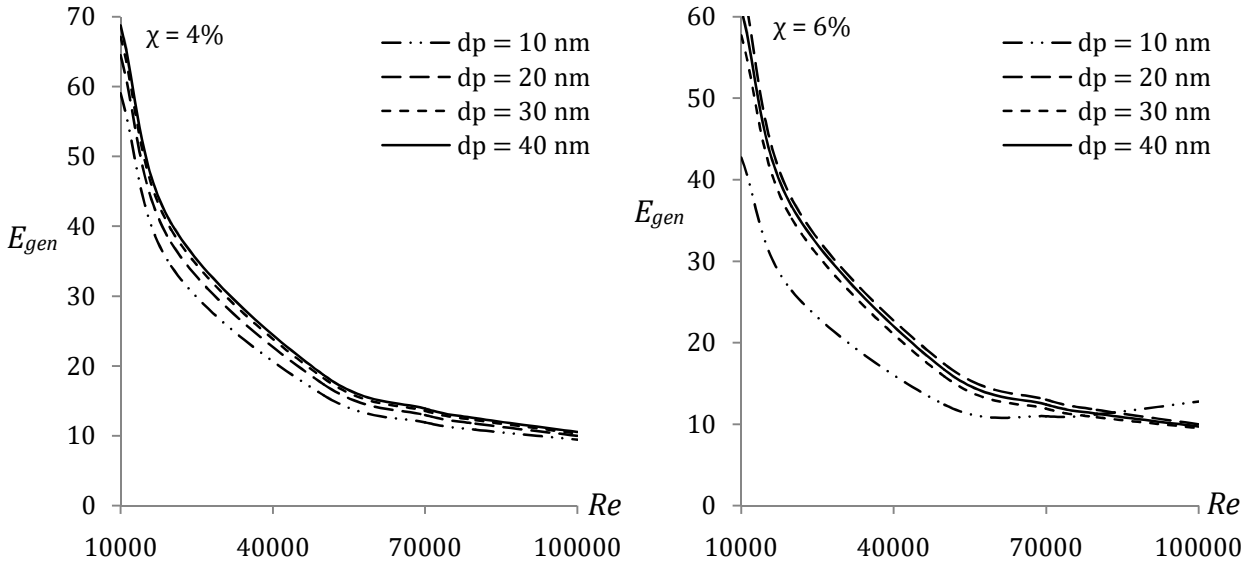

(a) Al_2O_3-H_2O nanofluid

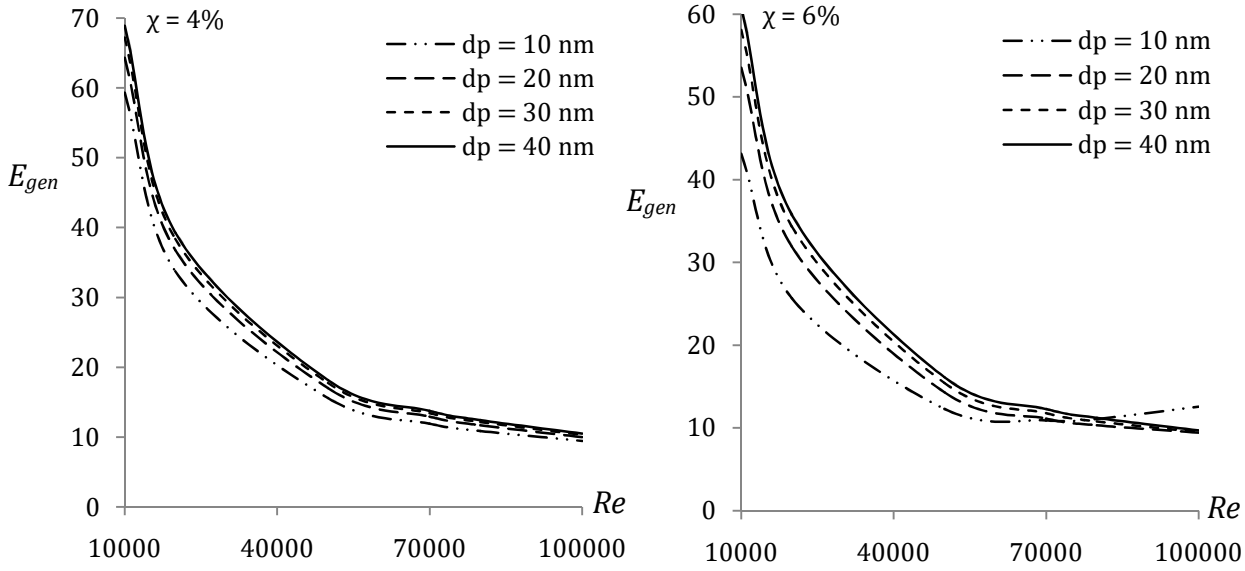

(b) TiO_2-H_2O nanofluid

Figure 7.6: Variations of total entropy generation with different Reynolds numbers for Al_2O_3-water and TiO_2-water nanofluids, nanoparticles concentration of 4% and 6% and nanoparticles diameter of 10, 20, 30 and 40 nm

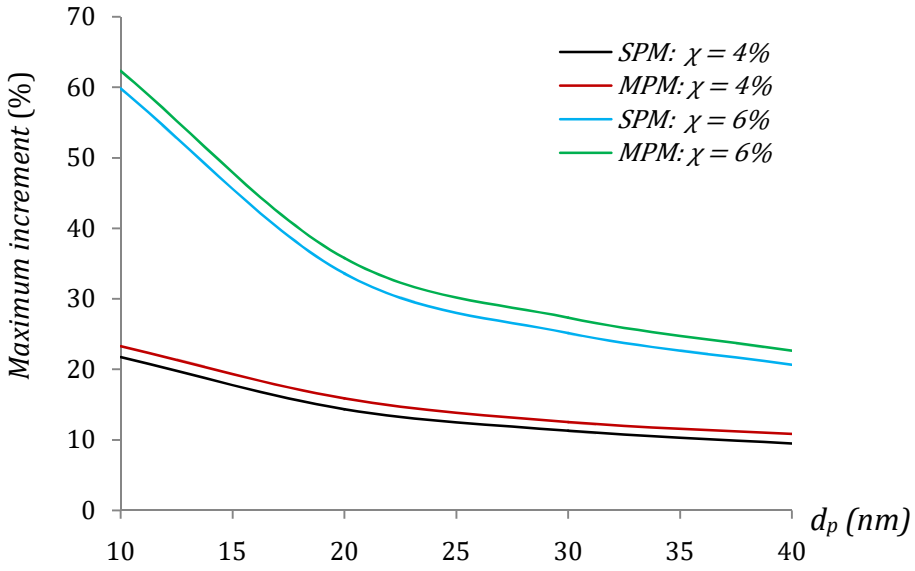

(a) Al_2O_3-H_2O nanofluid

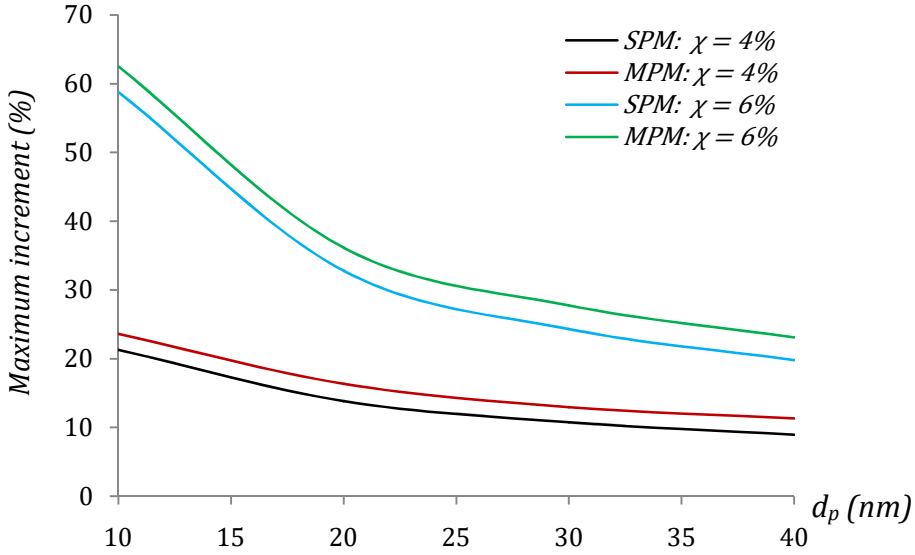

(b) TiO_2-H_2O nanofluid

Figure 7.7: Variations of maximum heat transfer enhancement (%) with different nanoparticles diameters for Al_2O_3-water and TiO_2-water nanofluids

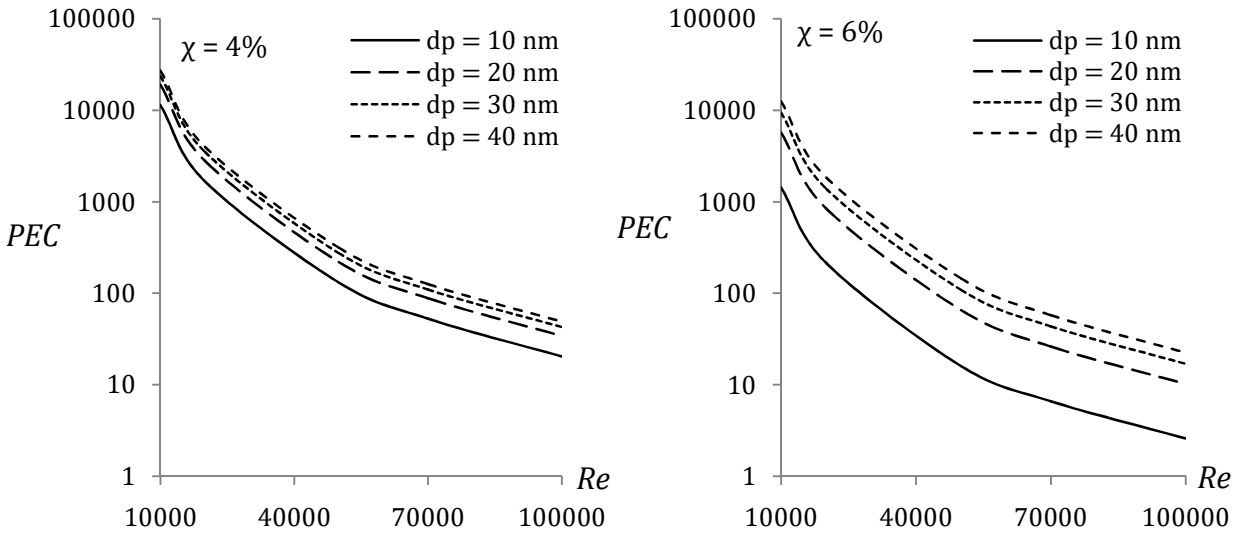

(a) Al_2O_3-H_2O nanofluid

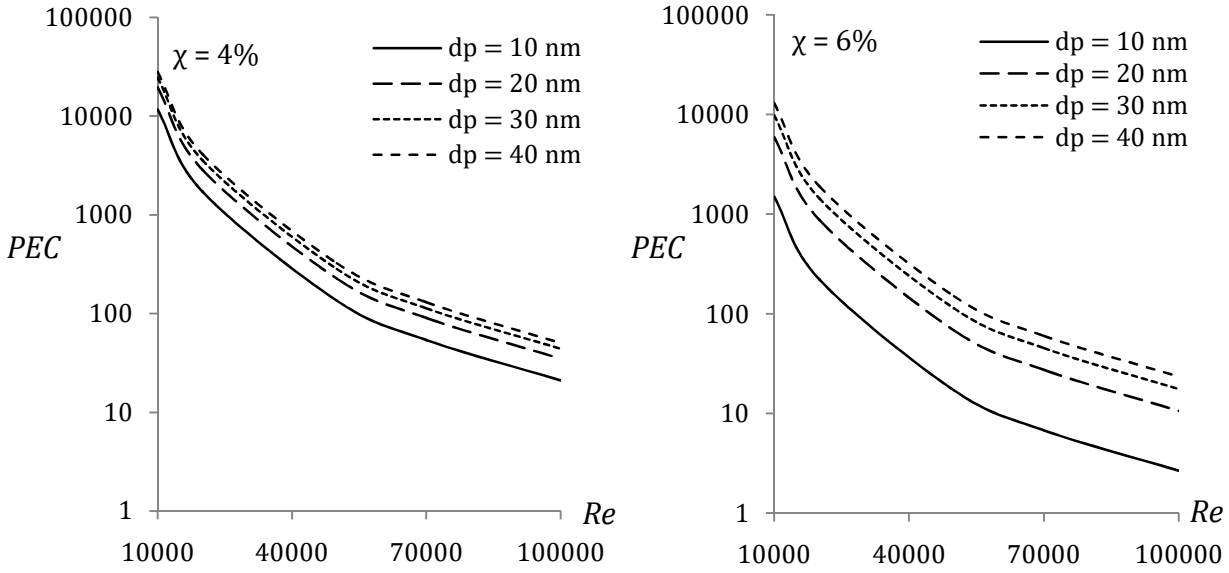

(b) TiO_2-H_2O nanofluid

Figure 7.8: Variations of performance evaluation criterion (*PEC*) with different nanoparticles diameters for Al_2O_3- H_2O and TiO_2- H_2O nanofluids for different *Re*

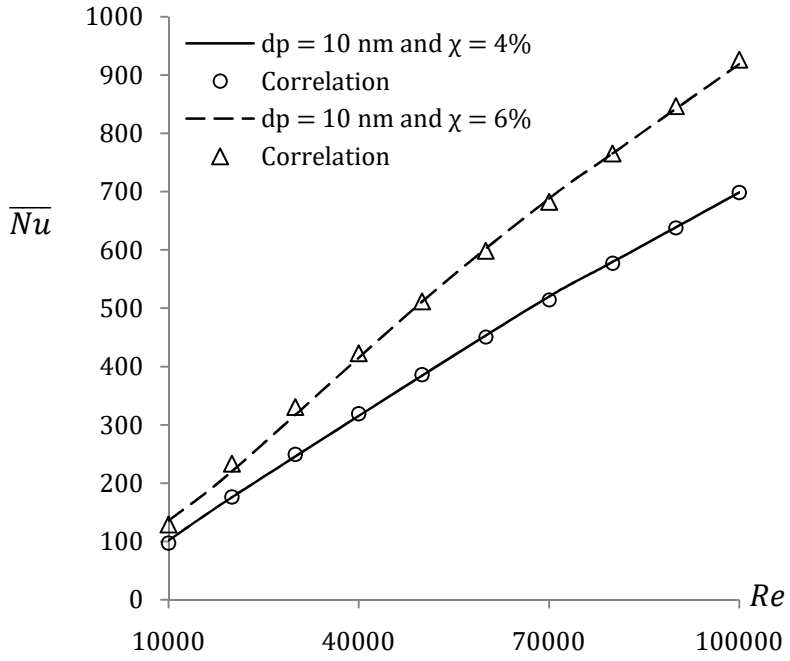

Al_2O_3-H_2O nanofluid

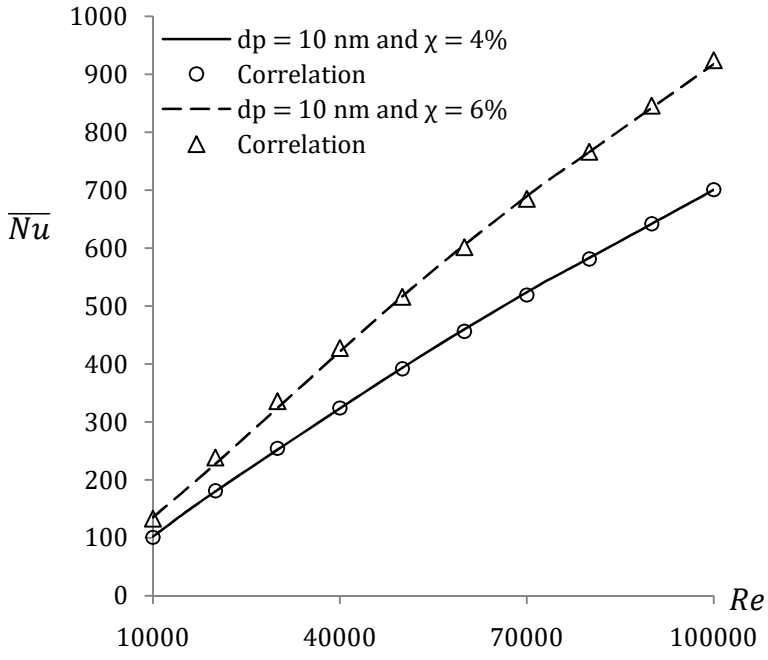

TiO_2-H_2O nanofluid

Figure 7.9: Comparisons of the proposed correlations with the numerical results for Al_2O_3-water and TiO_2-water nanofluids

Chapter 8

Transition to Turbulent Nanofluids Flow: Performance of a Discrete Phase Model

8.1 Introduction

Nanofluid is known as a new generation of fluid and it was introduced almost few decades ago. But its effectiveness in practical thermal engineering applications has started to reduce over time due to the several factors such as physical instability, complex procedure of the production of nanofluids and its cost, instability in the suspension of nanoparticles into a base fluid, choice of thermophysical properties and reliability of nanofluids. However, two different phases such as water and nanoparticles can be considered instead of a typical nanofluid which actually acts like a fluid-solid mixture. Hence, the interaction between the fluid and particles needs to be investigated to assess its performance. Besides, such simple mixture is not possible to be considered as nanofluids with its thermophysical properties. Also, this mixture will never behave like a pure fluid and so, it is not to be used in the single phase model. In addition, it will remain as a simple mixture of fluids and solids. That is why, it never satisfies the required mixture properties along with the thermo-physical properties of nanofluids. Such mixture can't be used in the multi-phase mixture model too.

In this chapter, Eulerian-Lagrangian discrete phase model (DPM) is used with temperature dependent thermophysical properties of water and nanoparticles to study the thermal performance behaviour of Al_2O_3 and TiO_2 nanoparticles inside a horizontal pipe within the transition to turbulent flow regimes. Moreover, the different types of thermophysical properties of nanofluids commonly used in single-phase and Eulerian-Eulerian mixture models play an important role in examining their hydrodynamic and thermal performances. Eulerian-Lagrangian discrete phase model (DPM), on the other hand, is fully independent of the thermophysical properties of nanofluids. And, two separate phases such as a continuum fluid phase

(water) as well as discrete nanoparticles phase are used in this model. DPM has shown a success in laminar nanofluid flow through a pipe [36-38] as discussed in §2.1 of Chapter 2, though no effort has been given to the date in investigating its performance under transition to turbulent flow regimes.

The physical flow geometry, axi-symmetric pipe with diameter$D_h = 0.019\ m$, remains to be the same in this chapter with the boundary conditions already described in the previous Chapters 4 to 7. However, the boundary conditions particularly required for the Eulerian-Lagrangian based discrete phase model are briefly explained below:

For nanoparticles:

It is assumed that nanoparticles are injected uniformly to face normal direction from the inlet surface. Also, nanoparticles diameter = 100 nm and temperature = 293 K are considered and the total flow rate of the nanoparticles is also defined as a initial condition.

For water:

At the pipe inlet, a uniform velocity ($v_{x,in}$) as well as a uniform temperature ($T_{in} = 293\ K$) with a turbulent intensity $I = 3\%$ for transition regime and $I = 0.16\ Re^{-1/8}$ for turbulent regime is stated.

At the pipe outlet, a static gauge pressure, $p_{gauge} = 0$ is specified.

On the pipe wall, a no-slip boundary condition is introduced with uniform heat flux, q'' = $5 \times 10^3\ W/m^2$ for transition regime and q'' = $50 \times 10^3\ W/m^2$ for turbulent regime.

8.2 Numerical Procedure and Validation

The dimensional steady-state governing equations for Eulerian-Lagrangian discrete phase model are considered in this chapter. It is assumed that flow is incompressible and Newtonian. Also, the Boussinesq approximation in the momentum equation and the compression work as well as the viscous dissipation term in the energy equations are neglected. SST $\kappa - \omega$ and Realizable $\kappa - \epsilon$ models are considered for the modelling of transition and turbulent flow fields respectively with an enhanced near wall treatment. The details of the governing equations and transition and turbulent models are given in §3.1.3, §3.2.2 and §3.2.3 of Chapter 3. Also, the details of the

temperature dependent physical properties of water and Al_2O_3 and TiO_2 nanoparticles are given in §3.3.5 and §3.3.6 of Chapter 3.

Grid sensitivity test carried out in §4.3 and §6.4 of Chapters 4 and 6 respectively also demonstrate that the combination of grids 500×100 used in this chapter is appropriate for resolving both the flow and thermal fields within the pipe geometry under consideration.

At first, the local Nusselt number for the fully developed laminar flow under the constant heat flux boundary condition is compared with the correlation of Shah and London [116] and experimental result of Kim *et al.* [49] in order to validate the present numerical results for water as shown in Fig. 8.1. A good agreement is observed between the results and it suggests that DPM model can be used to see the performance of the model when particle and fluid mixture is taken into account.

Shah Equation [116]:

$$Nu_x = \begin{cases} 1.302\, x_+^{-1/3} - 1, & x_+ \leq 0.00005 \\ 1.302\, x_+^{-1/3} - 0.5, & 0.00005 < x_+ < 0.0015 \\ 4.364 + 8.68\, (10^3 x_+)^{-0.506}, & x_+ \geq 0.0015 \end{cases} \tag{8.1}$$

where $x_+ = \frac{x}{Re\, Pr\, D_h}$

Fully developed radial velocity and turbulent kinetic energy profile for $Re = 21800$ and $Pr = 7.04$ have been is validated against the experimental data as well as the correlations. Additional validation is performed using the numerical results of Darcy friction factor and average Nusselt number against the existing correlations for different Re from 2300 to 100×10^3 and $Pr = 7.04$. A good agreement is received and the details of which are already given in §4.4 and §6.6.1 of Chapters 4 and 6 respectively.

8.3 Results and Discussion

Numerical investigations are carried out using the Al_2O_3-H_2O and TiO_2-H_2O nanofluids with the following parameters: Reynolds number from $Re = 250$ to 1200 (laminar flow regime), $Re = 2300$ to 10×10^3 (transition flow regime) and $Re = 10 \times 10^3$ to 100×10^3 (turbulent flow regime), Prandtl number from 7 to 10, nanoparticles concentration of 1 to 6%, and diameter of nanoparticles of 100 nm. The performance

of the simple mixture of water and Al_2O_3 / TiO_2 nanoparticles using the Eulerian-Lagrangian discrete phase model are presented and discussed in the following.

8.3.1 Average Shear Stress Coefficient Ratio Analysis

Figure 8.2 shows the variations of the average shear stress coefficient ratio with Reynolds number for Al_2O_3 and TiO_2 nanoparticles. Results reveal that the average shear stress coefficient ratio is enhanced with an increase in the nanoparticles concentration. It is due to the increase of nanofluids dynamic viscosity or pressure drop in the nanofluids. The average shear stress coefficient ratio of the Al_2O_3 nanoparticles are found to have a value, 1.10, 1.80, 2.80 and 1.12, 1.85, 2.89 for χ = 1%, 4% and 6% in the transition and turbulent flow regimes respectively in the figure. However, a lower average shear stress coefficient ratio is observed for the TiO_2 nanoparticles. In particular, the results of the average shear stress coefficient ratio for the Al_2O_3 nanoparticles in turbulent flow regime are compared with the works of Maiga *et al.* [59] and Bianco *et al.* [60]. Bianco *et al.* [60] carried out numerical investigation of turbulent flow using Eulerian-Eulerian mixture model whereas Maiga *et al.* [59] carried out similar investigation using single phase model. To compare, Eulerian-Lagrangian discrete phase model predicts lower average shear stress coefficient ratio than that obtained by the Eulerian-Eulerian mixture and single phase models. It suggests, the lower penalty in pumping power can be obtained using DPM than SPM as well as MPM, and it is due to the simple mixture of water and nanoparticles.

8.3.2 Average Heat Transfer Performance Analysis

Figure 8.3 shows the comparison of the present result with that of Bianco *et al.* [37] and Moraveji and Esmaeili [38] for different Al_2O_3-nanoparticles concentrations within the laminar flow regime. It is to be noted that Bianco *et al.* [37] as well as Moraveji and Esmaeili [38] used Eulerian-Lagrangian discrete phase model. It is seen in Fig. 8.3 that the results of average Nusselt number for different Reynolds number are in good agreement with the results of Bianco *et al.* [37] and Moraveji and Esmaeili [38] for temperature dependent properties. Also, maximum deviations of 5.12% and 3.80% for $\chi = 1\%, Re = 750$ and 12.88% and 9.09% for $\chi = 4\%, Re = 750$ are observed compared with the results of Bianco *et al.* [37] and Moraveji and Esmaeili [38]. However, results of Bianco *et al.* [37] for $\chi = 4\%$ seems to be inconsistent for

$Re = 500$ and $Re = 750$ respectively while similar behaviour is observed by Moraveji and Esmaeili [38] for $Re = 750$. Furthermore, Figs. 8.4 and 8.5 show the variations of average Nusselt number with Reynolds number and nanoparticles concentration using Al_2O_3 and TiO_2 nanoparticles under transition and turbulent flow regimes.

Moreover, performance of DPM model on heat transfer is presented and then a comparison is done with the heat transfer results of MPM of Al_2O_3 and TiO_2 – water nanofluids under the transition flow regime as shown in Fig. 8.4. It is observed that heat transfer rate increases with the increase of nanoparticles concentration. Such findings are realistic as it has been discussed in Chapter 4. It is also observed that the higher heat transfer rate is found using DPM when compared to the heat transfer results of MPM. This suggests, DPM predicts higher average Nu for higher size of d_p and it is to happen because of the simple mixture of fluid and nanoparticles and few other factors, for instances, particles interaction, sedimentation, clogging, erosion.

Besides, another comparison is made with the proposed correlations suggested by Pak and Cho [58] and Maiga *et al.* [59] for Al_2O_3 nanoparticles under turbulent flow regime in Fig. 8.5. Also, average Nusselt number results of multi-phase model is presented for both Al_2O_3 and TiO_2 – water nanofluids using different nanoparticles concentrations. For $\chi = 1\%$ and $10 \times 10^3 \leq Re \leq 70 \times 10^3$, it is observed that the variations among the present results, Pak and Cho [58] correlation, and MPM results are insignificant. But when $Re > 70 \times 10^3$, the values of average Nusselt number tends to differ from the correlation of Pak and Cho [58] and MPM results and a strong agreement is found with the correlation of Maiga *et al.* [59]. It is also observed that the results of average Nusselt number are in good agreement with Pak and Cho [58] and MPM results for $\chi = 4\%$ and 6% and $10 \times 10^3 \leq Re \leq 40 \times 10^3$,. Whereas for $Re > 40 \times 10^3$, present results deviate from the results of Pak and Cho [58] and MPM results and moves closer to the results of Maiga *et al.* [59]. But for $\chi = 6\%$ and $Re > 80 \times 10^3$, an significant deviation is observed with the correlations proposed by Pak and Cho [58], MPM results and Maiga *et al.* [59]. Moreover, a similar trend is observed for TiO_2 nanoparticles using Eulerian-Lagrangian discrete phase model. The reason behind such behaviour of both Al_2O_3 and TiO_2 nanoparticles is the augmentation of velocity in the different phases for the increase of Reynolds numbers and the strong interaction between the fluid particles and nanoparticles. This is also due to the strong coupling between the fluid and nanoparticles phases as well.

Different researchers attempted to explain the reason behind rapid enhancement of heat transfer rate using nanofluids. In particular, Buongiorno [78] mentioned, t if the wall temperature is higher than the bulk temperature then Prandtl number calculated at bulk properties will be higher than the Prandtl number calculated at laminar sublayer properties. This helps to increase the heat transfer rate. Such behaviour is also depends on two effects (Buongiorno [78]), that is $\mu_b > \mu_{ls}, \lambda_b < \lambda_{ls}$ and $\chi_b > \chi_{ls}$. Though the first effect is present in pure fluids, it is more dominant for nanofluids because of the more pronounced effect of dynamic viscosity and thermal conductivity in the laminar sub-layer regime for nanofluids. The second effect indicates that dynamic viscosity is strongly dependent on χ and as the χ increases, μ increases too. This plays a significant role in the reduction of Prandtl number at laminar sublayer.

Arani and Amani [117] also explained the increase of forced convective heat transfer coefficient by Macroscopic theory. They mentioned, the enhancement of convective heat transfer coefficient depends on the increase of thermal conduction. Such increase of thermal conduction is feasible due to the addition of nanoparticles into the base fluid. However, they also mentioned, the enhancement of heat transfer coefficient also depends on the increase of thermal conductivity and decrease of the thickness of thermal boundary layer as well. They also found that size diameter of the nanoparticles had a marginal effect on the enhancement of convective heat transfer rate which was possibly due to the nanoparticles migration mechanism [118].

Since nanofluid is a mixture of base fluid and nanoparticles, it is likely to consider this as two-phase solid-fluid interaction which is fully ignored in single and multi-phase mixture models. Keblinski *et al.* [119] suggested, the enhancement of heat transfer rate mainly depends on the movement of nanoparticles inside the fluid which helps to transport heat from one nanoparticles to another and increase the thermal conductivity. They have also suggested that fluid layering at fluid/nanoparticles interface, nanoparticles clustering and nature of heat transport in particles inside the domain of heat transfer play a significant role to increase the heat transfer rate. But, the above mentioned effects is not to be able to describe the theoretical and practical analysis of such enhancement because of the complex nature of nanofluid. Therefore, more experimental investigation are needed to understand how we treat nanofluid; and how we consider this as a pure solid-fluid mixture; or whether it will be simply two different phases with solid-fluid interactions or not.

8.4 Conclusion

In the present work, Eulerian-Lagrangian discrete phase model has been introduced to investigate the thermal performance of Al_2O_3 and TiO_2 nanoparticles in pipe with temperature dependent properties under transition to turbulent flow regimes. According to our findings, the following conclusions have been drawn and summarised as follows:

(1) It is seen that for $\chi = 4\%$ and 6% and $10 \times 10^3 \leq Re \leq 40 \times 10^3$, the results of heat transfer rate are very close to the experimental results of Pak and Cho [58] and MPM. However, results deviate from Pak and Cho [58] correlation as well as MPM for $Re > 40 \times 10^3$ and moves close to the numerical correlation of Maiga *et al.* [59].

(2) It is also seen that average shear stress coefficient ratio becomes inferior for high nanoparticles concentration compared with the results of single and multi-phase mixture models.

(3) Higher heat transfer enhancement is observed for Al_2O_3 nanoparticles than TiO_2 nanoparticles for all *Re* and χ.

Finally, it is seen that performance of DPM is excellent under laminar and turbulent flow regimes without using information about the behaviour of nanofluid and its thermophysical properties. Since this model only requires physical properties of water and nanoparticles, this approach has opened a new platform to study the behaviour of a simple mixture which is used in this model. At the end, more experimental research is necessary to understand the performance of new mixture.

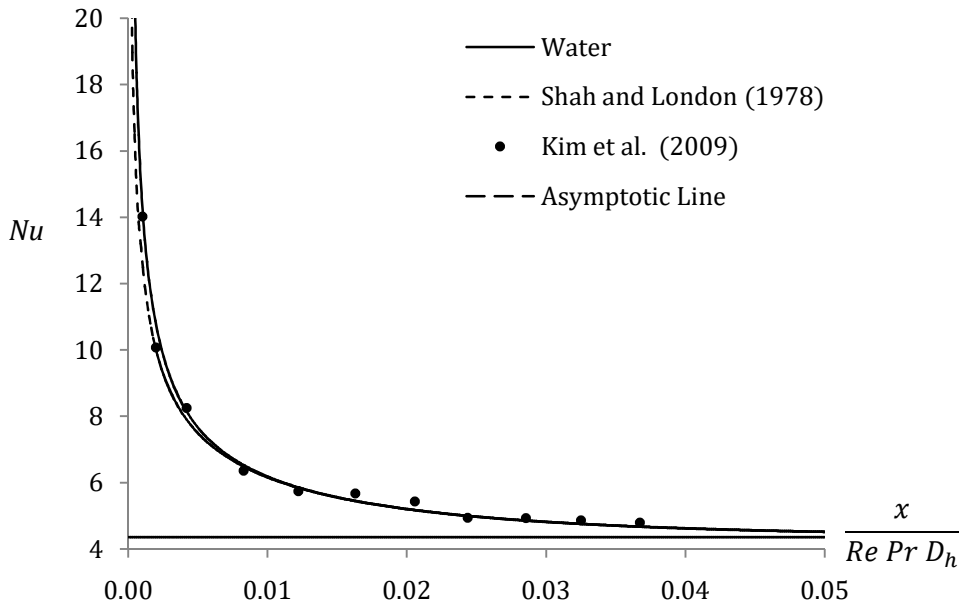

Figure 8.1: Comparisons of the present results with Shah and London [116] and Kim *et al.* [49] of local Nusselt number for water under fully developed laminar flow regime

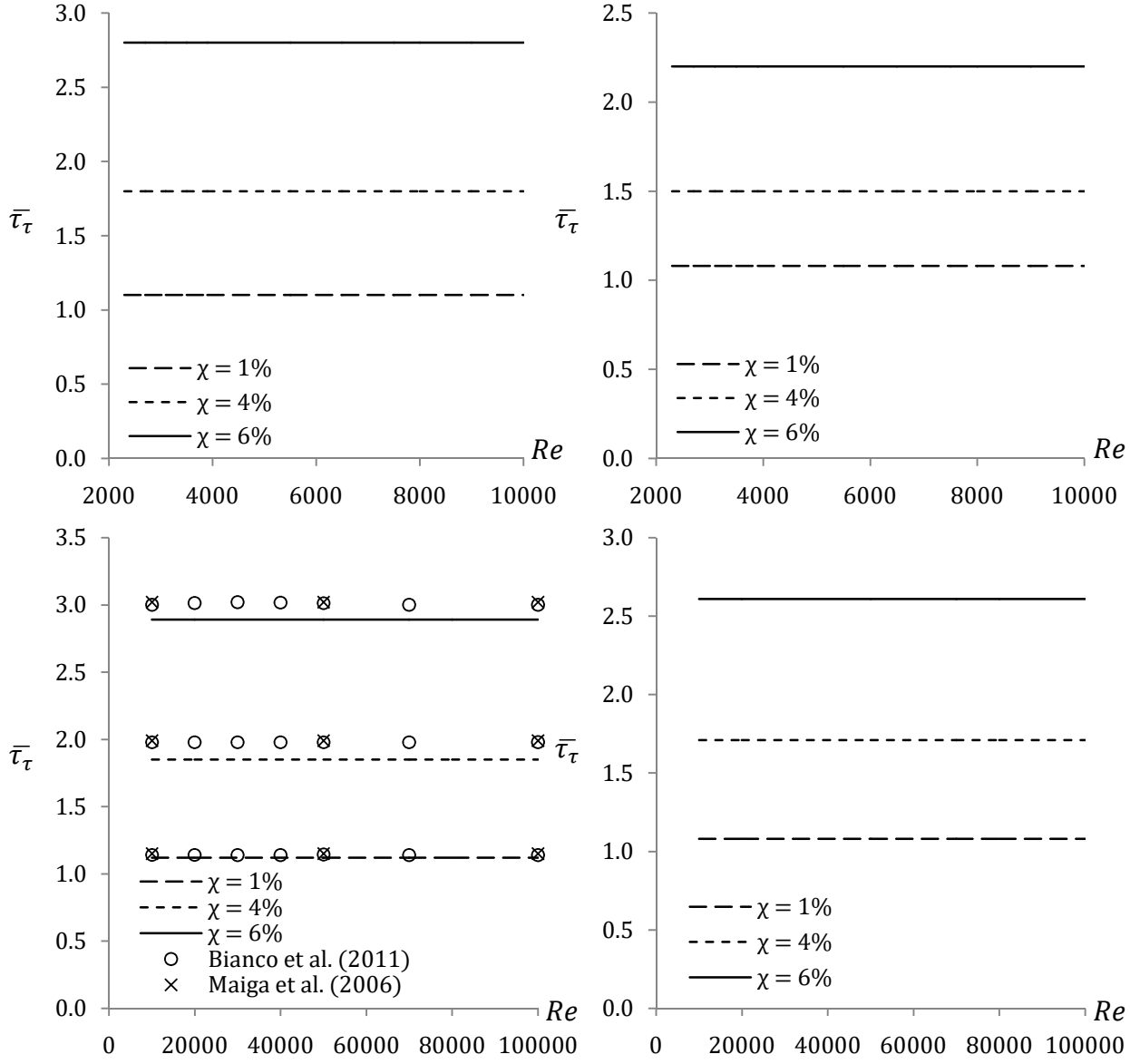

Al_2O_3-H_2O nanofluid

TiO_2-H_2O nanofluid

Figure 8.2: Variations of average shear stress coefficient ratio with different Reynolds numbers for different nanoparticles concentration and nanofluids

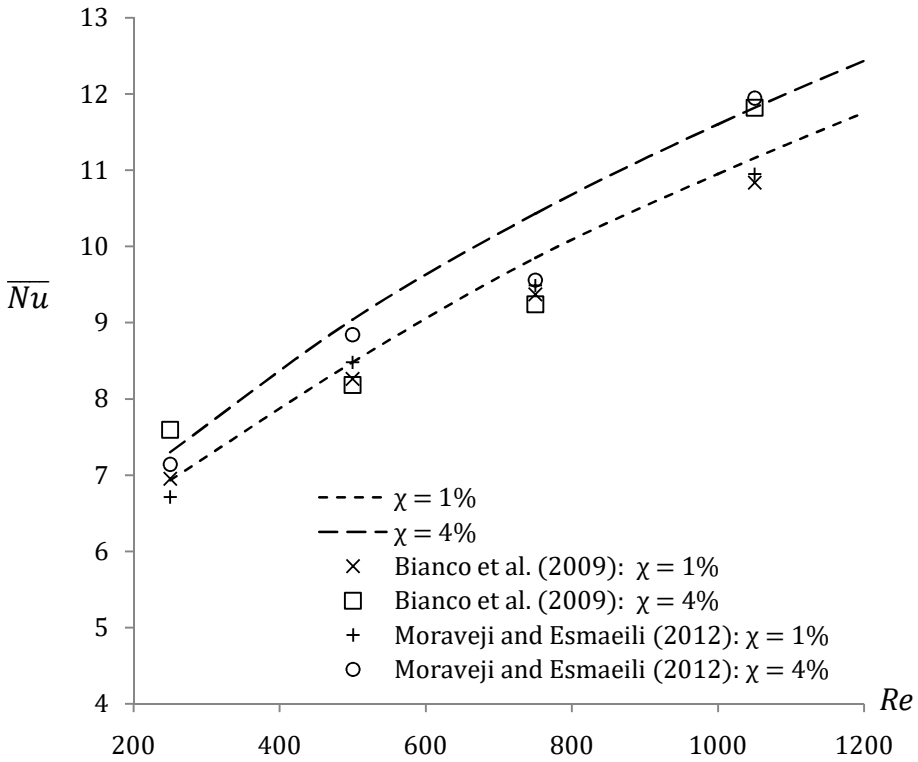

Figure 8.3: Variations of average Nusselt number with different Reynolds numbers for different nanoparticles concentrations and Al_2O_3-H_2O nanofluid under laminar flow regime

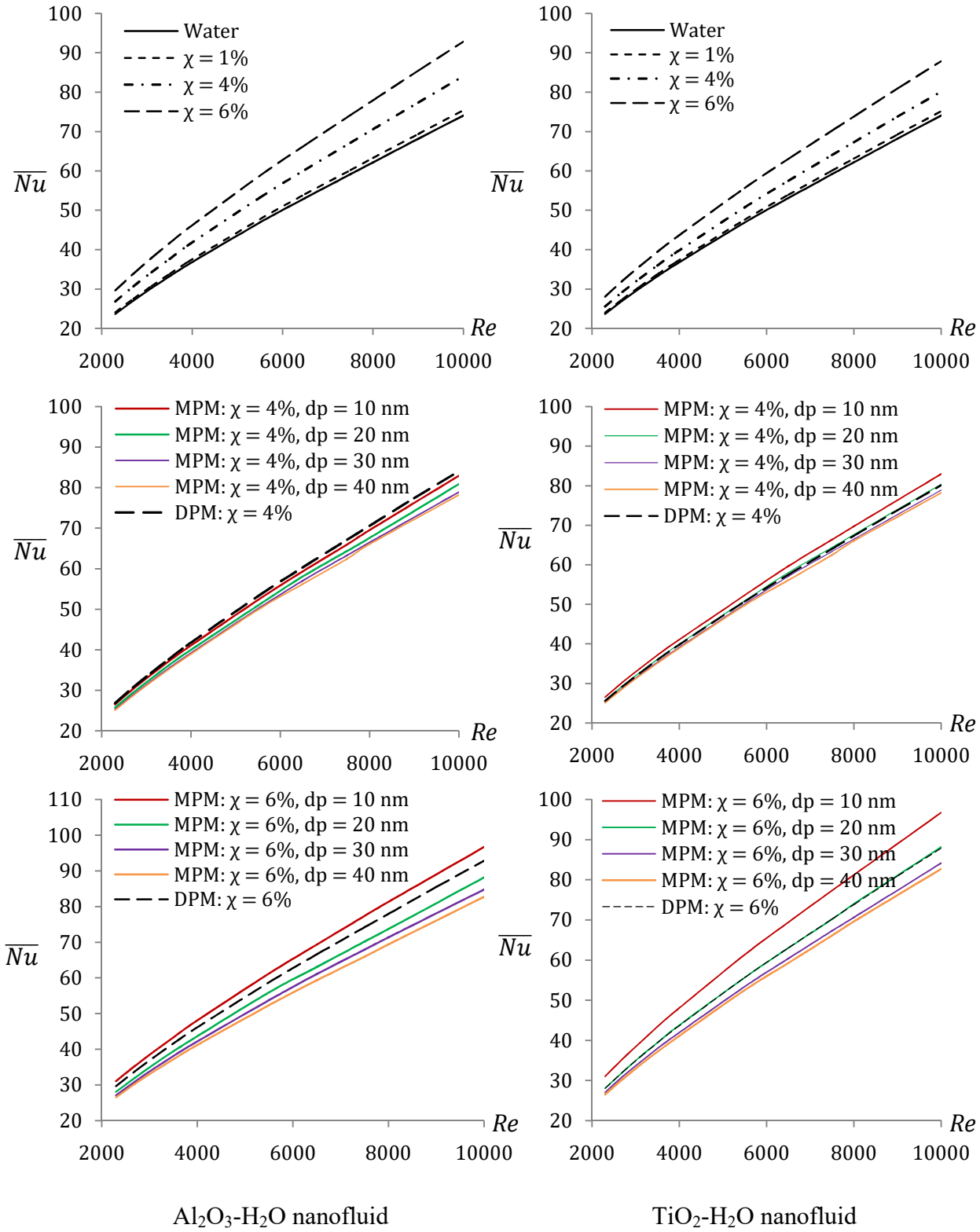

Figure 8.4: Variations of average Nusselt number with different Reynolds numbers for different nanoparticles concentrations and nanofluids under transition regime

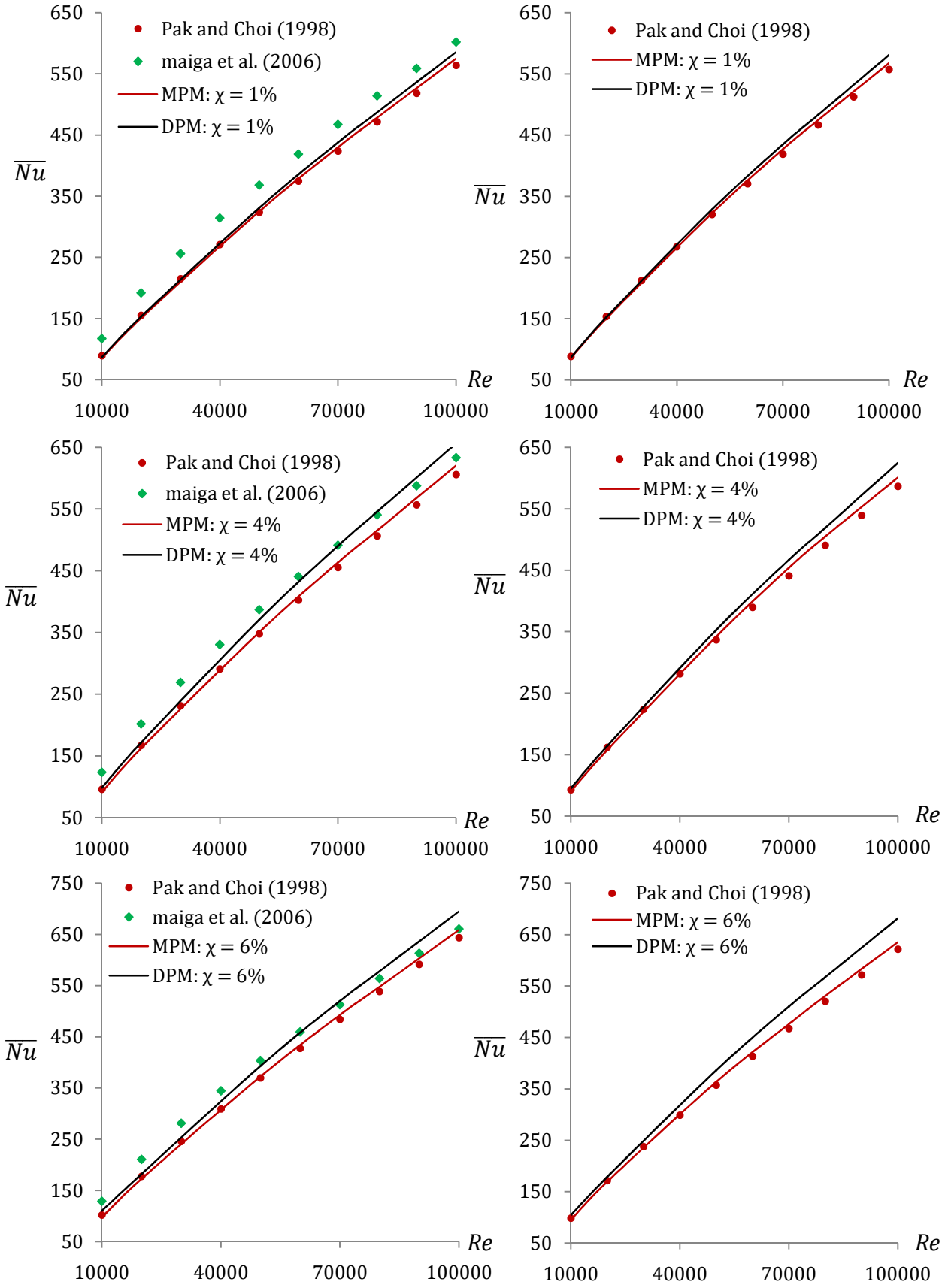

Al_2O_3-H_2O nanofluid TiO_2-H_2O nanofluid

Figure 8.5: Variations of average Nusselt number with different Reynolds numbers for different nanoparticles concentrations and nanofluids under turbulent regime

Chapter 9

Transition of Nanofluids Flow in an Inclined Heated Pipe

9.1 Introduction

A numerical study has been carried out to understand the heat transfer behaviour of Al_2O_3-H_2O and TiO_2–H_2O nanofluids flow in an inclined pipe using both the single and multi-phase models under transition flow condition in this chapter,. The SST $\kappa - \omega$ transitional model with different inclination angles from 0° to 75° has been used for simulating the transition flow regime. Previously, it was found that combination of the smaller size of nanoparticles (e.g. d_p = 10 nm) and the higher nanoparticles volume concentration (χ = 6%) had produced the highest thermal performance when the Brownian motion of nanoparticles had been taken into account. Details of these findings has been discussed in Chapters 4 and 5 respectively.

Literature review suggests that a very few experimental and numerical investigations have been carried out to the date on the laminar and turbulent nanofluid flow in an inclined or a vertical pipe [120-122]. And, we are the first to have investigated the nanofluid flow inside an inclined pipe in transition regime considering a smaller size but higher concentrations (mentioned above) of nanoparticles with the Brownian motion.

9.2 Physical Model and Boundary Conditions

Three-dimensional model of an inclined pipe with a length L of 1.0 m and a circular section with diameter D_h of 0.019 m is shown in Fig. 9.1. Besides, the inlet, outlet and wall boundary conditions used for modelling the mixed convection of nanofluids flow in inclined pipe have already been described in §4.2 of Chapter 4. Also, the Boussinesq approximation is introduced in the momentum equation for mixed convection nanofluids flow in the inclined pipe as shown in Eq. (3.23) of Chapter 3.

9.3 Grid Sensitivity Analysis

Grid sensitivity analysis has been carried out using different mesh volumes for the horizontal (θ = 0°) and inclined (θ = 45°) pipe orientations in order to achieve a suitable grid. The grid sensitivity results of radial velocity, temperature, turbulent kinetic energy and average Nusselt number with different mesh volumes for Al_2O_3-H_2O nanofluid are presented in Figs. 9.2 and 9.3.

Here, five different mesh control volumes considering a total element numbers of 274512, 275544, 294120, 462756 and 584022 have been considered respectively for a selected Reynolds number, *Re*, of 10000. The results of the radial velocity and temperature extracted at the location of x = 0.99 m where the flow fields seem to be fully developed shows insignificant variations along the radial direction with the mesh choices. However, a significant variation between the radial turbulent kinetic energy profiles is observed for a lower number of mesh volumes. But the results for the mesh volume of 462756 and 584022 are similar and so, 462756 are considered to be appropriate for the present investigation.

The variations of the average Nusselt number with different mesh volumes have also been presented in Fig. 9.3 in order to justify the final selection again. It clearly shows, in case of the mesh volume size being greater than 460000, any size of mesh volume can be adopted for nanofluids flow in pipe when the objective is to test the effect of inclination angles from 0° to 75°. It is significant that a uniform mesh distribution is considered along the pipe as well as the non-uniform mesh distributions are considered in other two directions in order to achieve better and accurate results of flow fields inside and near wall region of the pipe as shown in Fig. 9.4.

9.4 Results and Discussions

Here, Numerical investigations have been carried out using the Al_2O_3-H_2O and TiO_2-H_2O nanofluids with the following parameters: Reynolds number from Re = 2300 to 10×10^3 (transition regime), nanoparticles concentration, χ = 6%, diameter of nanoparticles, d_p = 10 nm and pipe inclination angles from θ = 0° to 75°., At first, a comparison between the results of the 2D axi-symmetric (carried out in the previous Chapter 4) and the 3D pipe model is presented in the following section. Then, contour plots of the axial velocity and turbulent kinetic energy are shown in order to

understand the flow behaviour. Later on, variation of the wall temperature and local Nusselt number as well as the Darcy friction factor and average Nusselt number with different inclination angles using the single and multi-phase models (SPM, MPM) are also presented and discussed.

9.4.1 Comparisons

Accuracy of the Darcy friction factor and average Nusselt number depend on the several factors such as good distribution of mesh along the axial; radial and tangential directions; choice of a transitional model; suitable boundary conditions near wall treatment as well as the physical geometry. Hence, it is important to compare the accuracy of the present results obtained in the 3D model geometry with some available experimental or numerical results. More essentially, comparison of the results obtained from the 2D axi-symmetric geometry has been done to gain further confidence in the full 3D modelling. A horizontal pipe with two water based Al_2O_3 and TiO_2 nanofluids is considered to do this. Here, the chosen parameters are: Re = 2300 to 10000, d_p = 10 nm, χ = 6% with the Brownian motion of nanoparticles.

Figure 9.5 shows the variations of the Darcy friction factor and average Nusselt number with different Reynolds numbers. It is observed that for the Al_2O_3-H_2O nanofluid, the maximum percentages of variations among the results of average Nusselt number obtained from the 2D axi-symmetric model are 3.12% and 4.27% respectively with the single and multi-phase models. However, such variations are found to be 4.06% and 4.98% respectively for the TiO_2-H_2O nanofluid. The maximum percentages of variations among the results of Darcy friction factor is found to be less than 1%. And, there is no significant difference found between the Darcy friction factor results while using the single and multi-phase models. Since the goal is to justify the accuracy of the simulated results of 3D model, Figure 9.5 shows a strong agreement compared with the results obtained using the 2D axi-symmetric model that have already been presented, verified and described in Chapter 4.

9.4.2 Velocity Contours

In this section, 2D contour plots of velocity have been generated by placing a horizontal plane along the pipe and also at different axial positions in order to understand the flow field behaviour in details for different inclination angles as

shown in Fig. 9.6. Only Al_2O_3-H_2O nanofluid with single phase model has been selected and the Reynolds number has been fixed to Re = 3500.

The transition phenomena observed previously in the axisymmetric model (Chapter 4) remains to be the same in case of θ = 0°. For example, the axial velocity initially behaves like a laminar flow and the transition begins at the hydrodynamic critical point. At this point, the hydrodynamic boundary layer thickness starts to grow and such development is found higher than the boundary layer growth observed in the upstream region. After the laminar breakdown point, the development of hydrodynamic boundary layer tends to become constant suggesting the flow to be fully developed. However, the development of a pair of unequal cells near the upstream at the top and bottom walls of the pipe is observed when the inclination angle is increased e.g. for θ = 0° to 30°. The upper one forms a larger size cell with a higher velocity magnitude than the lower one. It is also noticed that the development of lower sized cell is weak while the upper sized cell is stronger which dominates the flow at the upstream region. Also, the development of these two cells is seen to be limited within the region L < 0.3 m and this may be due to the buoyancy force which comes into effect due to the inclination angle. Besides, the flow starts to be fully developed further from the upstream and also in the downstream regions. And, such development is found to be identical because of the symmetry.

As the inclination angle is further increased from θ = 30° to 75°, the larger size cell starts to reduce but the smaller size cell starts to enhance. Similarly, the development area of these two cells decreases and is found to be less than 0.2 m. Moreover, as the lower cell moves towards the centreline region of the pipe, such rapid expansion forces the upper cell to reduce its size as which is clearly visible in frames (e, f). Since the lower cell becomes dominate in the pipe affecting the growth of the upper cell, it suggests that the upper cell is going to be diminished with the further increase of the inclination angle.

Moreover, Fig. 9.7 shows the variations of the velocity contours at different axial positions with different inclination angles. In case of θ = 15° and at x = 0.1 m, it is observed that the higher velocity region tends to move towards the upper wall zone and forms a large size of cell with lower velocity region that is likely to cover lower wall zone. Whereas for θ = 30° and x = 0.1 m, a rapid decrease of higher velocity region which tends to move more towards the upper wall region is observed and the

large size of cell forms a quarter moon type profile. Also, a small development of lower velocity zone seems to grow near the lower wall region. A degeneration of higher velocity region and moon type profile are seen near the top wall of the pipe and a rapid development of lower velocity region is observed for θ = 45° to 60° and x = 0.1 m. Though for θ = 75° and x = 0.1 m, a higher velocity cell seems to diminish and the whole region is almost covered with the lower velocity fluid. Again, it is observed that the higher velocity cell moves towards the upper wall region and forms a semi-circular profile while other regions are covered with the lower velocity magnitude of the nanofluid in case of θ = 15° to 30° and x = 0.25 m. However, for θ = 45° to 75° and x = 0.25 m, higher velocity region seems to diminish and the lower velocity fluid tends to cover the whole region. When x > 0.25 m, the flow tends to be fully developed and decrease of velocity magnitude is observed with the increase of inclination angles.

9.4.3 Turbulent Kinetic Energy Contours

Figures 9.8 and 9.9 show the variations of turbulent kinetic energy along the pipe with different inclination angles using single phase model for Al_2O_3-H_2O nanofluid. For θ = 0°, the initial blue region near the upstream indicates that the turbulent kinetic energy is almost constant and the flow behaviour seems to be laminar. This agrees well with the results reported in Chapter 4.

When L > 0.2 m, the turbulent kinetic energy starts to develop and a rapid increase is observed at the laminar breakdown point near the wall region. Though the laminar behaviour at the upstream tends to disappear and development of a large cell near the lower region of the pipe wall is observed for θ = 15° to 30°. Also, a small glimpse of the growth of higher magnitude of turbulent kinetic energy cell is visible inside the large and developed cell near the centreline position of the upstream. When 0.2 m < L < 0.4 m, the large cell is seen to cover almost the centreline area. And, another development of small cell which is connected to the large cell is evident near the upper wall. Besides, both the cells start to decrease when L > 0.4 m. Moreover, the growth of boundary layer start to be steady, constant and identical along the pipe at the downstream because of the symmetry boundary conditions and as the flow tends to be fully developed.

As the inclination angle increases from θ = 30° to 75°, the large cell starts to be reduced in size as well as the growth of higher magnitude of turbulent kinetic energy

inside the large cell starts to increase rapidly at the same time. Also, the development area of the large cell is decreased and is found to be less than 0.3 m. Moreover, the higher magnitude cell lying inside the large cell moves towards the centreline region and such augmentation forces the small cell located near the upper wall to be reduced. This is clearly visible in Figs. 9.8 and 9.9. As the inclination angle increases, the combination of higher magnitude cell and the large cell forms a womb like profile which is reduced with the increase of inclination angles.

9.4.4 Temperature Contours and Surface Temperature

In this section, variations of the temperature profile along the pipe for different inclination angles has been presented in Figs. 9.10 and 9.11 to understand how the Buoyancy force affects the thermal field as well.

For $\theta = 0°$, it is found that most of the region of the pipe is covered with the deep blue colour that refers to the lower temperature region. On the other hand, higher temperature is observed near the wall region. Also, the maximum temperature difference between the higher and lower temperature region is found to be approximately $6K$. Moreover, the growth of thermal boundary layer seems to be steady and fully developed when $x > 0.25\, m$. Again, it is worth noting that these behaviours agree well with the previous findings reported in Chapter 4.

For $\theta = 15°$, a sudden change in the growth of thermal boundary layer is observed near the bottom wall region when $x < 0.2\, m$. But after that region, a development of boundary layer seems to be steady and tends to be fully developed. Similar behaviour is also observed for $\theta = 30°$ and $45°$. This behaviour indicates the effect of the Buoyancy force when the Boussinesq approximation is considered. For $\theta = 60°$ and $75°$, a deformation of the growth of thermal boundary layer is observed near the top wall when $x < 0.2\, m$. However, the development of boundary layer seems to be more pronounced and higher boundary layer thickness is also observed for the increase of inclination angles when $x > 0.2\, m$ for the increase of inclination angles. This suggests, the thermal flow filed tends to behave more like a fully developed turbulent flow than that of transition flow.

In order to calculate the surface temperature, a circumference averaged wall temperature of the pipe has been calculated for different inclination angles. Figure

9.12 shows the variations of surface temperature with different inclination angles using the single and multi-phase models for Al_2O_3-H_2O and TiO_2-H_2O nanofluids. For all the cases, it is observed that the surface temperature increases rapidly near the upstream though it starts to decrease at the thermal critical point. Then, a steady state pattern is observed there and a slight monotonically increasing behaviour of surface temperature is seen along the pipe. It is also noticed that the surface temperature increases with the increase of inclination angles from θ = 0° to 75°. Also, higher surface temperature is observed in the single phase model than that in the multi-phase model.

In particular, the thermal critical distance decreases and moves towards the upstream region with the increase of inclination angles from θ = 0° to 45° for Al_2O_3-H_2O nanofluid. It suggests, the transition behaviour of the thermal filed starts to diminish due to the buoyancy force for the higher inclined pipe. Again, the existence of thermal critical point is not visible for θ = 60°. This suggests, the buoyancy force plays a dominant role in the mixed convection and transition behaviour of thermal field tends to vanish. On the other hand, the surface temperature starts to rise initially for θ = 75° though it suddenly decreases then. And it starts to rise rapidly again. This behaviour indicates, there is a quick transformation of surface temperature from transition to turbulent regime. Although such behaviour follows neither the transition nor the turbulent behaviours fully, results suggest that turbulence is more dominance in the flow and thermal fields. This can be justified further from Figs. 9.8 and 9.9 since the maximum turbulent kinetic energy found here is 0.01121 m^2/s^2, 0.014022 m^2/s^2, 0.02085 m^2/s^2, 0.024193 m^2/s^2, 0.024605 m^2/s^2 and 0.024665 m^2/s^2 for θ = 0°, 15°, 30°, 45°, 60° and 75° respectively.

Furthermore, the surface temperature at the thermal critical point has been found to be same in both of the single and multi-phase models for θ = 0°. But for θ > 0°, the surface temperature at the thermal critical point has been found higher in the single phase model than that in the multi-phase model. Besides, Al_2O_3-H_2O nanofluid has shown lower surface temperature than TiO_2-H_2O nanofluid for θ = 0°. It thus indicates. the forced convection plays an important role for nanofluids flow in horizontal pipe. However, TiO_2-H_2O nanofluid has shown lower surface temperature than Al_2O_3-H_2O nanofluid for θ > 0°. This means, the mixed convection plays an important role for nanofluids flow in an inclined pipe.

9.4.5 Local Nusselt Number Behaviour

Figure 9.13 shows the variations of local Nusselt number with different inclination angles for Al_2O_3-H_2O and TiO_2-H_2O nanofluids using single and multi-phase models. In all these cases, the local Nusselt number has always been found to be maximum near the upstream although it starts to decrease rapidly afterwards. And at the thermal critical point, it starts to rise again. Further, the local Nusselt number tends to become constant and steady from the thermal critical point as the flow tends to become fully developed. The local *Nu* is observed to decrease with the increase of inclination angles from θ = 0° to 75°. Again, the higher local Nusselt number is observed in the multi-phase model than in the single phase model. These findings are feasible because of the increase of surface temperature along with the increase of inclination angles from θ = 0° to 75°.

Once more, the local Nusselt number is found to be identical at the critical point and in both of the single and multi-phase models for θ = 0°. But for θ > 0°, the local *Nu* at the critical point is found to be higher in the multi-phase model than in the single phase model. However, the Al_2O_3-H_2O nanofluid shows the higher local *Nu* than the TiO_2-H_2O nanofluid while using both the single and multi-phase models for θ = 0°. But for θ > 0°, the TiO_2-H_2O nanofluid shows higher local Nusselt number than the Al_2O_3-H_2O nanofluid.

Another particular investigation has been carried out to understand the transitional behaviour of different inclination angles, θ = 45° to 75° as presented in Fig. 9.14. It is observed that transition behaviour actually exists for θ < 55° and then, no sudden changes of local *Nu* is visible for θ = 55° to 60° suggesting the diminish of transition behaviour. For θ = 60°, the critical point diminishes and this indicates the rapid increase of surface temperature that forces to decrease the local Nusselt number. Again, this number is found to be the maximum near the upstream and then it starts to decrease gradually for θ > 60°. After that, a sudden rapid rise and speedy decay is observed and it tends to be constant along the pipe. It specifies that local *Nu* behaves neither like a transition flow nor like a turbulent flow.

A detailed investigation has been carried out in order to understand the behaviour of hydrodynamic and thermal critical distances and the results are presented in Fig. 9.15. Here, both the hydrodynamic and thermal critical distances decrease with the

increase of inclination angles though no transition behaviour of the thermal flow field is observed for $\theta \geq 60°$. This is already shown in Fig. 9.13. It indicates, the transition behaviour of thermal flow field is more affected by the Buoyancy force in the mixed convection. Two different peak positions clearly visible in Fig. 9.13 is found to be present when $\theta > 60°$ These positions can be referred to the first and second transition points respectively. Another investigation has been carried out to understand the behaviour of thermal critical distance for $\theta \geq 60°$ and the results are presented in Fig. 9.16. Here, the first and second critical distances decrease with the increase of inclination angles when $\theta > 60°$. It is also observed that the first critical distance decreases with the increase of Reynolds number when $Re < 4000$. But, such distance becomes constant when $4000 \leq Re \leq 10000$. The second critical distance decreases with the increase of Reynolds number when $Re < 8000$ and then it becomes constant when $8000 \leq Re \leq 10000$. Such behaviour indicates that the way of flow separation and critical distances are quite different when $\theta \geq 60°$. Also, the flow separation causes more disturbance in the flow field and the separated flow tends to behave like more turbulent than transition due to the Buoyancy force.

Another particular investigation is done to understand the variations of maximum turbulent kinetic energy with different Reynolds number for different inclination angles as shown in Fig. 9.17. It is observed that the maximum turbulent kinetic energy increases with the increase of inclination angles when $\theta < 60°$. But it starts to decrease with the increase of inclination angles when $\theta \geq 60°$. Such behaviour supports the findings shown in Figs. 9.13 to 9.16. As it has been already discussed, the transition behaviour tends to diminish when $0° \leq \theta < 60°$ and both the local Nu and surface temperature T behave like neither fully transition nor fully turbulent flow when $\theta \geq 60°$. Such changes in behaviour are also visible in the results shown in Fig. 9.17. The hydrodynamic and thermal critical distances are strongly dependent on the Reynolds number as well as on the inclination angle but independent to the types of nanofluids, nanoparticles diameters and concentrations. These findings are realistic and physically valid with what has been shown in Chapter 4.

9.4.6 Darcy Friction Factor Behaviour

Darcy friction factor results are presented in Fig. 9.18 with a view to understand the pressure drop behaviour affected by the Buoyancy force inside the inclined pipe. To

do this, the variations of Darcy friction factor with different inclination angles and the Reynolds numbers for Al_2O_3-H_2O and TiO_2-H_2O nanofluids have been presented here. There is an insignificant difference between the Darcy friction factor results of nanofluids and base fluid (water) in the horizontal pipe. This has been described in Chapter 4. But, the Darcy friction factor increases with the increase of inclination angle from θ = 0° to 75° in the inclined pipe. Also, a higher Darcy friction factor is observed in the mixed convection case than that is seen in the forced convection. It is the additional buoyant force which compels to enhance the pressure drop inside the pipe. Again, more significant enhancement of Darcy friction factor in the mixed convection case is observed than that found in the forced convection case for low Reynolds number and θ = 30°. As the inclination angle increases, such rapid enhancement tends to reduce in comparison with the Darcy friction factor result of θ = 30°. This is again the buoyancy force which affects the flow and pressure fields. In addition, there have been insignificant differences among the Darcy friction factor results with different inclination angles while using both Al_2O_3-H_2O and TiO_2-H_2O nanofluids for the higher Reynolds number such as $Re \geq 8000$.

In the particular cases for Al_2O_3-H_2O nanofluid, the maximum percentages of the variations of Darcy friction factor are 12.86%, 22.13%, 29.41% and 32.80% respectively compared with the Darcy friction factor results in horizontal pipe with the inclination angles of 30°, 45°, 60° and 75°. However, the maximum percentages of the variations of Darcy friction factor are found to be 12.81%, 21.64%, 29.49% and 32.97% respectively in such cases of TiO_2-H_2O nanofluid with the inclination angles of 30°, 45°, 60° and 75°. These reveal, Al_2O_3-H_2O nanofluid shows the higher percentages of enhancement in Darcy friction factor than TiO_2-H_2O nanofluid for θ = 30° and 45°. Though, the opposite trend is observed in case of θ = 60° and 75°. Besides, the maximum percentages of the enhancement in Darcy friction factor is observed for θ = 75° while using TiO_2-H_2O nanofluid.

9.4.7 Average Nusselt Number Behaviour

Figure 9.19 shows the variations of average Nusselt number with the Reynolds number and different inclination angles from θ = 0° to 75° for Al_2O_3-water and TiO_2-water nanofluids. Here, both the single phase model (SPM) and multi-phase model (MPM) are considered. At this point, the average Nusselt number is observed to

decrease with the increase of inclination angles from θ = 0° to 75° and the higher average Nusselt number is found in the multi-phase model than in the single phase model. Also, the average Nusselt number of the nanofluids is always higher than that of water at any given Reynolds number for θ = 0° to 75°.

In particular, the maximum percentages of deviation are approximately 3.87%, 10.05%, 16.32% and 19.48% respectively for Al_2O_3-H_2Onanofluid, single phase model and θ = 30°, 45°, 60° and 75°. These are lower than that in the horizontal pipe. While for multi-phase model, these are approximately 3.81%, 9.89%, 16.21%and 19.31% respectively and lower than that in the horizontal pipe too. However, the maximum percentages of deviation are approximately 4.34%, 9.18%, 14.90% and 18.71% respectively for TiO_2-H_2Onanofluid, single phase model and θ = 30°, 45°, 60° and 75°. Similarly, these are approximately 4.28%, 9.02%, 14.76% and 18.58% respectively for multi-phase model. All of these percentages are lower than those in the horizontal pipe. These results indicate, the average Nusselt number in inclined pipes are lower than that of horizontal pipe and the maximum degeneration of heat transfer is observed for θ = 75° and Al_2O_3-H_2O nanofluid. The reason behind such degeneration of heat transfer rate in inclined pipe is the effect of buoyancy. Because, it forces to enhance the surface wall temperature resulting the reduction of heat transfer rate in comparison with the heat transfer rate in horizontal pipe.

9.5 Conclusion

As it is stated at the beginning, numerical investigation has been performed in order to understand the heat transfer behaviour of transition mixed convection in inclined pipe for this chapter. And, two different types of nanofluids such as Al_2O_3–water and TiO_2–water nanofluids have been considered as working fluid as well as two different models called the single and multi-phase models have been used throughout this investigation. Results are presented in terms of x-velocity and turbulent kinetic energy contours, surface temperature, local and average Nusselt number as well as Darcy friction factor. So, the following conclusions can be drawn from the outcomes:

- The contours of flow field and turbulent kinetic energy is found to be distorted near the upstream region along with the increase of inclination angles due to Buoyancy force.

- The surface temperature is observed to increase along with the increase of Reynolds number in the different inclination angles. Also, higher surface temperature is observed for the higher inclination angles. Such enhancement of wall temperature is responsible for the degeneration of heat transfer rate.
- The Darcy friction factor is increased along with the increase of Reynolds number in different inclination angles. Also, the higher Darcy friction factor is noticed in the higher inclination angles. And, such enhancement is found to be liable for the higher penalty in pumping power.
- The local Nusselt number is decreased with the increase of inclination angles. Also, it is found that transition behaviour of local Nusselt number exists for $0° < \theta < 55°$ and then it starts to diminish. And then, neither transition nor turbulent behaviour is seen when $\theta > 60°$.
- The average heat transfer rate is decreased along with the increase of Reynolds number in different inclination angles. It suggests, mixed convection has opposite effect on the inclined pipe than the forced convection on the horizontal pipe.

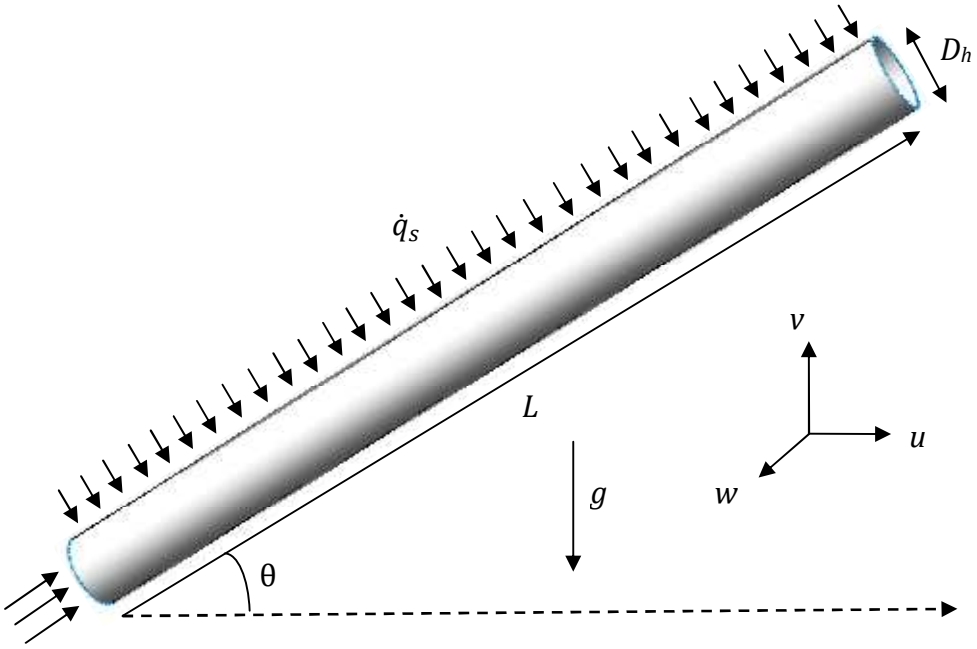

Figure 9.1: Schematic diagram of the geometry under consideration

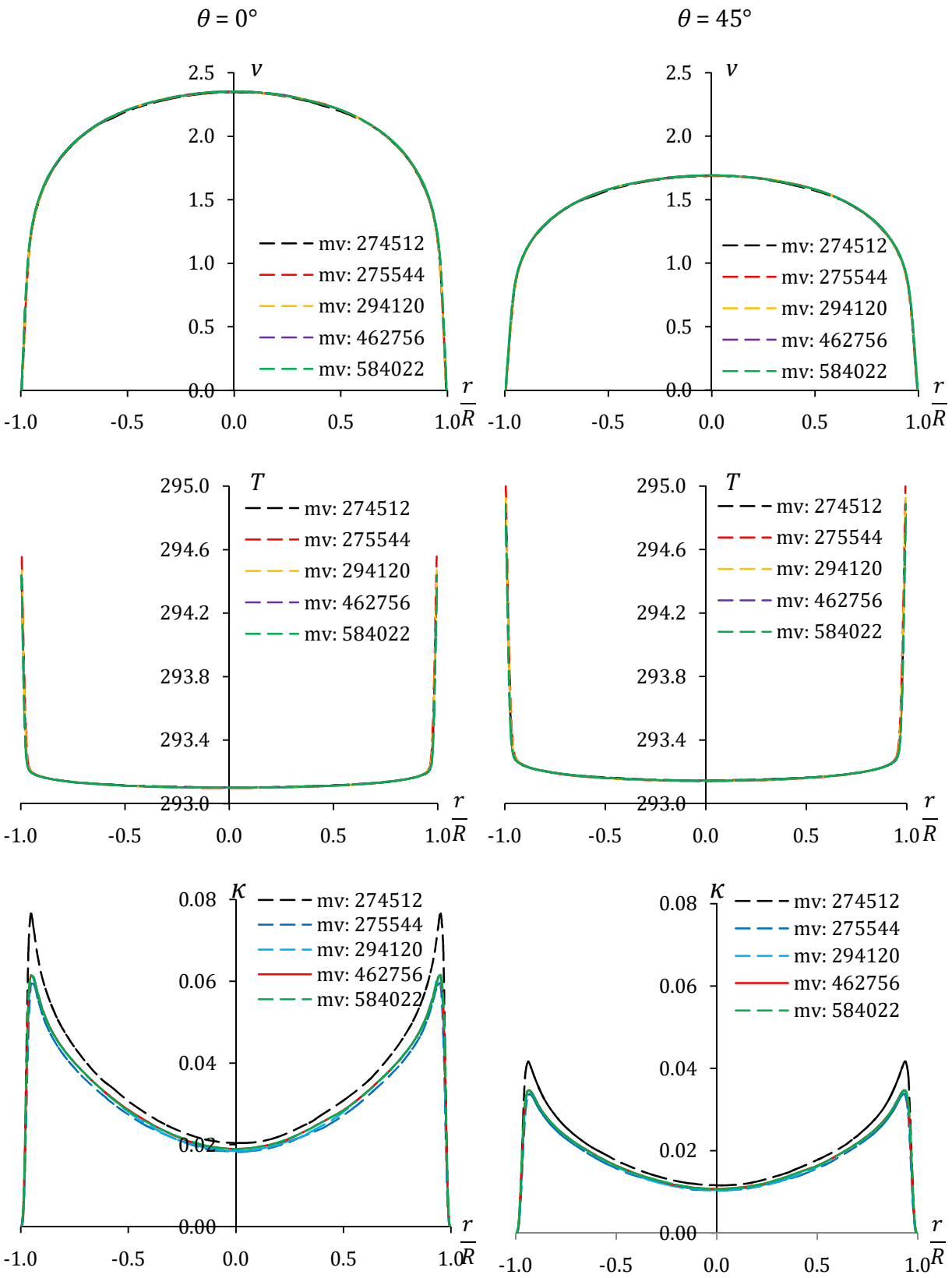

Figure 9.2: Variations of radial velocity, temperature and turbulent kinetic energy at x = 0.99 m with different mesh volumes for Re = 10000, θ = 0° and θ = 45°, and Al_2O_3-H_2O nanofluid (mv refers to mesh volume)

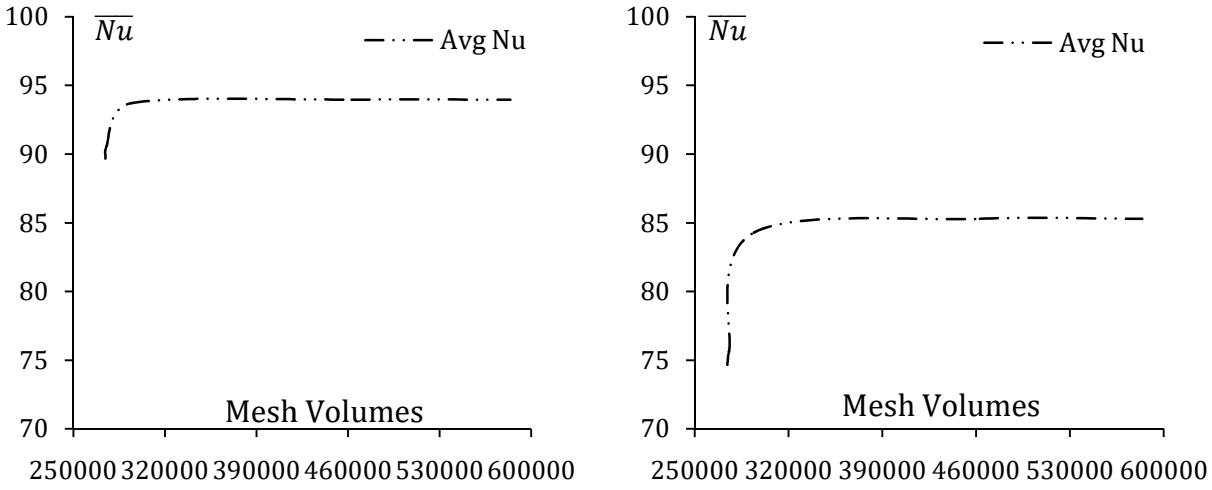

Figure 9.3: Variations of average Nusselt number with different mesh volumes for *Re* = 10000, θ = 0° and θ = 45°, and Al_2O_3-H_2O nanofluid

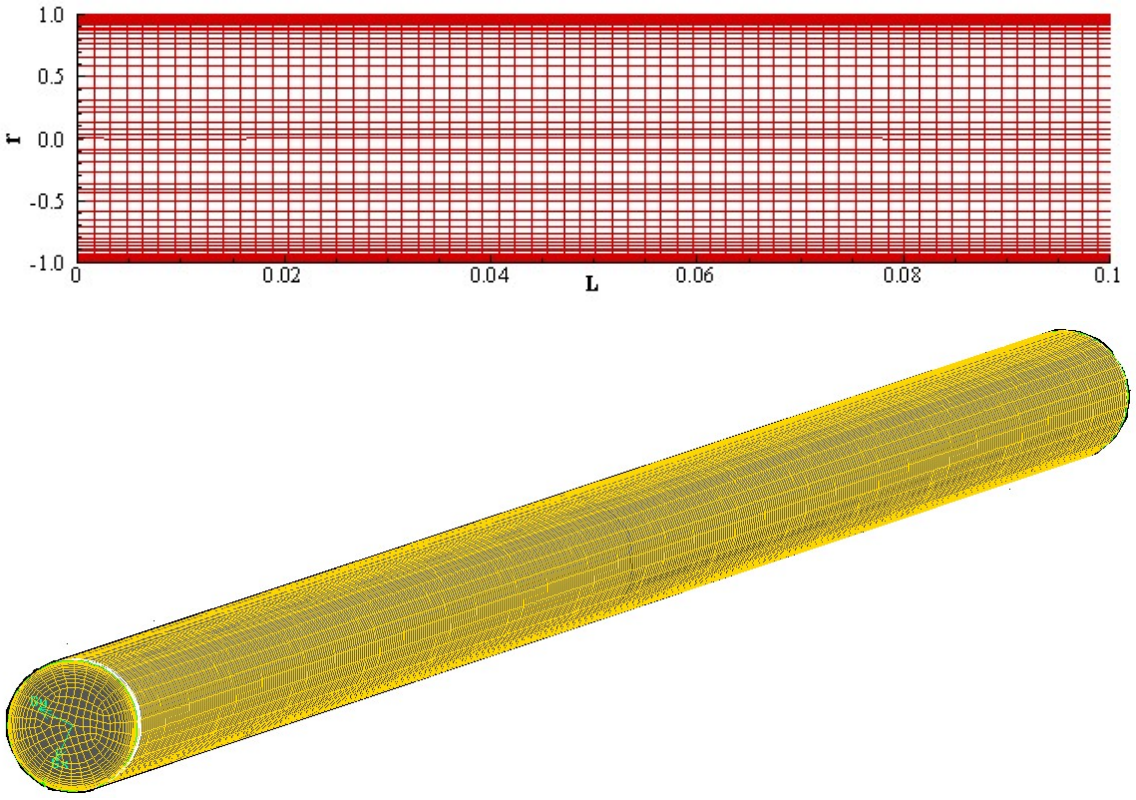

Figure 9.4: 2D and 3D view of mesh distributions along the pipe

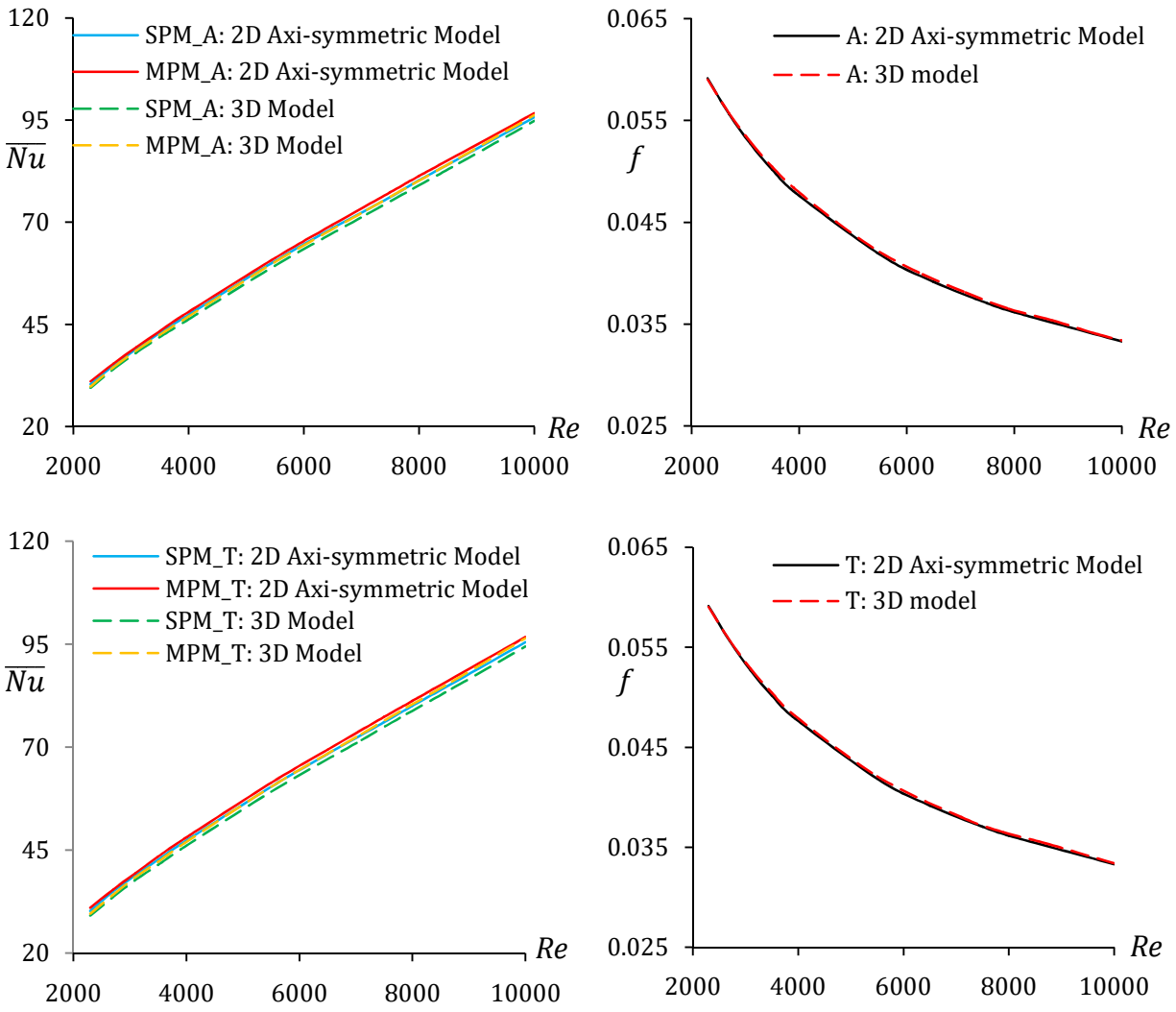

Figure 9.5: Comparisons between the results of average Nusselt number and Darcy friction factor of horizontal pipe with different Reynolds numbers using the 2D axi-symmetric and 3D models for A: Al_2O_3-H_2O and T: TiO_2-H_2O nanofluids

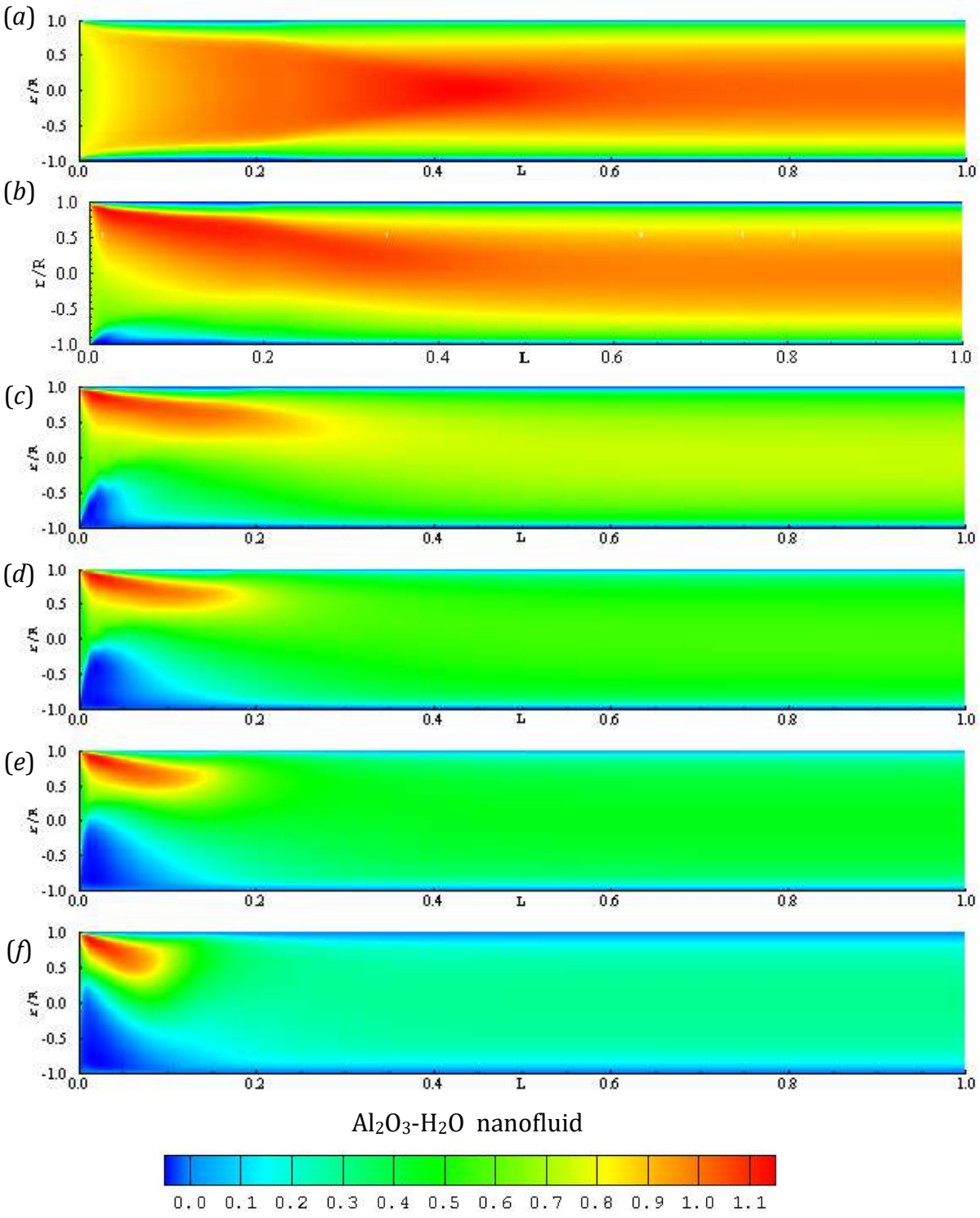

Figure 9.6: Variations of axial velocity along the pipe for different inclination angles (*a*) $\theta = 0°$, (*b*) $\theta = 15°$, (*c*) $\theta = 30°$, (*d*) $\theta = 45°$, (*e*) $\theta = 60°$, (*f*) $\theta = 75°$ and $Re = 3500$

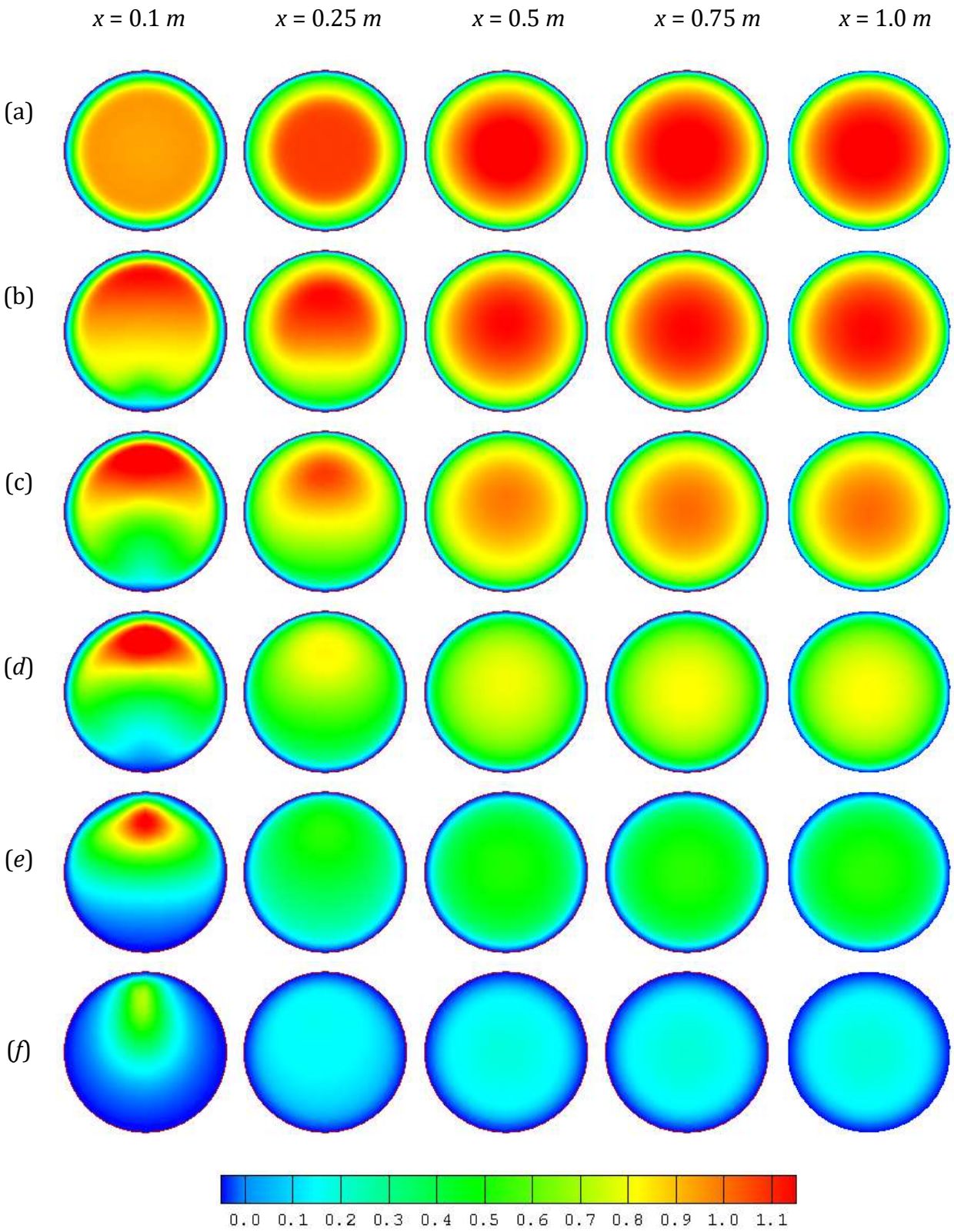

Figure 9.7: Velocity contours for different inclination angles (*a*) θ = 0°, (*b*) θ = 15°, (*c*) θ = 30°, (*d*) θ = 45°, (*e*) θ = 60°, (*f*) θ = 75° and *Re* = 3500 at axial position *x* = 0.1 *m*, 0.25 *m*, 0.5 *m*, 0.75 *m* and 1.0 *m*(left to right) respectively.

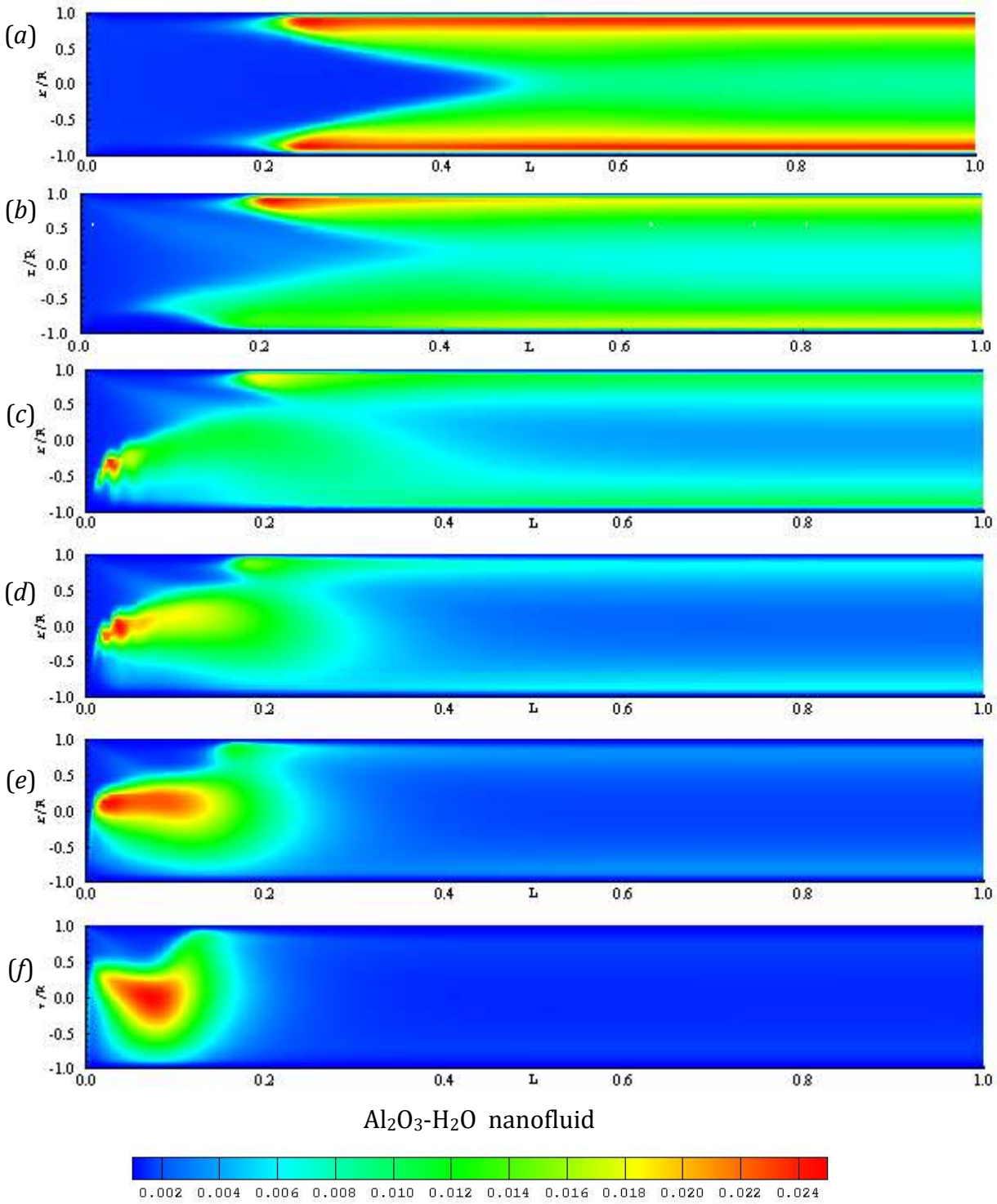

Figure 9.8: Variations of turbulent kinetic energy along the pipe for different inclination angles (*a*) θ = 0°, (*b*) θ = 15°, (*c*) θ = 30°, (*d*) θ = 45°, (*e*) θ = 60°, (*f*) θ = 75° and *Re* = 3500

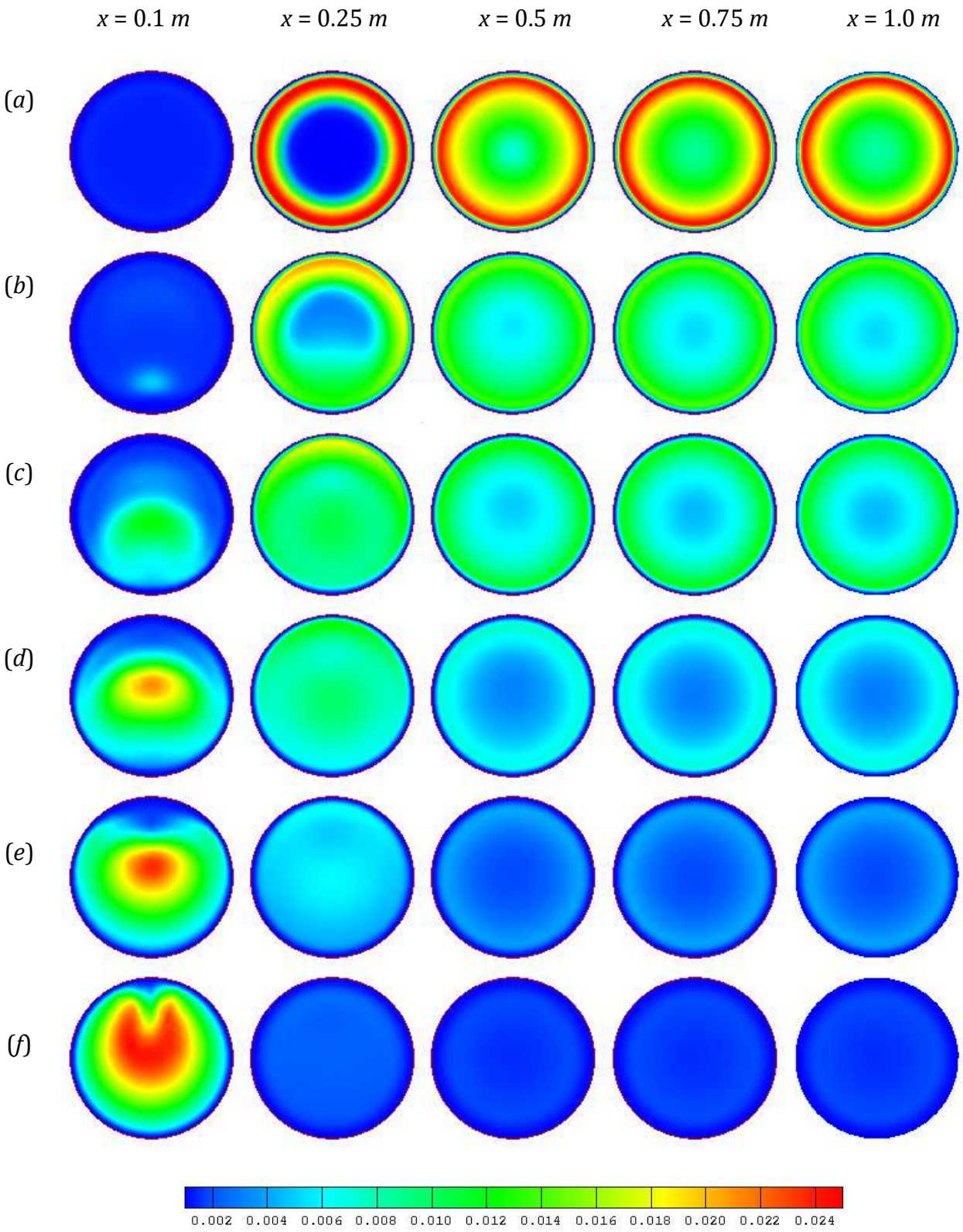

Figure 9.9: Turbulent kinetic energy contours for different inclination angles (*a*) θ = 0°, (*b*) θ = 15°, (*c*) θ = 30°, (*d*) θ = 45°, (*e*) θ = 60°, (*f*) θ = 75° and *Re* = 3500 at axial position *x* = 0.1 *m*, 0.25 *m*, 0.5 *m*, 0.75 *m* and 1.0 *m* respectively

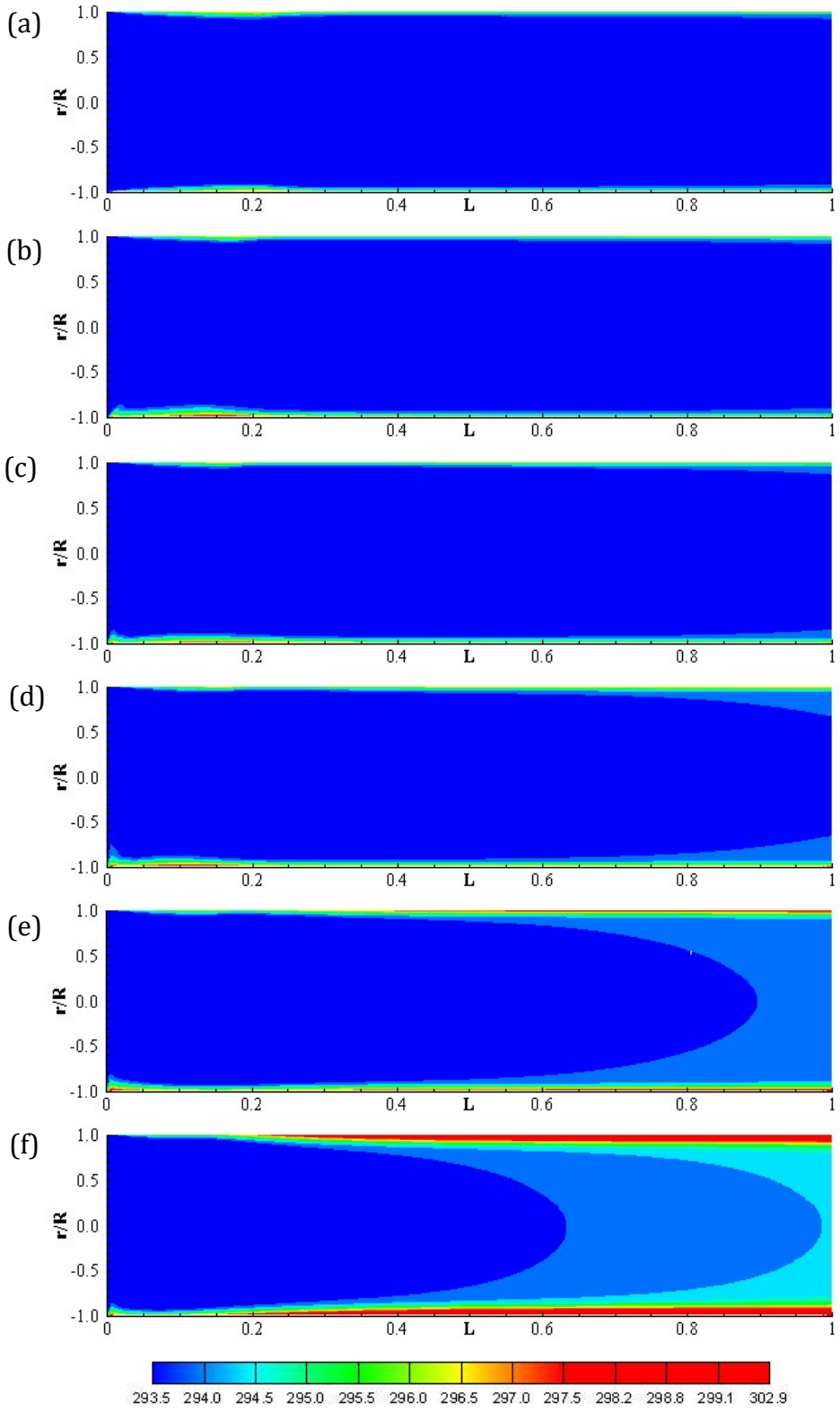

Figure 9.10: Variations of temperature along the pipe for different inclination angles (*a*) $\theta = 0°$, (*b*) $\theta = 15°$, (*c*) $\theta = 30°$, (*d*) $\theta = 45°$, (*e*) $\theta = 60°$, (*f*) $\theta = 75°$ and $Re = 3500$

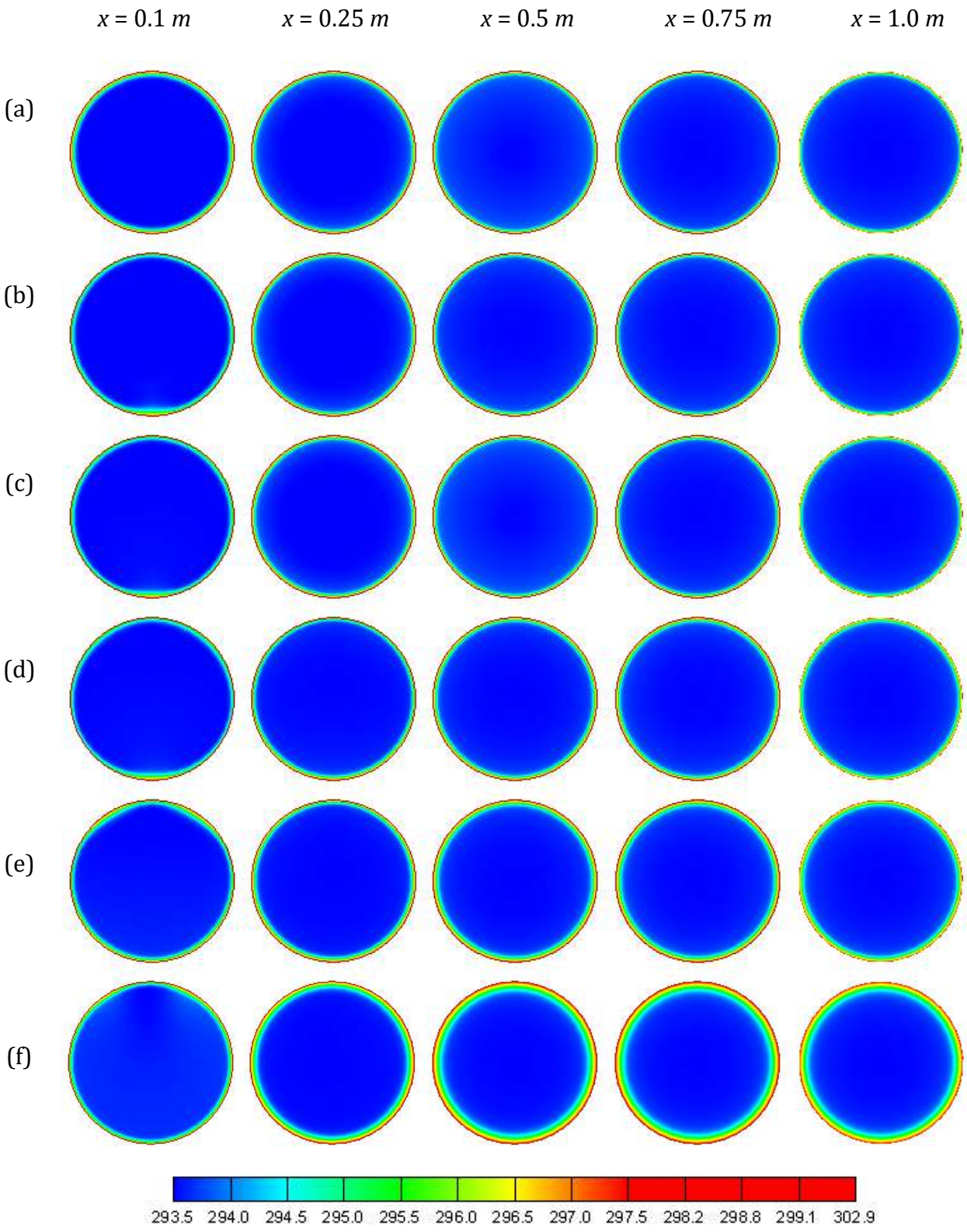

Figure 9.11: Temperature contours for different inclination angles (a) θ = 0°, (b) θ = 15°, (c) θ = 30°, (d) θ = 45°, (e) θ = 60°, (f) θ = 75° and Re = 3500 at axial position x = 0.1 m, 0.25 m, 0.5 m, 0.75 m and 1.0 m respectively

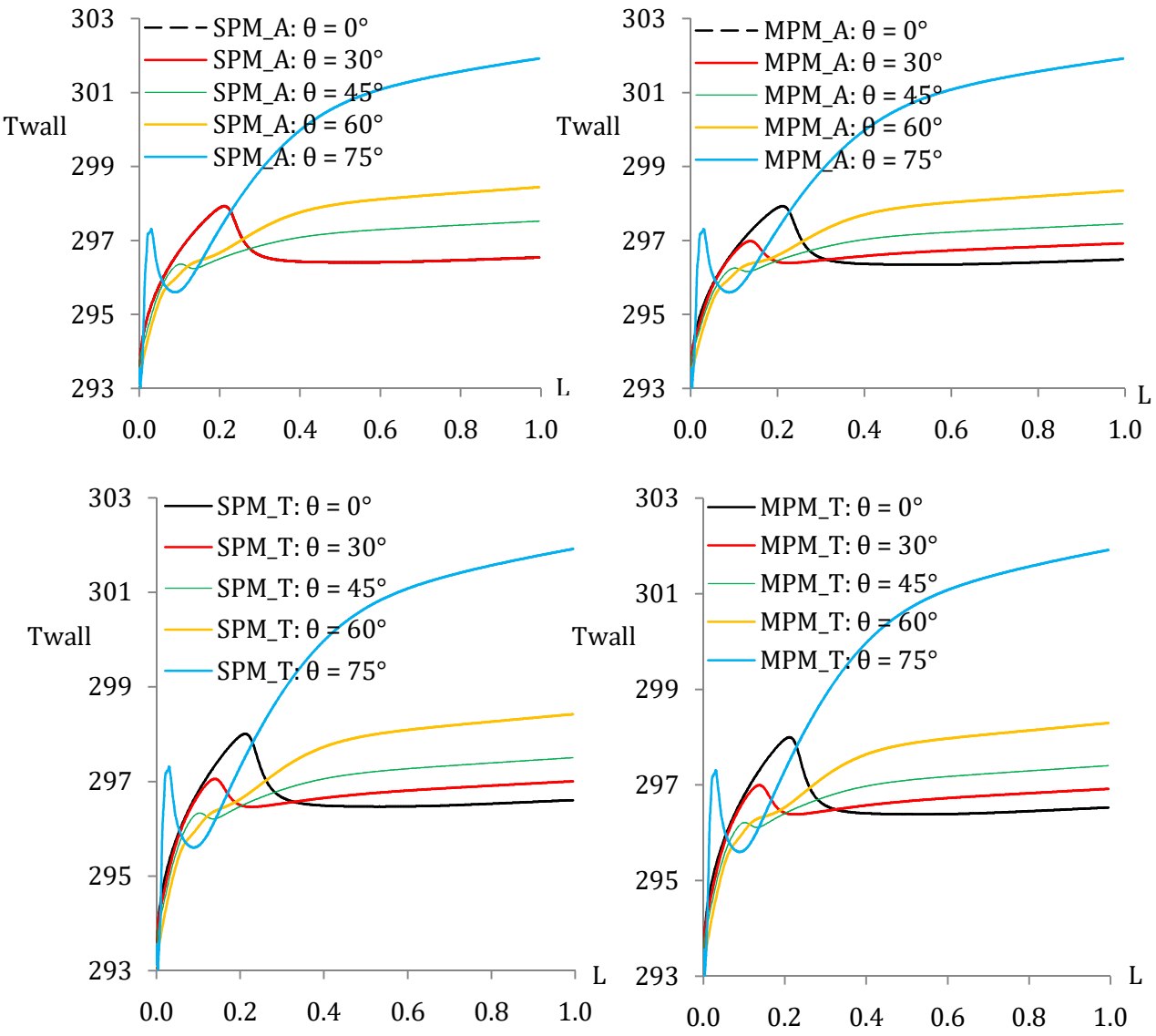

Figure 9.12: Variations of surface temperature with different inclination angles, θ = 0° to 75° for *Re* = 3500

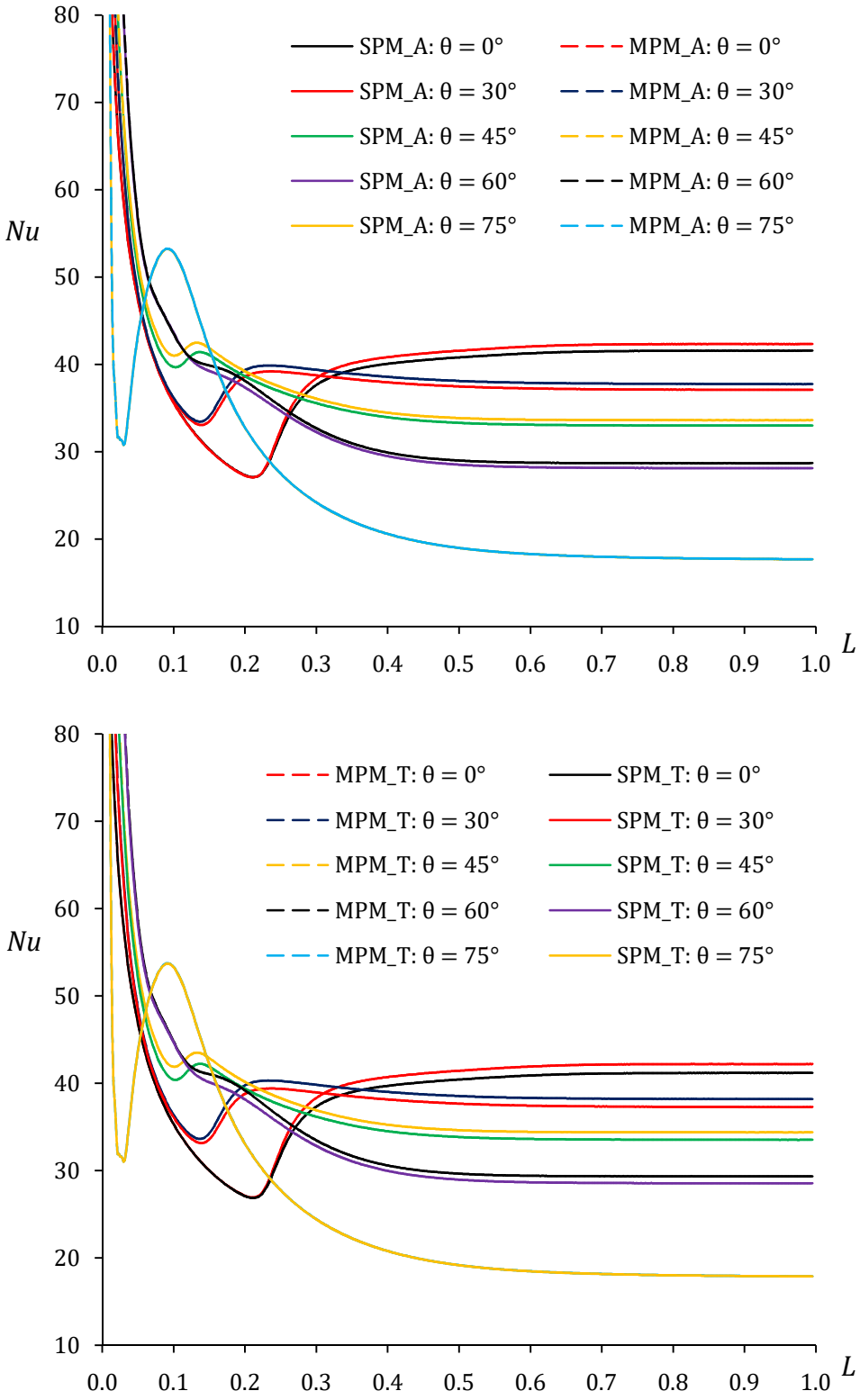

Figure 9.13: Variations of local Nusselt number with different inclination angles, θ = 0° to 75° for Re = 3500

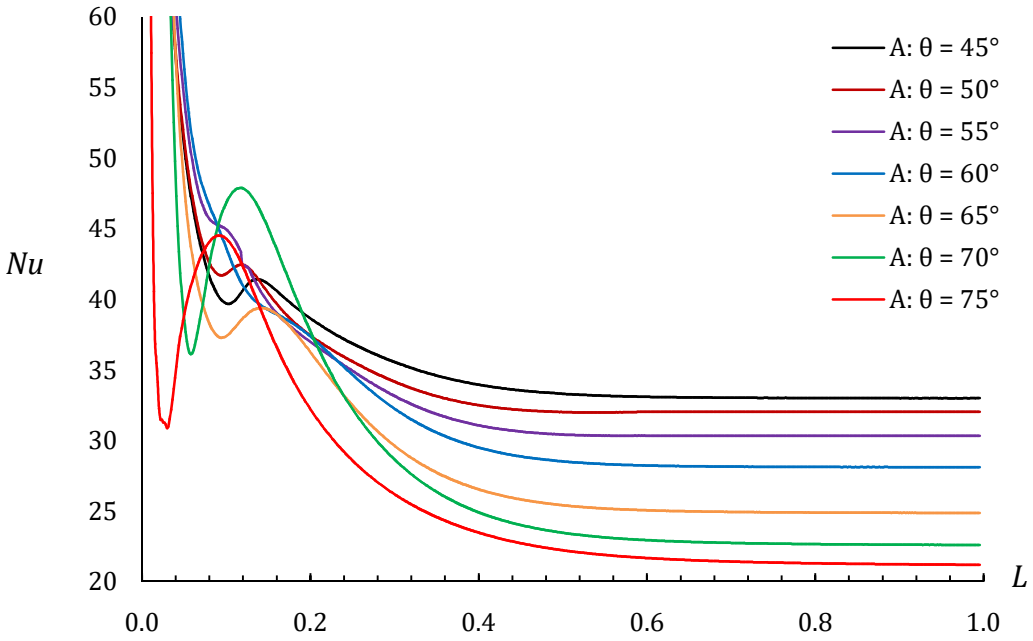

Figure 9.14: Variations of local Nusselt number with different inclination angles, θ = 45° to 75° for Re = 3500

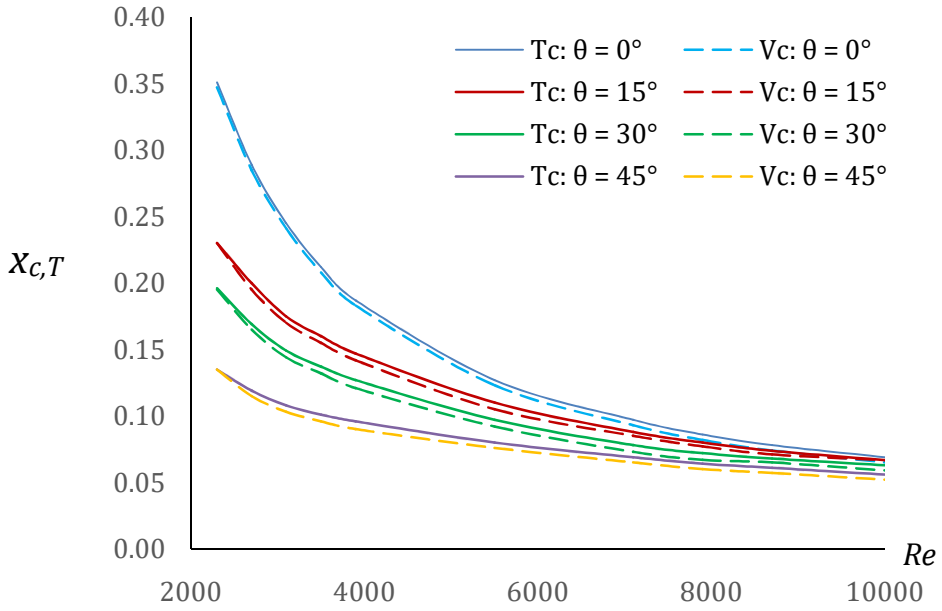

Figure 9.15: Variations of thermal and hydrodynamic critical distances with different Reynolds numbers for different inclination angles, θ = 0° to 45°

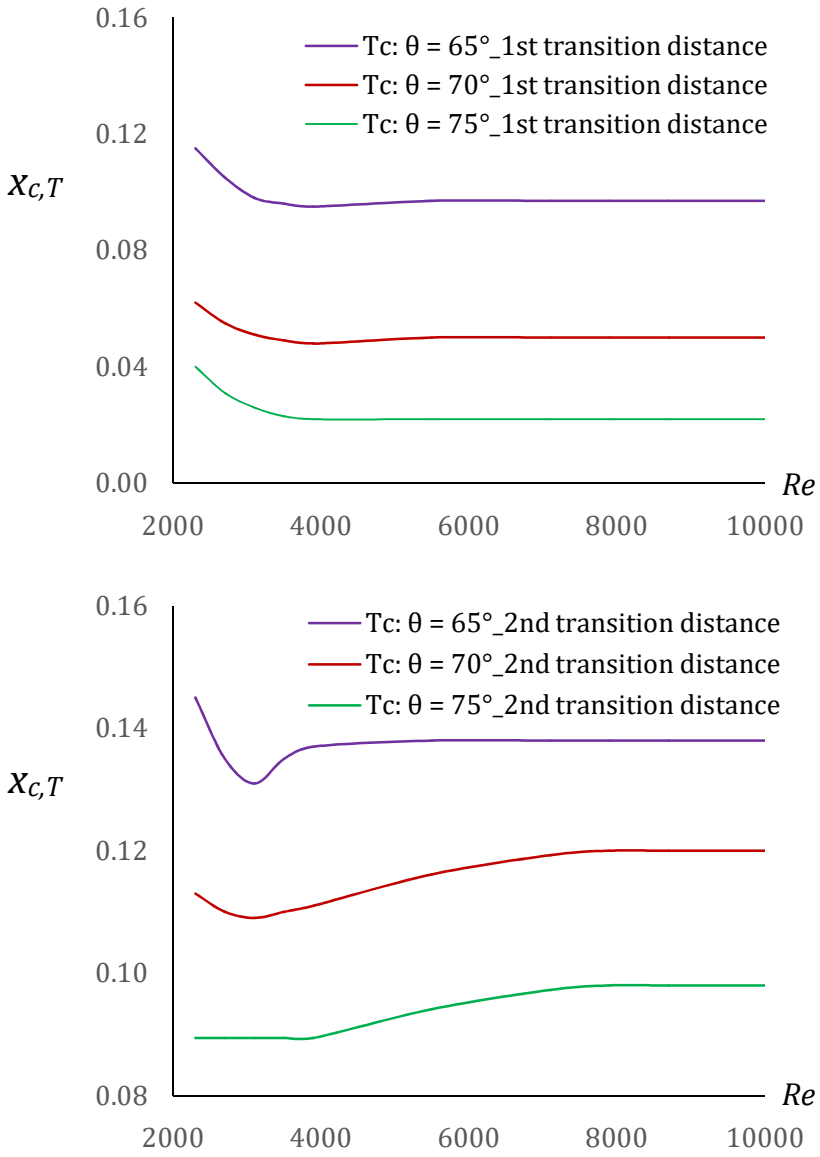

Figure 9.16: Variations of thermal critical distances with different Reynolds numbers for different inclination angles, θ = 65° to 75°

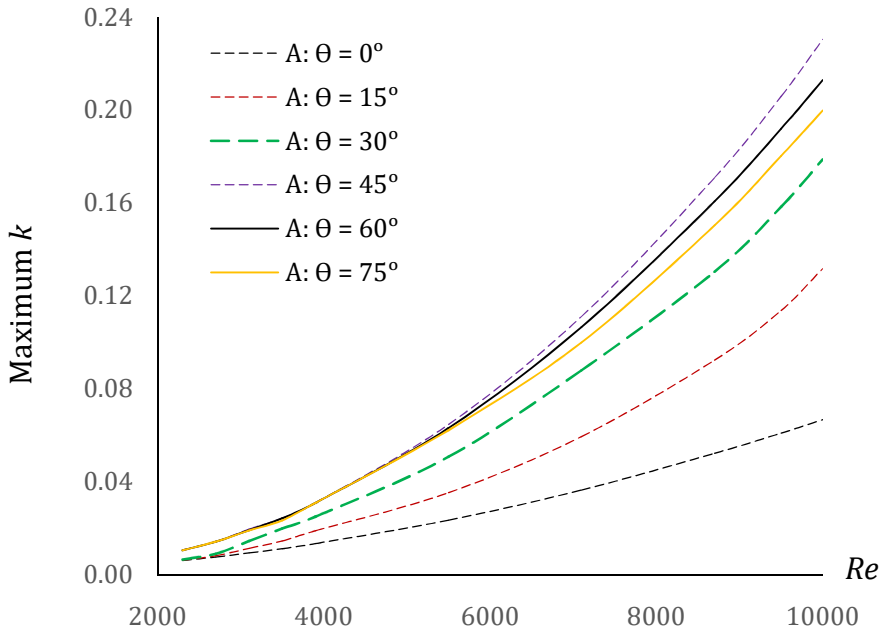

Figure 9.17: Variations of maximum turbulent kinetic energy (k) with Reynolds numbers for different inclination angles, θ = 0° to 75°

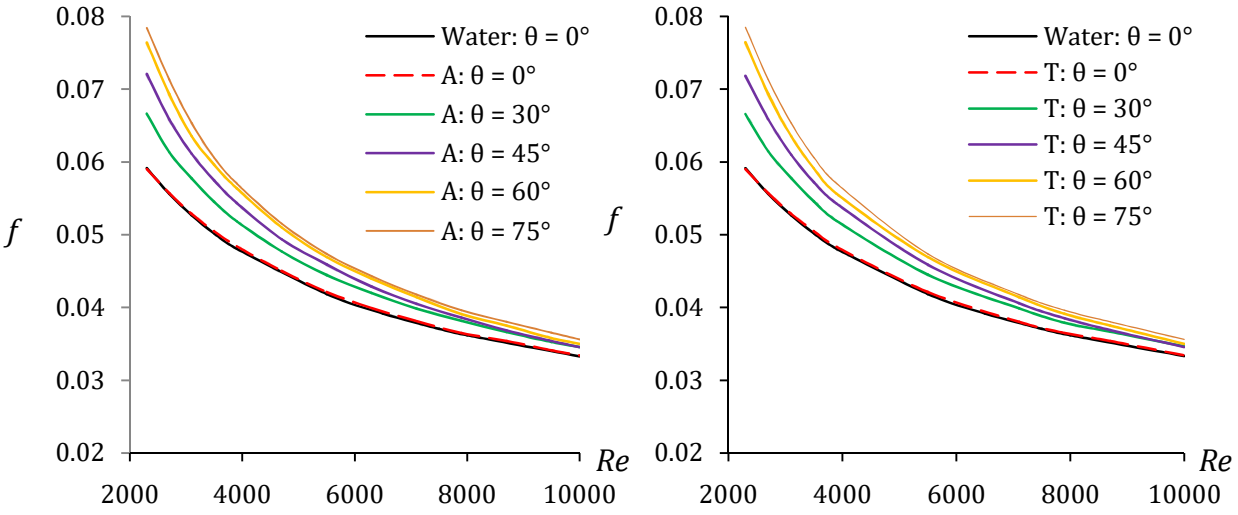

Figure 9.18: Variations of Darcy friction factor with different Reynolds numbers for different inclination angles, θ = 0° to 75°

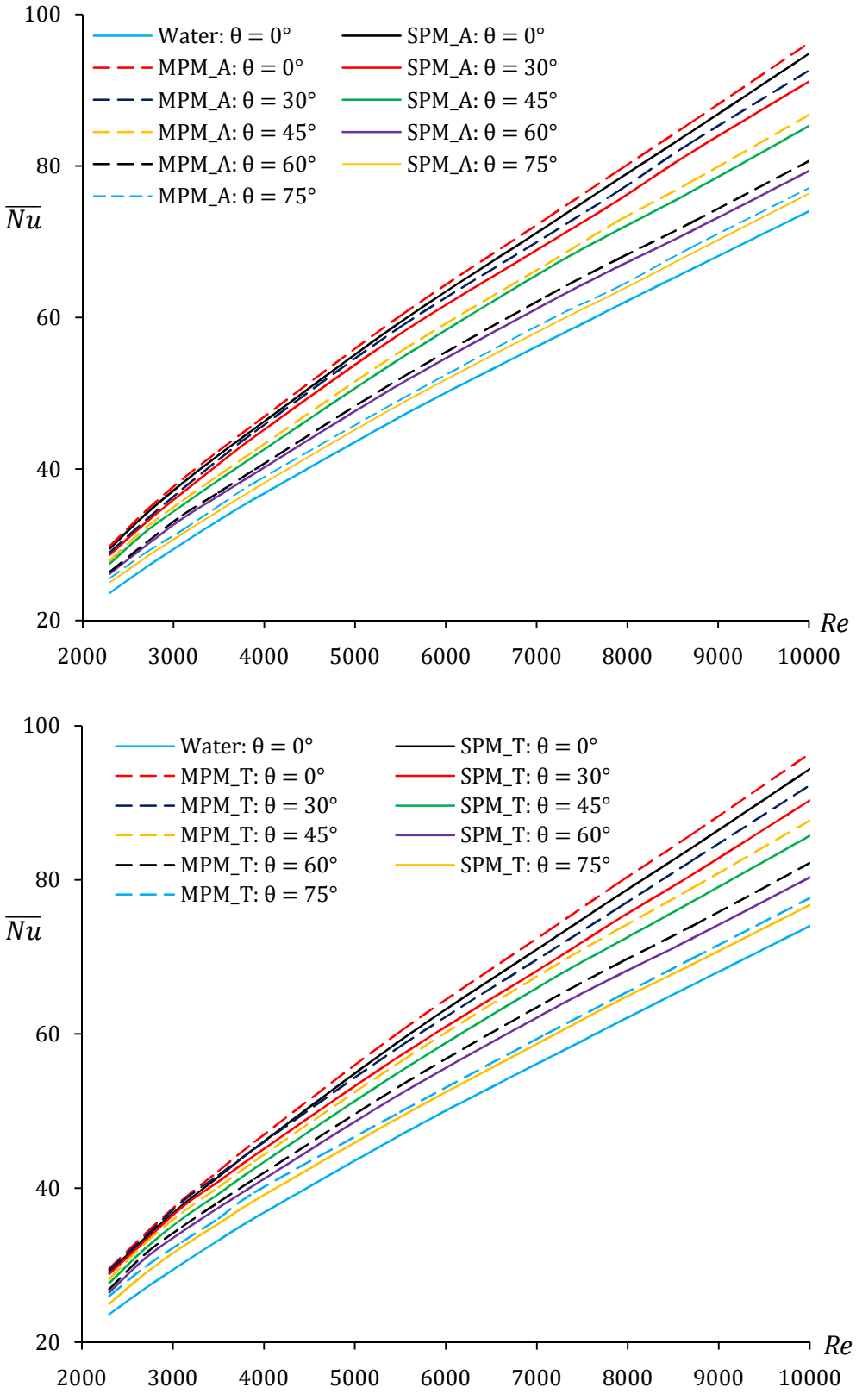

Figure 9.19: Variations of Average Nusselt number with different Reynolds numbers for different inclination angles, θ = 0° to 75°

Chapter 10

Conclusions and Future Work

Conclusions from the present research are given in Section 10.1 and some useful recommendations for future research are made in Section 10.2.

10.1 Conclusions

Numerical investigations of forced convection flow have been studied in a horizontal pipe under transition and turbulent flow regimes. Particular investigation has been done in order to assess the performance of rough wall surface under transition flow condition. Finally, the effect of inclination angle in mixed convection flow in an inclined pipe is presented. From the above studies, the following conclusions are drawn:

- Darcy friction factor results of water as well as nanofluids found to be identical and average Nusselt number results of nanofluids are found always higher compared to water for different nanoparticles diameter and concentrations under transition to turbulent flow regimes.

- The combination of smaller size nanoparticles and high concentrations with Brownian motion of nanoparticles shows the highest heat transfer rate under transition to turbulent flow regimes. Also, the higher heat transfer rate is found for the higher roughness conditions with uniform roughness applied to the pipe wall under transition regime. However, Darcy friction factor increases with the increase of roughness height which indicates higher penalty in pumping power.

- No optimal Reynolds number is found for the transition flow in pipe. But for d_p = 10 nm, χ = 6%, optimal Reynolds number is found for the turbulent flow in pipe which minimised the total entropy generation. Also, optimal Reynolds number is found for different roughness heights under transition flow condition.

- Heat transfer performance of DPM model is found quite satisfactory compared with the results obtained using SPM and MPM for low nanoparticles concentration. But for higher nanoparticles concentration, heat transfer performance deviates more from the experimental and numerical results and it, therefore, suggests that the DPM model cannot be useful to produce results with better accuracy.

- It is observed that the friction factor is increased along with the increase of Reynolds numbers in different inclination angles. Also, local Nusselt number is decreased with the increase of inclination angles. Moreover, it is also found that the transition behaviour of local Nusselt number exists for $0° < \theta < 55°$ and then neither transition nor turbulent behaviour is seen when $\theta > 60°$. It is also observed that the heat transfer rate decreases with the increase of inclination angles. It thus indicates that the heat transfer rate is higher in the forced convection than that in the mixed convection.

- Overall, heat transfer enhancement is observed while using both the single and multi-phase models. It is seen that there are insignificant difference between the results obtained using SPM and MPM. Such findings help us to conclude that single phase model can still be applied in the practical applications considering the limitations that there is no interaction between the fluid particles and nanoparticles. Darcy friction factor results of water as well as nanofluids found to be identical and average Nusselt number results of nanofluids are found always higher compared to water for different nanoparticles diameter and concentrations under transition to turbulent flow regimes.

10.2 Future Work

The present research shows the impact of two different environment friendly oxide nanofluids on heat transfer under transition and turbulent flow regimes. In the following section, some recommendations for future research work are presented to extend the present work potentially:

- The study of heat transfer behaviour in forced convection of nanofluids flow in micro and nano-sized pipe is very limited. More attention is necessary to

investigate such behaviour which will help to understand the use of nanofluids flow in micro and nano-sized pipe under laminar to turbulent flow regimes.

- It is important to understand the behaviour of fluid-nanoparticles mixture. Very limited information is available in the literature about the performance of Brownian force, Thermophoretic force and Saffman's lift force of nanoparticles on heat transfer enhancement under laminar to turbulent flow regimes. More experimental investigations are also necessary to justify the use of simple solid-fluid mixture instead of nanofluids.
- In order to gain knowledge on heat transfer enhancement, other physical models can be used. Also, the performance in the use of magnetic and other nanoparticles in different types of base fluids should be investigated.

References

[1] S.U.S. Choi, Enhancing Thermal Conductivity of Fluids with Nanoparticles, Developments and Applications of Non-Newtonian Flows, D.A. Siginer and H.P. Wang, eds, FED-vol. 231 / MD-vol. 66 ASME (1995) 99-105.

[2] D. Singh, J. Toutbort, G. Chen, Heavy vehicle systems optimization merit review and peer evaluation, in, Argonne National Laboratory (2006) 405-411.

[3] J.C. Nelson, D. Banerjee, R. Ponnappan, Flow loop experiments using polyalphaolefin nanofluids, Journal of Thermophysics and Heat Transfer 23 (2009) 752-761.

[4] D.P. Kulkarni, D.K. Das, R.S. Vajjha, Application of nanofluids in heating buildings and reducing pollution, Applied Energy 86 (2009) 2566–2573.

[5] J. Buongiorno, L.W. Hu, S.J. Kim, R. Hannick, B. Truong, E. Forrest, Nanofluids for enhanced economics and safety of nuclear reactors: An evaluation of the potential features, issues, and research gaps, Nuclear Technology 162 (2008) 80-91.

[6] S.M. You, J.H. Kim, K.H. Kim, Effect of nanoparticles on critical heat flux of water in pool boiling heat transfer, Applied Physics Letters 83 (2003) 3374-3376.

[7] P. Vassallo, R. Kumar, S.D. Amico, Pool boiling heat transfer experiments in silica–water nanofluids, International Journal of Heat and Mass Transfer 47 (2004) 407–411.

[8] M.F. Demirbas, Thermal energy storage and phase change materials: an overview, Energy Sources, Part B: Economics, Planning, and Policy 1 (2006) 85-95.

[9] T.P. Otanicar, P.E. Phelan, R.S. Prasher, G. Rosengarten, R.A. Taylor, Nanofluid-based direct absorption solar collector, Journal of Renewable and Sustainable Energy 2 (033102) (2010) 1-13.

[10] J. Zhou, Z. Wu, Z. Zhang, W. Liu, Q. Xue, Tribological behaviour and lubricating mechanism of Cu nanoparticles in oil, Tribology Letters 8 (2000) 213–218.

[11] L. Vekas, D. Bica, M.V. Avdeev, Magnetic nanoparticles and concentrated magnetic nanofluids: Synthesis, properties and some applications, China Particuology 5 (2007) 43–49.

[12] L. Zhang, Y. Jiang, Y. Ding, M. Povey, D. York, Investigation into the antibacterial behaviour of suspensions of ZnO nanoparticles (ZnO nanofluids), Journal of Nanoparticle Research 9 (2007) 479–489.

[13] X. Sun, Z. Liu, K. Welsher, J.T. Robinson, A. Goodwin, S. Zaric, H. Dai, Nano-graphene oxide for cellular imaging and drug delivery, Nano Research 1 (2008) 203- 212.

[14] X. Fan, H. Chen, Y. Ding, P.K. Plucinski, A.A. Lapkin, Potential of 'nanofluids' to further intensify micro-reactors, Green Chemistry 10 (2008) 670–677.

[15] T. Sharma, A.L.M. Reddy, T.S. Chandra, S. Ramaprabhu, Development of carbon nanotubes and nanofluids based microbial fuel cell, International journal of hydrogen energy 33 (2008) 6749–6754.

[16] Energy, Why nanoparticles are better than micro-particles, in, Argonne National Laboratory, 2004.

[17] A.K. Santra, S. Sen, N. Chakraborty, Study of heat transfer augmentation in a differentially heated square cavity using copper–water nanofluid, International Journal of Thermal Sciences 47 (2008) 1113–1122.

[18] A.K. Santra, S. Sen, N. Chakraborty, Study of heat transfer characteristics of copper-water nanofluid in a differentially heated square cavity with different viscosity models, Journal of Enhanced Heat Transfer 15 (2008) 273-287.

[19] W. Rashmi, A.F. Ismail, M. Khalid, Y. Faridah, CFD studies on natural convection heat transfer of Al_2O_3-water nanofluids, Heat and Mass Transfer 47 (2011) 1301-1310.

[20] E. Abu-Nada, Z. Masoud, A. Hijazi, Natural convection heat transfer enhancement in horizontal concentric annuli using nanofluids, International Communication in Heat and Mass Transfer 35 (2008) 657–665.

[21] E. Abu-Nada, Effects of variable viscosity and thermal conductivity of Al_2O_3-water nanofluid on heat transfer enhancement in natural convection, International Journal of Heat and Fluid Flow 30 (2009) 679-690.

[22] S.Z. Heris, M.N. Esfahany, S.G. Etemad, Experimental investigation of convective heat transfer of Al_2O_3/water nanofluid in circular tube, International Journal of Heat and Fluid Flow 28 (2007) 203–210.

[23] K.S. Hwang, S.P. Jang, S.U.S. Choi, Flow and convective heat transfer characteristics of water-based Al_2O_3 nanofluids in fully developed laminar flow regime, International Journal of Heat and Mass Transfer 52 (2009) 193–199.

[24] K.B. Anoop, T. Sundararajan, S.K. Das, Effect of particle size on the convective heat transfer in nanofluid in the developing region, International Journal of Heat and Mass Transfer 52 (2009) 2189–2195.

[25] E. Esmaeilzadeh, H. Almohammadi, S.N. Vatan, A.N. Omrani, Experimental investigation of hydrodynamics and heat transfer characteristics of Al_2O_3/water under laminar flow inside a horizontal tube, International Journal of Thermal Sciences 63 (2013) 31-37.

[26] M.S. Mojarrad, A. Keshavarz, M. Ziabasharhagh, M.M. Raznahan, Experimental investigation on heat transfer enhancement of alumina/water and alumina/water–ethylene glycol nanofluids in thermally developing laminar flow, Experimental Thermal and Fluid Science 53 (2014) 111-118.

[27] R. Davarnejad, S. Barati, M. Kooshki, CFD simulation of the effect of particle size on the nanofluids convective heat transfer in the developed region in a circular tube, SpringerPlus 2: 192 (2013) 1-6.

[28] S.E.B. Maıga, S.J. Palm, C.T. Nguyen, G. Roy, N. Galanis, Heat transfer enhancement by using nanofluids in forced convection flows, International Journal of Heat and Fluid Flow 26 (2005) 530–546.

[29] E.E. Bajestan, H. Niazmand, W. Duangthongsuk, S. Wongwises, Numerical investigation of effective parameters in convective heat transfer of nanofluids flowing under a laminar flow regime, International Journal of Heat and Mass Transfer 54 (2011) 4376–4388.

[30] J. Bayat, A.H. Nikseresht, Investigation of the different base fluid effects on the nanofluids heat transfer and pressure drop, Heat and Mass Transfer 47 (2011) 1089–1099.

[31] M.K. Moraveji, M. Darabi, S.M.H. Haddad, R. Davarnejad, Modelling of convective heat transfer of a nanofluid in the developing region of tube flow with computational fluid dynamics, International Communications in Heat and Mass Transfer 38 (2011) 1291–1295.

[32] J. Lin, Y. Xia, X. Ku, Friction factor and heat transfer of nanofluids containing cylindrical nanoparticles in laminar pipe flow, Journal of Applied Physics 116 (133513) (2014) 1-11.

[33] S. Mirmasoumi, A. Behzadmehr, Effect of nanoparticles mean diameter on mixed convection heat transfer of a nanofluid in a horizontal tube, International Journal of Heat and Fluid Flow 29 (2008) 557–566.

[34] M.H. Fard, M.N. Esfahany, M.R. Talaie, Numerical study of convective heat transfer of nanofluids in a circular tube two-phase model versus single-phase model, International Communications in Heat and Mass Transfer 37 (2010) 91–97.

[35] S. Goktepe, K. Atalik, H. Erturk, Comparison of single and two-phase models for nanofluid convection at the entrance of a uniformly heated tube, International Journal of Thermal Sciences 80 (2014) 83-92.

[36] Y. He, Y. Mena, Y. Zhao, H. Lu, Y. Ding, Numerical investigation into the convective heat transfer of TiO_2 nanofluids flowing through a straight tube under the laminar flow conditions, Applied Thermal Engineering 29 (2009) 1965–1972.

[37] V. Bianco, F. Chiacchio, O. Manca, S. Nardini, Numerical investigation of nanofluids forced convection in circular tubes, Applied Thermal Engineering 29 (2009) 3632–3642.

[38] M.K. Moraveji, E. Esmaeili, Comparison between single-phase and two-phases CFD modelling of laminar forced convection flow of nanofluids in a circular tube under constant heat flux, International Communications in Heat and Mass Transfer 39 (2012) 1297–1302.

[39] I.I. Ryzhkov, A.V. Minakov, The effect of nanoparticles diffusion and thermophoresis on convective heat transfer of nanofluid in a circular tube, International Journal of Heat and Mass Transfer 77 (2014) 956-969.

[40] C.C. Tang, S. Tiwari, M.W. Cox, Viscosity and Friction Factor of Aluminum Oxide–Water Nanofluid Flow in Circular Tubes, Journal of Nanotechnology in Engineering and Medicine 4 (2013) 1-6.

[41] Y.A. Cengel, Heat Transfer: A Practical Approach, 2nd ed., McGraw Hill, New York, 2003.

[42] K.V. Sharma, L.S. Sundar, P.K. Sarma, Estimation of heat transfer coefficient and friction factor in the transition flow with low volume concentration of Al_2O_3 nanofluid flowing in a circular tube and with twisted tape insert, International Communications in Heat and Mass Transfer 36 (2009) 503-507.

[43] M. Chandrasekar, S. Suresh, A.C. Bose, Experimental studies on heat transfer and friction factor characteristics of Al_2O_3/water nanofluid in a circular pipe under transition flow with wire coil inserts, Heat Transfer Engineering 32 (2011) 485-496.

[44] M.T. Naik, G.R. Janardana, L.S. Sundar, Experimental investigation of heat transfer and friction factor with water–propylene glycol based CuO nanofluid in a tube with twisted tape inserts, International Communications in Heat and Mass Transfer 46 (2013) 13-21.

[45] J.P. Meyer, T.J. McKrell, K. Grote, The influence of multi-walled carbon nanotubes on single-phase heat transfer and pressure drop characteristics in the transitional flow regime of smooth tubes, International Journal of Heat and Mass Transfer 58 (2013) 597–609.

[46] L. Qiang, X. Yimin, Convective heat transfer and flow characteristics of Cu-water nanofluid, Science in China (Series E) 45 (2002) 408-416.

[47] Y. Xuan, Q. Li, Investigation on convective heat transfer and flow features of nanofluids, Journal of Heat Transfer 125 (2003) 151–155.

[48] R.B. Mansour, N. Galanis, C.T. Nguyen, Effect of uncertainties in physical properties on forced convection heat transfer with nanofluids, Applied Thermal Engineering 27 (2007) 240–249.

[49] D. Kim, Y. Kwon, Y. Cho, C. Li, S. Cheong, Y. Hwang, J. Lee, D. Hong, S. Moon, Convective heat transfer characteristics of nanofluids under laminar and turbulent flow conditions, Current Applied Physics 9 (2009) 119–123.

[50] S.M. Fotukian, M.N. Esfahany, Experimental investigation of turbulent convective heat transfer of dilute γ-Al_2O_3-water nanofluid inside a circular tube, International Journal of Heat and Fluid Flow 31 (2010) 606–612.

[51] A.R. Sajadi, M.H. Kazemi, Investigation of turbulent convective heat transfer and pressure drop of TiO_2-water nanofluid in circular tube, International Communications in Heat and Mass Transfer 38 (2011) 1474–1478.

[52] S. Torii, Turbulent heat transfer behaviour of nanofluid in a circular tube heated under constant heat flux, Advances in Mechanical Engineering 917612 (2010) 1-7.

[53] M.H. Kayhani, H. Soltanzadeh, M.M. Heyhat, M. Nazari, F. Kowsary, Experimental study of convective heat transfer and pressure drop of TiO_2/water nanofluid, International Communications in Heat and Mass Transfer 39 (2012) 456-462.

[54] L.S. Sundar, M.T. Naik, K.V. Sharma, M.K. Singh, T.C.S. Reddy, Experimental investigation of forced convection heat transfer and friction factor in a tube with Fe_3O_4 magnetic nanofluid, Experimental Thermal and Fluid Science 37 (2012) 65–71.

[55] M.H. Esfe, S. Saedodin, M. Mahmoodi, Experimental studies on the convective heat transfer performance and thermophysical properties of MgO–water nanofluid under turbulent flow, Experimental Thermal and Fluid Science 52 (2014) 68-78.

[56] W.H. Azmi, K.V. Sharma, P.K. Sarma, R. Mamat, G. Najafi, Heat transfer and friction factor of water based TiO_2 and SiO_2 nanofluids under turbulent flow in a tube, International Communications in Heat and Mass Transfer 59 (2014) 30-38.

[57] A.R. Pouranfard, D. Mowla, F. Esmaeilzadeh, An experimental study of drag reduction by nanofluids through horizontal pipe turbulent flow of a Newtonian liquid, Journal of Industrial and Engineering Chemistry 20 (2014) 633-637.

[58] B.C. Pak, Y.I. Cho, Hydrodynamic and heat transfer study of dispersed fluids with submicron metallic oxide particles, Experimental Heat Transfer 11 (1998) 151-170.

[59] S.E.B. Maiga, C.T. Nguyen, N. Galanis, G. Roy, T. Mare, M. Coqueux, Heat transfer enhancement in turbulent tube flow using Al_2O_3 nanoparticles suspension, International Journal of Numerical Methods for Heat and Fluid Flow 16 (2006) 275-292.

[60] V. Bianco, O. Manca, S. Nardini, Numerical investigation on nanofluids turbulent convection heat transfer inside a circular tube, International Journal of Thermal Sciences 50 (2011) 341-349.

[61] P.K. Namburu, D.K. Das, K.M. Tanguturi, R.S. Vajjha, Numerical study of turbulent flow and heat transfer characteristics of nanofluids considering variable properties, International Journal of Thermal Sciences 48 (2009) 290–302.

[62] P. Kumar, A CFD study of heat transfer enhancement in pipe flow with Al_2O_3 nanofluid, World Academy of Science, Engineering and Technology 81 (2011) 746-750.

[63] A. Behzadmehr, M. Saffar-Avval, N. Galanis, Prediction of turbulent forced convection of a nanofluid in a tube with uniform heat flux using a two phase approach, International Journal of Heat and Fluid Flow 28 (2007) 211-219.

[64] M. Akbari, N. Galanis, A. Behzadmehr, Comparative assessment of single and two-phase models for numerical studies of nanofluid turbulent forced convection International Journal of Heat and Fluid Flow 37 (2012) 136-146.

[65] M. Hejazian, M.K. Moraveji, A. Beheshti, Comparative study of Euler and mixture models for turbulent flow of Al_2O_3 nanofluid inside a horizontal tube, International Communications in Heat and Mass Transfer 52 (2014) 152-158.

[66] V. Bianco, O. Manca, S. Nardini, Performance analysis of turbulent convection heat transfer of Al_2O_3 water-nanofluid in circular tubes at constant wall temperature, Energy 77 (2014) 403-413.

[67] V. Bianco, O. Manca, S. Nardini, Entropy generation analysis of turbulent convection flow of Al_2O_3–water nanofluid in a circular tube subjected to constant wall heat flux, Energy Conversion and Management 77 (2014) 306-314.

[68] Fluent 6.3 user guide, Fluent Inc., Lebanon, 2006.

[69] M. Manninen, V. Taivassalo, S. Kallio, On the mixture model for multiphase flow, Technical research centre of Finland 288 (1996) 9-18.

[70] A. Naumann, L. Schiller, A drag coefficient correlation, Z. Ver. Deutsch. Ing., 77 (1935) 318-320.

[71] A. Nicholas, S., C. Markatos, G., Transient flow and heat transfer of liquid sodium coolant in the outlet plenum of a fast nuclear reactor, International Journal of Heat and Mass Transfer 21 (1978) 1565-1579.

[72] E. Bacharoudis, M. Vrachopoulos, M.K. Koukou, D. Margaris, A.E. Filios, S.A. Mavrommatis, Study of the natural convection phenomena inside a- wall solar chimney with one wall adiabatic and one wall under a heat flux, Applied Thermal Engineering 27 (2007) 2266-2275.

[73] D.C. Wilcox, Turbulence Modelling for CFD, DCW Industries, Inc., La Canada, California, 1998.

[74] F.R. Menter, Two-equation eddy-viscosity turbulence models for engineering applications, AIAA Journal 32 (1994) 1598-1605.

[75] T.H. Shih, W.W. Liou, A. Shabbir, Z. Yang, J. Zhu, A new k-ϵ eddy viscosity model for high Reynolds number turbulent flows, Computers Fluids 24 (3) (1995) 227-238.

[76] B.E. Launder, D.B. Spalding, Lectures in mathematical models of turbulence, Academic Press, London, England, 1972.

[77] V. Yakhot, A.S. Orszag, S. Thangam, G.C. Speziale, Development of turbulence models for shear flows by a double expansion technique, Phys. Fluids 4 (1992) 1510-1521.

[78] J. Buongiorno, Convective transport in nanofluids, Journal of Heat Transfer 128 (2006) 240-250.

[79] M. Corcione, Empirical correlating equations for predicting the effective thermal conductivity and dynamic viscosity of nanofluids, Energy Conversion and Management 52 (2011) 789-793.

[80] W.M. Kays, M.E. Crawford, Convection heat and mass transfer, 2nd ed., McGraw Hill, New York, 1980.

[81] H. Masuda, A. Ebata, K. Teramae, N. Hishinuma, Alternation of thermal conductivity and viscosity of liquid by dispersing ultra-fine particles (dispersion of Al_2O_3, SiO_2 and TiO_2 ultra-fine particles), Netsu Bussei 40 (1993) 227-233.

[82] R.W. Powell, C.Y. Ho, P.E. Liley, Thermal conductivity of selected materials, United states department of commerce, National Bureau of standards, 1962.

[83] S.J. Smith, R. Stevens, S. Liu, G. Li, A. Navrotsky, J.B. Goates, B.F. Woodfield, Heat capacities and thermodynamic functions of TiO_2 anatase and rutile: analysis of phase stability, Am. Mineral 94 (2009) 236-243.

[84] T. Cebeci, P. Bradshaw, Momentum Transfer in Boundary Layers, Hemisphere Publishing Corporation, New York, 1977.

[85] A. Bejan, Entropy generation minimization, Boca Raton: CRC Press, 1996.

[86] E.B. Ratts, A.G. Raut, Entropy generation minimization of fully developed internal flow with constant heat flux, Journal of Heat Transfer 126 (2004) 656-659.

[87] K. Xu, B. Ruan, H. Meng, A thermal performance factor for evaluation of active engine cooling with asymmetric heating, Applied Thermal Engineering 73 (2014) 351-356.

[88] G. Roy, L. Gherasim, F. Nadeau, G. Poitras, C.T. Nguyen, Heat transfer performance and hydrodynamic behaviour of turbulent nanofluid radial flows, International Journal of Thermal Sciences 58 (2012) 120-129.

[89] O. Reynolds, An experimental investigation of the circumstances which determine whether the motion of water shall be direct or sinuous, and of the law of resistance in parallel channels, Philosophical Transactions of the Royal Society of London 174 (1883) 935-982.

[90] V.W. Ekman, On the change from steady to turbulent motion of liquids, Ark. f. Mat. Astron. Och Fys. 6 (12) (1910).

[91] W. Pfenniger, Boundary layer and flow control, LACHMAN, G. V. ed., Pergamon, 1961.

[92] L. Xiao-wei, M. Ji-an, L. Zhi-xin, Roughness enhanced mechanism for turbulent convective heat transfer, International Journal of Heat and Mass Transfer 54 (2011) 1775–1781.

[93] H. Blasius, Grenzschichten in Flussigkeiten mit kleiner reibung (German), Z. Math. Physics 56 (1908) 1-37.

[94] V. Gnielinski, New equations for heat and mass transfer in turbulent pipe and channel flow, International Chemical Engineering 16 (1976) 359-368.

[95] John Laufer, The structure of turbulence in fully developed pipe flow, Technical Note: 2954. National Bureau of Standards, NACA, Washington, 1953.

[96] S.W. Kim, A near-wall turbulence model and its application to fully developed turbulent channel and pipe flows, NASA Technical Memorandum 101399, 1988.

[97] J.P. Abraham, E.M. Sparrow, J.C.K. Tong, Heat transfer in all pipe flow regimes: laminar, transitional/intermittent, and turbulent, International Journal of Heat and Mass Transfer 52 (2009) 557-563.

[98] M. Schildknecht, J.A. Miller, G.E.A. Meier, The influence of suction on the structure of turbulence in fully developed pipe flow, Journal of Fluid Mechanics 90 (1979) 67-107.

[99] B.E. Launder, B.I. Sharma, Application of the energy-dissipation model of turbulence to the calculation of flow near a spinning disc, Letters in Heat Mass Transfer 1 (1974) 131-138.

[100] K.Y. Chien, Predictions of channel and boundary layers and heat transfer along compressor and turbine blades, Numerical Methods in Heat Transfer 19 (1982) 413-429.

[101] S. Fan, B. Lakshminarayana, M. Barnett, Low-Reynolds-number k-ϵ model for unsteady turbulent boundary-layer flows, Journal of AIAA 31 (1993) 1777-1784.

[102] W.P. Jones, B.E. Launder, The prediction of laminarization with a two-equation model of turbulence, International Journal of Heat and Mass Transfer 15 (1972) 301-314.

[103] W.P. Jones, B.E. Launder, The calculation of low-Reynolds-number phenomena with a two-equation model of turbulence, International Journal of Heat and Mass Transfer 16 (1973) 1119-1130.

[104] Y.G. Lai, R.M.C. So, On near-wall turbulent flow modelling, Journal of Fluid Mechanics 221 (1990) 641-673.

[105] H.K. Myong, N. Kasagi, A new approach to the improvement of k-ϵ turbulence model for wall-bounded shear flows, International Journal of JSME 33 (1990) 63-72.

[106] B.S. Petukhov, Heat transfer and friction in turbulent pipe flow with variable physical properties, New York, 1970.

[107] R.H. Notter, M.W. Rouse, A solution to the Graetz problem-III. Fully developed region heat transfer rates, Chemical Engineering Science 27 (1972) 2073-2093.

[108] S. Lee, S.U.S. Choi, S. Li, J.A. Eastman, Measuring thermal conductivity of fluids containing oxide nanoparticles, Journal of Heat Transfer 121 (1999) 280-289.

[109] X. Wang, X. Xu, S.U.S. Choi, Thermal conductivity of liquid with suspension of nanoparticles-fluid mixture, Journal of Thermophysics and Heat Transfer 13 (1999) 474-480.

[110] A. Einstein, Investigating on the theory of Brownian motion, New York, 1956.

[111] H.C. Brinkman, The viscosity of concentrated suspensions and solution, Journal of Chemical Physics 20 (1952) 571-581.

[112] S.E.B. Maiga, C.T. Nguyen, N. Galanis, G. Roy, T. Mare, M. Coqueux, Heat transfer enhancement in forced convection laminar tube flow by using nanofluids, in: CHT-04 International Symposium Advances Computational heat Transfer, Norway, 2004, pp. 25.

[113] R.L. Hamilton, O.K. Crosser, Thermal conductivity of heterogeneous two-component systems, I and EC Fundamentals 1 (1962) 187-191.

[114] S.K. Das, S.U.S. Choi, W. Yu, T. Pradeep, Nanofluids science and technology, John Wiley and Sons, 2008.

[115] R. Mosurkal, L.A. Samuelson, K.D. Smith, P.R. Westmoreland, V.S. Parmar, F. Yan, Nanocomposites of TiO_2 and siloxane copolymers as environmentally safe flame retardant materials, Journal of Macromolecular Science Part A Pure and Applied Chemistry 45 (2008) 924–946.

[116] R.K. Shah, A.L. London, Laminar flow forced convection in ducts, Supplement 1 to Advances in Heat Transfer, Academic Press, New York, 1978.

[117] A.A.A. Arani, J. Amani, Experimental investigation of diameter effect on heat transfer performance and pressure drop of TiO_2-water nanofluid, Experimental Thermal and Fluid Science 44 (2013) 520-533.

[118] D.S. Wen, Y.L. Ding, Effect on heat transfer of particle migration in suspensions of nanoparticles flowing through microchannels, Microfluid Nanolfuid, 1 (2005) 183-189.

[119] P. Keblinski, S.R. Phillpot, S.U.S. Choi, J.A. Eastman, Mechanisms of heat flow in suspensions of nanosized particles (nanofluids), International Journal of Heat and Mass Transfer 45 (2002) 855-863.

[120] Y. He, Y. Jin, H. Chen, Y. Ding, D. Cang, H. Lu, Heat transfer and flow behaviour of aqueous suspensions of TiO_2 nanoparticles (nanofluids) flowing upward through a vertical pipe, International Journal of Heat and Mass Transfer 50 (2007) 2272–2281.

[121] M. Akbari, A. Behzadmehr, F. Shahraki, Fully developed mixed convection in horizontal and inclined tubes with uniform heat flux using nanofluid, International Journal of Heat and Fluid Flow 29 (2008) 545–556.

[122] R.B. Mansour, N. Galanis, C.T. Nguyen, Experimental study of mixed convection with water-Al_2O_3 nanofluid in inclined tube with uniform wall heat flux, International Journal of Thermal Sciences 50 (2011) 403-410.